



UNIVERSITÀ DEGLI STUDI DI MILANO
DIPARTIMENTO DI BIOSCIENZE



UNIVERSITÀ DEGLI STUDI DI MILANO

Corso di Dottorato in Biologia molecolare e cellulare
XXXIII Ciclo

Dipartimento di Bioscienze

Tesi di dottorato di ricerca

**Cholesterol dysfunction in Huntington's disease:
working toward a therapeutical approach**

Giulia Birolini

Scientific tutor: Prof. Elena Cattaneo

Coordinator of the PhD School: Prof. Martin Kater

Academic year: 2019-2020

Table of content

p. 5	Abstract in English
p. 6	Abstract in Italian
p. 7	Aim
p. 8	1. Introduction
p. 8	1.1 Brain cholesterol in physiological condition
p. 8	1.1.1 Cholesterol roles in the brain
p. 9	1.1.2 Cholesterol synthesis in the brain
p. 11	1.1.3 Cross-talk between neurons and astrocytes
p. 12	1.1.4 Cholesterol elimination from the brain
p. 13	1.2 Brain cholesterol defect in Huntington's disease
p. 13	1.2.1 Huntington's disease genetics and clinical manifestation
p. 14	1.2.2 Huntington's disease neuropathological features
p. 15	1.2.3 Huntingtin (HTT) gain and loss of function
p. 18	1.2.4 Cholesterol dysfunction in Huntington's disease: evidences in mouse models
p. 20	1.2.5 Cholesterol dysfunction in Huntington's disease: evidences in patients
p. 20	1.2.6 The molecular mechanism underlying cholesterol dysfunction in Huntington's disease
p. 22	1.3 Brain cholesterol alterations in other neurodegenerative diseases
p. 22	1.3.1 Cholesterol and Niemann-Pick type C disease
p. 22	1.3.2 Cholesterol and Smith-Lemli-Opitz syndrome
p. 23	1.3.3 Cholesterol and Alzheimer's disease
p. 24	1.3.4 Cholesterol and Parkinson's disease
p. 25	1.4 Mouse models of Huntington's disease
p. 25	1.4.1 R6/2 mice
p. 27	1.4.2 zQ175DN mice
p. 28	1.5 Cholesterol delivery to the brain of HD mice
p. 28	1.5.1 First generation brain-permeable nanoparticles
p. 29	1.5.2 Osmotic minipumps
p. 30	1.5.3 Intranasal delivery
p. 31	1.5.4 Second generation brain-permeable nanoparticles

p. 32	2. Results and Discussion
p. 32	2.1 g7-NPs-<i>chol_2.0</i> cross the blood-brain barrier and reach different cell types in the brain
p. 36	2.2 Cholesterol is released from g7-NPs-<i>chol_2.0</i> in vivo
p. 36	2.2.1 Qualitative analysis
p. 39	2.2.2 Quantitative analysis
p. 43	2.3 Cholesterol delivery to the brain: comparison between g7-NPs-<i>chol_1.0</i> and g7-NPs-<i>chol_2.0</i>
p. 43	2.3.1 Endogenous cholesterol synthesis is influenced by g7-NPs- <i>chol_2.0</i>
p. 45	2.3.2 Cholesterol delivery prevents cognitive decline and ameliorate motor deficits in R6/2 mice in a dose-dependent manner
p. 50	2.4 Administration of g7-NPs-<i>chol_2.0</i> does not solicit a massive inflammation response
p. 53	2.5 Long term and cyclic treatments of g7-NPs-<i>chol_2.0</i> in zQ175DN mice ameliorate HD-related behavioral deficits
p. 60	2.6 Setting up of an in vivo paradigm for SREBP2 delivery to brain astrocytes
p. 63	2.6.1 In vivo characterization of AAV2/5-gfaABC1D-TdTomato and AAV2/5-gfaABC1D-hSREBP2-TdTomato
p. 66	2.6.2 Gene expression analysis of SREBP2-related pathways and cholesterol metabolism
p. 70	2.7 Glial hSREBP2 normalizes the level of some presynaptic proteins in synaptosomes from cortico-striatal tissues of R6/2 mice
p. 73	2.8 Glial hSREBP2 rescues mutant Huntingtin (<i>muHTT</i>) aggregation in the striatum of R6/2 mice
p. 74	2.9 Glial hSREBP2 restores the number of DRD2-positive MSNs in the striatum of R6/2 mice
p. 77	2.10 Glial hSREBP2 normalizes synaptic transmission of striatal neurons in R6/2 mice
p. 80	2.11 Glial hSREBP2 restores behavioral deficits in R6/2 mice
p. 83	3. Conclusions and Future Perspectives
p. 86	4. Materials and Methods
p. 86	4.1 Mice colony management
p. 86	4.2 Mice treatment
p. 86	4.2.1 NPs injections
p. 87	4.2.2 Viral injection

p. 87	4.3 IHC
p. 87	4.3.1 <i>In vivo</i> analysis of biodistribution and cholesterol release of g7-NPs- <i>chol</i> _2.0
p. 88	4.3.2 <i>Viral spread and tropism</i>
p. 89	4.3.3 <i>Mutant Huntingtin (muHTT) aggregates analysis</i>
p. 89	4.4 Image acquisition and quantification
p. 89	4.4.1 <i>In vivo</i> analysis of biodistribution and cholesterol release of g7-NPs- <i>chol</i> _2.0
p. 89	4.4.2 <i>Viral spread and tropism</i>
p. 90	4.4.3 <i>Mutant Huntingtin (muHTT) aggregates</i>
p. 90	4.5 Quantification analysis of d6-cholesterol
p. 90	4.6 Gas chromatography-mass spectrometry (GC-MS) analysis for neutral sterols and 24S-OHC
p. 90	4.7 Bioplex assay
p. 91	4.8 RNA extraction and qRT-PCR
p. 93	4.9 Synaptosomes preparation and Western Blot analysis
p. 94	4.10 X-Clarity and 2-photon imaging
p. 94	4.11 Behavioral tests
p. 95	4.12 Electrophysiological analysis
p. 95	4.13 Statistics
p. 97	5. References
p. 116	6. Appendix
p. 116	6.1 Contribution to published articles
p. 116	6.1.1 <i>Efficacy of Cholesterol Nose-to-Brain Delivery for Brain Targeting in Huntington's disease</i>
p. 117	6.1.2 <i>Striatal infusion of cholesterol promotes a dose-dependent behavioral benefit and exerts disease-modifying effects in Huntington's disease mice</i>
p. 118	6.2 Contribution to in progress articles
p. 118	6.2.1 <i>SREBP2 delivery to striatal astrocytes enhances brain cholesterol biosynthesis defect and ameliorates pathological features in Huntington's disease</i>
p. 119	6.2.2 <i>Brain-targeted hybrid nanoparticles boost cholesterol delivery to the central nervous system and rescues behavioral phenotypes in Huntington's disease</i>

Abstract in English

Cholesterol is a multifaceted membrane component particularly enriched in neurons and it is essential for brain function. In the adult brain, cholesterol is locally produced by astrocytes and transferred to neurons. Disruption of brain cholesterol pathways has been linked to several neurological diseases, including Huntington's disease (HD). HD is a genetic, neurodegenerative disorder caused by a CAG expansion in the gene encoding the huntingtin protein leading to behavioral deficits, synaptic dysfunction, and neuronal loss. Brain cholesterol biosynthesis and content are reduced in several HD models due to reduced activity of SREBP2, the transcription factor that regulates cholesterol synthesis. Abnormalities in brain cholesterol homeostasis are also detectable in HD patients since 24-hydroxy-cholesterol, a cholesterol catabolite that is brain specific and able to cross the blood-brain barrier, is progressively reduced in their plasma. Of note, the delivery of cholesterol to the HD brain via systemic administration of brain-permeable polymeric nanoparticles (g7-NPs-cho1_1.0) or directly into the striatum using osmotic-minipumps rescued key features of the disease.

Here, to transform these results into a testable therapeutic strategy for humans, we characterized *in vivo* second generation g7-NPs (g7-NPs-cho2_2.0), with an enhanced cholesterol loading capacity compared to g7-NPs-cho1_1.0, to deliver the proper amount of cholesterol to the brain without side effects. Furthermore, we showed that multiple cycles of g7-NPs-cho2_2.0 treatments lead to complete and long-term behavioral amelioration.

Finally, to test the impact of forced SREBP2 expression within HD brain, we used AAV2/5 to deliver SREBP2 in astrocytes. We found that exogenous SREBP2 stimulates the transcription of cholesterol biosynthesis genes resulting in restoration of synaptic transmission and rescue of behavioral deficits.

These results suggested that providing exogenous cholesterol or stimulating its biosynthesis in HD brain has a positive effect on behavioral decline and HD-related phenotypes, highlighting the translational potential of cholesterol-based strategies for this tremendous disease.

Abstract in Italian

Il colesterolo cerebrale, prodotto localmente dagli astrociti, è un componente essenziale per l'attività neuronale. Difetti del metabolismo del colesterolo cerebrale sono spesso stati collegati a malattie neurologiche, tra cui la Corea di Huntington (MH), una malattia genetica neurodegenerativa causata dall'espansione del tratto CAG nel gene che codifica per la proteina Huntingtina. La MH è caratterizzata da disturbi comportamentali, sinaptici e morte neuronale. La sintesi e, di conseguenza, i livelli di colesterolo sono ridotti nel cervello di numerosi modelli animali MH a causa della ridotta attività di SREBP2, il fattore di trascrizione che ne regola la sintesi. Anomalie nel metabolismo del colesterolo cerebrale sono misurabili anche nei pazienti MH.

La somministrazione di colesterolo al cervello di animali MH attraverso nanoparticelle polimeriche in grado di attraversare la BEE (g7-NPs-cho1_1.0) o direttamente nello striato tramite mini-pompe osmotiche ha portato ad un miglioramento di una serie di difetti tipici della malattia.

Con l'obiettivo di traslare questi risultati in una strategia terapeutica per l'uomo, sono state sviluppate nanoparticelle di seconda generazione (g7-NPs-cho1_2.0) in grado di veicolare più colesterolo rispetto alle g7-NPs-cho1_1.0. Tali NPs sono state testate *in vivo* per verificarne l'efficacia e l'eventuale presenza di effetti collaterali. Inoltre, è stato dimostrato che trattamenti ciclici con g7-NPs-cho1_2.0 portano ad un completo miglioramento comportamentale a lungo termine.

Infine, per studiare il ruolo di SREBP2 *in vivo*, abbiamo sovra-espresso questo fattore trascrizionale negli astrociti per aumentare la sintesi endogena del colesterolo nello striato di topi MH. L'over-espressione di SREBP2 mediata da AAV2/5 ha portato ad un aumento significativo della sintesi endogena del colesterolo cerebrale con conseguente ripristino della trasmissione sinaptica e recupero dei deficit comportamentali.

Questi risultati suggeriscono che strategie terapeutiche atte a ripristinare l'omeostasi del colesterolo nel cervello possono migliorare i fenotipi correlati alla MH.

Aim

An increasing number of studies highlights the importance of cholesterol homeostasis for brain function. Accordingly, disruption of brain cholesterol synthesis and/or catabolism has been linked to several neurological disorders, including Huntington's disease (HD). In particular, it has been shown that cholesterol biosynthesis - as judged by the measurement of cholesterol precursors by means of isotopic dilution mass spectrometry (ID-MS) - is reduced in the brain of different HD rodent models since pre-symptomatic stages of the disease. As a consequence, cholesterol content is reduced at later stages of the disease, likely contributing to impair cognition and synaptic transmission. Interestingly, it has been shown that the delivery of cholesterol to the brain through brain-permeable polymeric nanoparticles (g7-NPs-cho1_1.0) reversed synaptic alterations and prevented cognitive defects in R6/2 mice, a transgenic HD mouse model with a strong and fast-developing phenotype. Moreover, using osmotic-minipumps to infuse cholesterol directly into the striatum of R6/2 mice, the therapeutic dose able to rescue synaptic morphology and transmission, revers mutant Huntingtin aggregation, and prevent both cognitive and motor defects has been identified.

Based on these evidences, the aims of my thesis were to:

- 1) test *in vivo* the translational potential of cholesterol delivery to the brain in two different HD mouse models through second-generation nanoparticles (g7-NPs-cho1_2.0) as a future therapeutic approach in HD;
- 2) investigate the relevance *in vivo* of the molecular mechanism underlying cholesterol dysfunction in HD and the role of cholesterol cross-talk between astrocytes and neurons in HD mice through viral delivery of the active form of SREBP2, the transcription factor that activates cholesterol biosynthesis genes.

1. Introduction

1.1 Brain cholesterol in physiological condition

1.1.1 Cholesterol roles in the brain

Though accounting for only 2% of body weight, the brain is the most cholesterol-rich organ, with about 25% of the whole body's cholesterol (1, 2). The amount of cholesterol within the brain is 15–30 mg/g tissue, whereas the average in other tissues is 2–3 mg/g (3).

Brain cholesterol is essentially unesterified (>99.5%) and it is located in myelin sheaths (>70%) and at the plasma membranes of astrocytes and neurons (1, 4). Small amounts of desmosterol and cholesteryl ester are also present (5).

Circulating or dietary cholesterol can not cross the blood-brain barrier (BBB) (1), so almost all brain cholesterol depends on endogenous biosynthesis (6). Although brain cholesterol homeostasis is maintained constant during the entire life by the equilibrium among *de novo* synthesis, transport, storage, removal, and recycle, the concentration of total cholesterol varies markedly during those periods of development when brain size and degree of myelination are also rapidly changing. In mice, the highest cholesterol synthesis rate occurs during the first postnatal weeks, concomitantly with the peak of

myelination process. After myelination, brain cholesterol metabolism is characterized by a very low turnover, with estimated half-life of 2–6 months in rodents and 5 years in humans (6, 7).

Cholesterol plays many fundamental roles in the CNS: (i) up to 70% of brain cholesterol serves as a structural component of cellular membranes and myelin (1); (ii) it is the precursor of steroid hormones, which are involved in the modulation of receptor activity and in the regulation of myelination, and growth of axons and dendrites (8, 9); (iii) it is essential for normal brain development by promoting synaptogenesis, differentiation of dendrites and stability of presynaptic transmitter release (10, 11, 12); (iv) it is a structural component of membranes in neurons and glial cells and it acts by reducing membrane fluidity, thus providing a better permeability barrier, hindering membrane protein diffusion (13); (v) it is required for neurotransmitter release (14, 15, 16), and for axonal guidance.

For these reasons, cholesterol depletion leads to synaptic and dendritic spine degeneration, failed neurotransmission, and decreased synaptic plasticity (17).

Thus, cholesterol homeostasis must be finely regulated and cholesterol synthesis and metabolism must be in equilibrium.

1.1.2 Cholesterol synthesis in the brain

The pathway responsible for cholesterol synthesis occurs in the endoplasmic reticulum (ER) and it is described in Fig. 1.1.

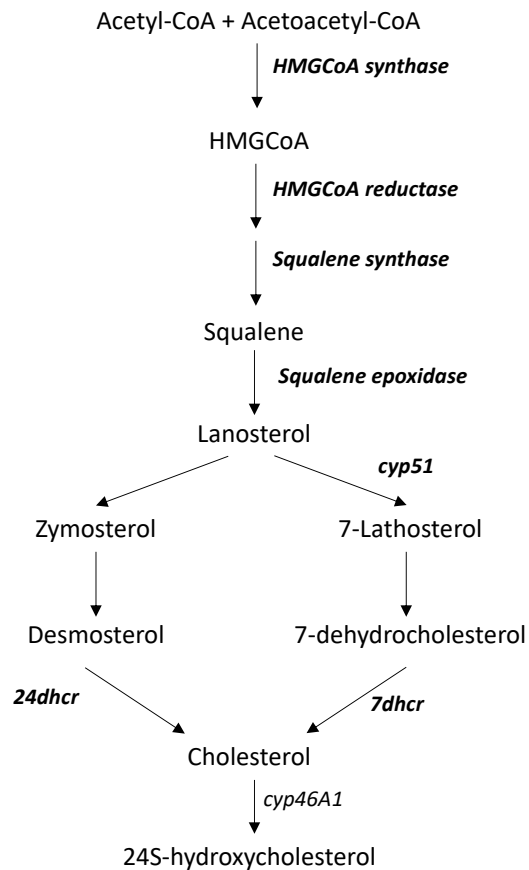


Figure 1.1 Cholesterol biosynthetic pathway

Cholesterol biosynthesis occurs through a series of steps, with the rate-limiting one being catalyzed by the highly regulated hydroxymethylglutaryl-coenzyme A reductase (HMGCR).

Isoprenoid intermediates of this pathway serve as precursors for several lipids involved in electron transport (heme A, ubiquinone), glycoprotein synthesis (dolichol) and protein prenylation (FPP, GGPP). After the production of the key sterol intermediate lanosterol, the route branches in the Bloch pathway and the Kandutsch-Russell pathway, respectively having desmosterol and 7-dehydrocholesterol as cholesterol precursors.

There are two cholesterologenic pathways in the brain: the Kandutsch-

Russel cholesterol synthetic pathway, and the Bloch pathway. In the past, the two ways were thought to be typical of neurons and astrocytes respectively (18, 19). Recently, by using stable isotope labeling and isotopomer analysis to trace sterol flux through the two pathways in mice, it has been clearly shown that use of the Bloch and Kandutsch-Russel pathways is highly variable and depends on tissues (20). Transcriptional regulation of cholesterol synthesis depends on the transcription factors sterol regulatory element binding proteins (SREBPs) (21, 22). In humans, three different SREBP isoforms were identified: SREBP1A, SREBP1C and SREBP2. SREBP1A is constitutively expressed and it targets all genes containing sterol response elements (SRE). By contrast, SREBP1C and SREBP2 are responsible for the expression of genes involved in fatty-acid and cholesterol metabolism respectively (23). SREBPs are synthesized as transcriptionally inactive precursors in the ER. When cholesterol levels are low, SREBP2 is cleaved by SREBP cleavage activation protein (SCAP), leading to SREBP2 activation and translocation from the ER to the Golgi apparatus. Within the Golgi, SREBP2 is cleaved by two proteases, site 1 (S1P) and site 2 (S2P), resulting into an active 68-kDa N-terminal fragment that moves to the nucleus, binds SRE

in the promoters of target genes and activates their transcription (3, 22, 24). When cells do not need to produce cholesterol, this process does not

occur because SREBP2 is retained in the ER by insulin-induced genes (INSIG1 and INSIG2) proteins (25) (Fig. 1.2).

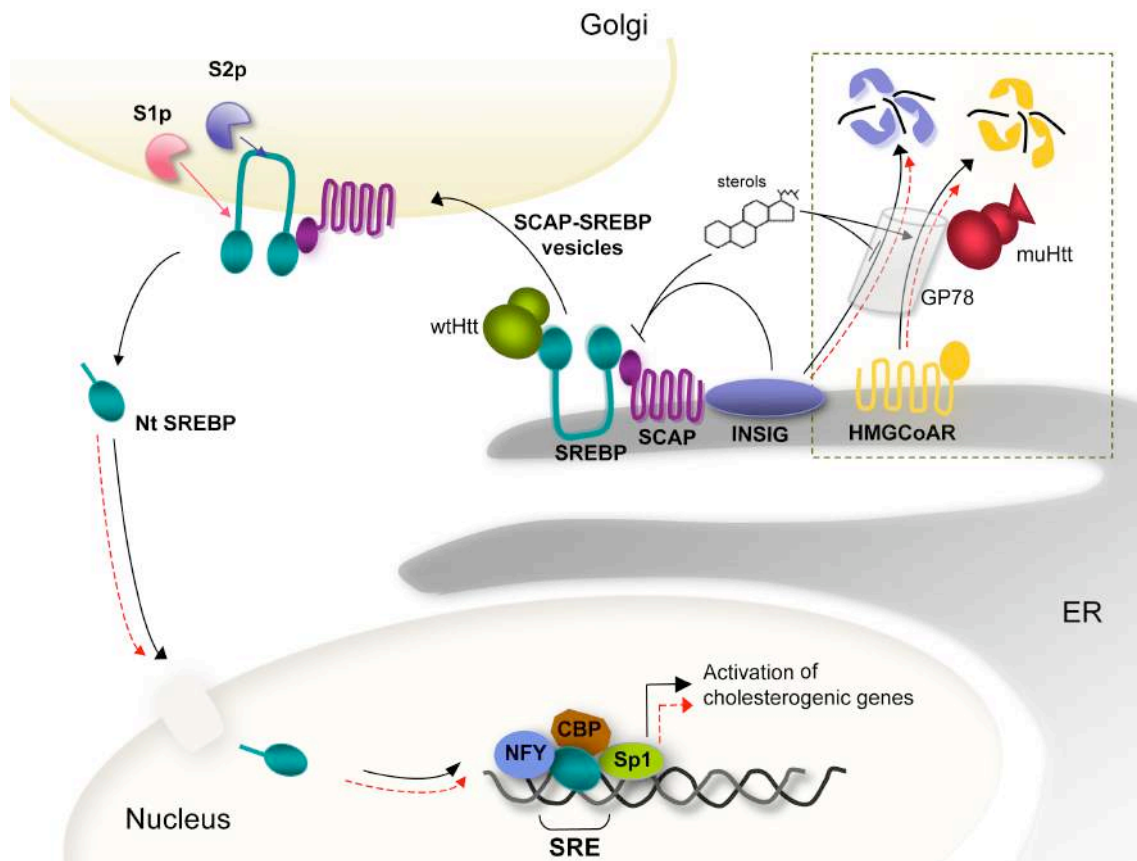


Figure 1.2 SREBP2 pathway

Schematic representation of how SREBP2 regulates cholesterol production in physiological (black arrows) and pathological (red arrows) conditions.

From Valenza & Cattaneo, *TINS*, 2011

The importance of SCAP was confirmed by evidence of reduced mRNA level of *Srebp2* and SRE-genes, reduced cholesterol content, brain morphology changes, gliosis, and impaired synaptic transmission and cognitive function in SCAP knockout mice (26). Furthermore, deletion of SCAP in astrocytes during the peak of myelination led to persistent CNS hypomyelination (27). Finally, deletion of SCAP in adulthood led to microcephaly, loss of cholesterol and

fatty acid synthesis, increased uptake of dietary lipids, progressive motor defects, dyskinesia, and premature death (28). The deletion of cholesterol synthesis by SREBP2 depletion in astrocytes resulted in a reduction of *Srebp2* transcript level: total brain cholesterol content was decreased 10–15% and mice suffered from microcephaly, reduced brain weight, and motor and cognitive abnormalities (29).

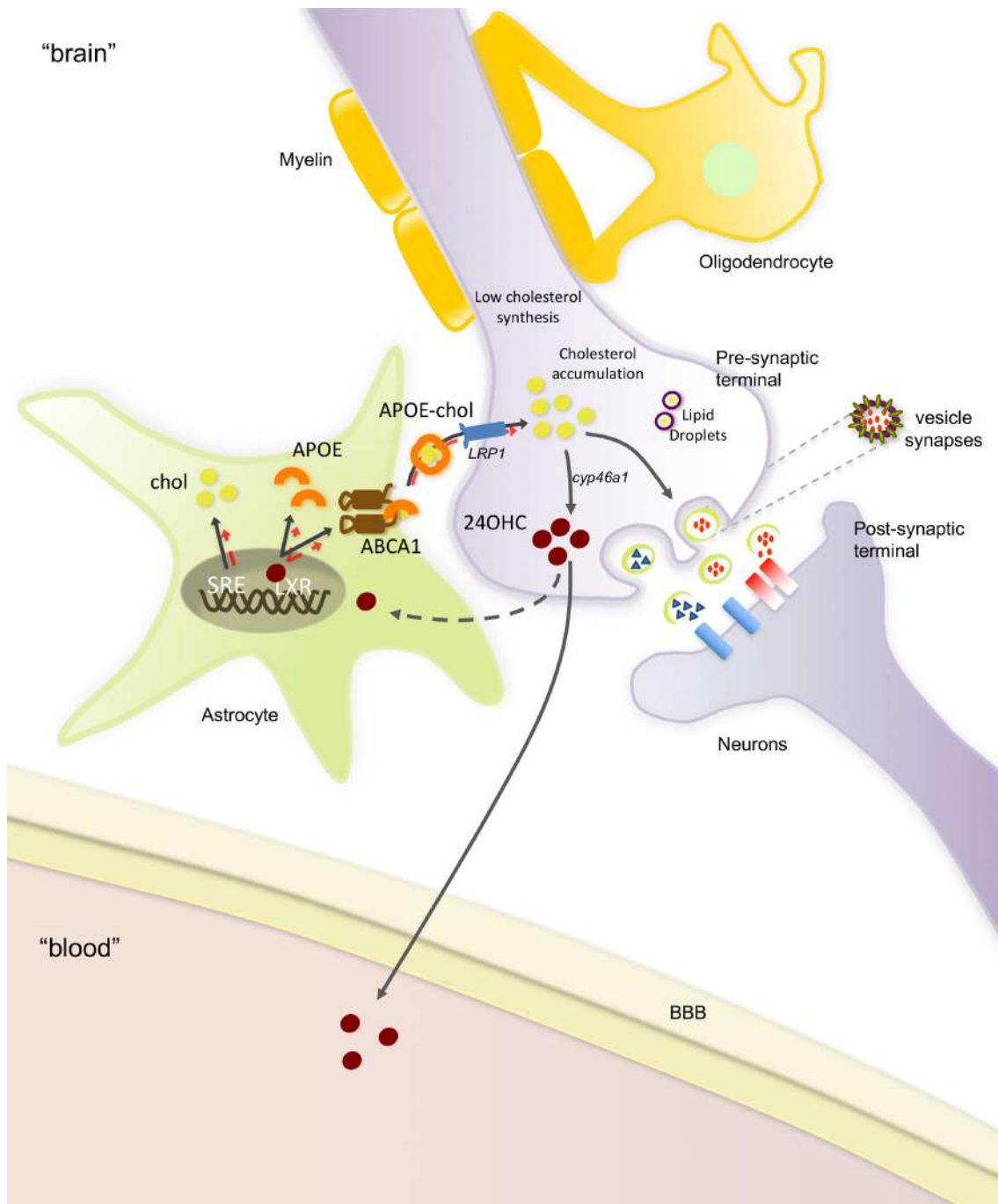


Figure 1.3 Neuron-astrocyte cholesterol cross-talk

Schematic representation of brain cholesterol metabolism and cross-talk between neurons and astrocytes. From Valenza & Cattaneo, *TINS*, 2011

1.1.3 Cross-talk between neurons and astrocytes

In the adult brain, astrocytes synthesize at least 2- to 3-fold more cholesterol than neurons (1). The amount of

cholesterol produced by neurons is enough for the differentiation of axons and dendrites but not for the formation of functional synapses. In fact, glial-derived cholesterol

produced by astrocytes is required to promote axon growth (30), biogenesis of synaptic vesicles (11, 31), and to maintain synaptic integrity (16, 32). Thus, neurons rely on the import of cholesterol from astrocytes (33), which is transported via apolipoproteins and lipids. Astrocytes are the major source of apolipoprotein E (ApoE) (34), a key lipoprotein required for extracellular transport of cholesterol and other lipids between astrocytes and neurons (35). Lipidation and secretion of ApoE are mediated by the ATP-binding cassette transporters (ABCA1) (30). The crucial role of ABCA1 was confirmed using knockout mice: these mice showed a significant decrease of ApoE lipidation, with consequent decline of cholesterol and ApoE level in brain and cerebrospinal fluid (CSF) (36, 37) together with cortical astrogliosis, increased inflammatory gene expression, altered synaptic transmission, and sensorimotor behavior (38).

Once ApoE-lipoproteins are lipidated, they are taken up by the Low-Density Lipoprotein Receptor-related Protein 1 (LRP1), which is mainly expressed by neuronal cells (39, 40, 41) (Fig. 1.3).

The interaction between ApoE-lipoproteins and LRP1 leads to the activation of several signaling pathways that are needed for neuronal survival and correct activity (30, 42). Of note, LRP1 removal in neurons led

to global impairment of cholesterol homeostasis and neurodegeneration, highlighting its importance for correct brain function (32).

1.1.4 Cholesterol elimination from the brain

Cholesterol turnover is finely regulated by mechanisms for sterol excretion from the CNS, including the 24-hydroxylation of cholesterol to 24S-hydroxycholesterol (24S-OHC) by a subset of neurons with very high metabolic rates (7). This metabolite is readily secreted from the CNS into the plasma. The enzyme responsible for this conversion is called Cholesterol 24-hydroxylase (CYP46A1) and it is part of the cytochrome P450 family (43). It is highly expressed in pyramidal neurons of the hippocampus and cortex, in Purkinje cells of the cerebellum, and in hippocampal and cerebellar interneurons (44). It has been calculated that the amount of 24S-OHC moving from the brain into the circulation is around 6-7 mg per day (7, 45). Once in the blood, 24S-OHC binds to LDL, is taken up by hepatocytes and finally excreted in bile salts (46). Whereas in mice 24S-OHC production has been reported also in the liver, human 24S-OHC is exclusively of cerebral origin (43, 47). Consequently, this molecule may be used as a marker for brain cholesterol homeostasis in humans (18, 48, 49, 50).

Furthermore, besides being a metabolite for cholesterol elimination, 24S-OHC takes part of the cholesterol cross-talk between neurons and astrocytes: in fact, 24S-OHC may act, together with cholesterol precursors such as desmosterol, as a signaling molecule that regulates cholesterol biosynthesis by activating the liver X receptor (LXRs). Accordingly, neuron-derived 24S-OHC may signal to astrocytes the neuronal cholesterol level and, through interaction with LXR, it may regulate the expression and the secretion of ApoE (33, 51).

The close correlation between cholesterol synthesis and catabolism was demonstrated using CYP46A1 knockout mice. Accordingly, sterol export from the brain was dramatically decreases in these mice (about 64%) together with a reduction (about 40%) in cholesterol synthesis (47).

1.2 Brain cholesterol defect in Huntington's disease

1.2.1 Huntington's disease genetics and clinical manifestation

Huntington's disease (HD) is an autosomal dominant neurodegenerative disorder with an incidence of 5–10 per 100,000 (52). In early stages, the disease is associated with personality, emotional, and psychiatric disturbances leading to cognitive dysfunctions (53). Later on, motor decline occurs together with

progressive dementia and gradual impairment of attention, learning, and planning ability (54, 55). Besides chorea, motor disturbances include dystonia, which comprises progressive motor disability, involuntary movements, and rigidity. Patients with advanced HD may become unable to walk, have poor food intake and become unable to care for themselves. Patients also suffer from non-neurological features, including weight loss, skeletal-muscle atrophy, osteoporosis, cardiac failure, metabolic, and immune disturbances (56).

The mutation responsible for HD was identified in 1993: it involved an abnormal expansion of a polymorphic (CAG)_n repeat in the first exon of the interesting transcript 15/huntingtin (*IT15/HTT*) gene, which maps on the short arm of chromosome 4 in the locus 4p16.3 (57). The CAG tract encodes for a polyglutamine (polyQ) stretch in the NH₂ terminus of a 348 kDa protein, called Huntingtin (HTT) (57). The study demonstrated that the number of CAG repeats in healthy people varied from 6 to 35, while HD patients carry expansions of 36 or more repeats (57, 58). Furthermore, there are some asymptomatic individuals with a number of CAG repeats ranging from 27 to 35 (59, 60): these people are at risk of transmitting the disease to their children, due to a phenomenon known as “genetic anticipation” (61).

The length of the expanded CAG tract and the age of symptoms onset are inversely correlated (59, 62): the peak age of adult-onset HD is between 35 and 50 years with death occurring 15–20 years after onset, but CAG repeat expansions ≥ 75 lead to juvenile onset with more prominent impairment (63, 64).

1.2.2 Huntington's disease neuropathological features

Concerning neuropathology, the most affected brain area in HD is the striatum (65) but cortex and other brain regions are compromised in late stages of the disease and in more severe cases. Neurodegeneration occurs years before the appearance of symptoms (66). The most affected neuronal population in HD is composed by striatal GABAergic medium-sized spiny neurons (MSNs) (67). This peculiar feature has been used to classify HD patients into five different severity grades (0–4). Patients in Grade 0 do not show neurodegeneration. Grade 1 is characterized by atrophy, neuronal loss, and astrogliosis, which consists in abnormal changes in the number and the morphology of astrocytes. Grades 2 and 3 comprise patients with progressive severe striatal atrophy. Grade 4 includes the most severe HD cases with striatal atrophy and neuronal loss of about 95% (67, 68, 69).

Immunohistochemical studies revealed differential loss of striatal projection neurons in HD (70). There are two major pathways, a direct (excitatory) and an indirect (inhibitory) one, that are used to describe the interaction between glutamatergic and dopaminergic neurotransmission in the striatum. According to this model, the overall effect of the direct pathway is to stimulate the cortex. The cortex provides excitatory input to the striatum. Striatal MSNs are inhibitory GABAergic neurons and their axons project to the internal globus pallidus (GPi) and to the substantia nigra reticulata (SNR). From here, MSNs project to the thalamus, from where excitatory pathways return to the cortex to synapse with the neurons of the corticospinal and corticobulbar tract to affect the planning of the movement.

On the contrary, the overall effect of the indirect pathway is the inhibition of the cortex. Inhibitory neurons from the striatum synapse with the external segment of the globus pallidus (GPe). Here, GPe inhibitory neurons project to the subthalamus (STN), which sends excitatory projections back to the GPi and SNR leading to thalamus inhibition. The final result of this pathways is a decreased activity of the cortical motor neurons, and consequential suppression of locomotor activity and movement.

The balanced activity between direct and indirect pathway is modulated by dopamine. Accordingly, in addition to their distinct projections, MSNs of the direct and indirect pathway expresses different dopamine (DA) receptors. DRD1 DA receptors are expressed by direct pathway MSNs, whereas DRD2 receptors are expressed by indirect pathway MSNs (71, 72).

Since MSNs are the most affected cells in HD, both direct and indirect pathways are involved. Degeneration occurs firstly in the indirect pathway MSNs, leading to motor dysfunction. In fact, DRD2 neurons become less effective in inhibiting the thalamus. Thus, the direct pathway results to be more active than the indirect one leading to an excessive activation of motor programs causing excessive un-normal movements such as chorea (73, 74). In late stages of the disease, also MSNs of the direct pathway are involved, leading to dystonia (75). In fact, degeneration occurs in DRD1 inhibitory neurons, leading to thalamus inhibition and impairment in cortex excitation (76).

Beside neurodegeneration, an additional neuropathological feature of HD is the reactive gliosis, especially in the dorsal striatum (68). Gliosis occurs as a response to all forms of CNS injury or disease and involves the proliferation or hypertrophy of several types of glial cells.

Another hallmark that characterizes HD consists in the accumulation of pathogenic N-terminal fragments of HTT, which arise from proteolysis and aberrant splicing of mutant HTT (muHTT) (77) leading to intracellular aggregates (78). Soluble monomeric and oligomeric forms of muHTT have been supposed to be the more toxic species of aggregates in HD (79, 80, 81), while other forms of aggregates seem to be even protective, supporting the hypothesis that muHTT aggregates are an attempt of the cells to sequester toxic soluble fragments (77, 82, 83, 84, 85).

1.2.3 Huntingtin (HTT) gain and loss of function

HTT is expressed ubiquitously in humans and rodents, but reaches the highest expression level in the brain, including neuronal and striatal cells (86, 87). Due to its high molecular weight it has always been difficult to elucidate its structure using crystals but full-length human HTT structure has been revealed using cryo-electron microscopy (88). The study has shown that HTT has an α -helical structure with three major domains: the amino-terminal domain (N-HEAT), where the majority of HTT interactor bind, and the carboxy-terminal domain (C-HEAT) connected by a bridge domain. HTT N-HEAT domain and HTT C-HEAT domain accommodates

multiple HEAT (Huntingtin, elongation factor 3, protein phosphatase 2A and lipid kinase TOR) repeats organized in a solenoid fashion, while the bridge domain carries different types of tandem repeats (88).

The pathogenesis of HD can be attributed to both the loss of normal HTT function and the gain of new toxic functions by muHTT due to the CAG tract elongation and morphological changes (89).

Here are some of the most important functions of HTT: (i) it is essential for embryonic development (90, 91, 92) and for the correct assembly of the architectural structure of cortex and striatum (93, 94); (ii) it plays a critical role in brain maturation, especially in establishing and maintaining cortical and striatal neuronal identity (95); (iii) it has an anti-apoptotic and pro-survival role by impairing the formation of a functional apoptosome complex leading to the activation of caspase-3 and caspase-9 (96, 97); (iv) it is required for the correct formation of cortical and striatal excitatory synapses (98) and it associates with vesicles in the presynaptic terminal (86); (v) it regulates the transcription of several genes. Accordingly, HTT recruits and sequesters the repressor element-1 transcription factor/neuron restrictive silencer factor (REST/NRSF) in the cytoplasm, thus the co-repressor complex does not form

at the NRSE sites and neuronal genes leading to the transcription of numerous neuronal genes, which include brain derived neurotrophic factor (BDNF), a cortical neurotrophin that is particularly important for the survival of striatal neurons and the activity of cortico-striatal synapses (99). When muHTT is present, this mechanism is impaired. Thus, BDNF loss may partially account for selective vulnerability of striatal neurons in HD (100). Besides BDNF production, HTT is also involved in BDNF vesicle trafficking along microtubules, through its interaction with the molecular motors dynein/dynactin and kinesin (101, 102, 103).

As mentioned above, many pathogenic mechanisms have been identified in HD including proteolysis and aggregation of muHTT (67, 104, 105), mitochondrial dysfunction (106, 107, 108), impaired protein degradation pathways (109, 110), and reduction of striatal BDNF (99, 102, 111). Moreover, polyQ expansion interferes with the ability of HTT to directly interact with postsynaptic density protein 95 (PSD95), a scaffolding protein that binds NMDA and kainate receptors, leading to NMDARs-mediated excitotoxicity (112). Two are the major mechanism that describe the aberrant activity of NMDA receptors: (i) changes in NMDA receptors protein level or subunits have been measured in HD

mice (113, 114, 115, 116); (ii) muHTT causes also the over activation (117) and the trafficking impairment of NMDA receptors (118, 119). Among its various role, the mutated protein is also involved in aberrant immune activation resulting in neuroinflammation (120) and cell-to-cell prion-like transmission of muHTT (121). In astrocytes, the presence of muHTT impairs glial glutamate (122, 123), potassium (124), calcium (125), and cholesterol (24) homeostasis leading to excitotoxicity and other dysfunctions that may contribute to HD pathogenesis.

All the described dysfunctions represent potential therapeutic target for HD treatment but, up to date, there are no effective disease-modifying drugs and the current pharmacological

treatment available for HD patients is only palliative, aimed at improving function and quality of life for people with HD, though some clinical trials are ongoing (126, 127, 128). Thanks to rapid advances in gene-modifying technology, lowering muHTT level is among the most promising strategy for developing disease-modifying treatments for HD. These strategies rely on zinc finger motif proteins to block messenger RNA (mRNA) transcription and synthesis, antisense oligonucleotides (ASOs) to avoid post-transcriptional processing and increase mRNA degradation, and small interfering RNA (siRNA) to hamper mRNA translation. Clinical trials based on these strategies are summarized in Table 1.1.

Registration ID	Intervention	Mechanism of action	Main outcome	Study design	Estimated Enrolment
NCT02519036	IONIS-HTTRx (or RG6042)	Allele-non selective ASO	Safety, Tolerability, Pharmacokinetics, and Pharmacodynamics. Completed; showed a dose-dependent reduction in CSF levels of mutant HTT; no serious adverse events were reported.	Randomized, Double-blind, Placebo-controlled study with 5 doses (10, 30, 60, 90, 120 mg) intrathecally administered every 4 or 8 weeks in patients with early manifest HD (Phase 1/2a).	46
NCT04000594	IONIS-HTTRx (or RG6042)	Allele-non selective ASO	Pharmacokinetics and Pharmacodynamics in CSF and Plasma, Safety and Tolerability	Non-Randomized, Placebo-controlled study with 3 doses intrathecally administered every 4 weeks in patients with manifest HD (Phase 1)	20
NCT03761849	IONIS-HTTRx (or RG6042)	Allele-non selective ASO	Efficacy and Safety at 101 weeks	Randomized, Multicenter, Double-Blind, Placebo-Controlled study with 1 dose (120 mg) intrathecally administered every 8 or 16 weeks in patients with manifest HD (Phase 3)	909
NCT03842969	IONIS-HTTRx (or RG6042)	Allele-non selective ASO	Long-Term Safety and Tolerability up to 5 years	Randomized study with 1 dose (120 mg) intrathecally administered every 8 or 16 weeks in patients in participants who have completed other IONIS studies in the development program for RG6042 (Phase 3)	1050
NCT03225833	WVE-120101	Stereopure ASO	Safety and Tolerability at 1 and 120 day	Randomized, Double-Blind, Placebo-Controlled study with 5 doses intrathecally administered in patients with early manifest HD carrying a targeted SNP rs362307. (Phase 1b/2a)	60
NCT03225846	WVE-120102	Stereopure ASO	Safety and Tolerability at 1 and 120 day	Randomized, Multicenter, Double-Blind, Placebo-Controlled study with 5 doses intrathecally administered in patients with early manifest HD carrying a targeted SNP rs362331. (Phase 1b/2a)	60

Table 1.1 Clinical trials for Huntington's disease

List of the ongoing clinical trials for Huntington's disease.

Of note, a randomized double-blinded phase 1/2a study (NCT02519036) was conducted in 46 HD patients with early-stage disease. Participants received escalating doses (10, 30, 60, 90, or 120mg) of intrathecally administered IONIS-HTT_{Rx}, an ASO designed to inhibit *Htt* mRNA (both wild-type and mutant) or placebo (ACSF). Overall, HTT_{Rx} was well tolerated and treatment resulted in significant dose-dependent reduction of muHTT in CSF (129).

Based on these promising results, there are three ongoing clinical trials with IONIS-HTT_{Rx} (NCT04000594; NCT03761849; NCT03842969), including a randomized, multicenter, double-blind, placebo-controlled phase 3 study aimed at evaluating the efficacy and the safety of intrathecally administered IONIS-HTT_{Rx} in manifest HD patients. Furthermore, two phase 1b/2a clinical studies (NCT03225833; NCT03225846) are currently investigating the safety of single and multiple doses of two ASO that are specific for *muHtt* mRNA through recognition of two specific single nucleotide polymorphisms (SNPs) in early HD patients.

1.2.4 Cholesterol dysfunction in Huntington's disease: evidences in mouse models

Brain cholesterol homeostasis is affected in different chronic neurodegenerative disorders,

including HD. The first evidence of brain cholesterol dysfunction in HD emerged from a microarray study performed in 2002 on striatal-derived cells expressing the N-terminal 548-amino-acid portion of either wild-type or muHTT in an inducible way. In this cellular model of HD, many genes involved in the biosynthesis of cholesterol and fatty acids were down-regulating following muHTT expression (130).

The first *in vivo* confirmation come in 2005: a study performed in R6/2 mice, a transgenic HD animal model over-expressing human muHTT exon 1 with around 150 CAG (131), confirmed the transcriptional deregulation of cholesterologenic genes (*Hmgcr*, *Dhcr7* and *Cyp51*) within mice striatum and cortex. Moreover, the study highlighted a significant decrease in brain sterol content (132).

These results were confirmed in several HD rodent models: reduced activity of HMGCoAR, the rate-controlling enzyme of cholesterol biosynthesis pathway, together with reduced level of cholesterol precursors, were observed in R6/2 mice (133), YAC128 mice (134, 135), YAC46 and YAC72 mice (136), heterozygous (HdhQ7/111) and homozygous (HdhQ111/111) knock-in mice and transgenic HD rats (137). Decreased content of the total amount of cholesterol was measured by gas chromatography-mass spectrometry

(GC-MS) in all the animal models tested so far but only at later time points, when HD symptoms are evident (134, 135, 138).

Other studies in these animal models described brain cholesterol accumulation (139, 140, 141). This discrepancy was due to the low sensitive and non-specific, colorimetric and enzymatic, methods used for cholesterol content detection, instead of more reliable analytical method such as GC-MS (142). Moreover, these measurements were performed in samples not prepared in an appropriate manner, such as lipid extracts of brain tissues from mice not perfused with saline (139), which avoid blood derived cholesterol contamination.

To demonstrated further that the primary defect of decreased cholesterol content in the HD brain is its decreased synthesis, a study in heterozygous knock-in Q175 mice (143) was performed to quantify the rate of *de novo* brain cholesterol biosynthesis, by heavy water ($2\text{H}_2\text{O}$) labeling method. From early stages of the disease (5 weeks of age), prior to motor defects, the striatal daily rate of cholesterol synthesis was found significantly reduced, whereas cholesterol content was found decreased in the same region only in presence of manifest symptoms (at 54 weeks of age) (138). Additionally, isotopic-dilution mass spectrometry

(ID-MS) analysis revealed an inverse correlation between lathosterol level, the direct precursor of cholesterol, and the CAG size in an allelic series of knock-in mice (Q7, Q20, Q80, Q111, Q175), at symptomatic stages (138).

At late stages of the disease, as consequence of the primary cholesterol biosynthesis dysfunction, also cholesterol catabolism is altered in HD brain. Accordingly, decreased level of 24S-OHC was measured in brain and plasma of rodent HD models (134, 135). Recently, over-expression of CYP46A1, the enzyme catalysing the conversion of cholesterol into 24S-OHC, was used to modulate cholesterol catabolism in HD mice. These studies were based on evidences showing reduced level of CYP46A1 in the striatum of both R6/2 and Q175 mice (141, 144). Accordingly, knock-down of CYP46A1 in wild-type mice induced an HD-like phenotype, including motor deficits. In these works, the over-expression of CYP46A1 via adeno-associated virus delivery into the striatal neurons of R6/2 and Q175 mice delayed the progression of motor deficits and decreased the number of muHTT aggregates (141, 144). Of note, in both R6/2 and Q175 mice, this strategy led to an increase of mRNAs encoding for cholesterologenic enzymes (*Hmgcr*, *Cyp51*, *Dhcr24*, *Dhcr7*) together with increased level of cholesterol precursors, suggesting that

the primary defect of brain cholesterol biosynthesis is restored by CYP46A1 delivery (141, 144).

1.2.5 Cholesterol dysfunction in Huntington's disease: evidences in patients

Brain cholesterol dysfunction can be detected also in HD patients. First evidences come from studies performed on post-mortem caudate specimens from HD patients and on patients-derived fibroblasts: these studies highlighted reduced expression of genes related to cholesterol synthesis, compared to controls (132). Additional evidence from fasted HD patients revealed that total plasma cholesterol level declined according to disease progression (145). A recent study confirmed these findings in both pre-manifest and manifest fasted HD subjects (146).

Furthermore, cholesterol precursors, lanosterol, and lathosterol were found to be lower in plasma from fasted HD patients respect to controls, at any disease stage (145).

Regarding cholesterol catabolism, reduced level of 24S-OHC was measured in plasma of HD patients (145, 147) and in pre-symptomatic HD patients who are close to the onset of the disease (49). The progressive decrease of plasma 24S-OHC from pre-manifesting individuals to HD patients was found to be proportional to the

degree of caudate atrophy and striatal volumes reduction measured by MRI (49, 147) and to the motor impairment in HD patients (147). Moreover, 24S-OHC was proposed to reflect the number of metabolically active neurons located in the grey matter of the brain (48, 148). Longitudinal studies are ongoing to validate the prognostic value of plasmatic level 24S-OHC as a biomarker in HD. Furthermore, cholesterol metabolite 27-OHC, which is of peripheral origin, is lower in plasma from HD patients respect to controls, at any disease stage (145). Recently, also the expression of CYP46A1 was found reduced in the putamen of grade 2/3 HD patients (141).

These data suggest that whole body cholesterol homeostasis is disturbed in HD patients: defects in cholesterol synthesis, indirectly measured by reduced level of 24S-OHC, are already present at pre-symptomatic stages of the disease, while defects in cholesterol metabolism, measured by reduced level of CYP46A1, appears at later stages as a consequence of reduces cholesterol synthesis.

1.2.6 The molecular mechanism underlying cholesterol dysfunction in Huntington's disease

One of the possible mechanisms underlying cholesterol dysfunction in HD relies on a reduced activity of SREBP2, linked to muHTT

expression. Accordingly, reduced nuclear translocation of SREBP2 was observed in HD cellular models and in the striatum of R6/2 and YAC128 mice (132, 149). Furthermore, reduced activity of SRE was measured in HD cells using reporter genes (132). Finally, reduced nuclear level of SREBPs in both HD cells and mouse brain tissue was measured (132, 150), suggesting impaired nuclear translocation of the cleaved active form of SREBP2. Supporting this hypothesis, it was recently demonstrated that muHTT binds to the SREBP2/importin β complex required for nuclear import and sequesters it in the cytoplasm (149).

An additional key mechanism involved in brain cholesterol dysfunction is the cross-talk between neurons and astrocytes. In the adult brain, neurons rely on cholesterol produced and secreted by astrocytes but this process is altered in HD. Accordingly, the expression of key genes for cholesterol biosynthesis is reduced in primary astrocytes cultured from R6/2 and YAC128 mice compared to wild-type together with reduced mRNA level of *Abca1* and *ApoE* (135). Furthermore, in HD mice CSF, ApoE was associated with smaller lipoprotein particles (135), suggesting that HD astrocytes display reduced cholesterol biosynthesis and efflux (135). To confirm this dysfunction, a recent study

highlighted that astrocytes derived from both neural stem knock-in cells, carrying increasing CAG repeats, and from R6/2 mice secrete lower level of cholesterol bound to ApoE lipoproteins in the culture medium, leading to a reduced availability of cholesterol for HD neurons that in turns affected neurite outgrowth and synaptic related properties (150). The work also showed that glia-conditioned medium (GCM) from wild-type astrocytes rescued neurite outgrowth defect in NS-derived HD neurons, as well as cholesterol administration. This beneficial effect of wild-type GCM was abolished by silencing ABCA1 or SREBP2 in wild-type astrocytes (150). On the contrary, GCM derived from HD astrocytes fails to support neurite outgrowth in NS-derived HD neurons. However, the over-expression of ABCA1 or the N-terminal active fragment of SREBP2 in HD astrocytes led to increased cholesterol synthesis and ApoE/cholesterol release in the medium. In accord, GCM from R6/2 astrocytes over-expressing SREBP2 reverses neurite outgrowth and synaptic defects in HD neurons (150).

Taken together, these observations suggested that in HD there is a reduced ApoE mediated cholesterol transport and supply from astrocytes to neurons. Thus, restoring astrocytes-neurons cholesterol cross talk could be a potential therapeutic approach

to ameliorate neuronal dysfunction for HD patients.

1.3 Brain cholesterol alterations in other neurodegenerative diseases

Cholesterol synthesis and metabolism are affected in many neurodegenerative disorders. Besides HD, dysregulation of brain cholesterol homeostasis has been linked to Niemann-Pick type C disease, Smith-Lemli Opitz syndrome, Alzheimer's disease, and Parkinson's disease.

1.3.1 Cholesterol and Niemann-Pick type C disease

Niemann-Pick type C (NPC) is an autosomal, recessive, inherited, neurovisceral lipid storage disorder characterized by massive loss of neurons, motor defects such as delay in developmental motor milestones, gait problems, falls, and cognitive problems including cerebellar ataxia, and progressive dementia. NPC has an estimated incidence of 1:120.000 individuals.

The disease is directly related to impairment in cholesterol metabolism, since it is caused by mutations in the genes encoding for the NPC1 (95% of families) or NPC2 proteins, which are involved in intracellular cholesterol trafficking (151) due to unesterified cholesterol and glycosphingolipids sequestration and accumulation within the endocytic pathway (152).

Up to date there is no cure for NPC: the current available therapies for NPC disease rely on miglustat, a glucosylceramide synthase inhibitor, and 2-hydroxypropyl- β -cyclodextrin, a cyclic oligosaccharide that binds and enhances the water solubility of cholesterol (153, 154, 155). Recently, adeno-associated virus mediated delivery of functional NPC1 gene in a mouse model of NPC resulted in robust NPC1 expression in various tissues, including brain, leading to Purkinje cell survival, restored locomotor activity and coordination, and increased mice lifespan, suggesting that AAV-based gene therapy is a promising means to treat NPC disease (156).

1.3.2 Cholesterol and Smith-Lemli-Opitz syndrome

Smith-Lemli-Opitz syndrome (SLOS) is an autosomal recessive sterol biosynthesis disorder characterized by multiple congenital malformations such as cardiac defects, hypospadias, and microcephaly, and intellectual disability. In the most severe cases, the mutation causes fetal or newborn death, due to major abnormalities and multiple organ failure. Estimated incidence ranges from 1:20.000 to 1:50.000.

SLOS is caused by mutations in the gene encoding for 7-dehydrocholesterol reductase (DHCR7), the enzyme that catalyzes the final step in the

cholesterol biosynthetic pathway. The mutation leads to increased level of 7-dehydrocholesterol in parallel with a dramatic decrease in cholesterol amounts within the cells, plasma and the brain (157, 158). The developmental abnormalities observed in SLOS patients might also be due to reduced activity of the sonic hedgehog (SHH) linked to alterations in cholesterol metabolism (159, 160). Up to date, administration of cholesterol and statins are the most commonly studied therapeutic approach for SLOS, even if antioxidants, prenatal cholesterol supplementation, and gene therapy are under investigation (161).

1.3.3 Cholesterol and Alzheimer's disease

Alzheimer's disease (AD) is a chronic neurodegenerative disease that leads to memory loss and cognitive decline. As the disease worsens, symptoms include problems with language, disorientation, mood swings, loss of motivation, and finally patients became unable to self-care. The hallmark of AD is the presence of extracellular deposits of β -amyloid ($A\beta$) plaques and intracellular neurofibrillary tangles that contain hyperphosphorylated tau proteins leading to neuronal loss (162, 163). Regarding the incidence, cohort longitudinal studies estimated rates between 10-15:1.000 persons each

year for all dementias and 5–8 for AD (163).

The cause of Alzheimer's disease is poorly understood but many genes are thought to be involved (164). The best-known genetic risk factor is the inheritance of the ApoE ϵ 4 allele, with an incidence between 40 and 80% of people with AD (165), suggesting that impairment in cholesterol metabolism has a major role in the development of AD. This ApoE isoform is involved in cholesterol transport leading to altered synaptic function, CNS cholesterol metabolism, $A\beta$ aggregation and clearance in the brain. Together with ApoE ϵ 4 allele, *ABCA1*, *ABCA7* and *APOJ/CLU*, which are involved in lipid transport, are linked to AD (166, 167): accordingly, *ABCA1* deficiency led to increased amyloid deposition (168), while its over-expression had the opposite effect in AD mice (169).

Based on these evidences, pre-clinical studies with drugs that target cholesterol metabolism are ongoing as a possible therapeutic strategy for AD. The administration of statins, which inhibit HMGCR and lower cholesterol levels, reduced $A\beta$ formation in AD mice (170).

Despite these promising results, there some conflicting data regarding cholesterol metabolism in AD: several studies have shown reduced level of cholesterol in the hippocampus of AD patients. *In vitro* studies suggested

that amyloid oligomers may decrease cholesterol by activating CYP46A1, inhibiting ApoE-cholesterol uptake from astrocytes, modifying lipid rafts, and inhibiting HMGCR and SREBPs (166).

1.3.4 Cholesterol and Parkinson's disease

Parkinson's disease (PD) is the second most common progressive neurodegenerative disorder after AD. PD mainly affects the motor system with symptoms that includes shaking, rigidity, slowness of movement, and difficulty with walking. At later stages non-motor symptoms become common and patients suffers from dementia and anxiety, together with sensory, sleep, and emotional problems (171, 172). PD is characterized by the accumulation of Lewy bodies, which are α -synuclein-immunoreactive inclusions made up of neurofilament proteins together with proteins responsible for proteolysis. Similarly to AD, a low number of PD cases are caused by mutations in specific genes, including α -synuclein, parkin, LRRK2, PINK1, DJ-1, and ATP13A2 (173).

The first study linking PD with cholesterol metabolism showed that cholesterol biosynthesis was decreased in fibroblasts from PD patients owing to reduced HMGCR activity (174). Accordingly, the proportion of cholesterol in membrane

lipid rafts appeared to be reduced in the brain of PD patients and animal models (175). Some contrasting data are present in the literature, showing that high level of brain cholesterol seems to aggravate PD phenotype in mice. Indeed, high cholesterol diet increases brain cholesterol level and reduction of striatal dopamine with motor behavioral defects in a mouse model of PD (176).

Up to date, there are no studies measuring cholesterol level in the brain of PD patients (177). Instead, it has been reported that the level of 24S-OHC, which possibly reflects brain cholesterol metabolism, is decreased in their plasma (178, 179). A link between PD and cholesterol can be established by the role of cholesterol for α -synuclein aggregation, as it seems to mediate the interaction of oligomeric α -synuclein with the cell membrane (180). Furthermore, it has been demonstrated that the process of α -synuclein fibrilization is accelerated by elevated level of oxidized cholesterol metabolites in Lewy body (181).

Since increased cholesterol level was observed in the brain of α -synuclein transgenic mice (182), treatments aimed at reducing cholesterol in the PD brain may be beneficial. Accordingly, treatment of cells and mice with methyl- β -cyclodextrin, a drug commonly used to extract cholesterol from membranes, highlighted decreased

level of α -synuclein in membrane fractions and reduced accumulation of α -synuclein in neuronal cell body and in synapses, preventing its aggregation (183). Of note, it is important to remind that cyclodextrin represents a rather harsh treatment that can bind and redistribute other lipids potentially affecting other pathways.

On the other hand, statins reduced the aggregation of α -synuclein in cultured neurons and in animal models of synucleinopathies, suggesting again that high cellular cholesterol could be at the base of this pathological sign (184).

Further assessment of these pathological mechanisms is needed because these data were obtained in cells and animals with normal and not high cholesterol level. Moreover, the role of statins on antioxidant and anti-inflammatory pathways may be taken into consideration.

1.4 Mouse models of Huntington's disease

Since the discovery of the HTT gene, several HD mouse models that recapitulate many of the features of the human disease have been genetically engineered (185, 186, 187). These genetic models have contributed significantly to study HD pathogenesis and offer tremendous potential to evaluate new therapeutics (188, 189, 190, 191).

The models differ in the methods by which they were engineered, their CAG repeat numbers, size and species of origin (mouse or human) of the HTT protein, promoters driving the protein expression, genetic backgrounds, and disease onset and severity.

Genetic models can be classified into 3 different groups:

- N-terminal transgenic models, carrying the 5' portion of the, including exon 1 that contains the CAG repeat region;
- full-length transgenic models, expressing full-length muHTT;
- knock-in models, in which mouse HTT is substituted by a portion of human muHTT gene carrying CAG repeats of varying length into its genomic locus.

1.4.1 R6/2 mice

R6/2 mice express exon 1 from the 5' end of the human HTT gene, with approximately 150 CAG repeats, under the control human HTT promoter. This mouse line was the first transgenic lines produced (131) and it has been the most extensively studied and utilized mouse model of HD up to date. Since this model was engineered via pronuclear injection, each transgene is integrated in a random fashion at a unique site in the mouse genome. The CAG tract carried in the transgene is subject to length instability, therefore CAG repeat length must be carefully evaluated in each transgenic animal

chosen for studies to avoid large CAG expansion. Accordingly, the phenotype varies greatly as a function of CAG repeat size: increasing the CAG repeat length from 50 to 160 exacerbated the R6/2 phenotypes, while when the CAG repeat size exceeds 200, the onset of HD motor symptoms and pathology tends to be delayed due to decreased levels of muHTT (193, 194).

R6/2 mice are characterized by a very aggressive, rapidly progressing phenotype, resembling the juvenile form of HD in humans. They develop normally, most of the behavioral symptoms appear around 8-9 weeks of age and average life expectancy is around 13-14 weeks.

Behavioral symptoms comprehend both motor and cognitive dysfunctions. Motor symptoms include resting tremor, chorea-like movements, stereotypic involuntary grooming movements, and clasping behavior (131, 195). Starting from 3 weeks of age, mice display locomotor hyperactivity (196), while around 8 weeks of age they become hypoactive (195, 197). From 10 weeks of age, they suffer from severe epileptic seizures. In parallel, their body weight progressively declines and at the end of their life is approximately 70% less than their wild-type (131). Cognitive abnormalities precede the onset of motor defects (198). At 3.5 weeks they show impairment in the spatial learning task as assessed by Morris

water maze test (198, 199). Starting from 8 weeks of age, also procedural memory and long-term memory are compromised as measured by the two-choice swim T-maze test (198) and the novel object recognition test respectively (200, 201).

Regarding neuropathology, although little neuronal loss is seen in these mice before their premature death (202), R6/2 mice show robust brain atrophy, with the striatum most affected (203, 204). Another neuropathological sign is the presence of muHTT aggregates already at birth. They first appear in the striatum and the cortex and progressively increase until late symptomatic phase in which around 98% of the striatal projection neurons exhibit muHTT inclusions (204, 205).

Several studies highlighted abnormal neurotransmission in R6/2 mice at early stages of the disease, including increased glutamate release in pre-symptomatic stage (206). In parallel, increases in spontaneous GABAergic synaptic currents and postsynaptic receptor function occur (207). Finally, R6/2 mice show a progressive deafferentation that continues until their death, together with loss of pre and postsynaptic marker proteins (206).

Taken together, these severe alterations make R6/2 mice a very useful HD mouse model to test therapeutic strategy for HD in a rapid

way and obtain preliminary proof-of-concept that must be validated in other HD models.

1.4.2 zQ175DN mice

As opposed to the N-terminal and full-length HD transgenic models, knock-in HD models are generated using homologous recombination techniques, thus a precise number of CAG repeats are introduced directly into the mouse *Htt* gene. Given that the CAG repeats are carried in the context of the mouse *Htt* gene, these mice best mimic the human condition from a genetic perspective: as well as HD patients, these mice are heterozygous and carry one wild-type *Htt* allele and one CAG-expanded allele (64, 100, 208, 209, 210).

The most utilized HD knock-in mouse model is the zQ175 line. This colony, carrying around 190 CAG, arose from a spontaneous expansion of the CAG copy number in the CAG 140 knock-in colony (143). As well as R6/2 mice, zQ175 mice show behavioral abnormalities including motor and cognitive defects. Homozygous mice showed a stronger phenotype compared to heterozygous one. Accordingly, their muscular strength is decreased starting from 8 weeks of age respectively, as assessed by grip strength test (143). At 35 weeks of age, they show impairment in motor coordination, as measured

using the rotarod test, while cognitive decline appears at around 10-12 months of age (143, 211). Regarding heterozygous mice, deficits were measured in the dark phase of the diurnal cycle from around 4.5 months of age. Decreased body weight was observed in both heterozygotes and homozygotes at late time points (45 weeks of age), along with significantly reduced survival in the homozygotes (143).

Regarding neuropathology, muHTT starts to appear in both striatum and cortex at around 25 weeks of age (212). Moreover, *in vivo* longitudinal structural MRI on whole brain performed from 3 months to 12 months of age revealed significant atrophy in the striatum and neocortex at an early age in heterozygous zQ175 mice (212), together with an early and significant decrease of striatal gene markers starting from 12 weeks of age (143, 212).

Neurotransmission is also impaired: MSNs from zQ175 mice display a progressive hyperexcitability compared to wild-type. Furthermore, excitatory synapses of the striatum display reduced transmission together with decreased striatal and cortical volumes from 3 and 4 months of age in homo- and heterozygous mice, respectively (211).

Recently, an enhanced zQ175 new knock-in mouse model, called

zQ175DN, has been developed and characterized. The zQ175 knock-in allele retains a floxed neomycin resistance cassette upstream of the *Htt* gene locus leading to reduced muHTT expression compared to the wild-type allele, leading to a mild HD-like phenotype. zQ175 were crossed with mice expressing Cre in germ line cells to remove the neo cassette. This resulted in a ~2-fold increase in muHTT level leading to stronger HD-like phenotypes. Furthermore, zQ175DN mice exhibit earlier disease onset compared to zQ175 mice, making them valuable for preclinical studies (213).

Deregulation in behavioral, electrophysiological, and histopathological features make zQ175 mice a valuable model to study HD-like pathophysiology and to evaluate the potential of therapeutic strategies to slow the progression of disease in a genetic context that is similar to HD in humans and allows long-term analysis.

1.5 Cholesterol delivery to the brain of HD mice

Given the fundamental role of brain cholesterol for synapses formation and synaptic transmission, several studies are ongoing to assess the therapeutic potential of brain cholesterol delivery to the brain of HD mice. One of the major problems arising targeting the brain is

the presence of the blood-brain-barrier (BBB). Different strategies have been developed to overcome this obstacle and to deliver cholesterol to the HD brain.

1.5.1 First generation brain-permeable nanoparticles

Recently, polymeric nanoparticles (NPs) modified on their surface to target the BBB has been described (214). Accordingly, nanoparticles were prepared using poly(lactic-co-glycolic acid) (PLGA), a synthetic polymer approved by the US Food and Drug Administration (FDA) and European Medicine Agency (EMA) for biomedical devices. PLGA has a very high biodegradability (215): it enters into the Krebs cycle and it is degraded by non-enzymatic hydrolysis leading to the formation of lactic acid, glycolic acid, CO₂ and H₂O.

To cross the BBB, NPs were engineered on their surface with a simi-opioid glycosylated hepta-peptide, called g7. Characterization experiments showed that, starting from 4h after a single intraperitoneal (I.P.) injection in mice, up to 10% of g7-PLGA-NPs crossed the BBB via endocytosis and micropinocytosis and reached the brain (216, 217, 218, 219). Once in the brain, g7-PLGA-NPs are able to release their content, as demonstrated by loading Loperamide in g7-PLGA-NPs, an opioid drug that cannot cross

the BBB. Following its delivery with g7-PLGA-NPs, animals developed antinociceptive effects, demonstrating that the drug reached the brain and exerted its effect (217).

This system has been recently used to deliver cholesterol to the brain of a transgenic mouse model of HD, e.g. the R6/2 mice. Accordingly, g7-NPs were loaded with cholesterol (g7-NPs-chol_1.0) and they were administered to R6/2 mice starting from a pre-symptomatic stage of the disease (5 weeks of age) until 10 weeks of age, with 2 I.P. injections/week, resulting in around 15 μg of cholesterol administered to the brain. This dose was sufficient to completely prevent the cognitive decline of HD mice, while no effect on motor phenotype were measured (214). Furthermore, cholesterol rescued synaptic activity in R6/2 mice: the frequency of spontaneous inhibitory postsynaptic currents (IPSCs), which is known to be significantly higher in MSNs from R6/2 mice compared to wild-type, was significantly reduced by cholesterol supplementation (214). Furthermore, cholesterol positively influenced the protein level of synaptic machinery, including PSD95 and NMDA receptors, confirming its fundamental role for correct synaptic function (214).

Taken together, these data highlighted the first proof-of-concept that brain cholesterol metabolism may be

a therapeutic target for HD and cholesterol supplementation may be beneficial.

1.5.2 Osmotic minipumps

To define the most efficacious dose of cholesterol able to contrast both cognitive and motor dysfunction in R6/2 mice, studies using mini-pumps were performed (for details of my contribution on this work see the Appendix 6.1.2). Mini-pumps are devices that can be attached to a catheter to infuse directly into the striatum, which is the most affected area in HD, well-defined drug doses in a continuous manner at a constant rate. Three escalating doses of cholesterol (e.g., 15 μg - low, 185 μg - medium, and 369 μg - high) were infused in the striatum of R6/2 mice for 4 weeks (220). All the doses completely prevented cognitive decline in R6/2 mice, confirming previous results (214). Importantly, the highest dose attenuated also disease-related motor phenotypes, as assessed by the rotarod test and the activity cage test. Along with behavioral benefits, the delivery of a high dose of cholesterol led to morphological and functional recovery of both excitatory and inhibitory synapses. Accordingly, striatal infusion of a high dose of cholesterol resulted in a significant increase of the frequency of sEPSCs in R6/2 chol-high mice together with a rescue of the number of total and

docked synaptic vesicles. Concerning GABAergic synapses, striatal infusion of cholesterol led to a significant reduction of the average frequency of sIPSCs, bringing this parameter close to the one observed in wild-type MSNs and indicating that exogenous cholesterol reestablishes inhibitory synaptic transmission. Regarding structural changes, cholesterol infusion reduced the increased density of inhibitory synapses in treated mice (220).

In addition, striatal infusion of exogenous cholesterol induces changes in the endogenous sterol metabolism in HD mice by increasing level of the brain-specific cholesterol catabolite 24S-OHC, suggesting that the excess of cholesterol is catabolized and eliminated. This process likely stimulated and enhanced endogenous cholesterol biosynthesis in glial cells, restoring the primary cholesterol defect in HD. At the cellular level, cholesterol reduced the number and the size of muHTT aggregates by reducing lysosome accumulation and probably restoring normal autophagic flux (220).

Overall, these experiments allowed to identify the therapeutic dose of cholesterol to prevent behavioral abnormalities in R6/2 mice. Furthermore, these data highlighted that cholesterol exert its beneficial function by acting on several

mechanisms, including improving the function of residual synaptic circuits, partnering specifically with cellular proteins and influencing cell physiology, and restoring the primary defect of brain cholesterol biosynthesis in HD mice.

1.5.3 Intranasal delivery

Recently, a non-invasive approach to deliver cholesterol to the HD brain has been developed (for details of my contribution on this work see the Appendix 6.1.1). The strategy was based on nose-to-brain delivery to overcome the BBB. In fact, the neuroepithelium of the olfactory region is the only part of the body where the peripheral environment is in direct contact with the brain. With this strategy, the delivery is mediated by olfactory and trigeminal nerve pathways that settle drug transport from the nasal cavity to the CNS by an extracellular route that does not require drug binding to any receptor (221, 222, 223).

Liposomes loaded with labelled cholesterol (d6-cholesterol) were developed and delivered via intranasal administration as a non-invasive strategy for cholesterol delivery to the HD brain (224). Liposomes are spherical vesicles formed by one or multiple concentric lipid bilayers with an aqueous solution core. They are biocompatible and can both entrap

and protect water-soluble molecules in their internal water compartment and hydrophobic drugs into their membranes (225).

With this delivery system, it has been demonstrated that, following an acute treatment, d6-cholesterol accumulates in the brain of both wild-type and R6/2 mice. Furthermore, by performing repeated intranasal administration of liposomes, d6-cholesterol distributed and accumulated without differences in striatum, cortex, and cerebellum of R6/2 mice, giving the basis for further preclinical studies to evaluate the therapeutic potential of this approach to supply cholesterol to the HD brain.

1.5.4 Second generation brain-permeable nanoparticles

Given that high doses of cholesterol are needed to obtain full rescue of HD-related phenotypes, to overcome the limitation of g7-NPs-cho1_1.0 used in

214 such as low drug-content, hybrid second generation g7-NPs (herein g7-NPs-cho1_2.0), made of cholesterol and PLGA were produced (226, 227). These g7-NPs-cho1_2.0 were formulated using nanoprecipitation (MIX 1) and single emulsion (MIX 2). Pluronic was used as a surfactant in g7-NPs-cho1_2.0 MIX 1 while PVA was used in MIX 2. The maximal percentage of cholesterol present in g7-NPs-cho1_2.0 MIX 1 and MIX 2 with respect to PLGA content is $57\pm 5\%$ and $44\pm 2\%$ respectively. Thus, cholesterol content is at least 40 times higher than the amount found in g7-NPs-cho1_1.0 (214).

This improvement will allow to potentially deliver an amount of cholesterol similar to the most efficacious dose identified with minipumps. Table 1.2 summarizes the features of g7-NPs-cho1_2.0 used in this work.

Experiment	NPs	Concentration (mg/mL)	Z-av (nm)	PDI	Z-pot (mV)	Amount of chol (mg)
Biodistribution	cy5-g7-NPs-cho1_2.0 MIX 1	5,9	287	0,230	-22	N/D
	cy5-g7-NPs-cho1_2.0 MIX 1	7,5	240	0,180	-20	N/D
	cy5-g7-NPs-cho1_2.0 MIX 2	7,8	234	0,180	-21	N/D
	cy5-g7-NPs-cho1_2.0 MIX 2	7,0	250	0,130	-21	N/D
Chol release: qualitative analysis	cy5-g7-NPs-bodipy-cho1_2.0 MIX 1	8,5	246	0,210	-18	N/D
	cy5-g7-NPs-bodipy-cho1_2.0 MIX 2	8,8	270	0,160	-19	N/D
Chol release: quantitative analysis	g7-NPs-d6-cho1_2.0	8,9	230	0,210	-14	33,00
	g7-NPs-d6-cho1_2.0	8,5	225	0,195	-22	29,00
	g7-NPs-d6-cho1_2.0	7,3	203	0,253	-21	22,00
	g7-NPs-d6-cho1_2.0	9,0	225	0,234	-22	22,00
Behavioral analysis in R6/2 mice	g7-NPs-cho1_1.0	9,0	180	0,050	-22	0,90
	g7-NPs-cho1_2.0	8,5	255	0,280	-23	35,00
	g7-NPs-cho1_2.0	8,5	244	0,260	-24	36,00
	g7-NPs-cho1_2.0	9,4	240	0,270	-24	35,00
	g7-NPs-cho1_2.0	9,8	256	0,280	-24	42,00
	g7-NPs-cho1_2.0	7,7	243	0,260	-29	38,00
	g7-NPs-cho1_2.0	8,0	255	0,310	-19	34,90
Behavioral analysis in Q175 mice	g7-NPs-cho1_2.0	8,0	255	0,310	-19	34,90
	g7-NPs-cho1_2.0	8,0	295	0,350	-21	35,00
	g7-NPs-cho1_2.0	8,4	225	0,280	-21	35,73
	g7-NPs-cho1_2.0	9,0	260	0,300	-30	30,00
	g7-NPs-cho1_2.0	8,7	250	0,280	-35	32,00
	g7-NPs-cho1_2.0	8,5	240	0,220	-35	30,00
	g7-NPs-cho1_2.0	8,4	264	0,370	-25	28,00

Table 1.2 NPs used in the study

List of the different NPs formulations used in the study.

2. Results and Discussion

2.1 g7-NPs-*chol*_2.0 cross the blood-brain barrier and reach different cell types in the brain

As well as g7-NPs-*chol*_1.0, g7-NPs-*chol*_2.0 were designed to cross the BBB, and previous studies indicated that about 10% of the injected NPs modified with the g7 peptide are estimated to penetrate the brain (216, 217, 218, 219, 228, 229). First of all, both g7-NPs-*chol*_2.0 MIX 1 and MIX 2 were tested in 7-week-old wild-type

mice (wt, BL6CBAF1/J) to verify that g7-NPs-*chol*_2.0 are up taken *in vivo* and to study their distribution (n=2 mice/MIX/time point).

To this aim, we performed immunohistochemical analysis on the brain and on peripheral tissues following a single or multiple (n=3) intraperitoneal (I.P.) injection of g7-NPs-*chol*_2.0 MIX 1 or MIX 2 labelled with cyanine 5 (cy5-g7-NPs-*chol*_2.0). Mice were sacrificed at different time points (4 h, 24 h, 1 week and 2 weeks after the I.P. injection) to analyze the localization of the red signals (Fig. 2.1).

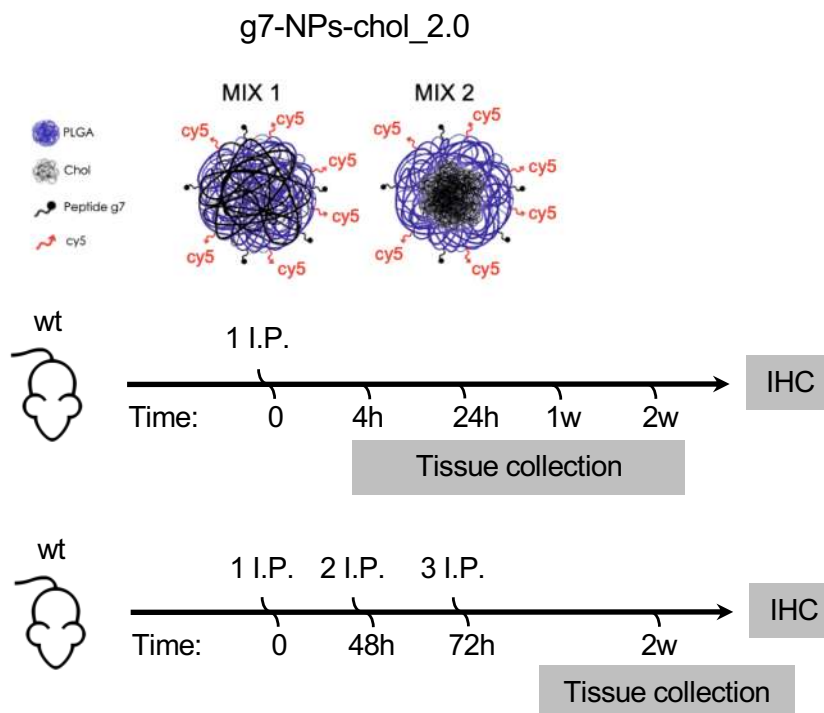


Figure 2.1 Characterization of g7-NPs-*chol*_2.0 distribution *in vivo*

Experimental paradigm used in the study. Wild type mice (n=2 mice/MIX/time point) were treated with a single or multiple I.P. injection of g7-NPs-*chol*_2.0 (MIX 1 or MIX 2) and sacrificed at different time point. Brain, liver and lung were collected for distribution analysis.

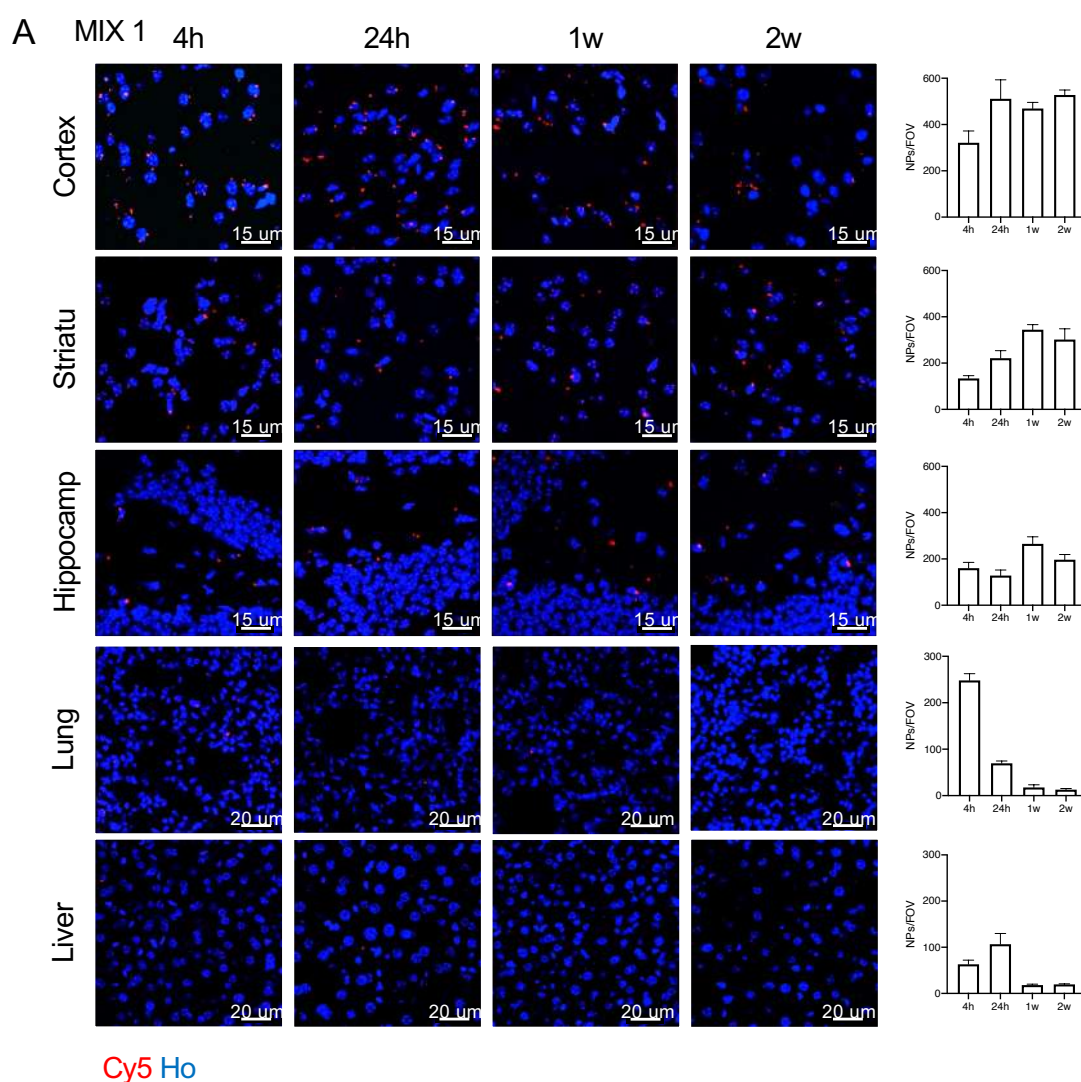
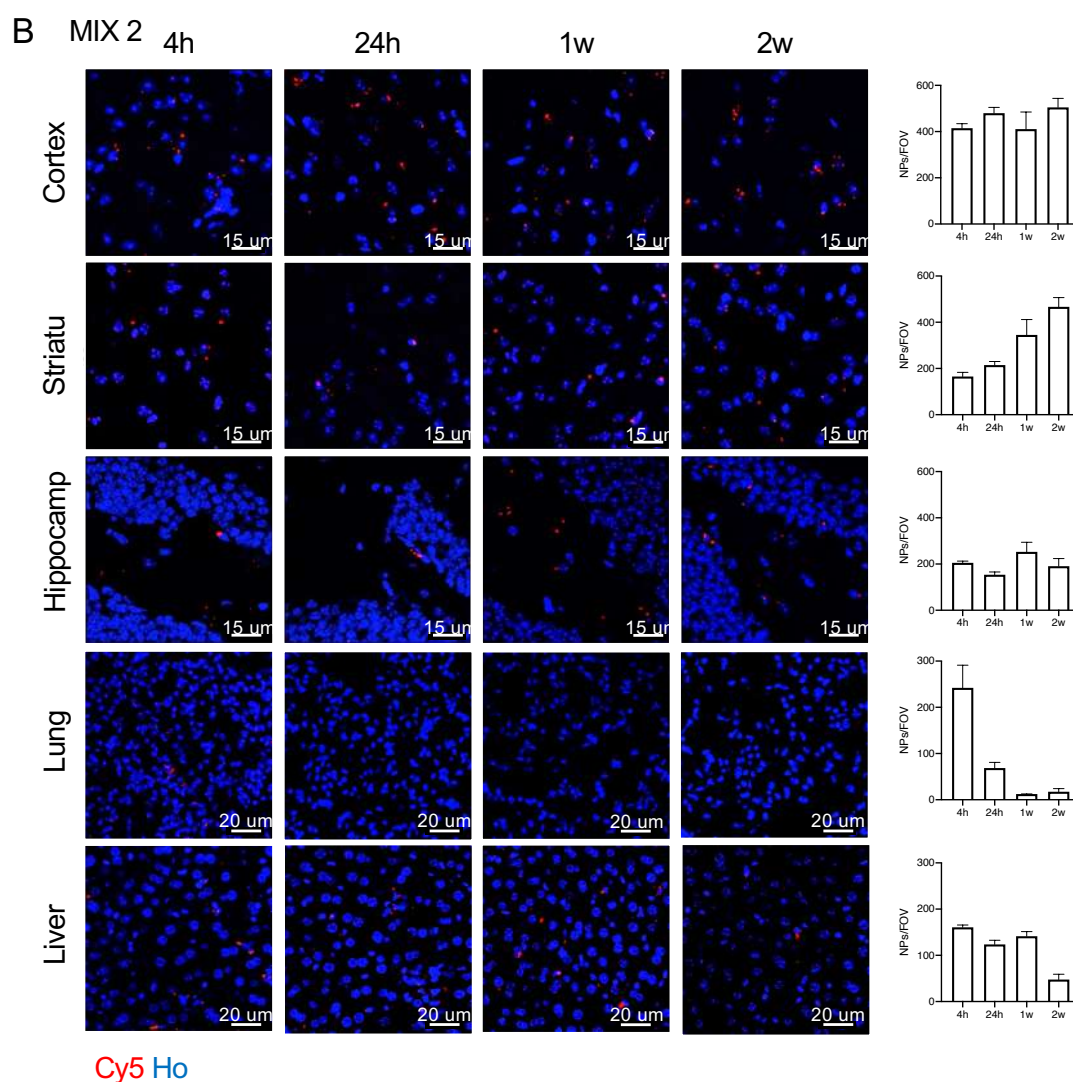


Figure 2.2 Characterization of g7-NPs-cholesterol 2.0 distribution in vivo following a single I.P. injection

A-B. Representative confocal images of cortex, striatum, hippocampus, lung, and liver slices from wt mice I.P. injected with g7-NPs-cholesterol 2.0 (MIX 1 in A or MIX 2 in B) and sacrificed after 4h, 24h, 1w, and 2w with relative quantification.

Hoechst were used to counterstain nuclei (Ho, blue).

Data are expressed as the number of g7-NPs for 1 field of view \pm SEM.



4 h after a single I.P. injection, cy5-g7-NPs-cholesterol_{2.0} were detected in brain (both in striatum, cortex and hippocampus) as well as in lung and liver (Fig. 2.2A and B). Successive quantification of cy5-g7-NPs-cholesterol_{2.0} revealed that the kinetic of cy5-g7-NPs-cholesterol_{2.0} in peripheral tissues was quite fast, since cy5 signal strongly decreased 24 h after the I.P. injection (Fig. 2.2A and B). Importantly, NPs were accumulating

in the brain over time since the cy5 signal was still present 24 h, 1 weeks and 2 weeks after the I.P. injection (Fig. 2.2A and B) and more NPs were detected following multiple injections (Fig. 2.3). The biodistribution was similar between cy5-g7-NPs-cholesterol_{2.0} MIX 1 and MIX 2 even if cy5-g7-NPs-cholesterol_{2.0} MIX 2 showed higher aggregation in peripheral tissues. This was particularly evident after multiple I.P. injections (Fig. 2.3).

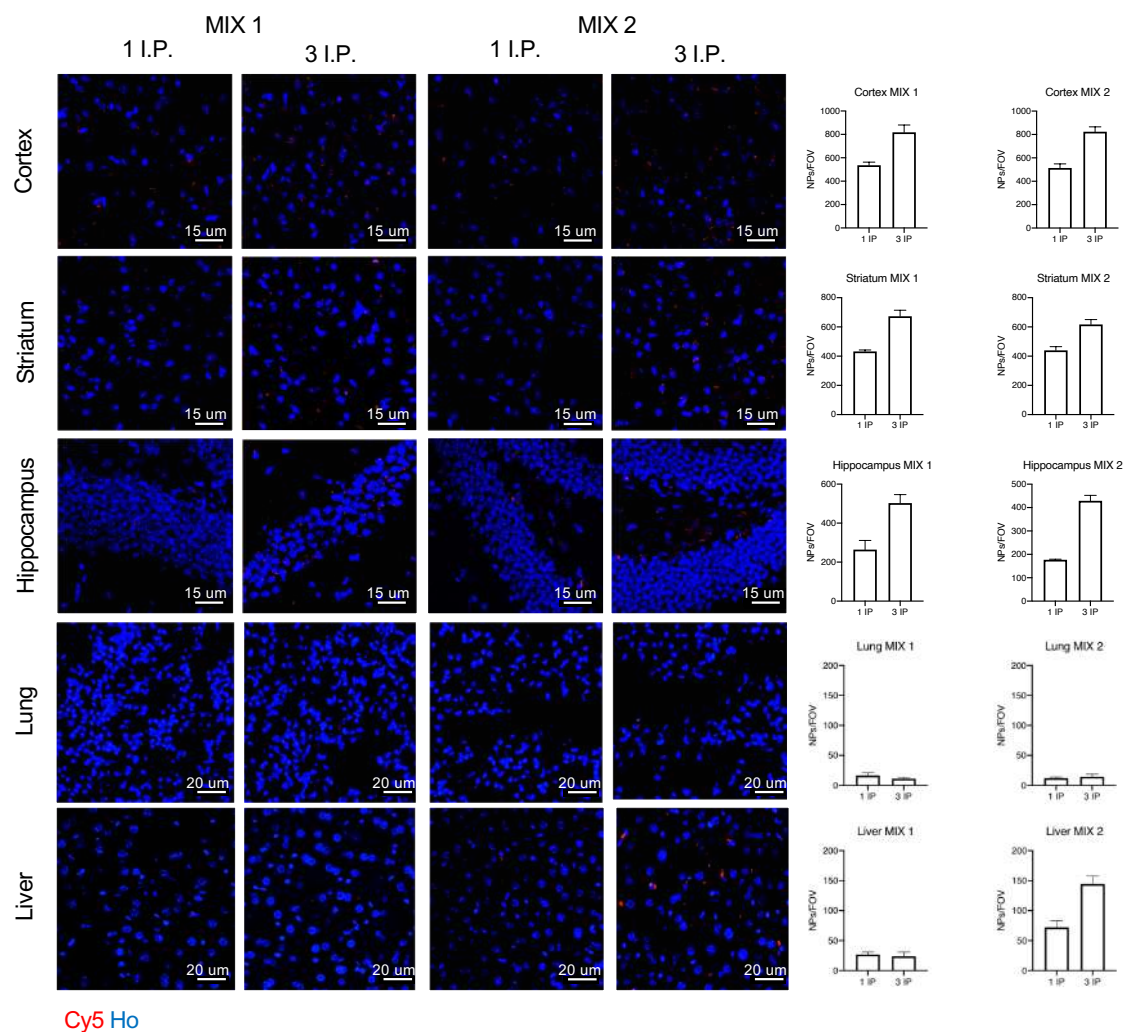


Figure 2.3 Characterization of g7-NPs-cho1_2.0 distribution in vivo following multiple I.P. injections
 Representative confocal images of cortex, striatum, hippocampus, lung, and liver slices from wt mice that received 1 or 3 I.P. injection of g7-NPs-cho1_2.0 (MIX 1 or MIX 2) and sacrificed after 2w with relative quantification.
 Hoechst were used to counterstain nuclei (Ho, blue).
 Data are expressed as the number of g7-NPs for 1 field of view \pm SEM.

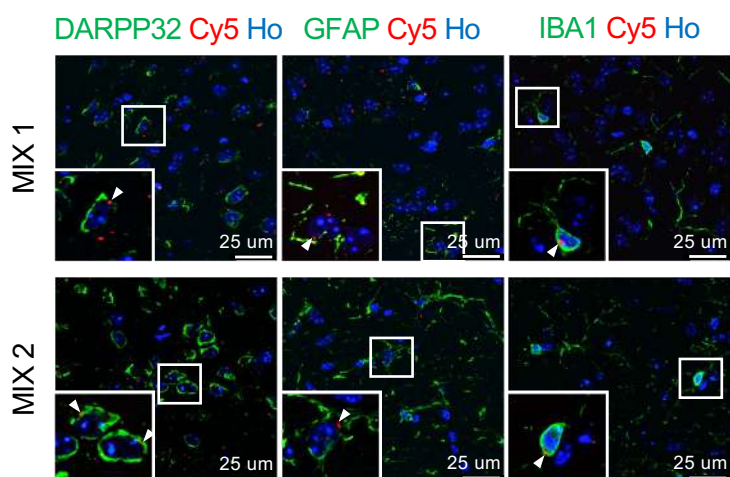


Figure 2.4 g7-NPs-cho1_2.0 reach different brain cell types

Representative confocal images of immunostaining against DARPP32, GFAP, and IBA1 (green) on coronal sections of brains isolated from wt mice I.P. injected with g7-NPs-cho1_2.0 labelled with cy5 (red) and sacrificed 2 weeks after the injection. White arrowheads indicate intracellular g7-NPs.

Hoechst were used to counterstain nuclei (Ho, blue).

Data are expressed as the number of g7-NPs for 1 field of view \pm SEM.

High-magnification confocal images indicated the presence of cy5-g7-NPs-*chol_2.0* in different neuronal and glial cell types such as DARPP32 positive MSNs, GFAP positive astrocytes, and IBA1 immuno-reactive microglial cells (Fig. 2.4).

Overall, these results highlighted that the distribution of *g7-NPs-*chol_2.0** is similar to that of *g7-NPs-*chol_1.0** (214).

2.2 Cholesterol is released from *g7-NPs-*chol_2.0** in vivo

2.2.1 Qualitative analysis

To track cholesterol delivery and intracellular release by *g7-NPs-*chol_2.0**, we performed specific experiments using *cy5-g7-NPs-*chol_2.0** loaded with the fluorescent analogue bodipy cholesterol (*cy5-g7-NPs-bodipy-*chol_2.0**).

Bodipy cholesterol closely resembles the structure of native cholesterol, localizes in the membrane's interior and is commonly used to study lipid transport processes as well as lipid-protein interactions (230). We monitored *g7-NPs-*chol_2.0** degradation and consequent bodipy cholesterol release following the red spots and the green signal respectively. R6/2 mice, a well-established early onset transgenic mouse model of HD (131), were used for this analysis together with age matched wild-type littermates. Accordingly, 7-week-old wild-type and R6/2 mice ($n=3$ mice/MIX/time point/genotype) were treated with a single I.P. injection of *cy5-g7-NPs-bodipy-*chol_2.0** MIX 1 or MIX 2 and sacrificed at different time point (24 h, 1 week and 2 weeks after the I.P. injection) (Fig. 2.5).

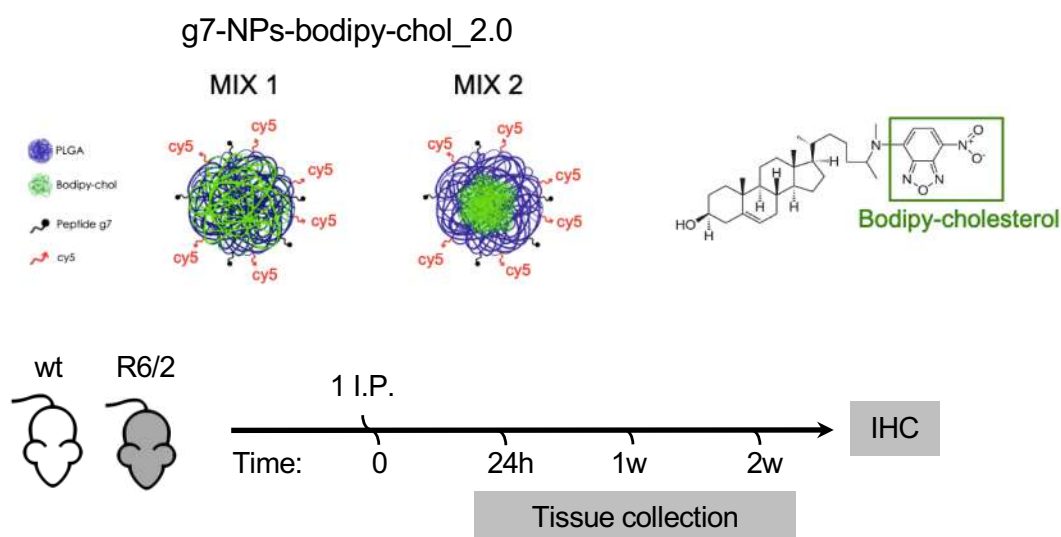


Figure 2.5 Cholesterol release from *g7-NPs-*chol_2.0**: qualitative analysis

Experimental paradigm used in the study. Wild type and R6/2 mice ($n=3$ mice/genotype/MIX/time point) were treated with a single I.P. injection of *g7-NPs-bodipy-*chol_2.0** (MIX 1 or MIX 2) and sacrificed at different time point. Brain and liver were collected for the analysis.

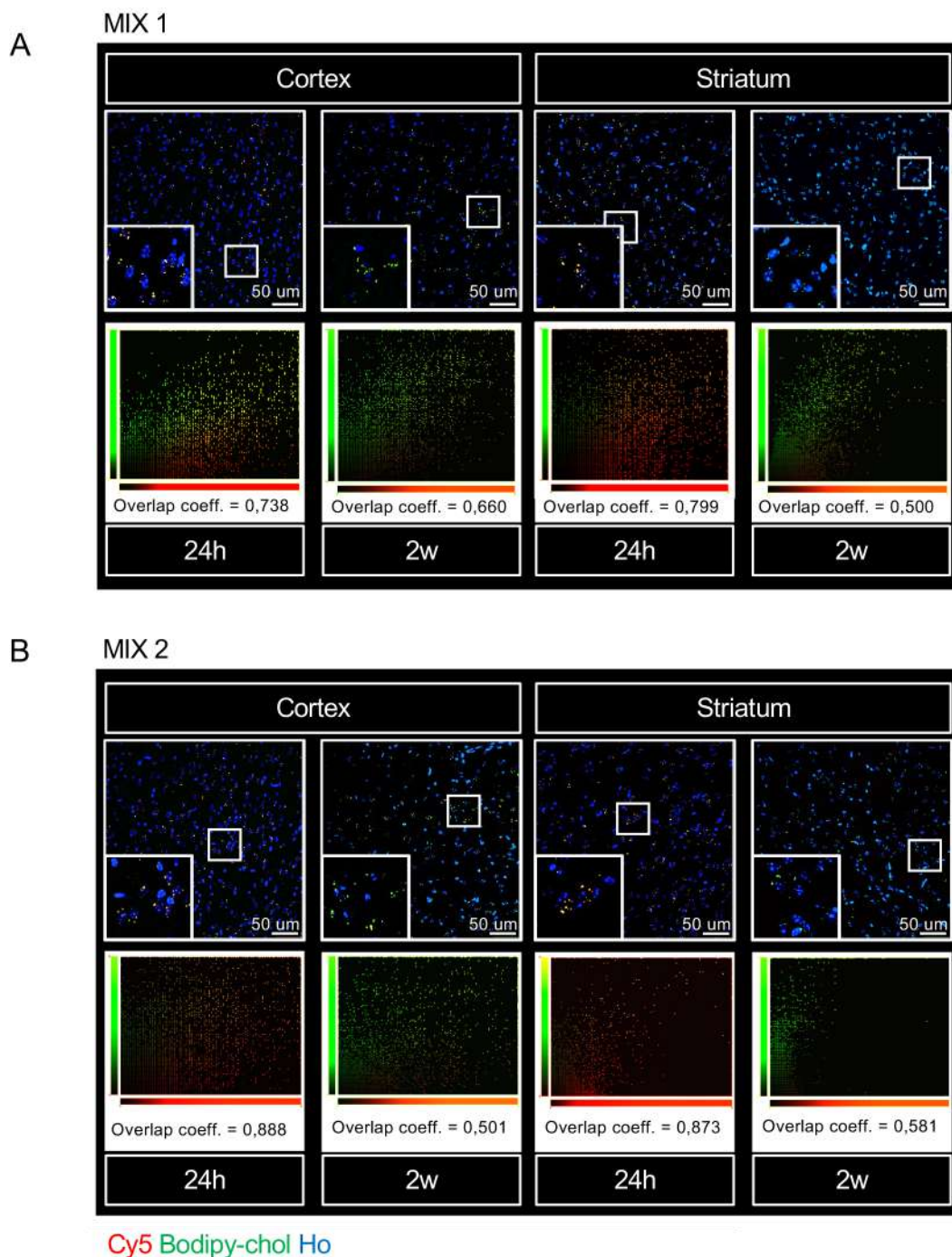
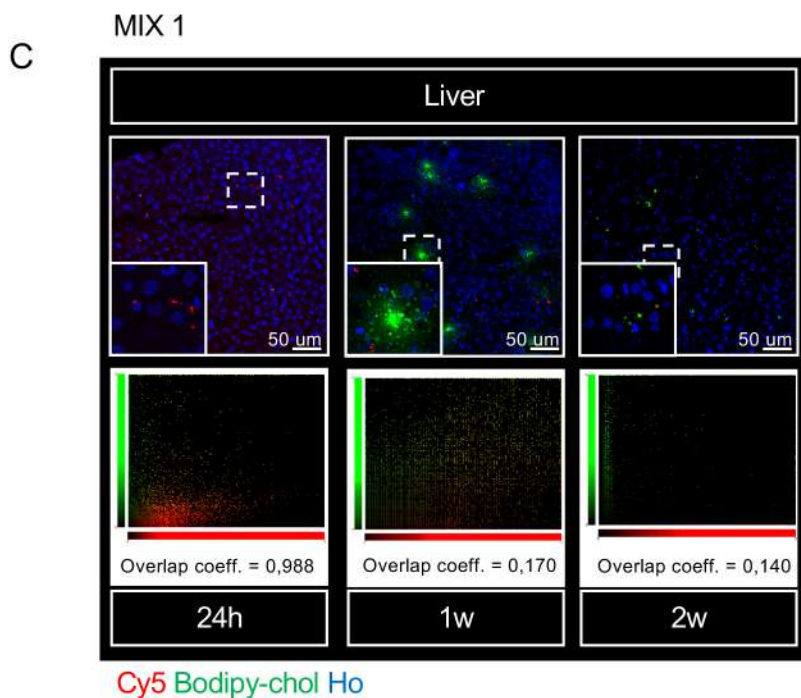


Figure 2.6 Cholesterol release from g7-NPs-cholesterol_2.0: qualitative analysis

A-B. Representative confocal image of brain slices from R6/2 mice I.P. injected with g7-NPs-bodipy-cholesterol_2.0 (MIX 1 in A or MIX 2 in B) and sacrificed after 24 h or 2 weeks and relative co-localization of bodipy-cholesterol and g7-NPs.

C. Representative confocal image of liver slices from R6/2 mice I.P. injected with g7-NPs-bodipy-cholesterol_2.0 (MIX 1) and sacrificed after 24h, 1 weeks or 2 weeks and relative co-localization of bodipy-cholesterol and g7-NPs.



With both MIXs, 24 h after a single I.P. injection of cy5-g7-NPs-bodipy-cholesterol_2.0, cy5 and bodipy cholesterol signals co-localized in brain cells as indicated by the scatterplot of red and green pixel intensities. However, successive analysis performed 1 week and 2 weeks after the I.P. injection highlighted a partial separation between cy5 and bodipy cholesterol signals (Fig. 2.6A and B). When analyzing the liver, we found that the kinetic of cholesterol release was faster compared to the brain. In fact, we measured complete overlap of red and green signal 24 h after the I.P. injection while 1 week after the I.P. injection all the cholesterol was released from the nanoparticles (Fig. 2.6C).

These findings demonstrated that around 10% of bodipy cholesterol is

released from NPs in the brain starting from 1–2 weeks after the injection, in parallel with a reduction in cy5 signal, probably due to NPs degradation. No differences in cholesterol release kinetic were found between wild-type and R6/2 mice, indicating that cholesterol release does not depend on mice genotype. Overall, these data highlighted that the release of cholesterol from NPs is quite slow. In particular, around 10% of the injected NPs reaches the brain (217) and 10% of cholesterol is released from these NPs in 2 weeks. Even if further analyses are necessary, we can speculate that around 20 weeks are needed to release all the encapsulated cholesterol.

Since g7-NPs-cholesterol_2.0 MIX 1 and MIX 2 exhibited similar bio-distribution

profile and kinetic of cholesterol release, we decided to use only g7-NPs-chol_2.0 MIX 1 (from now g7-NPs-chol_2.0) for this work since they are produced using Pluronic as a surfactant, that is approved by FDA, and they showed less aggregation compared to g7-NPs-chol_2.0 MIX 2.

2.2.2 Quantitative analysis

To study the kinetic of cholesterol release and to measure the total amount of cholesterol delivered, we performed two specific experiments using g7-NPs-chol_2.0 loaded with

deuterated cholesterol (g7-NPs-d6-chol_2.0). Accordingly, in the first experiment 7-week-old R6/2 mice (n=3 mice/time point) were treated with a single I.P. injection of g7-NPs-d6-chol_2.0 and sacrificed at different time point (30 minutes, 6 h, 24 h, 1 week and 2 weeks after the I.P. injection) (Fig. 2.7). Blood, kidney, lung, liver, cortex, striatum, and cerebellum were collected to measure the amount of d6-cholesterol in different tissues using mass spectrometry in collaboration with M. Salmona (M. Negri Institute, Milan).

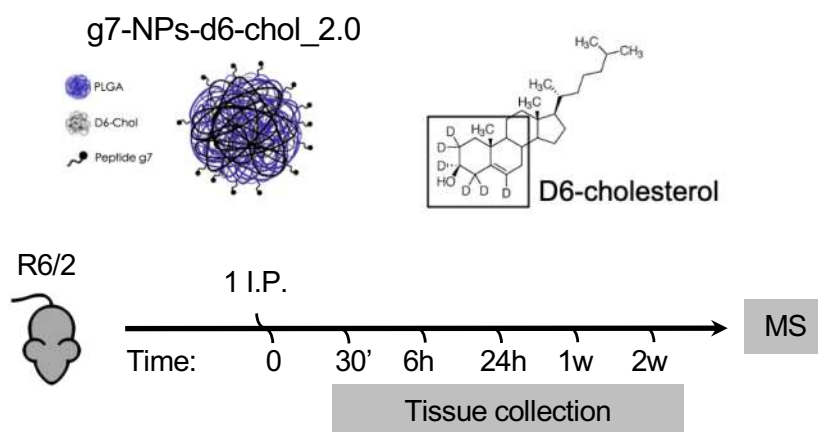


Figure 2.7 Cholesterol release from g7-NPs-chol_2.0: quantitative analysis

Experimental paradigm used in the study. R6/2 mice were treated with a single I.P. injection of g7-NPs-d6-chol_2.0 (MIX 1) and sacrificed at different time point. Striatum, cortex, cerebellum, liver, lung, kidney, and plasma and liver were collected for mass spectrometry analysis (n=3 mice/time point).

Samples were processed using a mild protocol that allow to measure only the d6-cholesterol that was released from g7-NPs-d6-chol_2.0, by preserving the integrity of NPs. Quantification revealed that 6 h after the I.P. injection, g7-NPs-d6-chol_2.0 reached the brain (striatum, cortex and cerebellum) and,

starting from 24 h-1 week after the treatment, cholesterol was released from NPs, confirming the results obtained with the bodipy-cholesterol (Fig 2.8). In the liver, cholesterol was rapidly released 30 minutes after the I.P. injection and it was degraded over the time. The kinetic in lung and kidney

was similar: NPs were detected around 6 h after the I.P. injection, the peak of cholesterol release occurred 1 week after the I.P. injection, and then it was rapidly eliminated. When analyzing the plasma, the maximum amount of cholesterol was measured 24 h after the I.P. injection. Importantly, this

quantity is not significant compared to the physiological amount of cholesterol that is present in the mouse blood (128 mg/100 mL). Table 2.1 shows the amount of d6-cholesterol measured in each tissue at different time points after a single I.P. injection of g7-NPs-d6-chol_2.0.

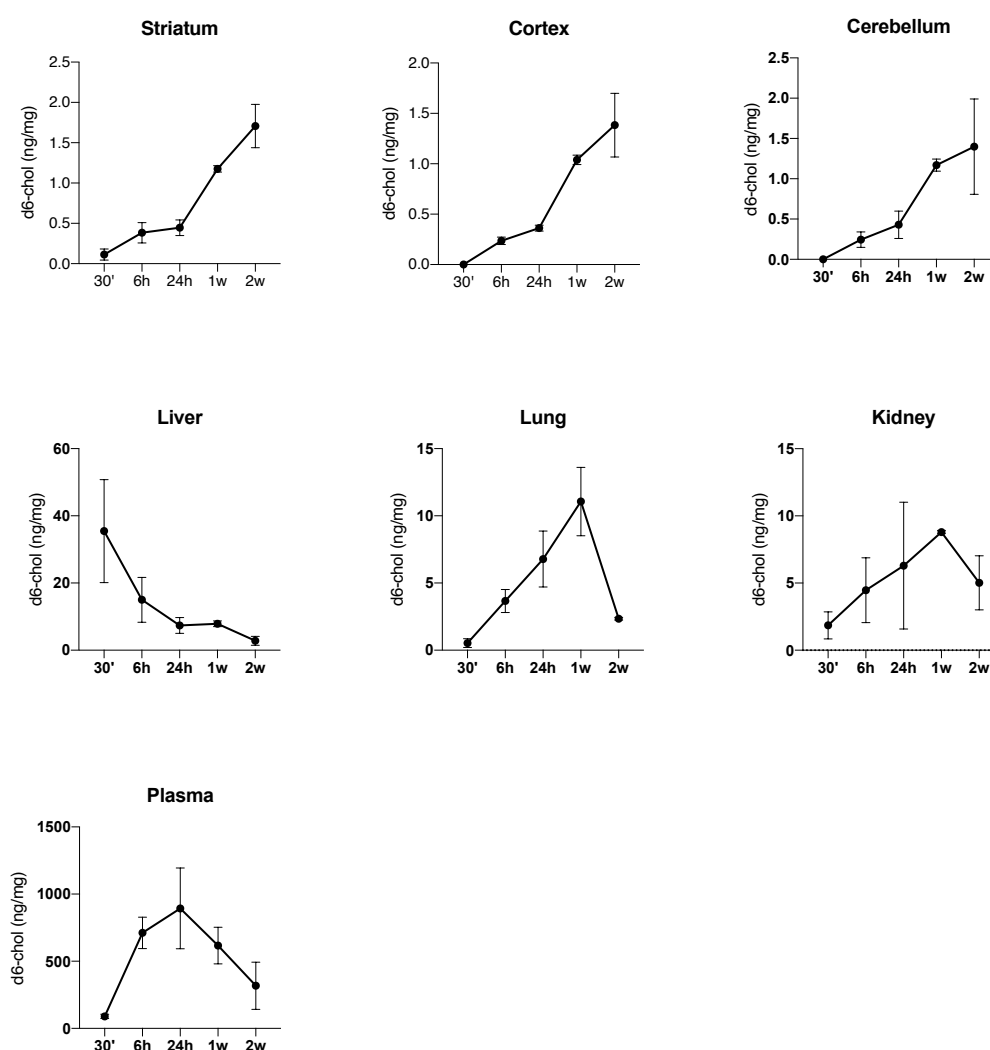


Figure 2.8 Cholesterol release from g7-NPs-cholesterol_2.0: quantitative analysis

Levels of d6-cholesterol in striatum, cortex, cerebellum, liver, lung, kidney, and plasma measured by LC-MS.

Data are expressed as means \pm SEM.

Tissue	Weight (mg or mL)	30'		6h		24h	
		Concentration (ng/mg)	Chol amount (ng)	Concentration (ng/mg)	Chol amount (ng)	Concentration (ng/mg)	Chol amount (ng)
Striatum	60	0,11 ± 0,069	6,60	0,38 ± 0,13	22,80	0,45 ± 0,10	27,00
Cortex	200	0,00 ± 0,00	0,00	0,24 ± 0,06	48,00	0,36 ± 0,07	72,00
Cerebellum	100	0,00 ± 0,00	0,00	0,25 ± 0,10	25,00	0,43 ± 0,17	43,00
Liver	3000	35,45 ± 15,34	106350,00	15,01 ± 6,69	45030,00	7,38 ± 2,34	21990,00
Lung	300	0,53 ± 0,32	159,00	3,66 ± 0,86	1098,00	6,79 ± 2,08	1947,00
Kidney	500	1,85 ± 1,00	925,00	4,47 ± 2,42	2235,00	6,30 ± 4,72	3855,00
Plasma	2	89,73 ± 15,36	179,46	711,3 ± 117,00	1422,60	893,30 ± 300,50	1850,66

Tissue	Weight (mg or mL)	1w		2w	
		Concentration (ng/mg)	Chol amount (ng)	Concentration (ng/mg)	Chol amount (ng)
Striatum	60	1,18 ± 0,04	70,80	1,71 ± 0,27	102,60
Cortex	200	1,04 ± 0,16	208,00	1,38 ± 0,55	276,00
Cerebellum	100	1,17 ± 0,07	117,00	1,40 ± 0,59	140,00
Liver	3000	7,88 ± 0,83	23640,00	2,81 ± 1,31	8430,00
Lung	300	11,07 ± 5,94	3321,00	4,89 ± 4,42	1467,00
Kidney	500	8,80 ± 0,12	4400,00	5,02 ± 2,01	2510,00
Plasma	2	616,67 ± 136,24	1233,34	317,67 ± 176,00	635,34

Table 2.1 Cholesterol release from g7-NPs-chol_2.0: quantitative analysis following a single I.P. injection

R6/2 mice were I.P. injected with a single dose of hybrid-g7-NPs-chol and sacrificed at different time point. Concentration of d6-chol in each tissue is expressed in ng/mg (or mL); d6-chol amount is expressed in ng.

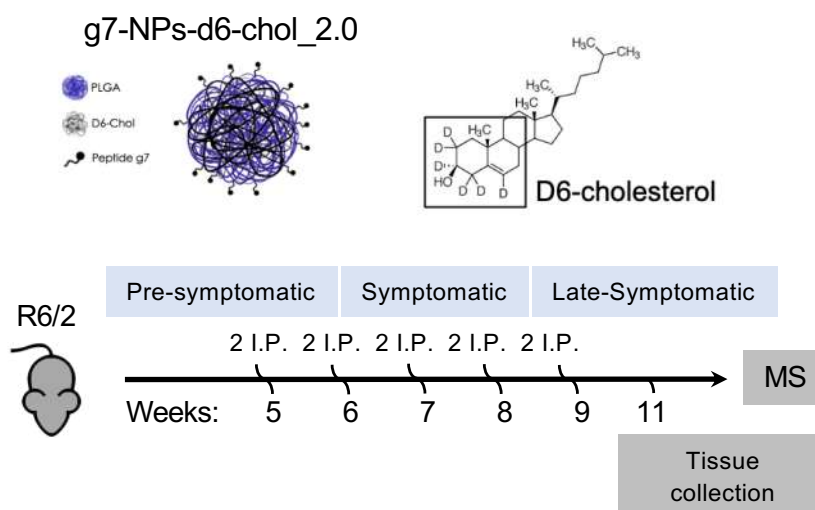


Figure 2.9 Cholesterol release from g7-NPs-chol_2.0: quantitative analysis

Experimental paradigm used in the study. R6/2 mice were treated with g7-NPs-d6-chol_2.0 (MIX 1) from 5 weeks of age to 9 weeks of age with 2 I.P. injection/week and sacrificed 2 weeks after the last I.P. injection. Striatum, cortex, cerebellum, liver, lung, kidney, and plasma and liver were collected for mass spectrometry analysis (n=3 mice).

In the second experiment, to measure the total amount of cholesterol delivered with the therapeutic regimen of interest, R6/2 mice (n=3) were treated from 5 to 9 weeks of age with 2 I.P. injections/week and sacrificed 2

weeks after the last I.P. injection (Fig. 2.9).

Quantification revealed that the amount of d6-cholesterol found in each tissue following 10 I.P. injections was around 10 times the quantity of

cholesterol measured 2 weeks after a single I.P. injections (Fig. 2.10A and B). Table 2.2 shows the total amount of d6-cholesterol measured in each tissue following chronic treatment.

Taken together, these results demonstrated that the kinetic of cholesterol release is different between the brain, the plasma, and peripheral tissues: cholesterol increased in the brain over time, while it decreased in peripheral tissues and in blood. Moreover, with a chronic

treatment of 10 I.P. injections, the total amount of measured cholesterol was around 10 times the quantity we found after a single I.P. injections, meaning that cholesterol accumulates in tissues. Finally, these data support further the idea that the kinetic of cholesterol release from NPs is quite slow. In fact, 2 weeks after a single I.P. injection we measured 1% of the total cholesterol delivered while 2 weeks after 10 I.P. injections we measured 10% of it.

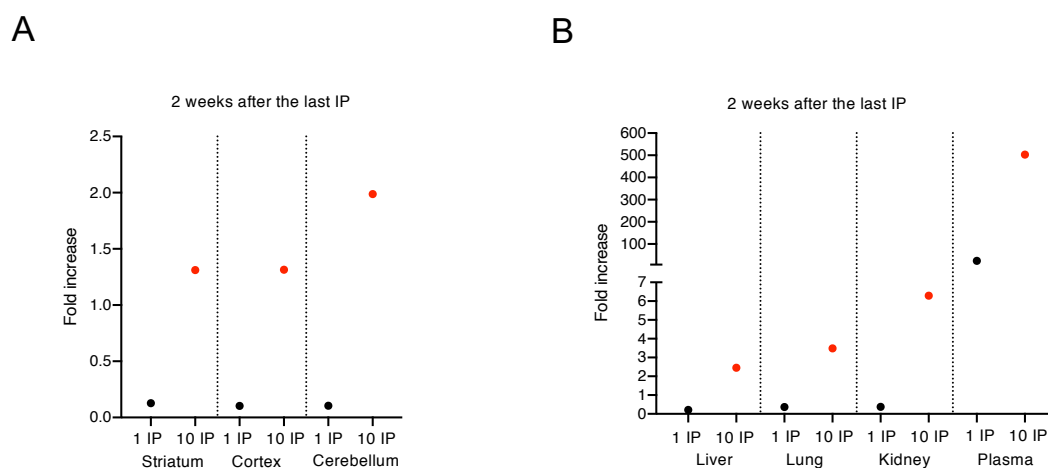


Figure 2.10 Cholesterol release from g7-NPs-cholesterol 2.0: quantitative analysis

A-B. Levels of d6-cholesterol in striatum, cortex, cerebellum (A), liver, lung, kidney, and plasma (B) measured by LC-MS (red dots). Black dots refer to the measurement represented in figure 2.8.

Data are expressed as means \pm SEM.

Tissue	Weight (mg or mL)	10 I.P. injections	
		Concentration (ng/mg)	Chol amount (ng)
Striatum	60	11,27 \pm 1,53	676,20
Cortex	200	11,83 \pm 1,15	2366,00
Cerebellum	100	14,07 \pm 11,17	1407,00
Liver	3000	14,87 \pm 17,23	44610,00
Lung	300	23,90 \pm 8,84	7170,00
Kidney	500	39,30 \pm 3,34	19650,00
Plasma	2	2010,00 \pm 1358,00	4020,00

Table 2.2 Cholesterol release from g7-NPs-cholesterol 2.0: quantitative analysis following 10 I.P. injections

R6/2 mice were injected with 10 I.P. of hybrid-g7-NPs-cholesterol and sacrificed 2 weeks after the last I.P. injection. Concentration of d6-cholesterol in each tissue is expressed in ng/mg (or mL); d6-cholesterol amount is expressed in ng.

2.3 Cholesterol delivery to the brain: comparison between g7-NPs-chol_1.0 and g7-NPs-chol_2.0

2.3.1 Endogenous cholesterol synthesis is influenced by g7-NPs-chol_2.0

Recently, we have demonstrated that a high dose of exogenous cholesterol together with increased endogenous cholesterol synthesis are needed to have a full rescue of HD-related parameters (220). As described in 226, g7-NPs-chol_2.0, with their hybrid structure, have at least 40 times more cholesterol than the amount found in g7-NPs-chol_1.0 used in 214. To analyze whether the

increased cholesterol delivered with g7-NPs-chol_2.0 compared to g7-NPs-chol_1.0 indirectly stimulate the endogenous cholesterol synthesis or catabolism in the brain of HD mice, R6/2 mice (n=4/group) were treated with g7-NPs-chol_1.0 or g7-NPs-chol_2.0 from 5 to 9 weeks of age with 2 I.P. injections/week and sacrificed 2 weeks after the last I.P. injection (Fig. 2.11).

Striatum was collected and processed to measure the total amount of lathosterol, desmosterol, lanosterol, and 24S-OHC by mass spectrometry in collaboration with Carlo Besta Neurological Institute of Milan.

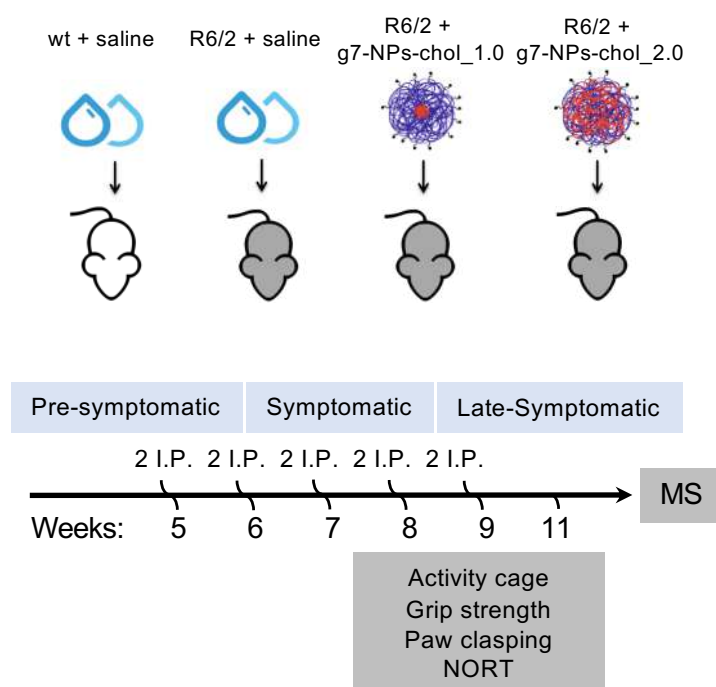


Figure 2.11 Chronic administration of g7-NPs-chol_1.0 and g7-NPs-chol_2.0 to R6/2 mice

Experimental paradigm used in the study. R6/2 mice were treated with g7-NPs-chol_1.0 and g7-NPs-chol_2.0 from 5 weeks of age to 9 weeks of age with 2 I.P. injection/week. Wt and R6/2 littermates were treated with saline solution as controls. Behavioral tests were performed at 9 and 11 weeks of age. Striatum and cortex were collected at 11 weeks of age for mass spectrometry analysis (n=3 mice/time point).

As expected, a robust deficit in level of the key cholesterol precursors lathosterol, desmosterol, and lanosterol was found in the striatum of R6/2 mice treated with saline compared to wild-type littermates (Fig. 2.12A), indicating that cholesterol synthesis is decreased in the brain of HD mice and confirming further previous results (134, 135, 220).

When we compared the level of these metabolites in R6/2 mice treated

with g7-NPs-*chol*_1.0 and g7-NPs-*chol*_2.0, we found a significant increase in striatal level of desmosterol and lanosterol only in R6/2 mice treated with g7-NPs-*chol*_2.0 (Fig. 2.12B).

Of note, level of the cholesterol catabolite 24S-OHC, which are known to be reduced in R6/2 mice compared to wild-type (Fig. 2.12A), was not influenced neither by g7-NPs-*chol*_1.0 nor g7-NPs-*chol*_2.0 (Fig. 2.12B).

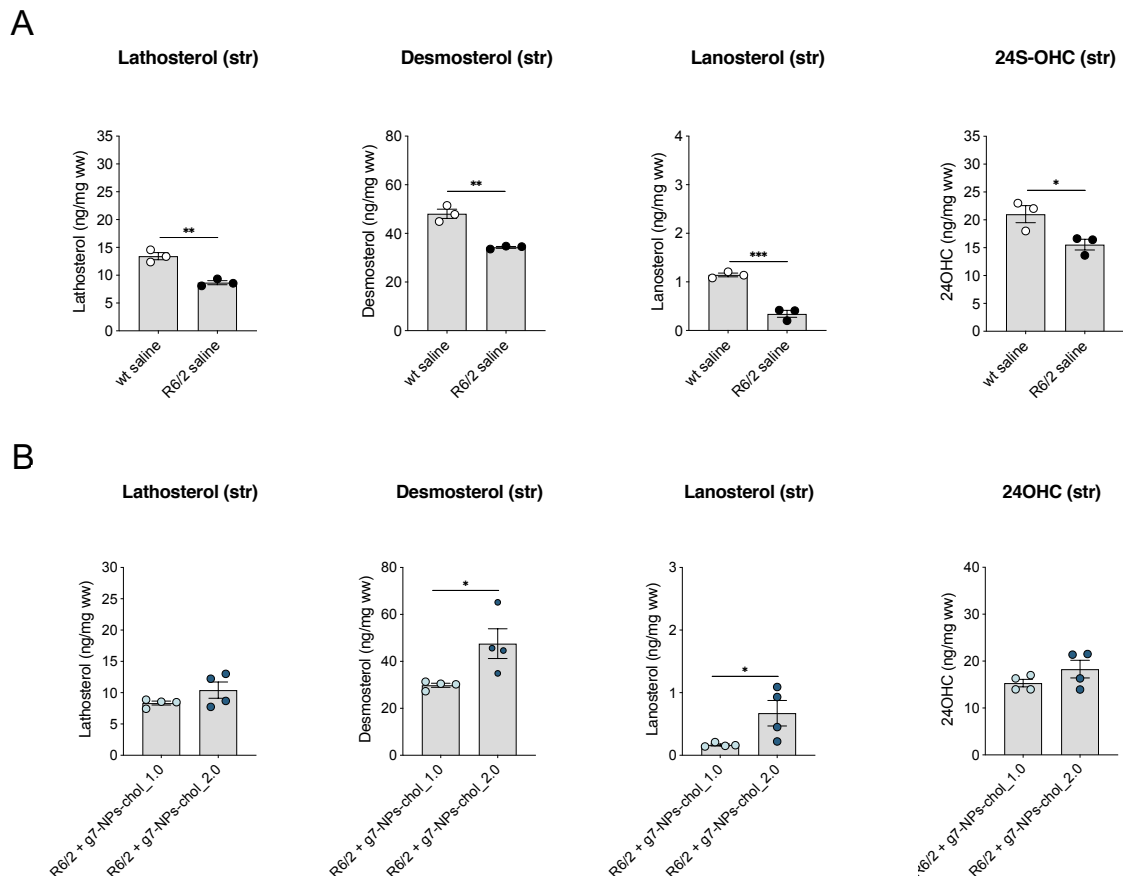


Figure 2.12 Endogenous cholesterol catabolism and synthesis following cholesterol supplementation
A-B. Lathosterol, desmosterol, lanosterol, and 24S-OHC level measured by GC-MS in striatum and cortex of wt saline, R6/2 saline (B), R6/2 + g7-NPs-*chol*_1.0, and R6/2 + g7-NPs-*chol*_2.0 (C) mice at 11 weeks of age ($n=4$ mice/group).

Data are expressed as means \pm SEM. Each dot corresponds to the value obtained from each animal. Statistics: unpaired Student *t*-test (* $p<0.05$; ** $p<0.01$).

Even if it seems counterintuitive, these data confirm that the excess of exogenous cholesterol might operate in a positive feedback on endogenous cholesterol biosynthesis, which is already compromised in R6/2 mice, as demonstrated in 220. The low dose of cholesterol delivered with g7-NPs-chol_1.0 was not sufficient to operate this feedback, while the high dose of cholesterol supplied to the HD brain with g7-NPs-chol_2.0 was sufficient to increase the level of cholesterol precursors. Taken together, these results confirmed that a high dose of exogenous cholesterol is needed to have a positive feedback and stimulate the endogenous synthesis of cholesterol.

2.3.2 Cholesterol delivery prevents cognitive decline and ameliorate motor deficits in R6/2 mice in a dose-dependent manner

R6/2 mice develop a progressive neurological phenotype characterized by cognitive and motor symptoms resembling those present in HD (196, 197, 199, 200). It has already been shown that I.P. injections of g7-NPs-chol_1.0 (15 µg of cholesterol to the HD brain) partially restored GABAergic and glutamatergic transmission in striatal MSNs, prevented cognitive decline and partially restored the level of synaptic proteins in R6/2 mice (214). However, this dose of cholesterol was

not sufficient to have a beneficial effect on the motor phenotype of R6/2 mice. To assess whether g7-NPs-chol_2.0 are a better tool to counteract R6/2 behavioral phenotypes compared to g7-NPs-chol_1.0, we investigated the impact of cholesterol supplementation with the two strategies on behavioral abnormalities in R6/2 mice by using standard motor and cognitive tasks. Accordingly, we performed 3 independent trials with the experimental paradigm shown in Fig. 2.11 comparing:

- n = 25 wild-type mice treated with saline
- n = 17 R6/2 mice treated with saline
- n = 9 R6/2 mice treated with g7-NPs-chol_1.0
- n = 17 R6/2 mice treated with g7-NPs-chol_2.0

We did not test empty g7-NPs-chol_1.0 since it has already been demonstrated that they do not have any effect on the behavior of R6/2 mice (214). Regarding g7-NPs-chol_2.0, since they have a hybrid structure where cholesterol is both the therapeutic molecule and a structural component, it was not possible to produce empty g7-NPs-chol_2.0.

The rotarod test was used to evaluate motor coordination at 8 and 10 weeks of age. Mice were tested on a rotating bar with accelerating speed and their latency to fall was measured. Starting from 8 weeks of age, R6/2 mice

showed a progressive deterioration in fine motor coordination, as shown by the shorter latency to fall compared to wild-type littermates.

When comparing R6/2 mice treated with g7-NPs-*chol*_1.0 or g7-NPs-*chol*_2.0, no differences were found (Fig. 2.13).

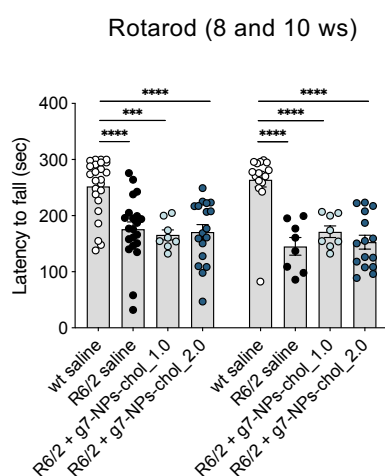


Figure 2.13 Motor abilities of R6/2 mice assessed by rotarod test following cholesterol supplementation

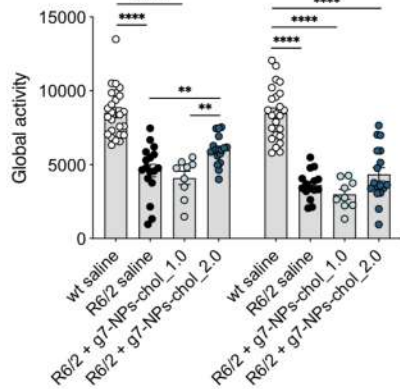
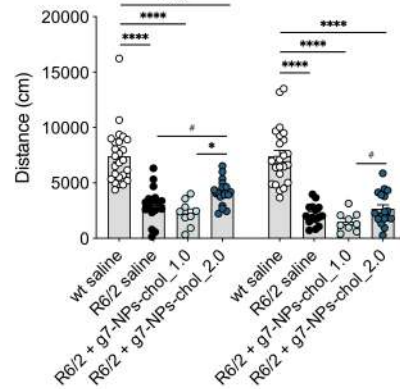
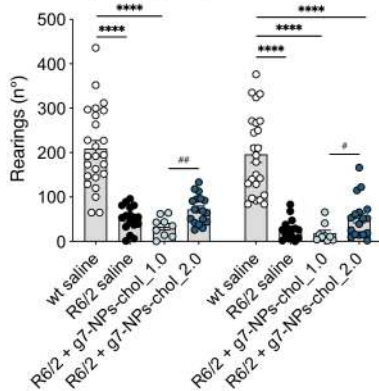
Latency to fall (seconds) from an accelerating rotarod at 8 and 10 weeks of age in wt saline ($n=24-25$), R6/2 saline ($n=15-17$), R6/2 + g7-NPs-*chol*_1.0 ($n=9$), and R6/2 + g7-NPs-*chol*_2.0 ($n=17$).

Data are from three independent trials and shown as scatterplot graphs with means \pm SEM. Each dot corresponds to the value obtained from each animal.

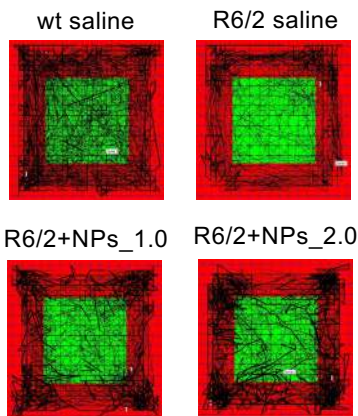
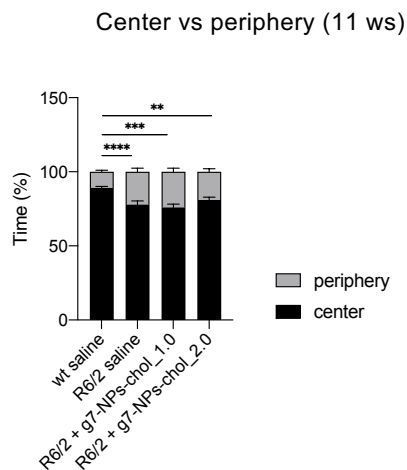
Statistics: one-way ANOVA with Newman-Keuls post-hoc test (** $p < 0.001$; **** $p < 0.0001$).

To test motor abilities further, the activity cage test was used to analyze spontaneous locomotion activity. At 9 and 11 weeks of age, mice were placed for one hour into a squared arena surrounded by infrared detectors. At 9 weeks, R6/2 mice typically showed

a severe hypokinetic phenotype as demonstrated by reduced global activity, number of rearing and total distance travelled compared to wild-type, indicating severely impaired motor function. At this time point, mice treated with g7-NPs-*chol*_2.0 had a better performance compared to those treated with g7-NPs-*chol*_1.0 and to untreated R6/2 littermates. These differences were lost at 11 weeks of age, suggesting that even the amount of cholesterol delivered with g7-NPs-*chol*_2.0 is not sufficient to counteract motor deficits at a late symptomatic time point, when the HD phenotype worsen (Fig. 2.14A). When we looked at the total distance travelled and the number of rearings, R6/2 mice treated with g7-NPs-*chol*_2.0 had a better performance compared to R6/2 mice treated with g7-NPs-*chol*_1.0 but the scores was not significant compared to control R6/2 mice, indicating that the amount of cholesterol delivered with g7-NPs-*chol*_2.0 is still not sufficient to rescue these parameters (Fig. 2.14B, C). As a measure of anxiety-like behavior, we also evaluated the time that mice spent exploring the periphery or center area of the arena during the activity cage test (Fig. 2.15A). R6/2 animals spent more time in the periphery compared to wild-type mice, indicating anxiety related behavior. Cholesterol supplementation did not rescue this parameter (Fig. 2.15B).

A Global activity (9 and 11 ws)**B** Distance (9 and 11 ws)**C** Rearings (9 and 11 ws)**Figure 2.14 Motor abilities of R6/2 mice following cholesterol supplementation**

A-C. Global motor activity (A), total distance travelled (B), and number of rearings (C) in an open-field test at 9 and 11 weeks of age in wt saline ($n=24-25$), R6/2 saline ($n=15-17$), R6/2 + g7-NPs-cho1_1.0 ($n=9$), and R6/2 + g7-NPs-cho1_2.0 ($n=17$). Data are from three independent trials and shown as scatterplot graphs with means \pm SEM. Each dot corresponds to the value obtained from each animal. Statistics: one-way ANOVA with Newman-Keuls post-hoc test (* $p<0.05$; ** $p<0.01$; *** $p<0.001$; **** $p<0.0001$) or unpaired Student t -test (# $p<0.05$; ## $p<0.01$).

A**B****Figure 2.15 Anxiety-related behavior of R6/2 mice following cholesterol supplementation**

A-B. Representative track plots (A) generated from the open-field test from wt saline ($n=24-25$), R6/2 saline ($n=15-17$), R6/2 + g7-NPs-cho1_1.0 ($n=9$), and R6/2 + g7-NPs-cho1_2.0 ($n=17$) and relative quantification (B) of the time spent in the center and in the periphery (%) of the arena at 11 weeks of age.

Data are from three independent trials and shown as histogram with means \pm SEM.

Statistics: one-way ANOVA with Newman-Keuls post-hoc test (** $p<0.01$; *** $p<0.001$; **** $p<0.0001$).

The grip strength test assessed mice neuromuscular functions and strength by measuring the force developed by the mouse when the operator tries to retire it out of a bar. Muscular strength was reduced in R6/2 mice from 9 weeks of age and it was completely rescued by g7-NPs-*chol*_2.0 at both 9 and 11 weeks of age, while the amount of cholesterol delivered with g7-NPs-*chol*_1.0 was not sufficient to rescue this parameter (Fig. 2.16).

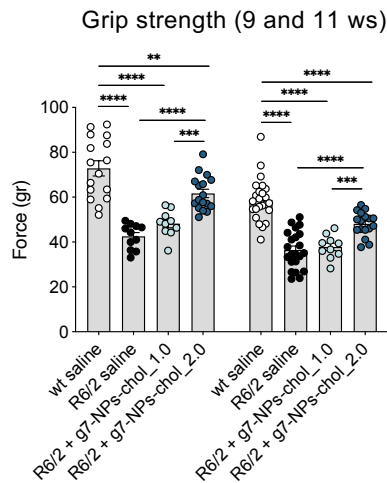


Figure 2.16 Muscular strength of R6/2 mice following cholesterol supplementation

Grip strength (grams) at 9 and 11 weeks of age in wt saline ($n=16-24$), R6/2 saline ($n=11-22$), R6/2 + g7-NPs-*chol*_1.0 ($n=10$), and R6/2 + g7-NPs-*chol*_2.0 ($n=17$).

Data are from three independent trials and shown as scatterplot graphs with means \pm SEM. Each dot corresponds to the value obtained from each animal.

Statistics: one-way ANOVA with Newman-Keuls post-hoc test (** $p < 0.01$; *** $p < 0.001$; **** $p < 0.0001$).

The paw clasping test was used at 8 and 10 weeks of age to measure dystonic movements, which is a marker of neurodegeneration in

several mouse models of brain diseases. Mice were suspended by the tail for 30 seconds: a score of 0 was assigned when the hindlimbs were away from the abdomen, consistently splayed outward, a score of 1 or 2 was assigned when one or both hindlimb was retracted toward the abdomen; a score of 3 was assigned if hindlimbs were entirely retracted and touching the abdomen. Of note, only R6/2 mice treated with g7-NPs-*chol*_2.0 ameliorated this phenotype (Fig. 2.17).

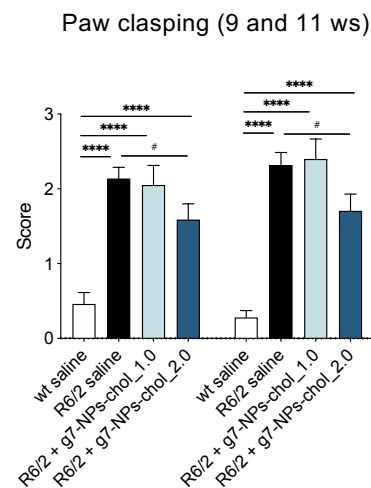


Figure 2.17 Paw clasping behavior of R6/2 mice following cholesterol supplementation

Paw clasping at 9 and 11 weeks of age in wt saline ($n=25$), R6/2 saline ($n=22$), R6/2 + g7-NPs-*chol*_1.0 ($n=10$), and R6/2 + g7-NPs-*chol*_2.0 ($n=17$).

Data are from three independent trials and shown as histogram with means \pm SEM.

Statistics: one-way ANOVA with Newman-Keuls post-hoc test (**** $p < 0.0001$) or unpaired Student *t*-test (# $p < 0.05$).

Finally, the novel object recognition (NOR) test was used at 9 and 11 weeks of age to evaluate the effect of cholesterol delivery on cognitive

function. The test is based on the spontaneous tendency of rodents to spend more time exploring a new object than a familiar one, reflected by a positive discrimination index (DI). As expected, long-term memory declined during disease progression in R6/2 mice, with a marked impairment in the ability to discriminate novel and familiar objects at 11 weeks of age. R6/2 mice treated with g7-NPs-*chol*_2.0 performed similarly to wild-type mice, indicating that this treatment completely prevents the cognitive defects at both 9 and 11 weeks of age. Contrarily, g7-NPs-*chol*_1.0 rescued the defect only at 11 weeks of age (Fig. 2.18).

During the trials, mice were weighted once a week. As expected, weight loss was observed in R6/2 mice starting from late time point (10 weeks of age). Remarkably, this parameter was rescued in male R6/2 mice treated with g7-NPs-*chol*_2.0 (Fig. 2.19A, B). Collectively, these results indicate an overall behavioral recovery in HD mice after cholesterol administration, confirming that the low dose of cholesterol administered with g7-NPs-*chol*_1.0 is sufficient to protect mice from cognitive decline while higher doses are needed to rescue motor dysfunction together with restoration of endogenous cholesterol synthesis, which occurs only when high doses of cholesterol are administered.

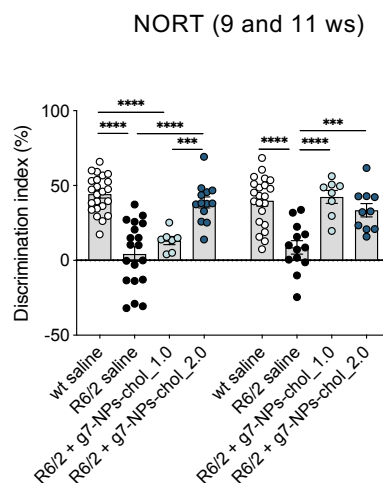


Figure 2.18 Cognitive abilities of R6/2 mice following cholesterol supplementation

Discrimination index (DI %) in the novel object recognition test of wt saline ($n=22-23$), R6/2 saline ($n=13-19$), R6/2 + g7-NPs-*chol*_1.0 ($n=7-8$), and R6/2 + g7-NPs-*chol*_2.0 ($n=10-13$) at 9 and 11 weeks of age. DI above zero indicates a preference for the novel object; DI below zero indicates a preference for the familiar object.

Data are from three independent trials and shown as scatterplot graphs with means \pm SEM. Each dot corresponds to the value obtained from each animal.

Statistics: one-way ANOVA with Newman-Keuls post-hoc test (** $p < 0.001$; **** $p < 0.0001$).

Accordingly, the dose of cholesterol administered with g7-NPs-*chol*_2.0 is sufficient to have a partial rescue of motor abilities at 9 weeks of age but higher doses are needed to completely counteract the defect when the phenotype worsens. Furthermore, it is important to highlight that the kinetic of cholesterol release from NPs is slow and the phenotype of R6/2 mice is too fast and aggressive to have a full rescue. In fact, at the time point analyzed, around 20% of the delivered cholesterol is released from

g7-NPs-*chol_2.0*, thus only a very small percentage of the administered cholesterol is available for neuronal activity.

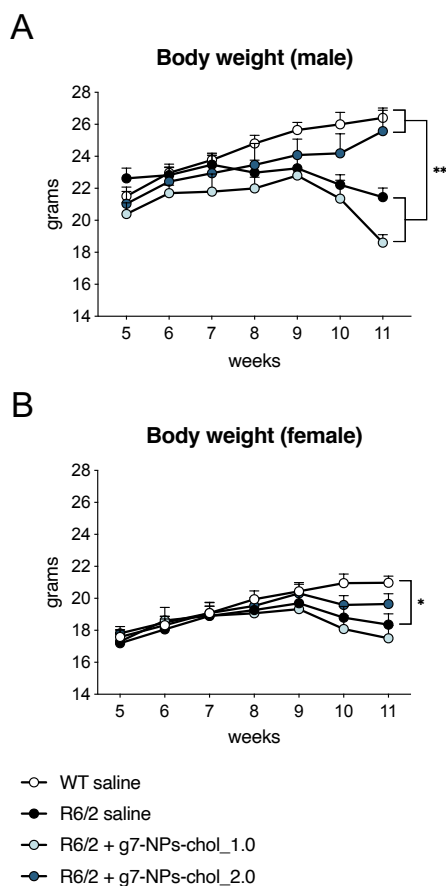


Figure 2.19 Body weight of R6/2 mice following cholesterol supplementation

A-B. Body weight (grams) of male (A) and female (B) mice at different time point.

Data are from three independent trials and shown as graphs with means \pm SEM.

Statistics: one-way ANOVA with Newman-Keuls post-hoc test (* $p < 0.05$; ** $p < 0.01$).

2.4 Administration of g7-NPs-*chol_2.0* does not solicit a massive inflammation response

We sought to assess if the chronic administration of g7-NPs-*chol_2.0* (2 I.P. injections/week, from 5 to 9 weeks of age) influences the inflammation

status of R6/2 mice. To this aim, we used the Bioplex assay, which is based on color-coded magnetic beads and allows the simultaneous detection of 23 cytokines in a single well of a 96-well microplate (Fig. 2.20). Cytokines, chemokines, and growth factors are cell signaling proteins, mediating a wide range of physiological responses, including immunity and inflammation. They are also associated with a spectrum of neurodegenerative diseases including Huntington's and Parkinson's disease. We performed a first pilot experiment to analyze the inflammation status of untreated wild-type and R6/2 mice ($n=5$ /genotype) in striatum, cortex, liver, and plasma. This study revealed that wild-type and R6/2 mice have a similar cytokines and chemokines profile, indicating a normal inflammation status (Table 2.3). The only differences we measured were cortical reduction of IL-13, indicating decreased inhibition of inflammatory cytokines, and plasmatic reduction of GM-CSF, indicating reduced neurogenesis and neuroplasticity, in R6/2 mice compared to wild-type littermates (Table 2.3). When we compared R6/2 mice treated with saline and R6/2 mice treated with g7-NPs-*chol_2.0* ($n=5$ /genotype) we found that Eotaxin is down-regulated in the cortex of cholesterol treated mice compared to R6/2 and wild-type littermates (Table 2.4). Eotaxin

is a cytokine belonging to the CC chemokine family. It is implicated in allergic responses by recruiting eosinophils and inducing their chemotaxis. Increased Eotaxin level in plasma are associated with aging in mice and humans. Furthermore, it has been shown that young mice exposed to Eotaxin or to the plasma of older mice, containing high level of Eotaxin, exhibited decreased neurogenesis and impaired cognitive performance (231).

Clinical observation of mice during

chronic administration regimen did not reveal any case of mortality in the treated and control groups. There were no signs of abnormal behavioral reactions and general clinical symptoms.

Overall, these results suggested that chronic administration of g7-NPs-*chol_2.0* do not lead to inflammation in brain, liver, and plasma, while it reduced the amount of Eotaxin in cortex, indicating that cholesterol may have a beneficial effect on neurogenesis and cognitive decline.

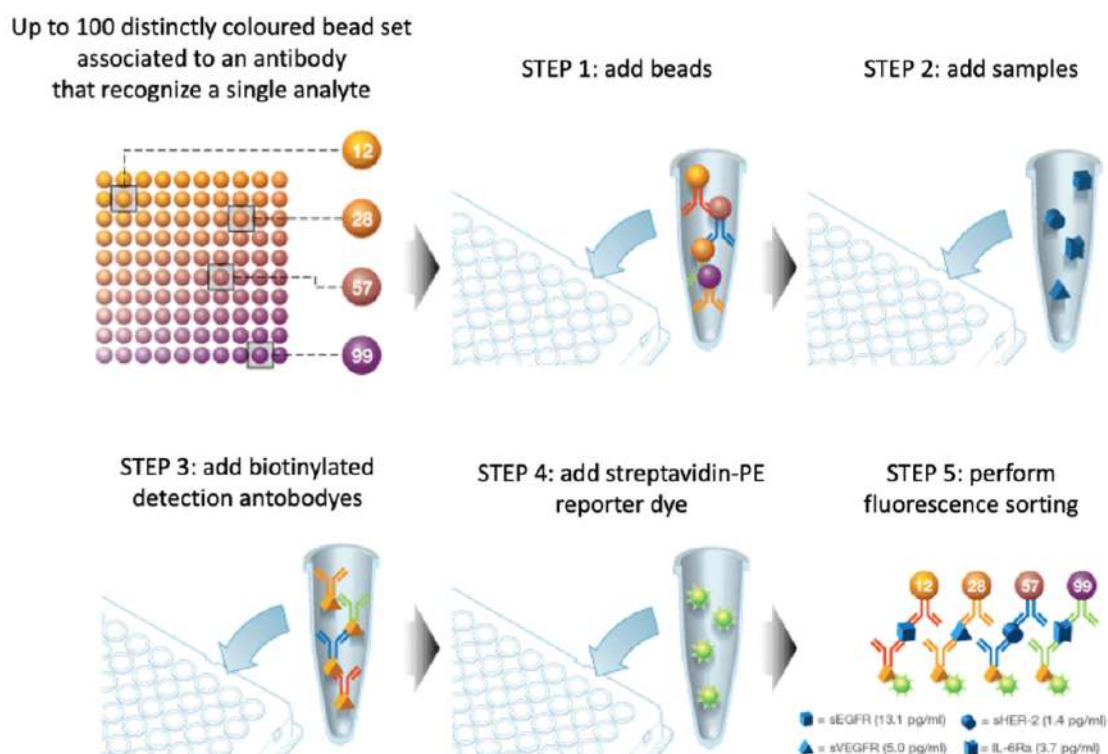


Figure 2.20 Inflammatory response of R6/2 mice following cholesterol supplementation

Assay scheme. The Bio-plex assay is carried out in a 96-well plate in which up to 100 distinctly colored beads set associated to an antibody the recognize a specific analyte can accommodate. In the first step, the beads of interest are added. Then, samples are added in the wells where they bind to the specific antibodies. Biotinylated antibodies are added for the detection while streptavidin-PE antibodies are used as reporter dye. Analytes are sorted exploiting fluorescence.

Analyte	Striatum		Cortex		Liver		Plasma	
	wt (vs R6/2)		wt (vs R6/2)		wt (vs R6/2)		wt (vs R6/2)	
	Mean	SEM	Mean	SEM	Mean	SEM	Mean	SEM
IL-1a	1,159	0,063	1,268	0,112	0,898	0,041	1,055	0,684
IL-1b	1,473	0,218	1,247	0,122	1,078	0,098	0,887	0,265
IL-2	1,029	0,157	1,568	0,397	0,885	0,022	0,445	0,121
IL-3	1,011	0,206	0,803	0,175	1,217	0,121	N/D	N/D
IL-4	1,333	0,144	1,028	0,104	1,306	0,082	0,985	0,142
IL-5	1,401	0,075	0,741	0,096	0,936	0,058	0,911	0,238
IL-6	1,080	0,267	0,947	0,388	1,107	0,059	N/D	N/D
IL-9	1,311	0,071	1,164	0,119	1,113	0,023	N/D	N/D
IL-10	1,160	0,069	0,889	0,054	0,970	0,026	0,957	0,035
IL-12 (p40)	1,322	0,291	0,943	0,279	0,991	0,043	0,860	0,412
IL-12 (p70)	1,097	0,173	0,944	0,053	0,916	0,050	N/D	N/D
IL-13	1,072	0,188	1,377	0,122	1,003	0,142	1,078	0,119
IL-17	1,081	0,115	0,631	0,133	1,172	0,145	0,799	0,278
Eotaxin	1,078	0,076	1,070	0,028	1,069	0,038	0,892	0,138
G-CSF	1,233	0,202	0,985	0,158	1,099	0,135	2,685	0,642
GM-CSF	1,439	0,326	0,475	0,151	1,006	0,150	2,017	0,653
ING-gamma	1,024	0,166	0,936	0,184	0,916	0,053	0,886	0,082
KC	1,443	0,330	0,713	0,113	0,953	0,078	1,078	0,213
MCP-1	1,631	0,453	0,818	0,238	0,675	0,092	0,477	0,201
MIP-1a	1,625	0,122	0,685	0,126	0,692	0,045	1,411	0,808
MIP-1b	1,647	0,551	1,060	0,199	1,297	0,279	1,325	0,595
Ranteg	0,976	0,197	1,450	0,055	0,902	0,036	0,897	0,173
TNF-a	1,073	0,056	1,250	0,154	1,259	0,044	0,685	0,189

Table 2.3 Inflammatory response of R6/2 mice following cholesterol supplementation

Analysis of cytokines and chemokines by Bio-Plex array on the striatum, cortex, liver, and plasma of wt vs R6/2 mice (n=5 mice/group).

Data are normalized on R6/2 mice and are expressed as means \pm standard error of the mean.

Statistics: unpaired Student t-test (*p<0.05).

Analyte	Striatum		Cortex		Liver		Plasma	
	R6/2 + g7-NPs-cholesterol_2.0 (vs R6/2 saline)		R6/2 + g7-NPs-cholesterol_2.0 (vs R6/2 saline)		R6/2 + g7-NPs-cholesterol_2.0 (vs R6/2 saline)		R6/2 + g7-NPs-cholesterol_2.0 (vs R6/2 saline)	
	Mean	SEM	Mean	SEM	Mean	SEM	Mean	SEM
IL-1a	1,010	0,025	0,927	0,033	0,976	0,111	0,212	0,032
IL-1b	1,055	0,200	0,747	0,134	1,088	0,184	0,920	0,381
IL-2	1,415	0,076	0,708	0,013	1,159	0,179	0,398	0,081
IL-3	1,012	0,298	0,771	0,097	1,031	0,038	N/D	N/D
IL-4	0,632	0,110	1,472	0,499	0,744	0,182	0,429	0,184
IL-5	1,264	0,165	1,276	0,561	0,924	0,158	0,330	0,085
IL-6	1,061	0,132	1,019	0,102	0,889	0,133	N/D	N/D
IL-9	0,789	0,143	0,836	0,145	0,900	0,112	N/D	N/D
IL-10	1,020	0,291	0,678	0,123	1,109	0,354	1,175	0,000
IL-12 (p40)	1,666	0,435	0,668	0,176	1,843	0,113	0,921	0,236
IL-12 (p70)	0,944	0,242	0,798	0,138	0,803	0,116	N/D	N/D
IL-13	0,950	0,072	0,835	0,069	0,977	0,097	1,099	0,152
IL-17	1,345	0,414	0,892	0,125	1,194	0,104	1,345	0,414
Eotaxin	1,695	0,359	0,521	0,096	0,958	0,215	0,809	0,195
G-CSF	0,943	0,203	0,914	0,153	1,001	0,120	0,987	0,148
GM-CSF	1,025	0,222	1,060	0,220	1,090	0,080	0,724	0,188
ING-gamma	1,413	0,272	0,899	0,102	1,155	0,184	0,749	0,322
KC	1,337	0,302	1,340	0,169	0,988	0,313	0,489	0,086
MCP-1	0,947	0,375	0,907	0,196	1,657	0,414	1,365	0,689
MIP-1a	1,133	0,326	0,816	0,138	1,065	0,126	0,525	0,222
MIP-1b	1,511	0,186	0,731	0,137	0,920	0,192	0,614	0,452
Ranteg	1,010	0,075	1,020	0,134	0,882	0,087	0,998	0,231
TNF-a	1,173	0,276	0,854	0,249	1,100	0,352	0,851	0,371

Table 2.4 Inflammatory response of R6/2 mice following cholesterol supplementation

Analysis of cytokines and chemokines by Bio-Plex array on the striatum, cortex, liver, and plasma of R6/2 saline mice vs R6/2 + g7-NPs-cholesterol_2.0 mice (n=5 mice/group).

Data are normalized on R6/2 saline mice and are expressed as means \pm standard error of the mean.

Statistics: unpaired Student t-test (*p<0.05).

2.5 Long term and cyclic treatments of g7-NPs-*chol_2.0* in zQ175DN mice ameliorate HD-related behavioral deficits

Since g7-NPs-*chol_2.0* take some weeks to release the encapsulated cholesterol, and R6/2 mouse model has a fast-developing phenotype that does not allow to test the effect of the treatment when all the encapsulated cholesterol has been released, we took advantage of another mouse model of HD to validate further our strategy. In particular, we used the knock-in mouse model zQ175DN, which expresses the neo-deleted knock-in allele encoding the human HTT exon 1 sequence with a ~190 CAG repeat tract, replacing the

mouse *Htt* exon 1.

Conversely to R6/2 mice, this knock-in animal model has a longer lifespan (12 months) with a slower disease progression, more resembling HD in humans (213).

Accordingly, zQ175DN mice (n=15) were treated with g7-NPs-*chol_2.0* from 5 to 9 weeks of age (pre-symptomatic stage) with 2 I.P. injections/week. As control mice, zQ175DN (n=10) and wild-type littermates (wt, C57BL6/J) (n=18) were treated with saline. The impact of cholesterol supplementation on behavioral abnormalities was evaluated by using standard motor and cognitive tasks at 20 weeks of age (Fig. 2.21).

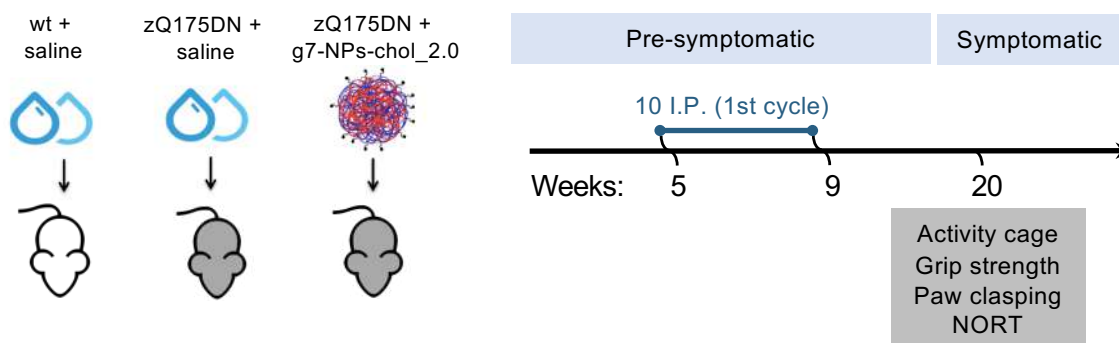
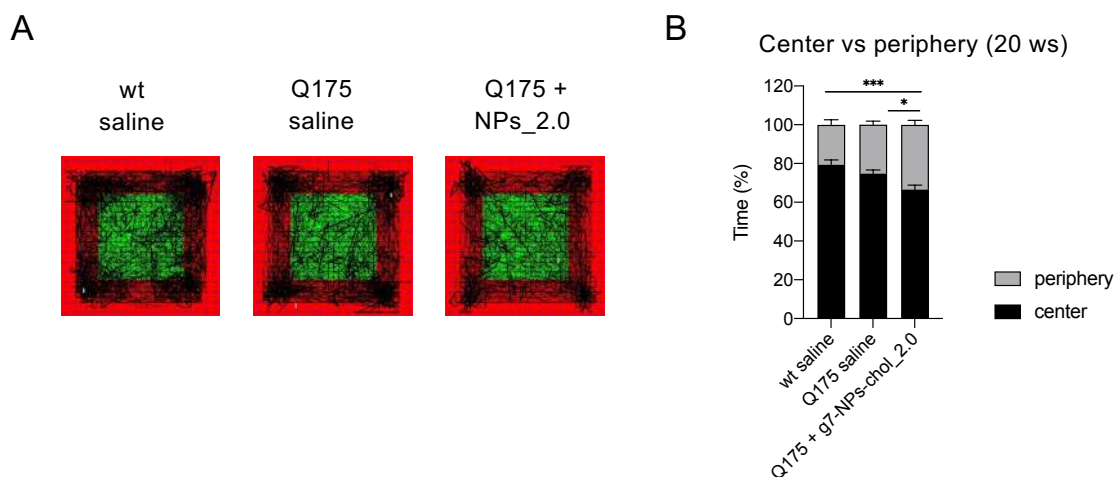
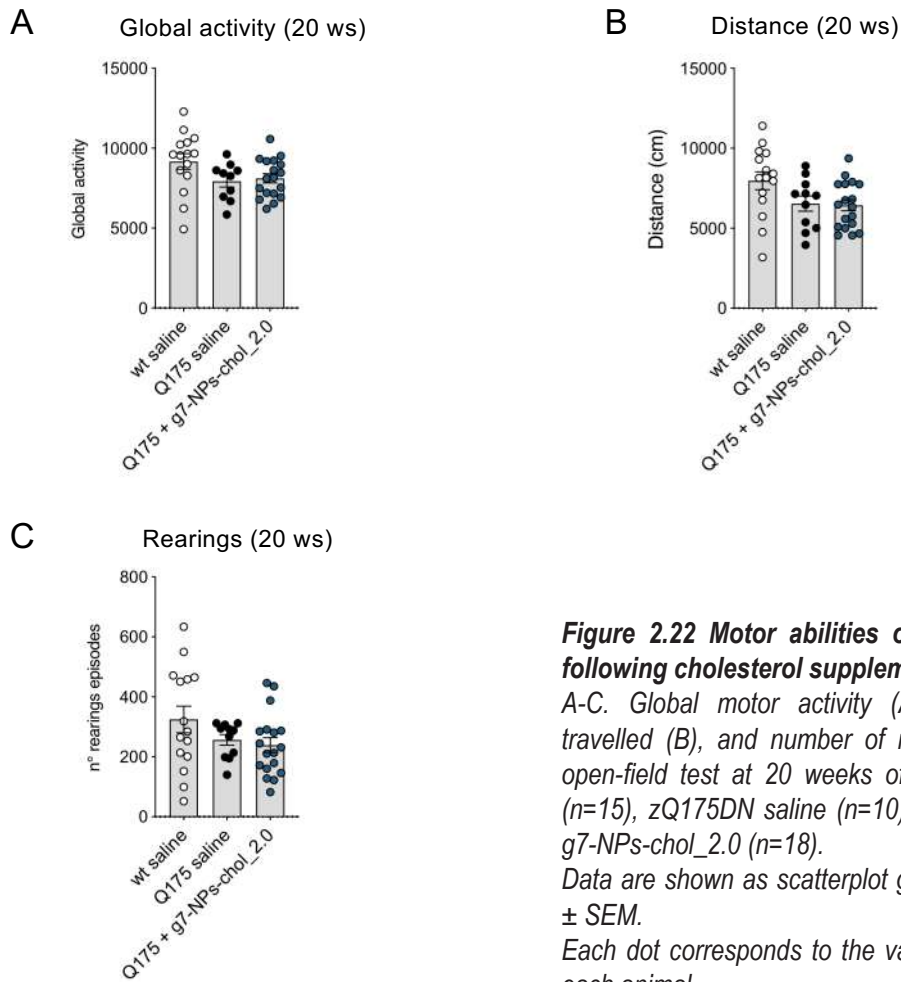


Figure 2.21 Chronic administration of g7-NPs-*chol_2.0* to zQ175DN mice

Experimental paradigm used in the study. zQ175DN mice were treated with g7-NPs-*chol_2.0* from 5 weeks of age to 9 weeks of age with 2 I.P. injection/week. Wt and zQ175DN littermates were treated with saline solution as controls. Behavioral tests were performed at 20 weeks of age.

At this time point, zQ175DN mice did not show any defect in motor abilities compared to wild-type littermates, as measured by the global activity, total distance travelled, and number of rearings analyzed by the activity cage test (Fig. 2.22A, B, C). Furthermore,

zQ175DN mice did not manifest any anxiety-like behavior since there were no differences in the time spent exploring the periphery or center area of the arena during the activity cage test between wild-type and HD mice (Fig. 2.23A, B).



When we measured the muscular strength of zQ175DN mice using the grip strength test, we observed that at 20 weeks of age knock-in mice exhibited less muscular strength compared to controls and cholesterol supplementation completely restored this defect (Fig. 2.24).

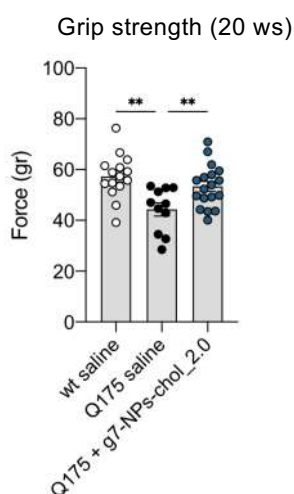


Figure 2.24 Muscular strength of zQ175DN mice following cholesterol supplementation

Grip strength (grams) at 20 weeks of age in wt saline ($n=15$), zQ175DN saline ($n=11$), and zQ175DN + g7-NPs-chol_{2.0} ($n=18$).

Data are shown as scatterplot graphs with means \pm SEM. Each dot corresponds to the value obtained from each animal.

Statistics: one-way ANOVA with Newman–Keuls post-hoc test (** $p<0.01$).

Regarding the clasping behavior, zQ175DN mice manifest low clasping activity at 20 weeks of age which was not rescued in cholesterol-treated mice (Fig. 2.25).

Finally, at this time point, zQ175DN mice exhibited a pronounced cognitive deficit, as assessed by NORT. The amount of cholesterol released from g7-NPs-chol_{2.0} at this time point was

sufficient to totally rescue cognitive defect in zQ175DN mice (Fig. 2.26).

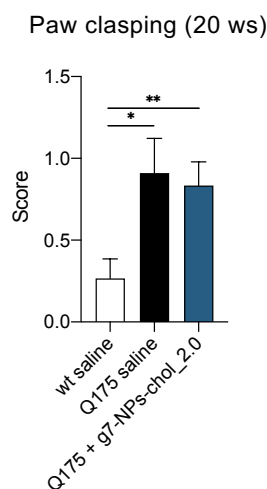


Figure 2.25 Paw clasping behavior of zQ175DN mice following cholesterol supplementation

Paw clasping at 20 weeks of age in wt saline ($n=15$), zQ175DN saline ($n=11$), and zQ175DN + g7-NPs-chol_{2.0} ($n=18$).

Data are shown as histogram with means \pm SEM. Statistics: one-way ANOVA with Newman–Keuls post-hoc test (* $p<0.05$; ** $p<0.01$).

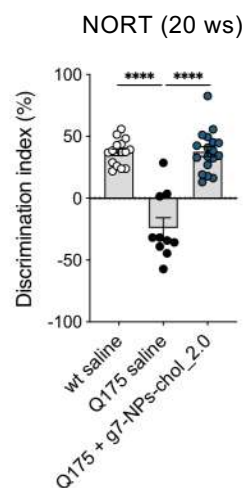


Figure 2.26 Cognitive abilities of zQ175DN mice following cholesterol supplementation

Discrimination index (DI %) in the novel object recognition test of wt saline ($n=15$), zQ175DN saline ($n=10$), and zQ175DN + g7-NPs-chol_{2.0} ($n=18$) at 20 weeks of age. Data are shown as scatterplot graphs with means \pm SEM. Each dot corresponds to the value obtained from each animal.

Statistics: one-way ANOVA with Newman–Keuls post-hoc test (**** $p<0.0001$).

Since cholesterol is gradually released from g7-NPs-*chol_2.0*, we tested these animals again at 29 weeks of age (Fig. 2.27).

In parallel, we performed a second cycle of treatment from 21 to 25 weeks

of age (symptomatic stage) in which zQ175DN mice were treated with g7-NPs-*chol_2.0* with 2 I.P. injections/week (n=9). Behavioral tests were performed at 29 weeks of age (Fig. 2.27).

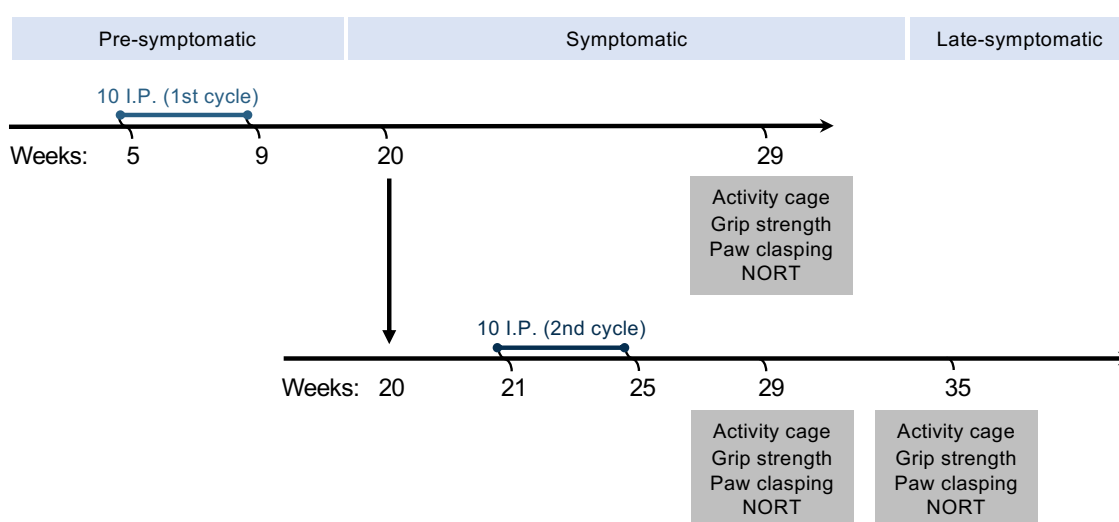


Figure 2.27 Chronic administration of g7-NPs-*chol_2.0* to zQ175DN mice

*Experimental paradigm used in the study. zQ175DN mice were treated with g7-NPs-*chol_2.0* from 5 weeks of age to 9 weeks of age with 2 I.P. injection/week. Wt and zQ175DN littermates were treated with saline solution as controls. Some mice received a second cycle of treatment from 21 to 29 weeks of age with 2 I.P. injection/week. Behavioral tests were performed at 29 weeks of age. To see how does the effect last, behavioral tests were performed again at 35 weeks of age.*

We found that also at 29 weeks of age, zQ175DN mice did not show any defect in motor abilities or anxiety-like behavior compared to wild-type littermates, as assessed by activity cage test (Fig. 2.28A, B, C, D, E). Interestingly, both group of mice treated with 1 cycle or 2 cycles of g7-NPs-*chol_2.0* exhibited higher muscular strength compared to zQ175DN mice treated with saline, indicating an

amelioration of this phenotype (Fig. 2.29).

The same result was obtained with the paw clasping test: accordingly, all the zQ175DN mice treated with cholesterol had a clasping behavior similar to wild-type mice (Fig. 2.30).

Finally, NORT revealed that cholesterol treatment was able to totally rescue the cognitive defect of zQ175DN mice also at this time point (Fig. 2.31).

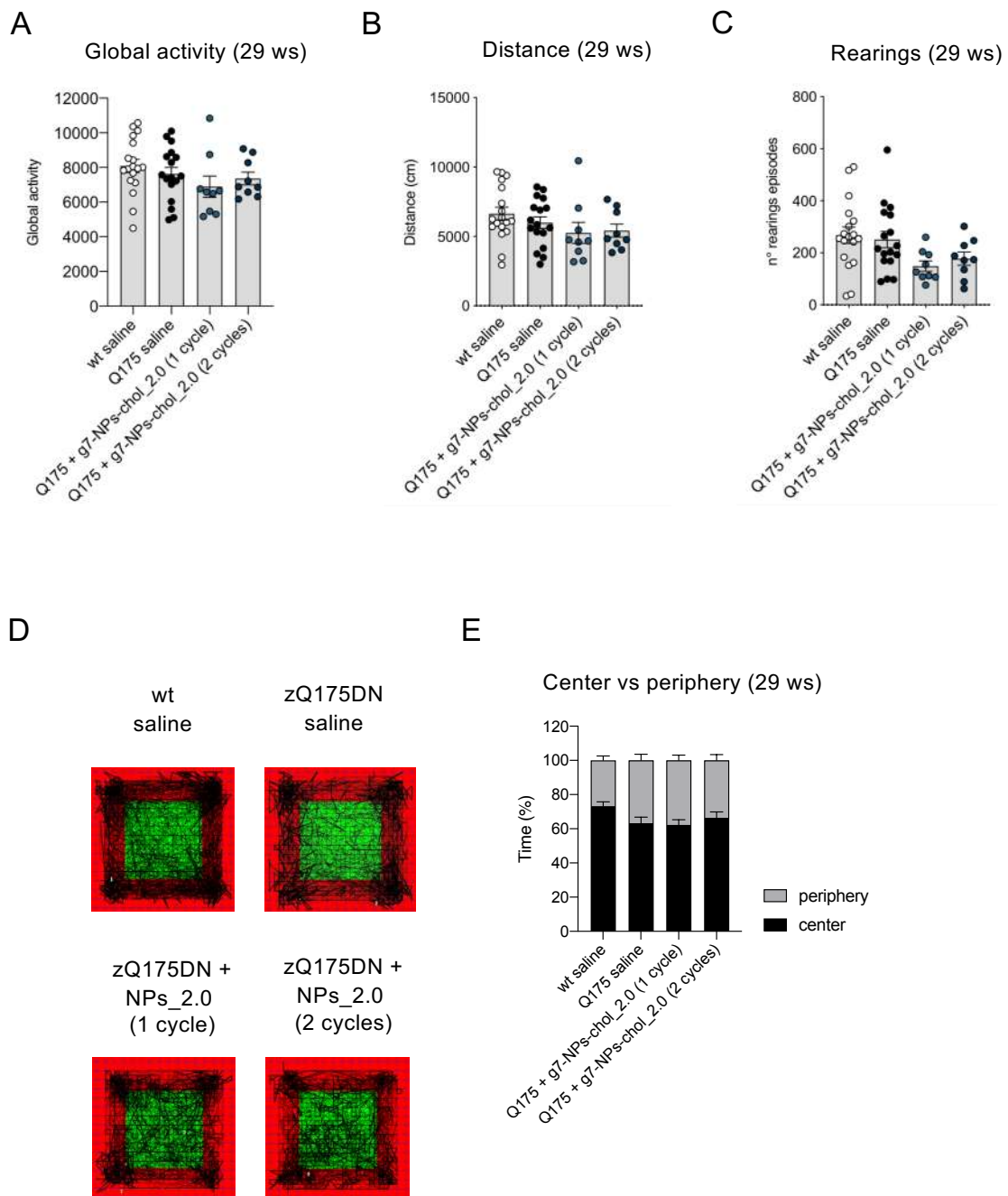


Figure 2.28 Motor abilities of zQ175DN mice following cholesterol supplementation

A-C. Global motor activity (A), total distance travelled (B), and number of rearings (C) in an open-field test at 29 weeks of age in wt saline ($n=18$), zQ175DN saline ($n=17$), zQ175DN + g7-NPs-chole_2.0 (1 cycle) ($n=9$), and zQ175DN + g7-NPs-chole_2.0 (2 cycles) ($n=9$).

D-E. Representative track plots (D) generated from the open-field test from wt saline ($n=18$), zQ175DN saline ($n=17$), zQ175DN + g7-NPs-chole_2.0 (1 cycle) ($n=9$), and zQ175DN + g7-NPs-chole_2.0 (2 cycles) ($n=9$) and relative quantification (E) of the time spent in the center and in the periphery (%) of the arena at 20 weeks of age.

Data are shown as scatterplot graphs (A-C) or histograms (E) with means \pm SEM. Each dot corresponds to the value obtained from each animal.

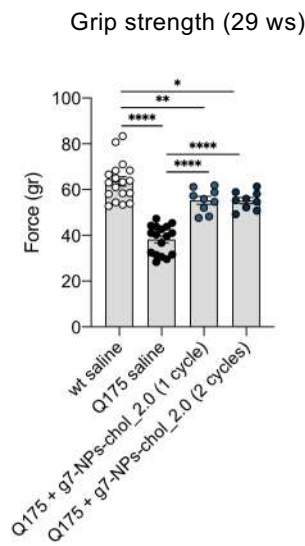


Figure 2.29 Muscular strength of zQ175DN mice following cholesterol supplementation

Grip strength (grams) at 29 weeks of age in wt saline ($n=18$), zQ175DN saline ($n=17$), zQ175DN + g7-NPs-cholesterol_2.0 (1 cycle) ($n=9$), and zQ175DN + g7-NPs-cholesterol_2.0 (2 cycles) ($n=9$).

Data are shown as scatterplot graphs with means \pm SEM. Each dot corresponds to the value obtained from each animal.

Statistics: one-way ANOVA with Newman–Keuls post-hoc test ($*p<0.05$; $**p<0.01$; $***p<0.0001$).

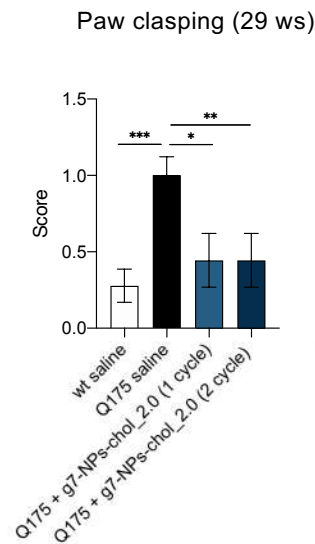


Figure 2.30 Claspings behavior of zQ175DN mice following cholesterol supplementation

Paw claspings at 29 weeks of age in wt saline ($n=18$), zQ175DN saline ($n=17$), zQ175DN + g7-NPs-cholesterol_2.0 (1 cycle) ($n=9$), and zQ175DN + g7-NPs-cholesterol_2.0 (2 cycles) ($n=9$).

Data are shown as histogram with means \pm SEM.

Statistics: one-way ANOVA with Newman–Keuls post-hoc test ($*p<0.05$; $**p<0.01$; $***p<0.001$).

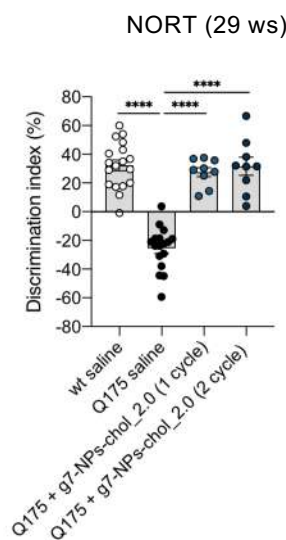


Figure 2.31 Cognitive abilities of zQ175DN mice following cholesterol supplementation

Discrimination index (DI %) in the novel object recognition test of wt saline ($n=18$), zQ175DN saline ($n=17$), zQ175DN + g7-NPs-cholesterol_2.0 (1 cycle) ($n=9$), and zQ175DN + g7-NPs-cholesterol_2.0 (2 cycles) ($n=9$) at 29 weeks of age. DI above zero indicates a preference for the novel object; DI below zero indicates a preference for the familiar object.

Data are shown as scatterplot graphs with means \pm SEM. Each dot corresponds to the value obtained from each animal.

Statistics: one-way ANOVA with Newman–Keuls post-hoc test ($****p<0.0001$).

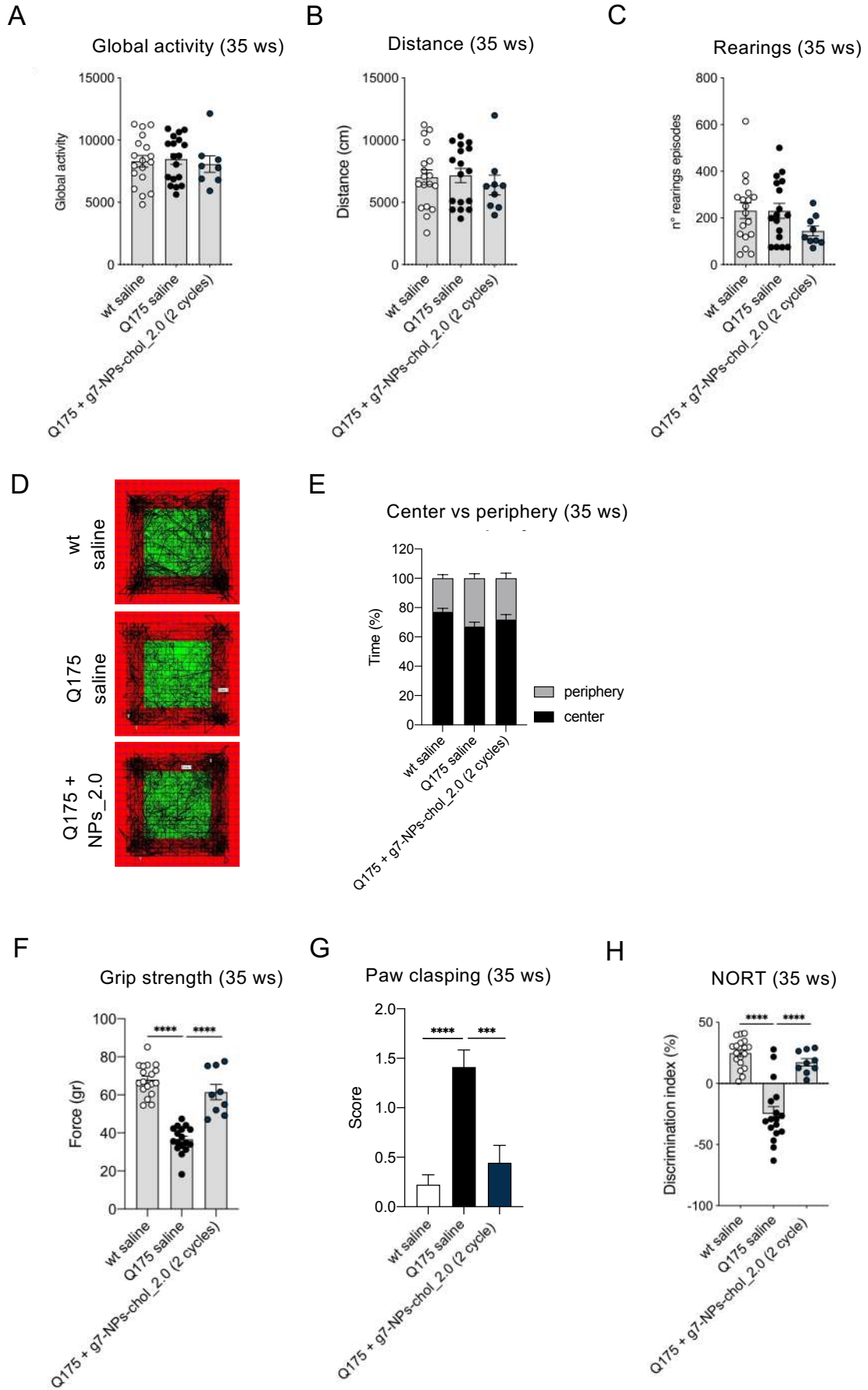


Figure 2.32 Motor and cognitive abilities of zQ175DN mice following cholesterol supplementation

A-E. Global motor activity (A), total distance travelled (B), and number of rearings (C) in an open-field test at 29 weeks of age in wt saline (n=18), zQ175DN saline (n=17), zQ175DN + g7-NPs-*chol_2.0* (1 cycle) (n=9), and zQ175DN + g7-NPs-*chol_2.0* (2 cycles) (n=9). Representative track plots (D) generated from the open-field test from wt saline (n=18), zQ175DN saline (n=17), zQ175DN + g7-NPs-*chol_2.0* (1 cycle) (n=9), and zQ175DN + g7-NPs-*chol_2.0* (2 cycles) (n=9) and relative quantification (E) of the time spent in the center and in the periphery (%) of the arena at 20 weeks of age.

F. Grip strength (grams) at 29 weeks of age in wt saline (n=18), zQ175DN saline (n=17), zQ175DN + g7-NPs-*chol_2.0* (1 cycle) (n=9), and zQ175DN + g7-NPs-*chol_2.0* (2 cycles) (n=9).

G. Paw clasping at 29 weeks of age in wt saline (n=18), zQ175DN saline (n=17), zQ175DN + g7-NPs-*chol_2.0* (1 cycle) (n=9), and zQ175DN + g7-NPs-*chol_2.0* (2 cycles) (n=9).

H. Discrimination index (DI %) in the novel object recognition test of wt saline (n=18), zQ175DN saline (n=17), zQ175DN + g7-NPs-*chol_2.0* (1 cycle) (n=9), and zQ175DN + g7-NPs-*chol_2.0* (2 cycles) (n=9) at 29 weeks of age. DI above zero indicates a preference for the novel object; DI below zero indicates a preference for the familiar object.

Data are shown as scatterplot graphs with means \pm SEM. Each dot corresponds to the value obtained from each animal.

Statistics: one-way ANOVA with Newman-Keuls post-hoc test (* $p < 0.05$; ** $p < 0.01$; **** $p < 0.0001$; *** $p < 0.001$).

To analyze the long-term effect of cholesterol delivery, we performed behavioral tests also at 35 weeks of age. Even if no motor deficits in zQ175DN mice compared to wild-type littermates were measured (Fig. 2.32A-E), the rescue on muscular strength (Fig. 2.32F), clasping behavior (Fig. 2.32G), and cognitive decline (Fig. 2.32H) by g7-NPs-*chol_2.0* delivery were maintained also at this time point. Taken together, these results highlighted that, at 20 weeks of age, the amount of cholesterol released from g7-NPs-*chol_2.0* is sufficient to rescue muscular strength and to reverse cognitive decline in zQ175DN mice. At 29 weeks of age, these rescues persist, and the increased amount of released cholesterol reversed also clasping behavior of HD mice. Finally, when we performed a second cycle of treatment with g7-NPs-*chol_2.0*, we observed

that cholesterol administration rescued HD-related behavioral deficits in a long-term manner.

2.6 Setting up of an *in vivo* paradigm for SREBP2 delivery to brain astrocytes

Since the molecular mechanism underlying cholesterol dysfunction in HD is a reduced activity of SREBP2 likely in glial cells (132, 149, 150) and it has been demonstrated that delivery of exogenous cholesterol to the brain is beneficial for HD mice (214, 220), we aimed at forcing the expression of SREBP2 *in vivo* to stimulate the biosynthesis of endogenous cholesterol in striatal astrocytes of a transgenic mouse model of HD (R6/2 mice). To this end, we produced two viral vectors carrying the active N-terminal portion of human SREBP2 and able to express the transgene

specifically in astrocytes, which are the major producers of cholesterol in the adult brain. The first viral vector was derived from a Herpes Simplex virus (HSV, in collaboration with M. Simonato and G. Verlengia, University of Ferrara and San Raffaele Institute) (232, 233), which is attractive because it contains many non-essential genes that can be replaced (up to 30 kb) with multiple therapeutic transgenes. The second viral vector is a recombinant serotype of an adeno-associated virus (AAV2/5, in collaboration with M. Giacca and L. Zentilin, ICGEB, Trieste), which is known to be highly specific for glial cells (124). In the first experiment we tested HSV (JDNI8-gfaABC1D-

TdTomato, 5×10^9 pfu/mL) and AAV2/5 (AAV2/5-gfaABC1D-TdTomato, $1,7 \times 10^{14}$ U/mL) expressing the reporter gene TdTomato under the control of a glial promoter (gfaABC1D) to strengthen the infection of astrocytes.

Accordingly, we infected 7-week-old wild-type mice ($n=3-7$ /virus) into the striatum ($2 \mu\text{L}$, $12 \mu\text{L}/\text{h}$, stereotaxic coordinates 2 mm mediolateral, 0.74 mm anteroposterior, 3.5 mm dorsoventral; from Paxinos G and Watson C. The Rat Brain in Stereotaxic Coordinates. Academic Press, San Diego) (Fig. 2.33).

Mice were sacrificed 4 weeks after the infection to study viral spread and tropism.

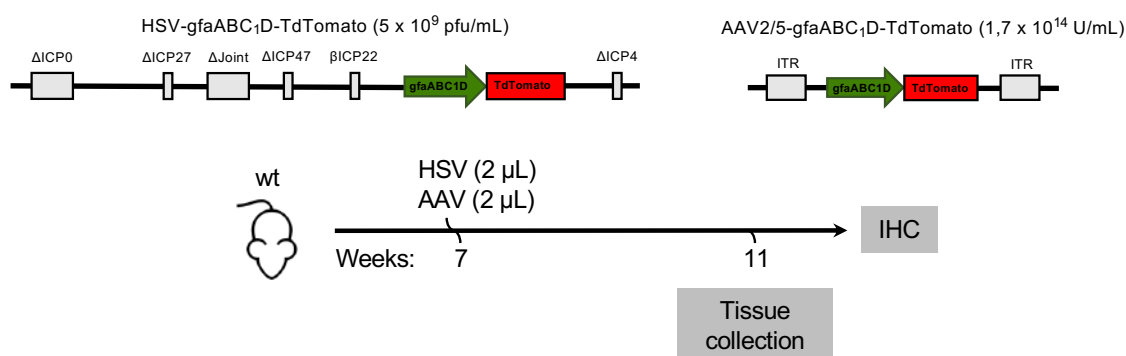


Figure 2.33 *In vivo* characterization of HSV-gfaABC1D-tdTomato and AAV2/5-gfaABC1D-tdTomato

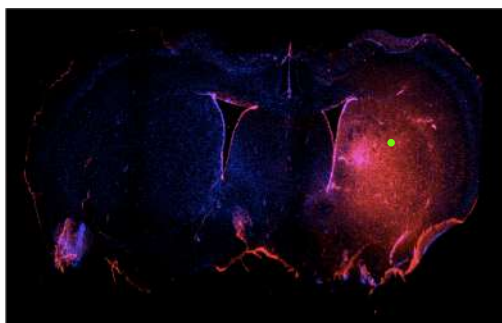
Scheme of the viruses and experimental paradigm used in the study. 7-weeks old wt mice were unilaterally infected in the right striatum with HSV or AAV expressing tdTomato under the control of gfaABC1D promoter. Mice were sacrificed 4 weeks later and brains were collected to study viral spread and tropism.

When we analyzed the presence of the viruses in brain coronal sections, we found that both of them consistently diffuse in the striatum and in some parts of the cortex in the infused hemisphere in several subsequent slices, indicating a good spread from the injection site (Fig. 2.34A, B). Accordingly, the signal of TdTomato was detectable in a range of 2,5 mm and it covered $61,51\% \pm 4,85$ of the infused hemisphere. We then analyzed the co-localization between the signal of TdTomato and the signal of both

neuronal (DARPP32, NeuN) and glial (GFAP, S100B, IBA1) markers to study the tropism of both viruses.

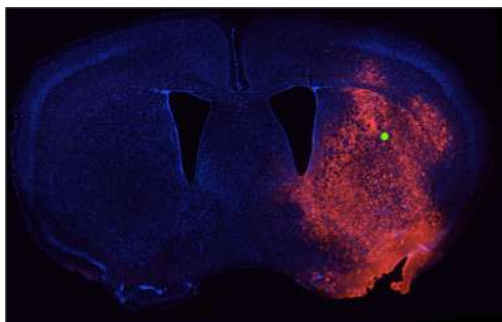
Unfortunately, HSV infects only neuronal cells (Fig. 2.35A) while AAV2/5 has a specific tropism for glial cells (Fig. 2.35B). For this reason, we decided to use AAV2/5 to over-express hSREBP2 in astrocytes. Overall, AAV2/5 was proven to be a good tool to target glial cells in a very wide brain area, thus AAV2/5-gfaABC1D-hSREBP2-tdTomato ($1,7 \times 10^{13}$ U/mL) was produced.

A



TdTomato Ho

B



TdTomato Ho

Figure 2.34 Spread of HSV-gfaABC1D-tdTomato and AAV2/5-gfaABC1D-tdTomato

A-B. Representative large images of coronal brain slices of wt mice infected with HSV-gfaABC1D-tdTomato or AAV2/5-gfaABC1D-tdTomato with immunostaining against tdTomato (red) to visualize HSV (A) and AAV (B) spread. Hoechst were used to counterstain nuclei (Ho, blue).

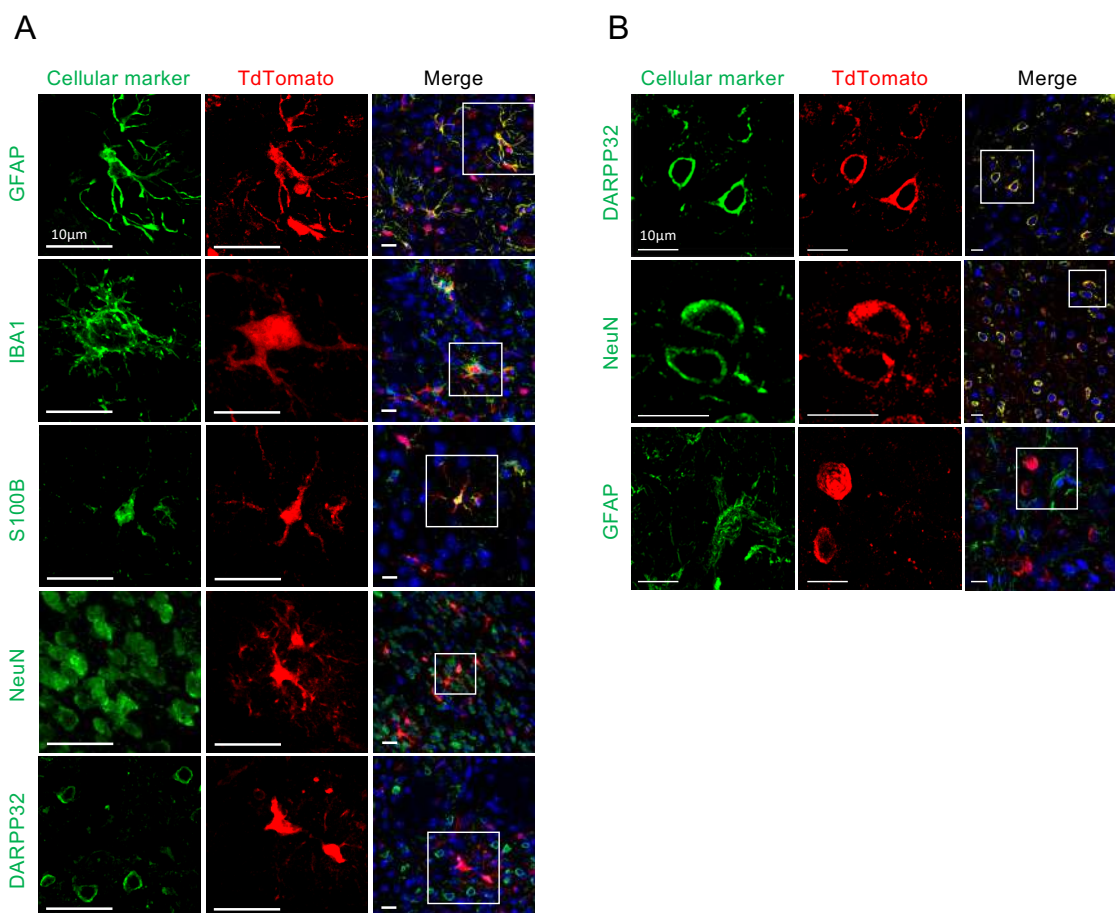


Figure 2.35 Tropism of HSV-gfaABC1D-tdTomato and AAV2/5-gfaABC1D-tdTomato

A-B Representative confocal images of coronal brain slices of wt mice infected with HSV-gfaABC1D-tdTomato (A) or AAV2/5-gfaABC1D-TdTomato (B) with immunostaining against tdTomato (red) and GFAP, IBA1, S100B, NeuN, and DARPP32 (green) to visualize viral tropism. Hoechst were used to counterstain nuclei (Ho, blue).

2.6.1 In vivo characterization of AAV2/5-gfaABC1D-TdTomato and AAV2/5-gfaABC1D-hSREBP2-TdTomato

To verify the expression and the activity of hSREBP2, RT-qPCR and Western Blot were performed on the infused striatum and ipsi-lateral cortex of:

- n = 3 untreated wild-type mice
- n = 3 untreated R6/2 mice

- n = 3-4 R6/2 mice infected with AAV2/5-gfaABC1D-TdTomato (R6/2-Tom)

- n = 3-4 R6/2 mice infected with AAV2/5-gfaABC1D-hSREBP2-TdTomato (R6/2-hBP2)

The viral vectors (2 µL) were injected in the right striatum of mice at 7 weeks-of-age and the animals were sacrificed 4 weeks after (Fig. 2.36).

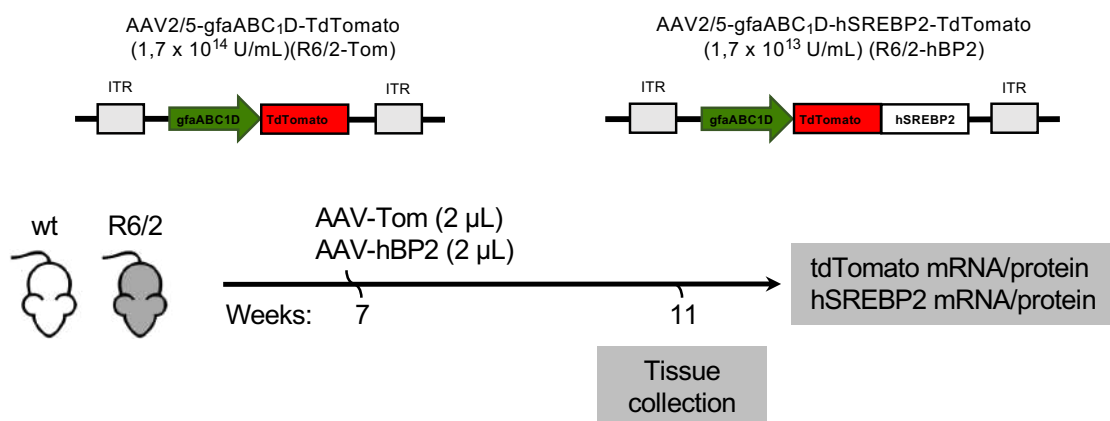


Figure 2.36 *In vivo* characterization of AAV2/5-gfaABC1D-tdTomato and AAV2/5-gfaABC1D-hSREBP2-tdTomato.

Scheme of the viruses and experimental paradigm used in the study. 7-weeks old wt and R6/2 mice were unilaterally infected in the right striatum with AAV2/5-gfaABC1D-tdTomato or AAV2/5-gfaABC1D-hSREBP2-tdTomato. Mice were sacrificed 4 weeks later and brains were collected to measure tdTomato and hSREBP2 mRNA and protein.

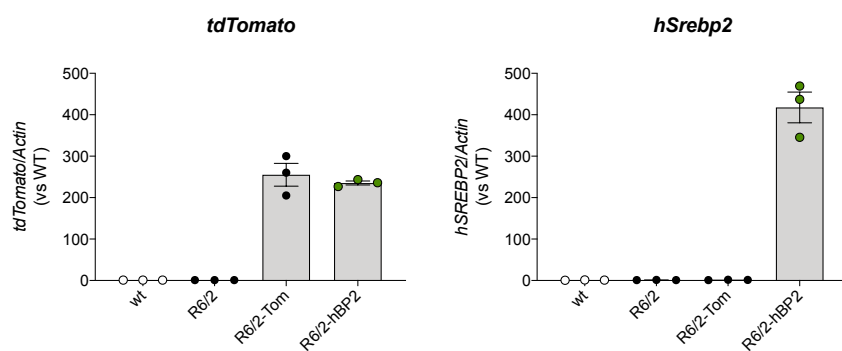
As shown in Fig. 2.37A, mRNA of *TdTomato* was not present in wild-type and R6/2 brain, while it was detected and quantified in R6/2-Tom and R6/2-hBP2 samples. As expected, *hSrebp2* was detected only in R6/2-hBP2 mice (Fig. 2.37A). At protein level, TdTomato was measured in R6/2-Tom mice but not in R6/2-hBP2 mice, suggesting that TdTomato fused downstream to hSREBP2 was not efficiently translated in AAV2/5-gfaABC1D-hSREBP2-TdTomato (Fig. 2.37B). Although specific antibodies for the human form of SREBP2 are not available, Western Blot analysis with an antibody able to recognize both the endogenous (mouse) and exogenous (human) SREBP2 revealed an increase in total SREBP2 protein level in three out of four R6/2-hBP2 mice (Fig. 2.37B). Moreover, we checked

the over-expression of hSREBP2 in the infused striatum of R6/2-hBP2 mice by immunofluorescence analysis, as shown in Fig. 2.37C. Finally, we measured a significant reduction of the endogenous *mSREBP2* in R6/2, R6/2-Tom and R6/2-hBP2 mice compared to wild-type mice (Fig. 2.37D). When compared to *mSrebp2*, the level of *hSrebp2* mRNA was between 1.7-fold and 2.1-fold higher than the endogenous transcript in R6/2-hBP2 mice (Fig. 2.37E).

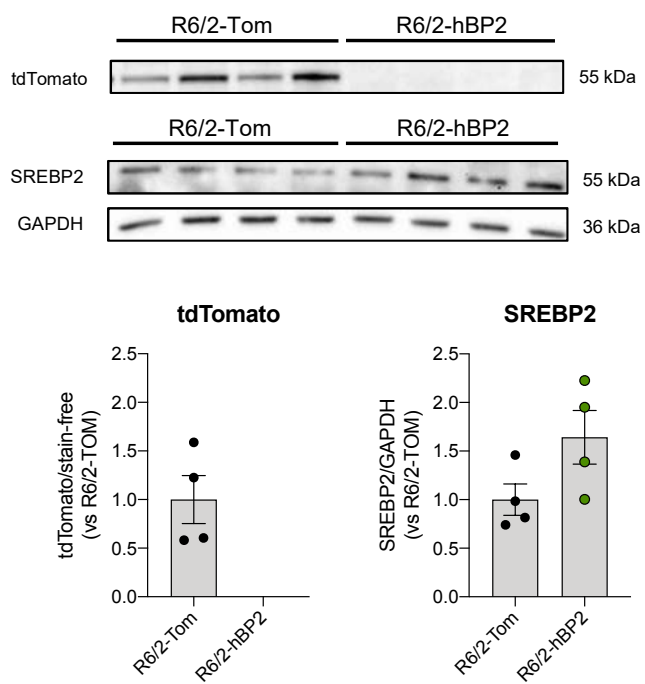
These results demonstrate that intrastriatal injection of AAV2/5-gfaABC1D-hSREBP2-TdTomato allows to express hSREBP2 at transcriptional and protein level in HD mice.

However, TdTomato in the same vector is not translated for unknown reasons and cannot be used as tag for the transgene expression.

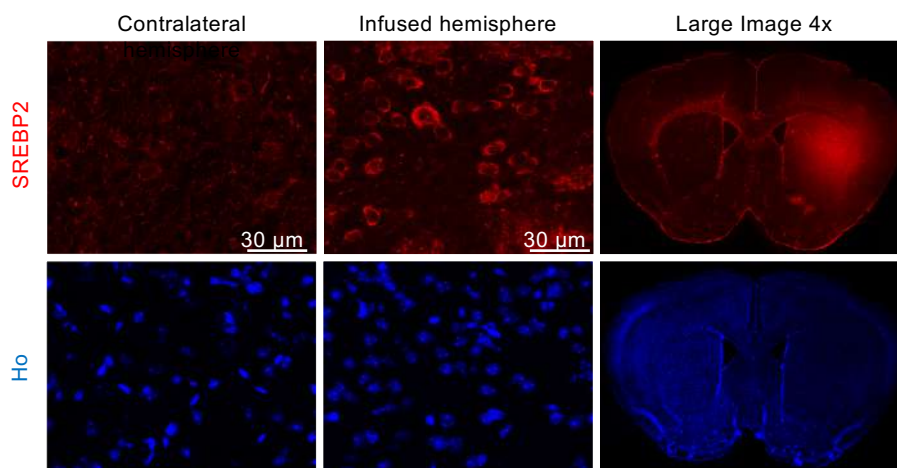
A



B



C



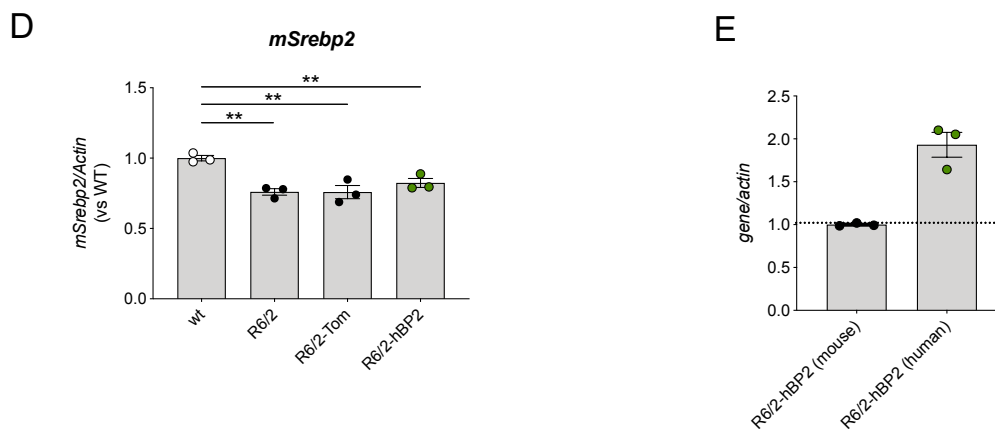


Figure 2.37 In vivo characterization of AAV2/5-gfaABC1D-tdTomato and AAV2/5-gfaABC1D-hSREBP2-tdTomato.

A. mRNA levels of *tdTomato* and *hSrebp2* (B) in the infused striatum and ipsi-lateral cortex from untreated wt mice, untreated R6/2 mice, R6/2 mice treated with AAV2/5-gfaABC1D-tdTomato (R6/2-Tom), and R6/2 mice treated with AAV2/5-gfaABC1D-hSREBP2-tdTomato (R6/2-hBP2) ($n=3$ mice/group).

B. Protein levels and relative densitometry quantification of *tdTomato* and *hSREBP2* in cytosolic fractions from the infused striatum and ipsi-lateral cortex from R6/2 mice treated with either AAV2/5-gfaABC1D-tdTomato (R6/2-Tom) or AAV2/5-gfaABC1D-hSREBP2-tdTomato (R6/2-hBP2) ($n=4$ mice/group). Stain-free imaging and GAPDH were used as a loading control and for normalization.

C. Representative large images with relative crops of coronal brain slices of R6/2-hBP2 mice with immunostaining against SREBP2 (red). Hoechst were used to counterstain nuclei (Ho, blue).

D. mRNA levels of *mSrebp2* in the infused striatum and ipsi-lateral cortex from untreated wt mice, untreated R6/2 mice, R6/2 mice treated with AAV2/5-gfaABC1D-tdTomato (R6/2-Tom), and R6/2 mice treated with AAV2/5-gfaABC1D-hSREBP2-tdTomato (R6/2-hBP2) ($n=3$ mice/group).

E. Comparison between the mRNA levels of *mSrebp2* and *hSrebp2* in the infused striatum and ipsi-lateral cortex from R6/2-hBP2 mice ($n=3$).

Data are shown as scatterplot graphs with means \pm SEM. Each dot corresponds to the value obtained from each animal.

Statistics: one-way ANOVA with Newman-Keuls post-hoc test (** $p<0.01$).

2.6.2 Gene expression analysis of SREBP2-related pathways and cholesterol metabolism

Since SREBP2 is the master regulator of genes involved in the biosynthesis of cholesterol, to establish the efficacy of hSREBP2 over-expression in glial cells to activate the expression of genes related to cholesterol biosynthesis, gene expression analysis was performed on the infused striatum and ipsi-lateral cortex of:

- $n = 3$ untreated wild-type mice
- $n = 3$ untreated R6/2 mice
- $n = 3$ R6/2 mice infected with AAV2/5-gfaABC1D-TdTomato (R6/2-Tom)
- $n = 3$ R6/2 mice infected with AAV2/5-gfaABC1D-hSREBP2-TdTomato (R6/2-hBP2)

Mice were unilaterally infected in the right striatum at 7 weeks-of-age and sacrificed 4 weeks after the infection.

The mRNA level of several genes located at different steps of the

cholesterol biosynthesis pathway was analyzed: *Hmgcr* as representative of the formation of mevalonate from acetate, *Mvk* of the conversion of mevalonate into isoprene, *Sqs/Fdft1* of the polymerization of isoprene to squalene and its cyclization to lanosterol, *Cyp51* and *Dhcr7* of the final conversion of lanosterol to cholesterol (Fig. 2.38A).

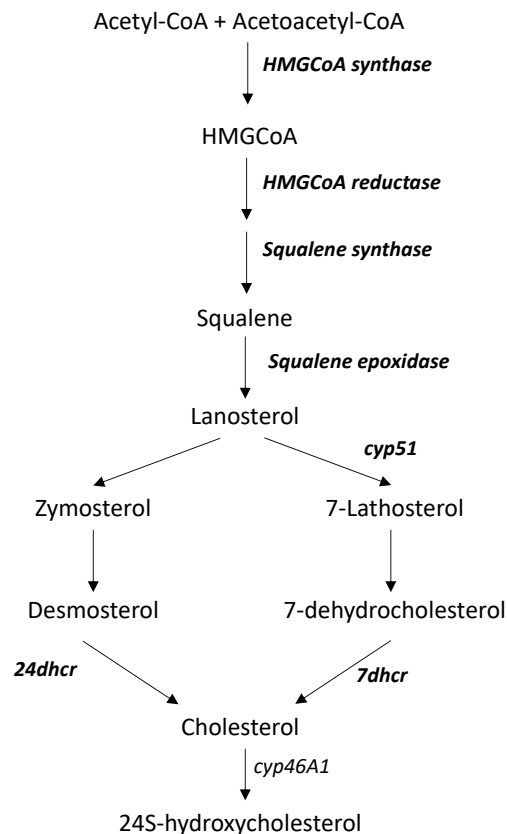
Transcript level of *Hmgcr*, *Mvk*, *Fdft1*, and *Cyp51* was significantly reduced in R6/2 and R6/2-Tom mice compared to wild-type controls. Of note, hSREBP2 over-expression normalized the level

of these genes in R6/2-hBP2 mice (Fig. 2.38B-E).

Dhcr7 mRNA level was significantly reduced in R6/2-Tom mice, but not in R6/2 mice, compared to wild-type littermates, and its transcript level was not influenced by hSREBP2 (Fig. 2.38F).

These findings indicate that the over-expression of hSREBP2 in striatal glial cells of HD mice compensates the dysfunctional activity of the endogenous mSREBP2 by reversing the reduced transcription of several cholesterol biosynthesis genes.

A



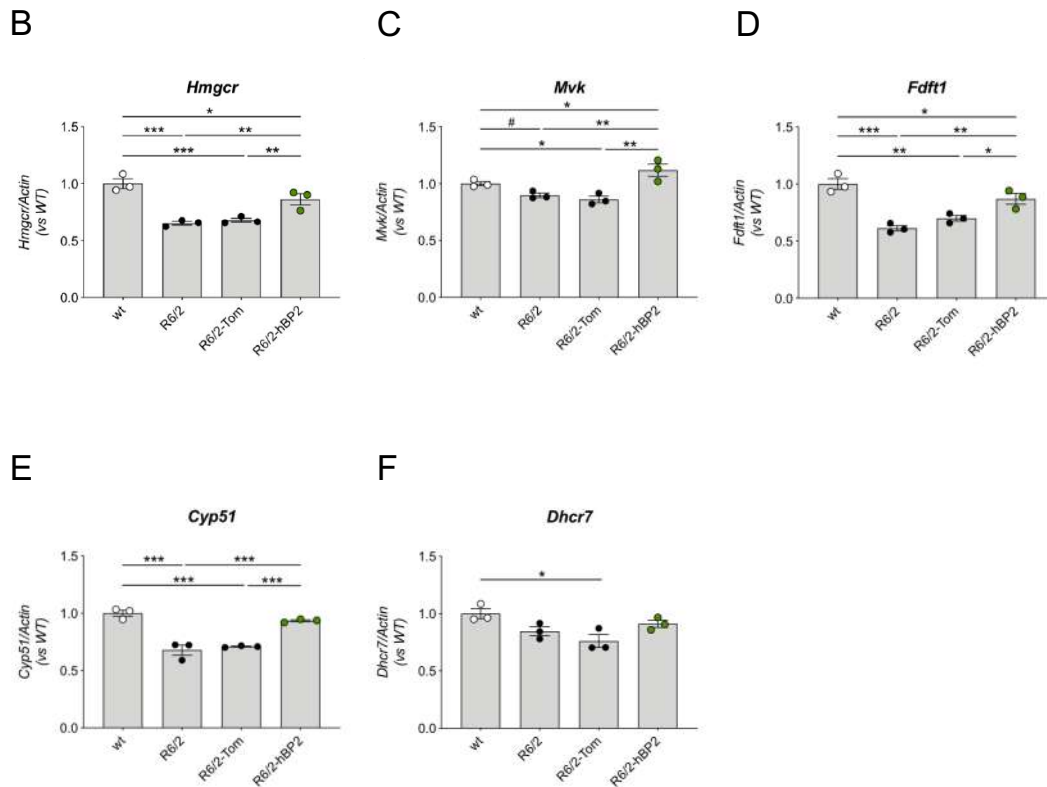


Figure 2.38 Gene expression analysis of SREBP2-related pathways and cholesterol metabolism

A. Cholesterol biosynthetic pathway: the enzymes whose expression was analyzed by qPCR are colored in red, whereas the products of the Bloch and Kandutsch-Russell pathways in blue and pink, respectively.

B-F. mRNA levels of *Hmgcr* (B), *Mvk* (C), *Fdft1* (D), *Cyp51* (E), and *Dhcr7* (F) in the infused striatum and ipsi-lateral cortex from untreated wt mice, untreated R6/2 mice, R6/2 mice treated with AAV2/5-gfaABC1D-tdTomato (R6/2-Tom), and R6/2 mice treated with AAV2/5-gfaABC1D-hSREBP2-tdTomato (R6/2-hBP2) ($n=3$ mice/group).

Data are shown as scatterplot graphs with means \pm SEM. Each dot corresponds to the value obtained from each animal.

Statistics: one-way ANOVA with Newman-Keuls post-hoc test ($*p<0.05$; $**p<0.01$; $***p<0.001$) or unpaired Student *t*-test ($\#p<0.05$).

To assess whether the enhancement of endogenous cholesterol biosynthesis in astrocytes by viral delivery of hSREBP2 was accompanied by a change in cholesterol efflux, transport, uptake and removal, the expression level of *Abca1*, *ApoE*, *Lrp1*, and *Cyp46a1* was evaluated by RT-qPCR. The mRNA level of *Abca1* was increased in both R6/2 and R6/2-

Tom mice compared to controls but striatal injection of AAV2/5-gfaABC1D-hSREBP2-TdTomato doesn't affect it (Fig. 2.39A). *ApoE* and *Lrp1* mRNA level was similar in the striatum and cortex of wild-type and R6/2 mice and was not changed in R6/2-Tom and R6/2-hBP2 mice (Fig. 2.39B, C). Finally, all the R6/2 mice showed reduced *Cyp46a1* mRNA compared

to controls indicating decreased cholesterol catabolism in HD mice, which was not reversed by hSREBP2 over-expression (Fig. 2.39D).

Overall, these data demonstrated that hSREBP2 delivered with AAV2/5 is functional. Accordingly, hSREBP2 is able to restore the level of genes related to cholesterol synthesis that are under the control of this transcription factor. On the other hand, these data indicated that viral delivery of hSREBP2 does not influence the transcription of the cholesterol efflux gene *Abca1* and

of the neuron-specific cholesterol removal gene *Cyp46a1*, which are known to be deregulated in HD mice. These may be due to incomplete vector coverage and extensive pathology at the time of intervention, also considering that AAV vectors exhibit a lag-phase before transgene expression following infection (234). Finally, exogenous hSREBP2 does not affect mRNA level of the efflux gene *ApoE* and the neuron-specific cholesterol uptake gene *Lrp1*, which per se are not impaired in R6/2 mice.

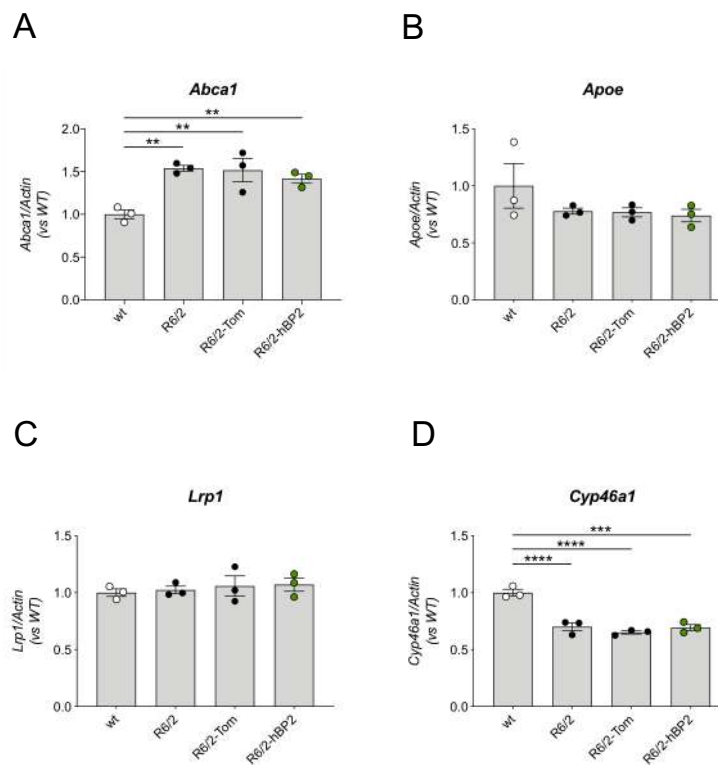


Figure 2.39 Gene expression analysis of cholesterol metabolism

A-D. mRNA levels of *Abca1* (A), *ApoE* (B), *Lrp1* (C), and *Cyp46a1* (D) in the infused striatum and ipsi-lateral cortex from untreated wt mice, untreated R6/2 mice, R6/2 mice treated with AAV2/5-gfaABC1D-tdTomato (R6/2-Tom), and R6/2 mice treated with AAV2/5-gfaABC1D-hSREBP2-tdTomato (R6/2-hBP2) ($n=3$ mice/group).

Data are shown as scatterplot graphs with means \pm SEM. Each dot corresponds to the value obtained from each animal.

Statistics: one-way ANOVA with Newman-Keuls post-hoc test (** $p<0.01$; *** $p<0.001$; **** $p<0.0001$).

2.7 Glial hSREBP2 normalizes the level of some presynaptic proteins in synaptosomes from cortico-striatal tissues of R6/2 mice

Since cholesterol secreted from glial cells was proven to be fundamental for synapse formation and maintenance (14), the level of several synaptic proteins was evaluated in two sets of synaptosomes purified from the infused striatum and ipsi-lateral cortex of:

- n = 3 untreated wild-type mice
- n = 3 untreated R6/2 mice
- n = 4 wild-type mice infected with AAV2/5-gfaABC1D-TdTomato (wt-Tom)
- n = 4 R6/2 mice infected with AAV2/5-gfaABC1D-TdTomato (R6/2-Tom)
- n = 4 R6/2 mice infected with AAV2/5-gfaABC1D-hSREBP2-TdTomato (R6/2-hBP2)

Mice were unilaterally infected in the right striatum at 7 weeks-of-age and sacrificed 4 weeks after the infection.

Our attention was focused on the analysis of:

- vesicle fusion molecules characteristic of the presynapses such as synaptophysin (SYP), synaptosome associated protein 25 (SNAP25) and vesicle associated membrane protein 1 (VAMP1)
- scaffolding proteins such as PSD95 and Shank3
- neurotransmitter receptors such as NMDA receptors.

The aim of these analyses was to identify a set of synaptic proteins whose expression was altered in HD to study whether hSREBP2 over-expression modulates synaptic protein machinery.

SYP level was increased in R6/2 mice compared to wild-type littermates. Accordingly, R6/2-Tom mice exhibited higher expression level than wt-Tom mice and hSREBP2 over-expression completely reversed this alteration (Fig. 2.40A).

Western Blot analysis for SNAP25 revealed similar level between wild-type and R6/2 mice, although a decrease was observed in two out of three R6/2 mice compared to wild-type mice and between wt-Tom and R6/2-Tom mice. hSREBP2 delivery increased SNAP25 level compared to wt-Tom and R6/2-Tom tissues (Fig. 2.40B).

VAMP1 protein level was similar in all tested mice and it was not influenced by hSREBP2 (Fig. 2.40C).

These findings highlighted that the presynaptic protein machinery is altered in cortico-striatal tissues of HD mice and the over-expression of hSREBP2, leading to subsequent enhancement of endogenous cholesterol biosynthesis in astrocytes, can partially reverse this alteration.

Regarding the postsynaptic site, PSD95 expression level was reduced in R6/2 mice with respect to wild-type mice.

However, no significant differences were found between wt-Tom mice and R6/2-Tom mice, although its level was reduced in three of four R6/2 mice. Of note, hSREBP2 over-expression in astrocytes significantly increased level of this protein in R6/2-hBP2 mice compared to R6/2-Tom mice (Fig. 2.40D). Conversely, SHANK3b did not show changes in all the tested mice and hSREBP2 over-expression didn't affect its level (Fig. 2.40E).

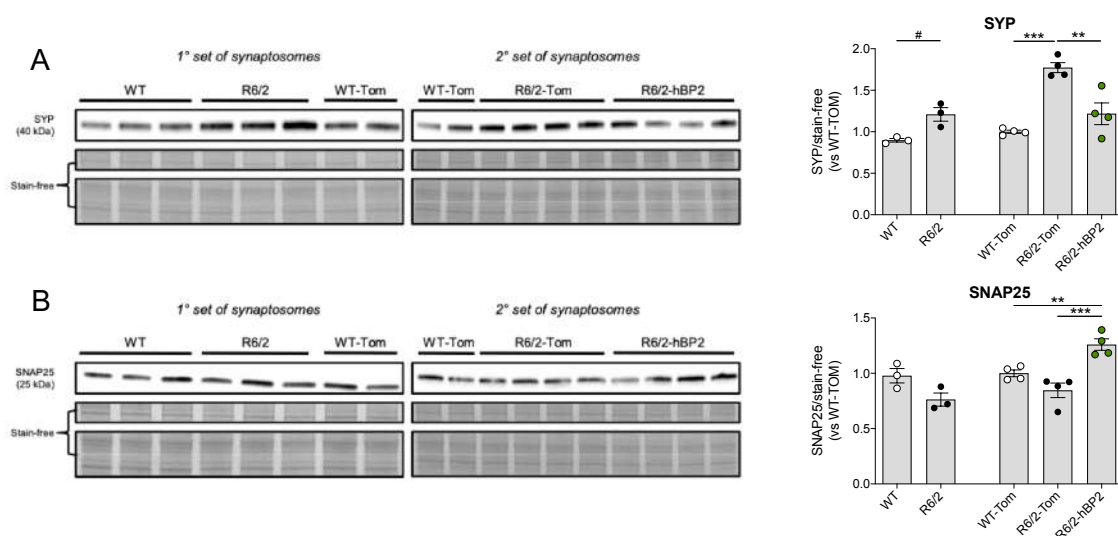
Finally, the protein level of NMDAR1 was reduced in R6/2 mice compared to wild-type mice. The same reduction was observed in R6/2-Tom mice with respect to wt-Tom mice. In R6/2 mice, the protein level was normalized to the level of wt-Tom mice by hSREBP2 over-expression (Fig. 2.40F).

The normalization of the level of SYP and NMDAR1 could be due to higher protein expression, stability or different

localization in synaptic compartments contributing to normalize synaptic defects in HD mice.

The latter hypothesis is supported by the observation that intra-striatal infusion of cholesterol via osmotic minipumps in R6/2 mice rescued synaptic communication of striatal neurons and increased the number of synaptic vesicles of glutamatergic synapses that are ready to be released (220). Indeed, glia-derived cholesterol is required for formation, maturation, and maintenance of synapses (14, 235).

Thus, restoring the endogenous cholesterol biosynthetic pathway by over-expressing hSREBP2 in astrocytes may provide to synapses the correct amount of cholesterol, leading to ameliorated synaptic function and making synapses less vulnerable to HD-related stresses.



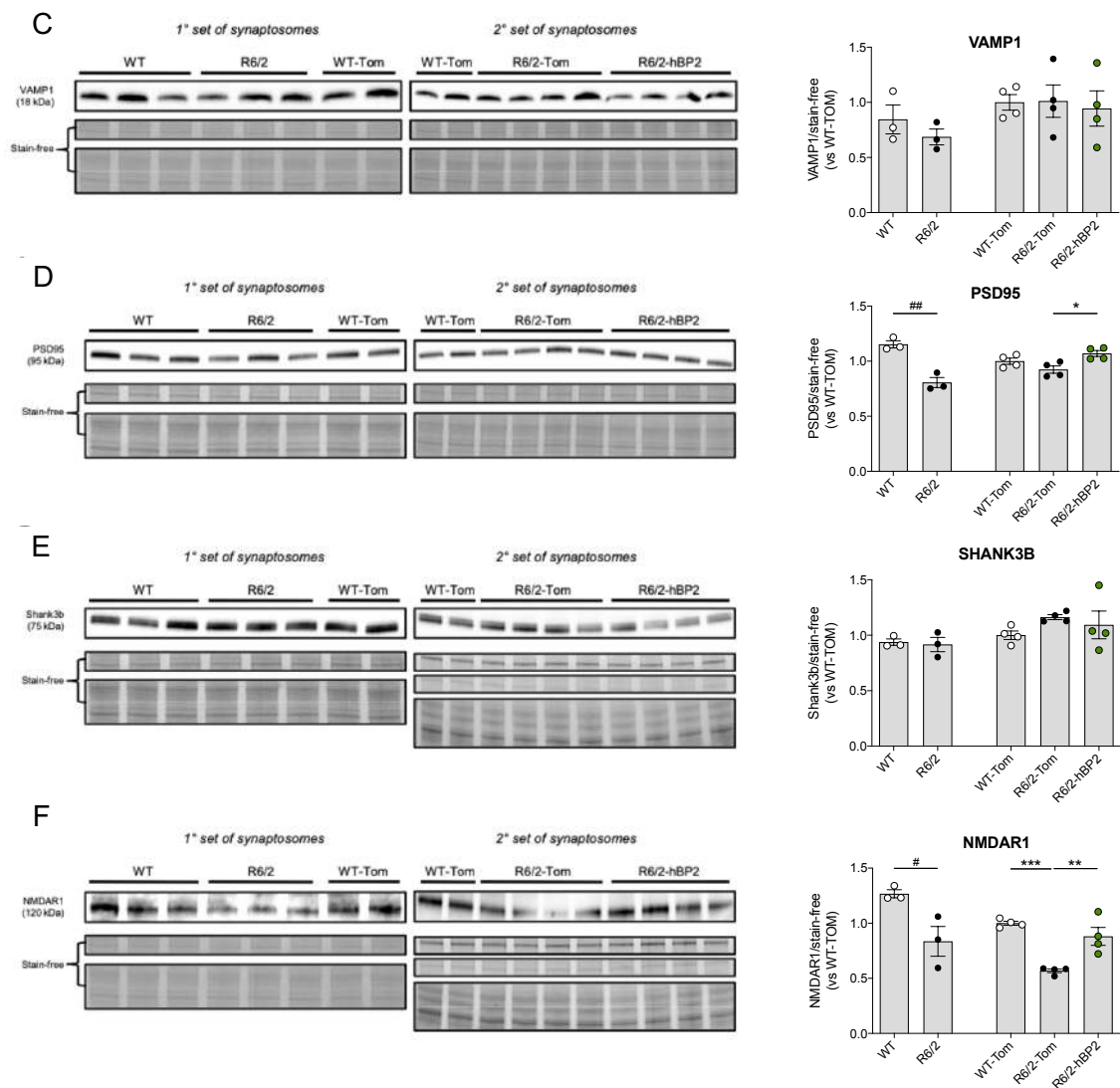


Figure 2.40 Western blot analysis of synaptic machinery

A-F. Protein levels and relative densitometry quantification of the synaptic vesicular membrane protein SYB (A), the SNARE complex proteins SNAP25 (B) and VAMP1 (C), the post-synaptic proteins PSD95 (D) and Shank3b (E), and NMDAR1 (F) in synaptosomes purified from the infused striatum and ipsi-lateral cortex from untreated wt mice, untreated R6/2 mice, wt mice treated with AAV2/5-gfaABC1D-tdTomato (wt-Tom), R6/2 mice treated with AAV2/5-gfaABC1D-tdTomato (R6/2-Tom), and R6/2 mice treated with AAV2/5-gfaABC1D-hSREBP2-tdTomato (R6/2-hBP2) ($n=3-4$ mice/group). Stain-free imaging was used as a loading control and for normalization.

Data are shown as scatterplot graphs with means \pm SEM. Each dot corresponds to the value obtained from each animal.

Statistics: one-way ANOVA with Newman-Keuls post-hoc test (* $p<0.05$; ** $p<0.01$; *** $p<0.001$) or unpaired Student *t*-test (# $p<0.05$; ## $p<0.01$).

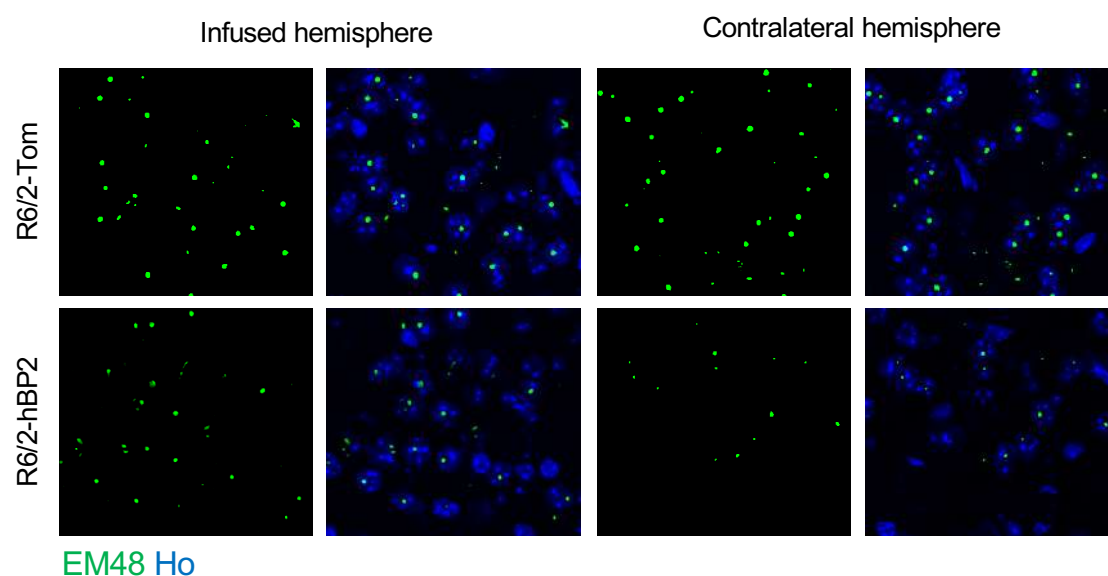
2.8 Glial *hSREBP2* rescues mutant *Huntingtin* (*muHTT*) aggregation in the striatum of R6/2 mice

A hallmark of HD is the presence of intracellular aggregates of muHTT (78). To test whether the over-expression of hSREBP2 in glial cells and the stimulation of endogenous synthesis of cholesterol for 4 weeks in the striatum of R6/2 mice influences muHTT aggregation, we performed immunofluorescence staining on brain sections of R6/2-Tom and R6/2-hBP2 mice with EM48 antibody, which specifically recognize the polyQ tract that is prone to aggregate (Fig. 2.41A). As expected, the control vector over-expressing TdTomato did not influence the number and the size of muHTT

aggregates, which are comparable between the contralateral and the infused hemisphere of R6/2-Tom mice. On the contrary, when we compared the infused and the contralateral striatum of R6/2-hBP2 mice, the number and the size of EM48-positive aggregates were significantly reduced (Fig. 2.41B, C).

Overall, these results indicated that glial over-expression of hSREBP2 promotes muHTT clearance, one of the main neuropathological landmarks in HD, confirming previous results showing that cholesterol and cholesterol precursors favour aggregate clearance in HD (144, 220) and in other neurodegenerative diseases (236, 237, 238).

A



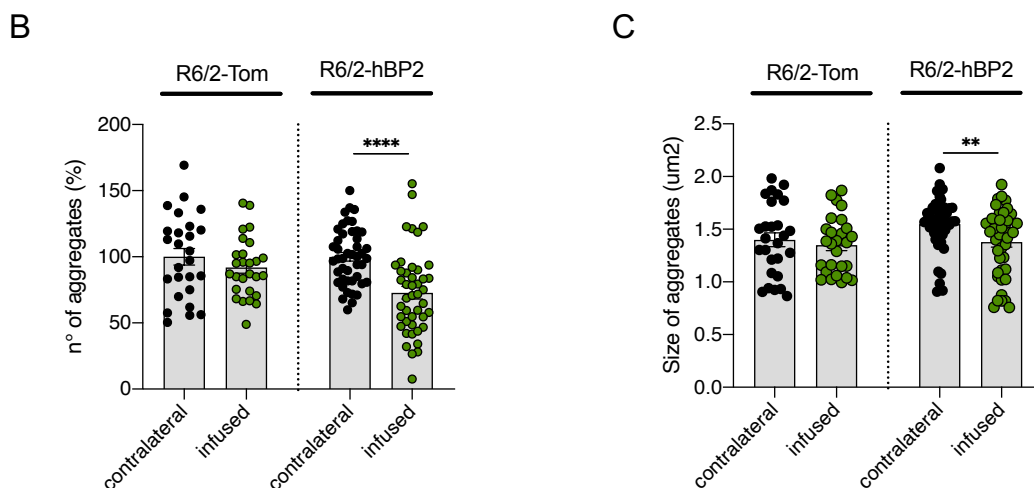


Figure 2.41 muHTT aggregates in R6/2 mice following hSREBP2 over-expression

A. Immunolabeling of muHTT aggregates (green) in the infused and contralateral striatum of R6/2 mice treated AAV2/5-gfaABC1D-tdTomato (R6/2-Tom) or with AAV2/5-gfaABC1D-hSREBP2-tdTomato (R6/2-hBP2) ($n=3-5$ /group). Hoechst (Ho, blue) was used to counterstain nuclei.

B-C. Relative quantification of number (B) and size (C) of aggregates.

Data are shown as scatterplot graphs with means \pm SEM. Each dot corresponds to an image.

Statistics: one-way ANOVA with Newman-Keuls post-hoc test (** $p<0.01$; **** $p<0.0001$).

2.9 Glial hSREBP2 restores the number of DRD2-positive MSNs in the striatum of R6/2 mice

Striatal degeneration in HD firstly occurs in the indirect pathway MSNs expressing DRD2, leading to motor dysfunction (73, 74). It has always been difficult to study neurodegeneration in R6/2 mice since this model shows normal morphology of the central nervous system (CNS) with no focal areas of malformation or neurodegeneration even if sections of the brains of these animals are consistently smaller than those of wild-type littermates (131).

The apparent absence of specific neurodegeneration in R6/2 mice supports the hypothesis that localized atrophy may be secondary to a primary

imbalance that is directly responsible for the clinical symptoms that are typical of HD (131).

However, the down regulation of *Drd2* transcript in striatal MSNs is an established early mark of disease progression that has been proposed as a sensitive measure of the effects of therapeutics (239).

To focus the attention on DRD2-expressing neurons, we took advantage of *Drd2*-GFP colony in which primary labelling was found to occur in DRD2 positive MSNs from the indirect basal ganglia pathway. Here we crossed R6/2 mice with *Drd2*-GFP to obtain an HD line with neurons from the indirect pathway expressing GFP. Since reduction of cholesterol biosynthesis in HD brain is earlier

and more evident in the striatum and it may at least partially account for striatal vulnerability (240), we aimed at quantifying the number of DRD2-expressing MSNs in large volume of striatum ($0,108 \text{ mm}^3 \pm 0,005 \text{ mm}^3$) to see whether decreased number of DRD2-positive MSNs is measurable in R6/2 mice. If this is the case, we would like to understand whether, following glial hSREBP2 over-expression, the expression of DRD2 in MSNs is normalized.

7-week-old Drd2GFP-wt and Drd2GFP-R6/2 mice were unilaterally infected in the right striatum as follow:

- n = 5 Drd2GFP-wt mice infected with AAV2/5-gfaABC1D-TdTomato

(Drd2GFP-wt-Tom)

- n = 4 Drd2GFP-R6/2 mice infected with AAV2/5-gfaABC1D-TdTomato

(Drd2GFP-R6/2-Tom)

- n = 4 Drd2GFP-R6/2 mice infected with AAV2/5-gfaABC1D-hSREBP2-TdTomato (Drd2GFP-R6/2-hBP2)

Mice were sacrificed 4 weeks after the infection and two 1 mm-thick brain coronal slices (comprehending the striatum) were prepared from each animal (Fig. 2.42).

From each slice, the portion including the infused and the contralateral striatum was isolated and clarified using the X-Clarity technology (in collaboration with M. Simonato, San Raffaele Institute).

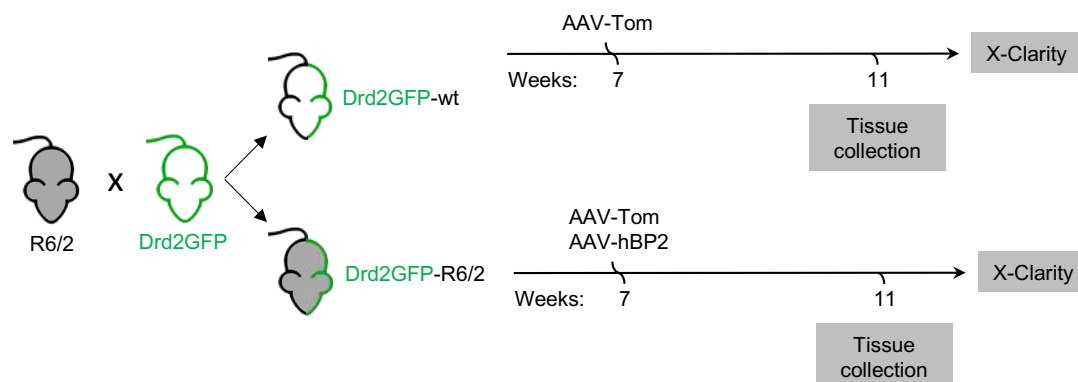


Figure 2.42 Experimental paradigm to obtain Drd2GFP-R6/2 mice

Experimental paradigm used in the study. R6/2 mice were crossed with mice having DRD2-expressing MSNs tagged with GFP to obtain an HD line with neurons from the indirect pathway expressing GFP. 7-weeks old Drd2GFP-wt mice were infected with AAV2/5-gfaABC1D-tdTomato (Drd2GFP-wt-Tom) while Drd2GFP-R6/2 mice were infected with AAV2/5-gfaABC1D-tdTomato (Drd2GFP-R6/2-Tom) or with AAV2/5-gfaABC1D-hSREBP2-tdTomato (Drd2GFP-R6/2-hBP2). Mice were sacrificed 4 weeks later and two 1 mm-thick brain coronal slices (comprehending the striatum) were prepared from each animal. From each slice, the portion including the infused and the contralateral striatum was isolated and clarified using the X-clarity technology (n=5 mice/group).

After the clarification, the endogenous GFP signal was acquired with a two-photon microscope (in collaboration with the ALEMBIC facility, San Raffaele Institute) (Fig. 2.43A). The quantification revealed that the number of MSNs expressing DRD2 is reduced in the infused striatum of *Drd2GFP-R6/2-Tom* mice compared to *Drd2GFP-wt-Tom* mice (Fig. 2.43B) and in the contralateral striatum of *Drd2GFP-R6/2-hBP2* (Fig. 2.43B). Of note, the number of DRD2-expressing

MSNs measured in the infused striatum of *Drd2GFP-R6/2-hBP2* was similar to that measured in *Drd2GFP-wt-Tom* mice (Fig. 2.43B), suggesting that glial over-expression of hSREBP2 allows these neurons to regain DRD2 expression and, supposedly, to improve their function in a non-cell-autonomous mechanism.

This represents an important *in vivo* proof that stimulation of cholesterologenesis in astrocytes has beneficial effects on neurons in HD.

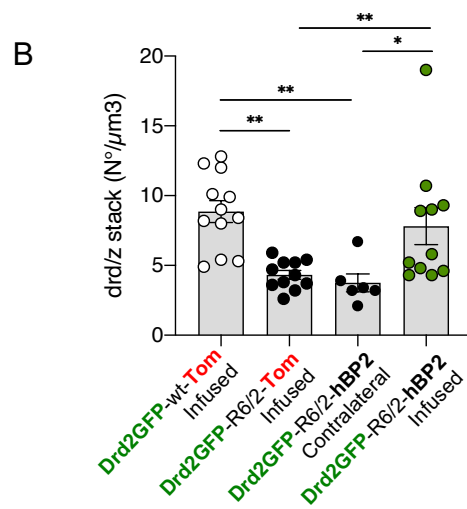
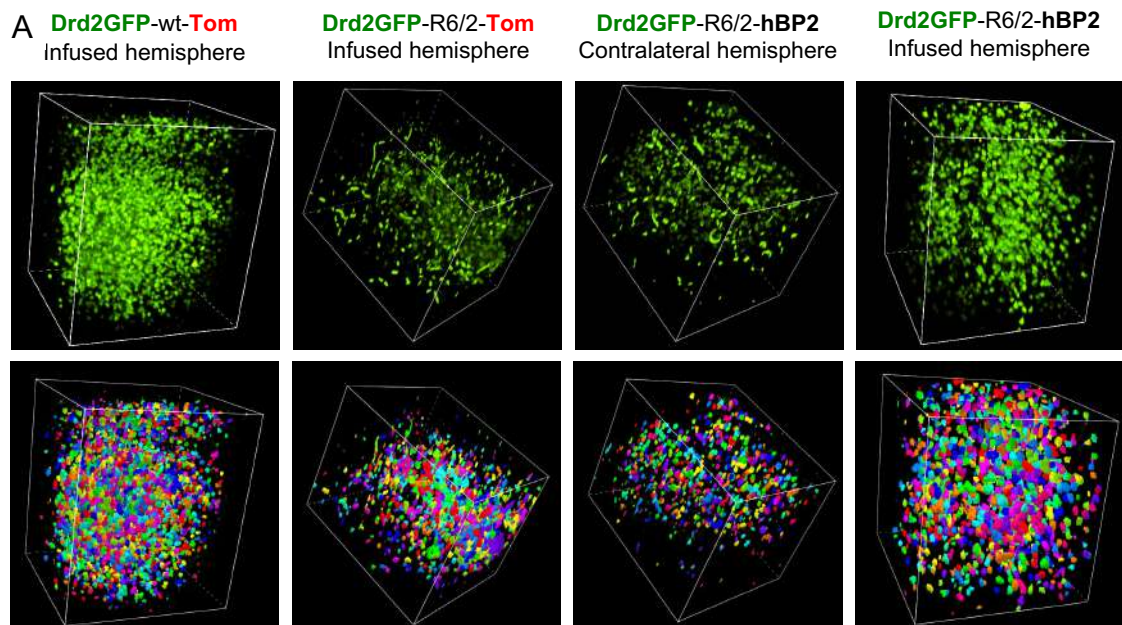


Figure 2.43 DRD2 neurons in R6/2 mice following hSREBP2 over-expression

A-B. Representative two-photon imaging of the endogenous signal of GFP (green) of 1 mm thick brain coronal slices from *Drd2GFP-wt-Tom* (infused hemisphere), *Drd2GFP-R6/2-Tom* (infused hemisphere), and *Drd2GFP-R6/2-hBP2* (contralateral and infused hemisphere) with relative 3D reconstruction (A) and quantification (B). Data are shown as scatterplot graphs with means \pm SEM. Each dot corresponds to an image. The number of neurons was normalized on the z-stack acquired. Statistics: one-way ANOVA with Newman-Keuls post-hoc test (* $p < 0.05$; ** $p < 0.01$).

2.10 Glial *hSREBP2* normalizes synaptic transmission of striatal neurons in R6/2 mice

It is known from the literature that striatal MSNs from R6/2 mice exhibit altered synaptic transmission during disease progression (206, 207), including a reduced membrane capacitance (C_m), a decrease in spontaneous excitatory postsynaptic current (sEPSCs), and an increase in spontaneous inhibitory postsynaptic current (sIPSCs) frequencies (206). Thus, we next explored whether glial over-expression of *hSREBP2* and restoration of endogenous cholesterol biosynthesis over a 4-weeks period restored synaptic parameters in HD mice.

We first compared whole-cell patch-clamp recordings of striatal MSNs from brain slices of R6/2-hBP2 mice, comparing the contralateral and the infused hemisphere.

The membrane capacitance, which is proportional to cell size, was decreased in R6/2-hBP2 mice compared to wild-type littermates with no differences between the contralateral and the infused hemisphere of R6/2-hBP2 mice (Fig. 2.44A).

On the contrary, input resistance, reflecting the number of ion channels expressed by the cell, was increased in both contralateral and infused hemisphere of R6/2-hBP2 mice compared to wild-type (Fig. 2.44B).

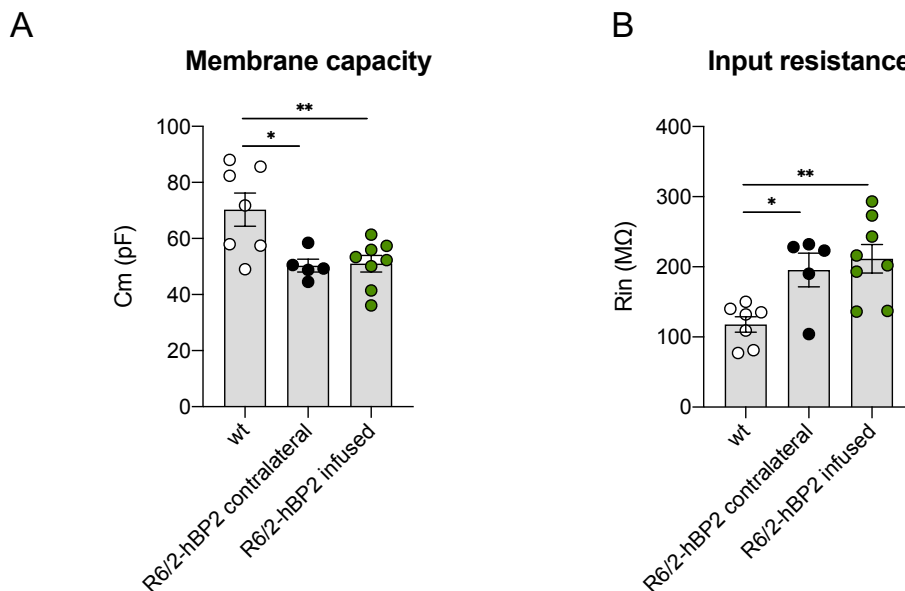


Figure 2.44 Passive properties in R6/2 mice following *hSREBP2* over-expression

A-B. Membrane capacitance (C_m , A) and the input resistance (R_{in} , B) were recorded from 11-weeks old wt mice ($n=6$) and from the contralateral ($n=5$) and infused ($n=7$) hemisphere of R6/2 mice treated with AAV2/5-*gfaABC1D-hSREBP2-tdTomato* (R6/2-hBP2).

Data are shown as scatterplot graphs with means \pm SEM. Each dot corresponds to the value obtained from each animal.

Statistics: one-way ANOVA with Newman-Keuls post-hoc test (* $p < 0.05$; ** $p < 0.01$).

To evaluate the effect of glial cholesterol on excitatory transmission, spontaneous excitatory postsynaptic currents (sEPSC) were recorded at a holding potential of -70 mV (Fig. 2.45A). Any significant differences were found in the average amplitude of sEPSCs between groups (Fig. 2.45B).

In agreement with previous studies (214, 220), glial over-expression of hSREBP2 led to a significant increase in the frequency of sEPSCs in the infused hemisphere of R6/2-hBP2 mice compared to the contralateral striatum, partially rescuing the defect (Fig. 2.45C).

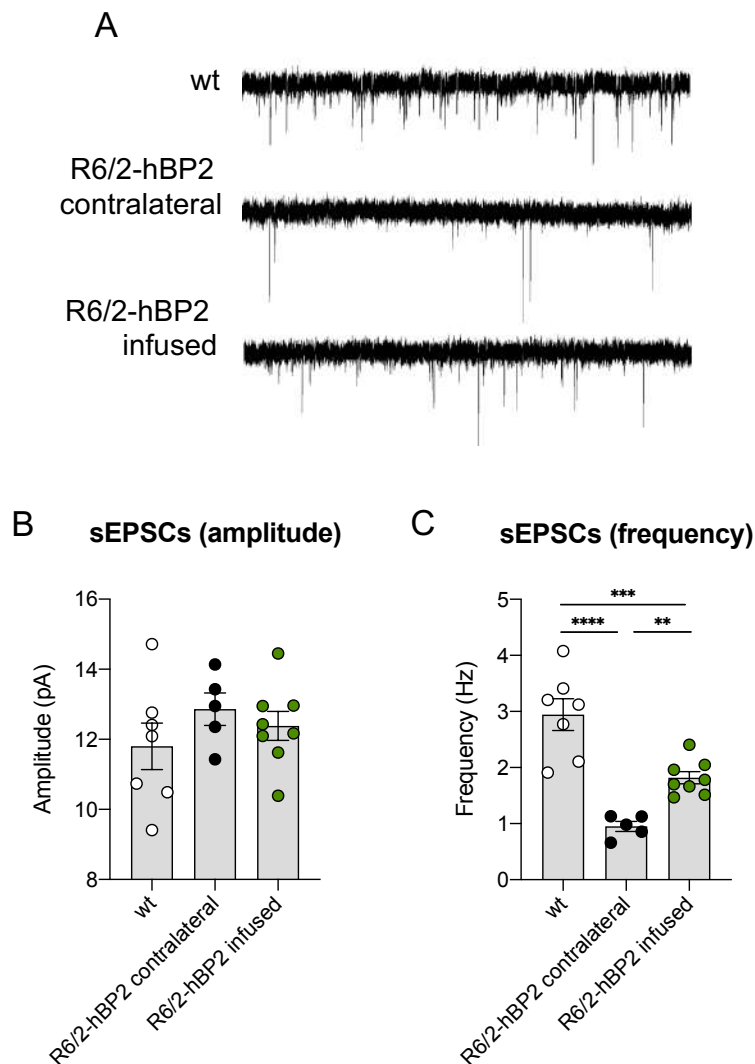


Figure 2.45 Spontaneous excitatory post-synaptic currents analysis in R6/2 mice following hSREBP2 over-expression

A. Spontaneous EPSCs were recorded from striatal MSNs at a holding potential of -70 mV.

B-C. Average amplitude (B) and average frequency (C) of EPSCs from wt and R6/2-hBP2 mice MSNs.

Data are shown as scatterplot graphs with means \pm SEM. Each dot corresponds to the value obtained from each animal.

Statistics: one-way ANOVA with Newman-Keuls post-hoc test (** $p < 0.01$; *** $p < 0.001$; **** $p < 0.0001$).

To test the effect of glial over-expression of hSREBP2 on the inhibitory synapses, we recorded spontaneous inhibitory synaptic currents (sIPSCs) in brain slices from R6/2-hBP2 mice, comparing the contralateral and the infused hemisphere (Fig. 2.46A). The average amplitude of sIPSCs was not affected by glial-cholesterol

production and it was similar between the analyzed groups (Fig. 2.46B). However, glial over-expression of hSREBP2 triggered a significant reduction in the average frequency of sIPSCs in the infused hemisphere compared to the contralateral one, bringing this parameter similar to the one measured in wild-type mice (Fig. 2.46C).

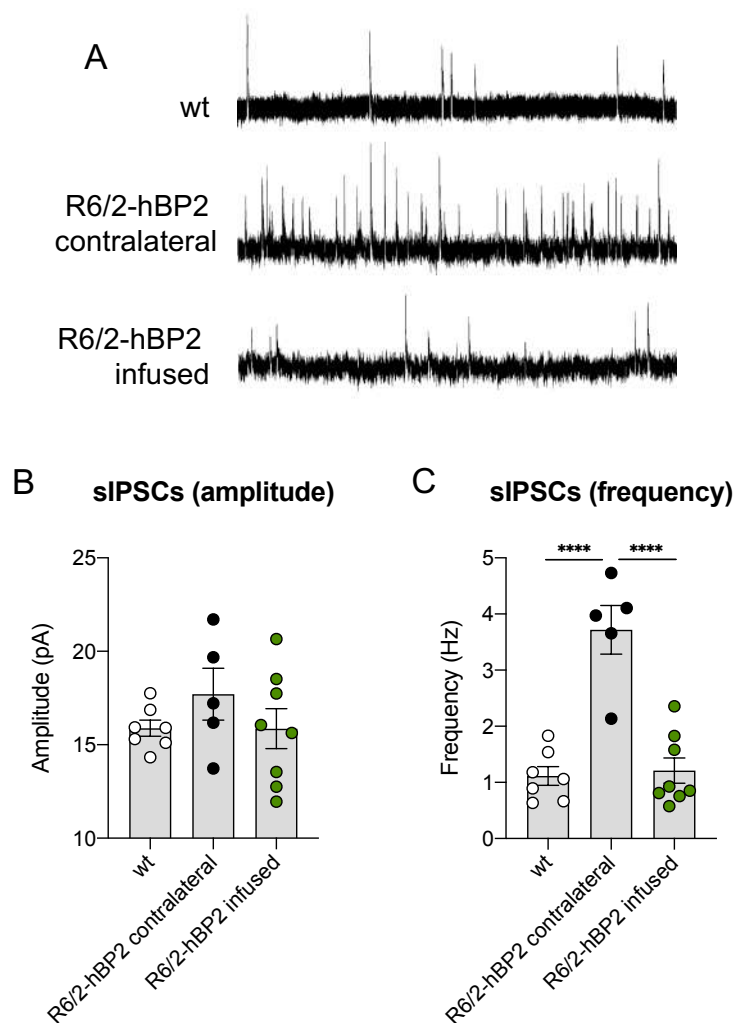


Figure 2.46 Spontaneous inhibitory post-synaptic currents analysis in R6/2 mice following hSREBP2 over-expression

A. Spontaneous IPSCs were recorded from striatal MSNs at a holding potential of 0 mV.

B-C. Average amplitude (B) and average frequency (C) of IPSCs from wt and R6/2-hBP2 mice MSNs.

Data are shown as scatterplot graphs with means \pm SEM. Each dot corresponds to the value obtained from each animal.

Statistics: one-way ANOVA with Newman-Keuls post-hoc test (**** $p < 0.0001$).

Taken together, these results demonstrated that the over-expression of glial SREBP2 acts differentially on excitatory and inhibitory synapses. In particular, we found that increased cholesterol synthesis partially rescued excitatory synaptic transmission while the recovery of the GABAergic frequency was total, suggesting circuit-specific signaling mechanisms in which cholesterol may act differently

2.11 Glial hSREBP2 restores behavioral deficits in R6/2 mice

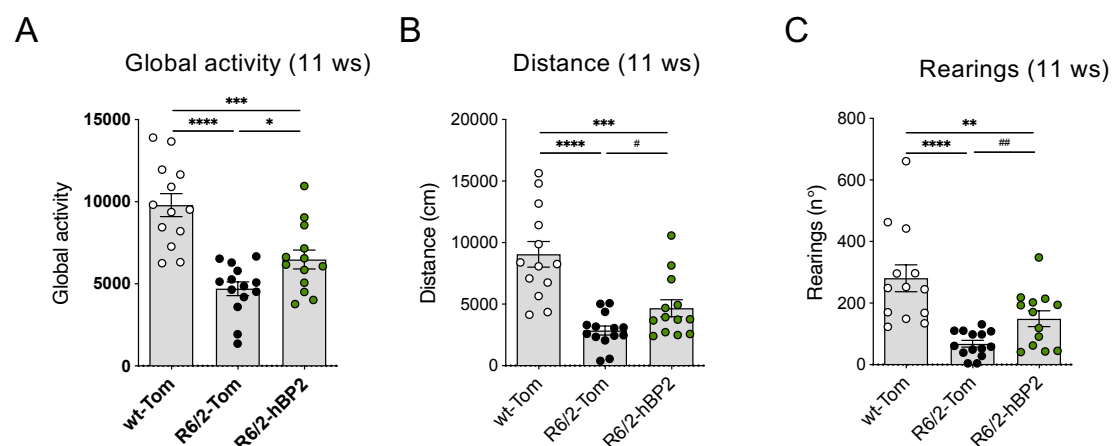
To assess whether the rescue of synaptic activity was correlated to a beneficial effect on the motor and cognitive deficits that characterize R6/2 mice, we performed two independent behavioral trials with the following experimental groups:

- n = 13 wild-type mice infected with AAV2/5-gfaABC1D-TdTomato (wt-Tom)
- n = 15 R6/2 mice infected with AAV2/5-gfaABC1D-TdTomato (R6/2-Tom)
- n = 13 R6/2 mice infected with

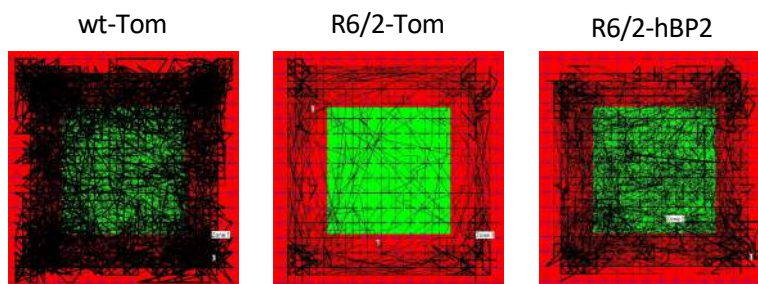
AAV2/5-gfaABC1D-hSREBP2-TdTomato (R6/2-hBP2)

Mice were infected at 7 weeks of age and behavioral tests were performed 4 weeks after the infection.

As expected, at 11 weeks of age R6/2-Tom mice showed reduced global activity compared to wild-type littermates. Furthermore, the total distance travelled in one hour and the number of rearing in the activity cage test were reduced respect to wild-type controls. Of note, glial over-expression of hSREBP2 led to slight but significant rescue of these parameters (Fig. 2.47A-C). To evaluate anxiety-related behavior, we also measured the time that mice spent exploring the periphery or center area of the arena during the activity cage test (Fig. 2.47D). As expected, R6/2-Tom mice spent more time in the periphery compared to wt-Tom mice, indicating increased anxiety. Of note, the behavior of R6/2-hBP2 mice was similar to the one of wt-Tom mice, indicating that glial cholesterol has a beneficial effect on this feature (Fig. 2.47E).



D



E

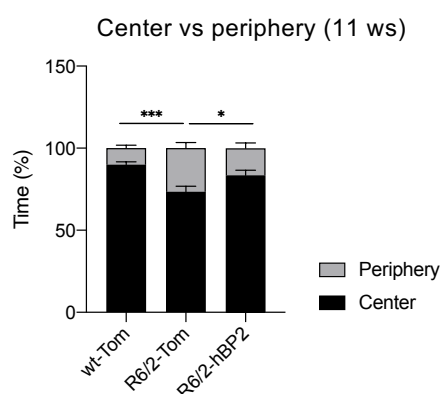


Figure 2.47 Motor abilities of R6/2 mice following hSREBP2 over-expression

A-C. Global motor activity (A), total distance travelled (B), and number of rearings (C) in an open-field test at 11 weeks of age in wt-Tom ($n=13$), R6/2-Tom ($n=14$), and R6/2-hBP2 ($n=13$).

D-E. Representative track plots (D) generated from the open-field test from wt-Tom ($n=13$), R6/2-Tom ($n=14$), and R6/2-hBP2 ($n=13$) and relative quantification (E) of the time spent in the center and in the periphery (%) of the arena at 11 weeks of age.

Data are shown as scatterplot graphs with means \pm SEM. Each dot corresponds to the value obtained from each animal.

Statistics: one-way ANOVA with Newman-Keuls post-hoc test ($*p<0.05$; $**p<0.01$; $***p<0.001$; $****p<0.0001$) or unpaired Student *t*-test ($\#p<0.05$; $\#\#p<0.01$).

When we evaluated the muscular strength of mice, we observed reduced strength in R6/2-Tom mice compared to wt-Tom mice. Importantly, glial over-expression of hSREBP2 has a beneficial effect on this phenotype (Fig. 2.48A).

Then, we performed the paw clasping test to study the clasping behavior of mice as index of neuronal dysfunction. R6/2-Tom mice had a worst performance compared to wt-Tom and

the treatment did not influence this parameter (Fig. 2.48B).

Finally, to analyze the effect of the enhancement of endogenous cholesterol synthesis on the cognitive decline of R6/2 mice we performed the NOR test: R6/2-Tom mice were not able to discriminate the novel object respect to the familiar one compared to wt-Tom and glial over-expression of hSREBP2 completely rescued cognitive decline (Fig. 2.48C).

Taken together these results demonstrated that glial over-expression of hSREBP2 leading to the enhancement of endogenous cholesterol synthesis is sufficient to prevent cognitive and motor decline of HD mice.

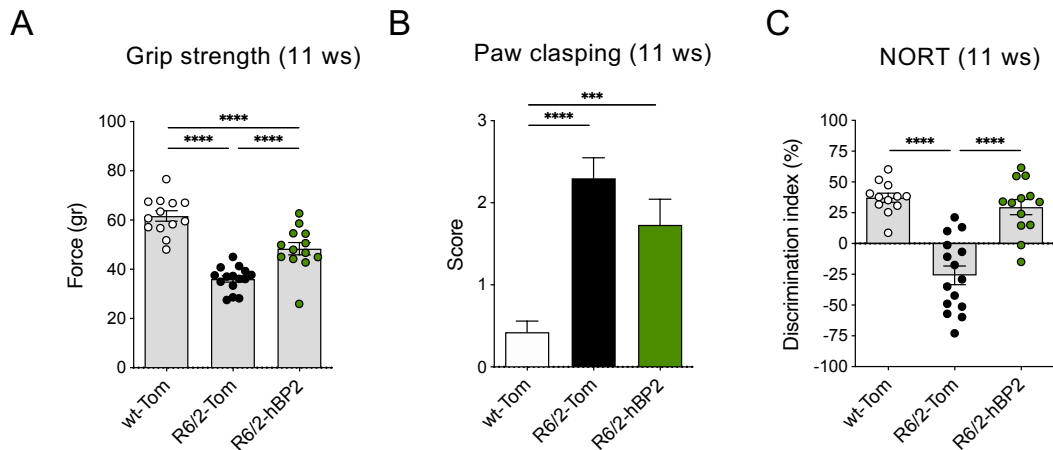


Figure 2.48 Cognitive and motor abilities of R6/2 mice following hSREBP2 over-expression

A. Grip strength (grams) at 11 weeks of age in wt-Tom ($n=13$), R6/2-Tom ($n=15$), and R6/2-hBP2 ($n=13$).

B. Paw clasping at 11 weeks of age in wt-Tom ($n=13$), R6/2-Tom ($n=15$), and R6/2-hBP2 ($n=13$).

C. Discrimination index (DI %) in the novel object recognition test of wt-Tom ($n=12$), R6/2-Tom ($n=15$), and R6/2-hBP2 ($n=13$) at 11 weeks of age. DI above zero indicates a preference for the novel object; DI below zero indicates a preference for the familiar object.

Data are shown as scatterplot graphs with means \pm SEM. Each dot corresponds to the value obtained from each animal.

Statistics: one-way ANOVA with Newman-Keuls post-hoc test (** $p < 0.001$; **** $p < 0.0001$).

3. Conclusions and Future Perspectives

In this project, we evaluated the importance of cholesterol-based strategies as emerging therapeutic approach for HD patients.

First of all, we characterized a new generation of polymeric nanoparticles (g7-NPs-*chol_2.0*) in R6/2 mice to evaluate their safety for clinical translation and their therapeutic efficacy. We demonstrated that g7-NPs-*chol_2.0* are a valuable tool to deliver cholesterol to the brain of HD mice. By performing pharmacokinetic experiments, we showed that cholesterol is slowly released from the injected nanoparticles (around 10% in 2 weeks) and it accumulates in the brain over time, while it decreased in peripheral tissues and in blood. By comparing g7-NPs-*chol_1.0* with g7-NPs-*chol_2.0*, we have confirmed that a high dose of cholesterol is needed to have a positive feedback to stimulate the endogenous synthesis of cholesterol, restoring the primary defect of cholesterol metabolism in HD. In accordance, only the high amount of cholesterol delivered with g7-NPs-*chol_2.0* led to a partial rescue of motor abilities in R6/2 mice at 9 weeks of age but higher doses are needed to completely counteract the defect when the phenotype worsen, confirming that the beneficial effect of

exogenous cholesterol on motor, but not on cognitive phenotype, is dose-dependent.

Importantly, we have confirmed these results using the zQ175DN knock in mice, with a milder and longer phenotype compared to R6/2 mice, more resembling the human HD condition and enabling to perform long-term and cyclic treatments. We have shown that a single cycle of treatment with g7-NPs-*chol_2.0* is sufficient to rescue HD-related behavioral defects. Furthermore, the delivery of cholesterol with cyclic treatments of g7-NPs-*chol_2.0* exerts a long-term effect on mice behavior.

Given these promising results, in collaboration with G. Tosi (University of Modena), we are now working on the development of a third generation of nanoparticles (g7-NPs-*chol_3.0*) with a different formulation that will enable to deliver higher amount of cholesterol. This will allow us to deliver the maximum amount of cholesterol and to reduce the number of injections/week to minimize handling stress in mice. Furthermore, the components of g7-NPs-*chol_3.0* will speed the kinetic of cholesterol release from NPs, which will be easily available for neurons.

To gain more information on the mechanism underlying cholesterol dysfunction in HD, we took advantage of a gene therapy approach consisting in unilateral intra-striatal injection of a

recombinant adeno-associated virus 2/5 targeting astrocytes and carrying the N-terminal fragment of human SREBP2 (hSREBP2) to restore the endogenous synthesis of cholesterol. We found that hSREBP2 was functional as it was able to increase mRNA level of key cholesterol biosynthetic genes and to normalize brain endogenous cholesterol biosynthesis R6/2 mice.

In the brain, astrocytes are important regulatory cells. They regulate neuronal and synaptic function by responding to neurotransmitters and by releasing gliotransmitters/molecules at tripartite synapses (241), which suggests that they have an active involvement in brain function and behavior. Over the time, several studies have been conducted on astrocyte-neuron interactions to analyze the role of astrocyte activity on neuronal function.

In HD, there is an evident and well-studied cross-talk between astrocytes and neurons regarding cholesterol production and impairment in astrocytic cholesterol synthesis negatively impact on neuronal properties. Accordingly, astrocytes derived from R6/2 mice secreted lower amount of cholesterol bound to ApoE lipoproteins in the culture medium, leading to a reduced availability of cholesterol for HD neurons that in turns affected neurite outgrowth and synaptic related properties (150). Furthermore, glia-conditioned medium (GCM) from

wild-type astrocytes rescued neurite outgrowth defect in NS-derived HD neurons, confirming the importance of astrocytes.

Recently, the effects of selective astrocytic stimulation on synaptic plasticity and memory has been investigated by over-expressing in the hippocampal astrocytes the hM3Dq DREADD, an engineered receptor that activates astrocytes upon stimulation with clozapine-N-oxide (CNO) (242). Interestingly they have shown that, in presence of CNO, astrocyte calcium activity and synaptic transmission were enhanced. Of note, the enhancement persisted over the time, suggesting that astrocyte activation is sufficient to induce long-term potentiation (LTP) of synapses. Furthermore, they have shown that this LTP is dependent on NMDA receptors.

Several evidences suggest that cholesterol depletion prevents NMDA-dependent Ca^{2+} influx in neuronal cells (243) and inhibits NMDA-induced hippocampal LTP (244). Accordingly, age-dependent decrease in hippocampal cholesterol content, leads to deficits in glutamate receptor internalization and consequent long-term depression (LTD) impairment, through a mechanism mediated by PI3K/Akt. Intracerebral infusion of cholesterol rescues age-related hippocampal LTD decrease and improves hippocampal-related

learning and memory processes in aging animals (166). Since LTP is commonly associated to enhanced memory and learning and since we have measured increased NMDA receptors level in synaptosomes of R6/2-hBP2 mice compared to R6/2-Tom, improved NORT performance of R6/2-hBP2 mice may be explained by astrocytic stimulation after hSREBP2 over-expression.

Furthermore, glial-derived cholesterol, together with the restoration of cholesterol biosynthetic pathway may also explain the reduction of muHTT aggregates that we have observed in R6/2-hBP2 mice. It is known from the literature that cholesterol precursors stimulate autophagy leading to decreased protein aggregation in some neurodegenerative diseases (238) including Parkinson's disease (236). Furthermore, SREBP2 is linked to stimulation of mTORC1 activity (245) leading to increased clearance pathways.

Finally, we have shown that glial hSREBP2 acts in a non-cell autonomous manner on neurons, normalizing the number of DRD2-positive MSNs. It would be of interest

to analyze whether this rescue is due to a closer contact between neurons and astrocytes. Accordingly, it has been demonstrated *in vivo* using the neuron-astrocyte proximity assay that astrocytes from R6/2 mice displayed smaller territories compared to wild-type astrocytes.

Furthermore, the number of the most proximate astrocyte processes to cortical inputs are decreased in symptomatic R6/2 mice, whereas this parameter is increased for thalamic inputs. Interestingly, these changes occurred before loss of cortical and thalamic presynaptic vGlut1 and vGlut2 assessed by immunostaining (246).

Given these promising results, it would also be interesting to perform long-term studies using zQ175DN knock-in mice, which would allow longer periods of viral infection.

Overall, results from our studies aimed at delivering exogenous cholesterol or at normalizing endogenous cholesterol synthesis highlighted the therapeutic potential of brain cholesterol in contrasting disease-related neurobehavioral impairments in two different mouse model of HD.

4. Materials and Methods

4.1 Mice colony management

All animal experiments were approved and carried out in accordance with Italian Governing Law (D. Lgs 26/2014; Authorization n.324/2015-PR issued May 6, 2015 by Ministry of Health and Authorization n.581/2019-PR issued July 29, 2019 by Ministry of Health); the NIH Guide for the Care and Use of Laboratory Animals (2011 edition) and EU directives and guidelines (EEC Council Directive 2010/63/UE).

Our R6/2 colony lifespan was approximately of 12-13 weeks and only males were used to maintain it (131). Transgenic 6-week-old R6/2 males were mated with wild-type females (B6CBAF1/J, purchased from Charles River). CAG repeat length that could affect strain productivity, general behavior, litter size, pup survival, genotype frequency, phenotype was monitored every 6 months with a range between 150-180 CAGs.

zQ175DN mice colony (213) was maintained using both males and females heterozygous mice. Accordingly, 6-week-old zQ175DN mice were mated with wild-type mice (C57BL6/J, purchased from Charles River).

Drd2-GFP colony was generated in 2003 by the GENSAT (Gene Expression Nervous System Atlas) project at Rockefeller University in

New York (247). Primary labelling was found to occur in DRD2 positive MSNs from the indirect basal ganglia pathway. In this work, 6-week-old Drd2 females were crossed with 6-week-old R6/2 males in order to label *in vivo* DRD2-expressing MSNs in an HD context.

For all the colonies, mice were weaned and then genotyped at 3 weeks of age (+/- 3 days). Mice were housed under standard conditions in enriched cage ($22 \pm 1^\circ\text{C}$, 60% relative humidity, 12 hours light/dark schedule, 3–4 mice/cage, with food and water ad libitum). After PCR genotyping (131, 247), male and female mice were included and randomly divided into experimental groups. Littermates were included as controls.

4.2 Mice treatment

4.2.1 NPs injections

The chemico-physical properties, concentration and cholesterol amount in g7-NPs used in this work, provided and characterized by G. Tosi (University of Modena and Reggio Emilia), are described in Table 1.2 (paragraph 1.5.4).

For biodistribution studies (paragraph 2.1), cholesterol release study (paragraph 2.2.1) and quantitative analysis (paragraph 2.2.2), 7-week-old wild-type or R6/2 mice were treated with 1 or 3 I.P. injections. For all the other experiments, R6/2 mice

were treated with 2 I.P. injections at week, from 5 to 9 weeks of age. With zQ175DN mice, cyclic treatments were performed. As well as for R6/2 mice, each cycle of treatment lasted 5 weeks in which mice received 2 I.P. injections/week. In the first cycle, mice were treated from 5 to 9 weeks of age (pre-symptomatic stage); the second cycle of treatment was performed from 21 to 25 weeks of age (symptomatic stage). In all the experiments, mice received 660 µg of cholesterol in each injection.

4.2.2 Viral injection

Avertin 100% was prepared diluting 5 g of 2,2,2-Tribromoethanol (Sigma Aldrich, #T48402-25G) in 5 mL of 2-methyl-2-butanol (Sigma Aldrich, #240486). Mice were deeply anesthetized using 15 µL of Avertin 2.5% per gram of body weight. Once responses to tail/toe pinches and intactness of the ocular reflex were assessed, scalp was shaved, and mice were placed into a stereotaxic apparatus (2-Biological Instrument). The virus of interest was injected by implantation of a borosilicate glass needle into the right striatum of pre-symptomatic 7-week-old mice via stereotaxic surgery using an automated infusion syringe pump (KD Scientific, KDS100), on which a 50 µL Gastight Syringe Model 1705 TLL with PTFE Luer Lock (Hamilton, 80920)

could be mounted (248). The following coordinates were used: 2 mm lateral to midline, 0.74 mm rostral to the bregma, 3.5 mm ventral to the skull surface; from Paxinos G and Watson C. The Rat Brain in Stereotaxic Coordinates. Academic Press, San Diego. The rate of injection was 12 µL/h with a total volume of 2 µL.

Following surgery, mice were removed from the stereotaxic apparatus and placed on a warm cover to awaken from anesthesia. Post-operative pain and distress were monitored using a specific table for pain scoring based on behavioral indicators of well-being and monitoring mice body weight (249).

4.3 Immunohistochemistry

4.3.1 In vivo analysis of biodistribution and cholesterol release of g7-NPs- chol_2.0

Mice were deeply anesthetized by I.P. injection of Avertin 2.5% and transcardially perfused with PFA 4%. Brains, lungs and liver were post-fixed for 2h in the same solution at 4°C (not longer to avoid fluorescence bleaching) and then in 30% sucrose to prevent ice crystal damage during freezing in OCT. 15 µm-thick brain coronal sections or lung and liver sections were counterstained with the nuclear dye Hoechst 33258 (1:10.000, Invitrogen) and then mounted under cover slips using Vectashield (Vector Laboratories). The fluorescence

signals of cy5 and bodipy-cholesterol were acquired the following day.

To analyze the co-localization of g7-NPs-chol_2.0 with neuronal and glial

markers, 15 μ m-thick brain coronal sections were incubated with primary antibodies described in Table 4.1 for 3h at RT:

Antibody	Host	Dilution	Producer	Catalogue number
DARPP32	Rabbit	1:100	Cell Signalling	2306
NeuN	Mouse	1:100	Millipore	MAB377
GFAP	Rabbit	1:250	Dako	Z0334
IBA1	Rabbit	1:100	Wako	019-1971

Table 4.1 Antibody used for the study

List of the antibodies used in this study, including host, dilution, producer, and catalogue number.

Anti-rabbitAlexa Fluor488-conjugated goat secondary antibodies (1:500; Invitrogen) or anti-mouse Alexa Fluor 488-conjugated goat secondary antibodies (1:500; Invitrogen) were used for detection (1h at RT). Sections were counterstained with the nuclear dye Hoechst 33258 (1:10.000, Invitrogen) and then mounted under cover slips using Vectashield (Vector Laboratories).

4.3.2 Viral spread and tropism

Mice were deeply anesthetized by

I.P. injection of Avertin 2.5% and transcardially perfused with PFA 4%. Brains were post-fixed overnight in the same solution at 4°C and then in 30% sucrose to prevent ice crystal damage during freezing in OCT.

Immunohistochemistry was performed on 15 μ m coronal sections or on free-floating 30 μ m coronal sections. Epitopes were demasked at 98°C with NaCitrate 10 mM and then slices were incubated with primary antibodies described in Table 4.2 for 3h at RT:

Antibody	Host	Dilution	Producer	Catalogue number
SREBP2	Mouse	1:100	Ls-Bio	LS-C179708
RFP	Mouse	1:100	Thermo Fisher	MA5-15257
RFP	Rabbit	1:100	MBL	PM005
DARPP32	Rabbit	1:100	Cell Signalling	2306
NeuN	Mouse	1:100	Millipore	MAB377
GFAP	Rabbit	1:250	Dako	Z0334
IBA1	Rabbit	1:100	Wako	019-1971

Table 4.2 Antibody used for the study

List of the antibodies used in this study, including host, dilution, producer, and catalogue number.

Anti-rabbit Alexa Fluor 568-conjugated goat secondary antibodies (1:500; Invitrogen), anti-rabbit Alexa Fluor 633-conjugated goat secondary antibodies (1:500; Invitrogen) or anti-mouse Alexa Fluor 488-conjugated goat secondary

antibodies (1:500; Invitrogen) were used for detection (1h at RT). Sections were counterstained with the nuclear dye Hoechst 33258 (1:10.000, Invitrogen) and then mounted under cover slips using Vectashield (Vector Laboratories).

4.3.3 Mutant Huntingtin (*muHTT*) aggregates analysis

Mice were deeply anesthetized by I.P. injection of Avertin 2.5% and transcardially perfused with PFA 4%. Brains were post-fixed overnight in the same solution at 4°C and then in 30% sucrose to prevent ice crystal

damage during freezing in OCT.

Immunohistochemistry was performed on 15 µm coronal sections. Epitopes were demasked at 98°C with NaCitrate 10 mM and then slices were incubated with primary antibodies described in Table 4.3 for 3h at RT:

Antibody	Host	Dilution	Producer	Catalogue number
EM48	Mouse	1:100	Millipore	MAB5374

Table 4.3 Antibody used for the study

List of the antibodies used in this study, including host, dilution, producer, and catalogue number.

Anti-mouse Alexa Fluor 488-conjugated goat secondary antibodies (1:500; Invitrogen) were used for detection (1h at RT). Sections were counterstained with the nuclear dye Hoechst 33258 (1:10.000, Invitrogen) and then mounted under cover slips using Vectashield (Vector Laboratories).

4.4 Image acquisition and quantification

4.4.1 In vivo analysis of biodistribution and cholesterol release of g7-NPs-*chol_2.0*

To study the biodistribution and cholesterol release of g7-NPs-*chol_2.0*, confocal images were acquired with a LEICA SP5 laser scanning confocal microscope. Laser intensity and detector gain were maintained constant for all images and 3-z steps images were acquired at 40x.

To quantify the number of g7-NPs-*chol_2.0* in each tissue, ImageJ software was used to measure the fluorescence of cy5. Images were divided into three-color channels and the same global threshold was set (n=4 images/mouse/tissue).

To quantify the released bodipy cholesterol from g7-NPs-*chol_2.0*, Volocity software was used using the plug-in “find objects” and “calculate object correlation” (n=6 images/mouse/tissue).

4.4.2 Viral spread and tropism

To study the spread of the viruses, large images were acquired with a Nikon Crest X-Light V2 microscope at 4x. To study the tropism of the viruses, confocal images were acquired with a LEICA SP5 laser scanning confocal microscope. Laser intensity and detector gain were maintained constant for all images and 3 to 10-z steps images were acquired at 40x.

4.4.3 Mutant Huntingtin (*muHTT*) aggregates

To count *muHTT* aggregates, confocal images were acquired with a LEICA SP5 laser scanning confocal microscope. Laser intensity and detector gain were maintained constant for all images and 5 to 10-z steps images were acquired at 40x. To count aggregates in the brain of AAV-treated mice, 18 images/mice from 9 sections throughout the infused and the contralateral striatum were taken. To quantify the number and the size of aggregates, ImageJ software was used to measure the fluorescence. Images were divided into three-color channels and the same global threshold was set.

4.5 Quantification analysis of d6-cholesterol

To quantify the amount of cholesterol released from g7-NPs-chol_1.0 and g7-NPs-chol_2.0, mice were deeply anesthetized by I.P. injection of Avertin 2.5%. Blood was collected from the venus sinus in a tube containing 20 μ L of heparin and centrifuged at 13.000 rpm at 4°C for 15 minutes to collect the plasma. Mice were transcardially perfused with PBS to avoid the contamination of cholesterol from the periphery. Striatum, cortex, cerebellum, lung, liver and kidney were collected and immediately frozen on dry ice. Mass spectrometry analysis were performed in collaboration with

M. Negri Institute (M. Salmona group) as described in 224.

4.6 Gas chromatography-mass spectrometry (GC-MS) analysis for neutral sterols and 24S-OHC

To quantify the amount of neutral sterols and 24S-OHC, mice were deeply anesthetized by I.P. injection of Avertin 2.5% and transcardially perfused with PBS to avoid the contamination of cholesterol from the periphery. Striatum and cortex were collected and immediately frozen on dry ice. Mass spectrometry analysis were performed in collaboration with C. Besta (V. Leoni and C. Caccia) as described in 220.

4.7 Bioplex assay

To measure cytokines and chemokines, mice were deeply anesthetized by I.P. injection of Avertin 2.5%. Blood was collected from the venus sinus in a tube containing 20 μ L of heparin and centrifuged at 13.000 rpm at 4°C for 15 minutes to collect the plasma. Tissues (striatum, cortex, and liver) were isolated and frozen. 10 mg of striatum, cortex and liver were homogenize using a tissue grinder in 1 mL of lysing solution composed of 40 μ L of factor 1, 20 μ L of factor 2, 9990 μ L of cell lysis buffer and 40 μ L of PMSF 500 mM (Bioplex® Cell Lysis Kit, Biorad, #171304011). The lysate was frozen at -80°C for 2 minutes and

then, following thawing on ice, it was sonicated at 40% for 20 seconds and centrifuged at 4.500 rcf at 4°C for 4 minutes to collect the supernatant.

The supernatant was quantified using DC™ Protein Assay Kit I (Biorad, #5000111) and samples were diluted to a final concentration of 500 µg/mL. To perform the Bioplex assay, 150 µL of assay buffer were added to 150 µL of samples.

Concerning the plasma, samples were centrifuged at 1.500 rcf at 4°C for 5 minutes. 60 µL of assay buffer and 120 µL of sample diluent were added to 60 µL of plasma.

Cytokines level was measured by using a Bioplex murine cytokine 23-Plex assay kit (Biorad, #M60009RDPD) which evaluated the level of: Eotaxin, IL-1a, IL-1b, IL-2, IL-3, IL-4, IL-5, IL-6, IL-9, IL-10, IL-12(p40), IL-12(p70), IL-13, IL-17, TNF-alpha, granulocyte colony-stimulating factor (G-CSF), granulocyte/macrophage colony-stimulating factor (GM-CSF), IFN-gamma, KC, RANTES, macrophage inflammatory protein (MIP-1a and MIP-1b) and monocyte chemotactic protein-1.

Briefly, magnetic beads were added to a 96-well plate which was fixed on a handheld magnetic washer. Samples were added and the plate was shaken at 300 rpm for 30 minutes at room temperature. After 3 washing steps, detection antibodies were added, and

the plate was shaken at 300 rpm for 30 minutes at room temperature. After 3 washing steps, streptavidin-PE was added, and the plate was shaken at 300 rpm for 10 minutes at room temperature. After 3 washing steps, assay buffer was added and the cytokines level was read on the Luminex 200 System, Multiplex Bio-Assay Analyzer and quantified based on standard curves for each cytokine in the concentration range of 1–32,000 pg/mL.

4.8 RNA extraction and qRT-PCR

Mice were sacrificed by cervical dislocation and tissues were isolated and frozen. Total RNA from the infused striatum and the ipsi-lateral cortex of treated mice was isolated with Trizol reagent according to the manufacture's instruction (Thermo Fisher, #15596026). To check the quality of the extracted RNA, total RNA was run on an agarose gel 1%. The genomic DNA present in the extracted RNA samples was digested using the Ambion® DNA-free™ Kit: DNase Treatment and Removal Reagents (Invitrogen, #AM1906).

Template cDNA was prepared by reverse transcription of 500 ng of RNA using the iScript cDNA synthesis kit (BioRad, #1708891). Two different reverse transcription were performed. For each reverse-transcribed product, one or two real-time PCR analyses

were performed for each of the analyzed genes. CFX96 real-Time System (BioRad) was used to evaluate gene expressions. Reactions were performed as described in the Table 4.4:

Reagent	Producer	Catalogue number	Volume
cDNA	/	/	5 µL
SsoFast™ EvaGreen® Supermix	Biorad	172-5204	7,5 µL
Fw Primer	Eurofins	/	0,5 µM
Rv Primer	Eurofins	/	0,5 µM
Nuclease-free water	Sigma Aldrich	W4502	1,5 µL

Table 4.4 Reagents used for qRT-PCR

List of the reagents used in this study to perform qRT-PCR.

Thermocycling conditions were designed as follows:

- enzyme activation at 98°C for 1 min;
- 40 cycles of denaturation at 98°C for 10 sec;
- annealing/extension at Ta for 10 sec;
- melting curve from 65° to 95°C by raising T of 1° every 0.5 sec.

Table 4.5 summarizes the primer sequences used in this work.

Primer	Sequence	Melting Temperature (°C)	Annealing Temperature (°C)	PCR product size (bp)
mb-Actin-FW	AGTGTGACGTTGACATCCGTA	57,9	60	112
mb-Actin-RV	GCCAGAGCAGTAATCTCCTTCT	60,3		
tdTomato-FW	CACCACCTGTTCCGGGG	60,5	57	89
tdTomato-RV	ATGACGGCCATGTTGTTGTC	57,3		
hSREBP2-FW	GTACAGCCGGTCACCATTCA	59,4	60	74
hSREBP2-RV	CCATTGGCCGTTTGTGTCAG	59,4		
mSREBP2-FW	GCCCTCCTTTAACCCCTTG	59,4	60	131
mSREBP2-RV	CCAGTCAAACCAGCCCCAG	63,5		
mHMGCR-FW	GGAGCATAGGCGGCTACA	58,2	60	191
mHMGCR-RV	ACCACCCACGGTTCCTATCT	59,4		
mMVK-FW	CCCTCCTGAAGCCAGGTCTA	61,4	60	87
mMVK-RV	TGGTCTCCCAGCAGTCAAAC	59,4		
mFDFT1-FW	ACTCAGCAGCAGCTTGAAGACC	62,1	60	152
mFDFT1-RV	TGTCATCCTCCACTGTATCCAG	60,3		
mCYP51-FW	GGCAGAGCGCTTGGACTTTA	59,4	60	97
mCYP51-RV	ATGACGCCAGCTCCAAATG	59,4		
mDHCR7-FW	GCTTCCTGACTTCTGCCACA	59,4	57	86
mDHCR7-RV	TGTTTACAACCCCTGCTGGA	57,3		
mSCD2-FW	GCCACATACTGCAAGAG	56,0	60	116
mSCD2-RV	CAGTGGTGAGAACTCTTTTCA	55,9		
mABCA1-FW	GTCAGCTGTTACTGGAAGTGG	59,8	60	198
mABCA1-RV	CGCCGGGAGTTGGATAACGG	63,5		
mAPOE-FW	GACAGATCAGCTCGAGTGGC	61,4	60	170
mAPOE-RV	CTTCCGTCATAGTGTCTCCAT	60,3		
mLRP1-FW	AGGCCACCTCTGCAGCTGT	61,0	60	112
mLRP1-RV	GCTGCGGATCTCGTTGTCATC	61,8		
mCYP46A1-FW	AGGACGATGAGGTTCTGCTGGA	62,1	60	175
mCYP46A1-RV	TCGTAGTCCAGGTGCCTCTT	59,4		
mGLT1-FW	TTGGTGCAGCCAGTATCCC	59,4	60	119
mGLT1-RV	TCTATCCAGCAGCCAGTCCA	59,4		

Table 4.5 Primers used for qRT-PCR

List of the primers used in this study to perform qRT-PCR.

4.9 Synaptosomes preparation and Western Blot analysis

Mice were sacrificed by cervical dislocation and tissues were isolated and frozen. Synaptosomes were purified from the infused striatum and the ipsi-lateral cortex of treated mice using Syn-PER Synaptic Protein Extraction Reagent (Thermo Fisher, #87793) accordingly to the manufacturer instruction. Briefly, 10 mL of Syn-PER Reagent per gram of tissue were added and tissues were homogenized on ice. The homogenate was centrifuged at 1.200 rcf for 10 minutes at 4°C to pellet the membrane fragments and nuclei. The resulting supernatant, containing the synaptosomes and the cytosolic fraction, was centrifuged at 15,000 rcf for 20 minutes at 4°C to pellet synaptosomes. The synaptosome pellet was resuspended in Syn-

PER Reagent with a volume of 1-2 mL per gram of sample so that to result in 3-4 µg/µL, as quantified with Pierce™ BCA Protein Assay Kit (Thermo Fisher, 23225).

Criterion TGX Stain Free Precast Gels with stacking gel 4% and resolving gel either 7.5% (BioRad, #5678023) or Any kD (BioRad, #5678123) were used for Western Blot analysis. After the electrophoretic run, the precast gel was transferred into the ChemiDoc MP System (BioRad) to measure the total amount of protein loaded in each lane of the gel thanks to the stain-free technology, by exploiting a proprietary trihalo compound to enhance the fluorescence of tryptophan amino acids when exposed to UV light. Membranes were incubated with primary antibodies described in Table 4.6 over night at 4°C:

Antibody	Host	Dilution	Producer	Catalogue number
SREBP2	Rabbit	1:1000	Ls-Bio	LS-B4695
RFP	Rabbit	1:1000	MBL	PM005
SYP	Mouse	1:500	Abcam	AB8049
SNAP25	Mouse	1:1000	Abcam	AB66066
VAMP1	Rabbit	1:1000	Abcam	AB151712
PSD95	Mouse	1:1000	SySy	124011
SHANK3	Rabbit	1:1000	SySy	162302
NMDAR1	Rabbit	1:500	Millipore	AB9864
GAPDH	Rabbit	1:5000	Abcam	AB37168

Table 4.6 Antibody used for the study

List of the antibodies used in this study, including host, dilution, producer, and catalogue number.

Goat anti-mouse IgG-HRP (1:3000; BioRad, #1706516) or Goat anti-rabbit IgG-HRP (1:3000; BioRad, #1706515) were used for detection (1h at RT). Proteins were detected

using Clarity Western ECL Substrate (BioRad, #1705061) or SuperSignal West Femto Maximum Sensitivity Substrate (Thermo Fisher, #34096) using ChemiDoc MP System (BioRad).

The detected chemiluminescent signal was quantified by a densitometric analysis and proteins level was normalized using GAPDH (for the cytosolic fraction) or using 6 different protein bands of the stain-free (for synaptosomes).

4.10 X-Clarity and 2-photon imaging

Mice were deeply anesthetized by intraperitoneal injection of Avertin 2.5% and transcardially perfused with PFA 4%. Brains were post-fixed overnight in the same solution at 4°C. Following washing to remove residual PFA, brain slicing was performed with a Leica VT1000S Vibrating blade microtome (Leica Biosystems). From each mouse, two 1-mm thick coronal brain slices were obtained, from which the infused and the contralateral striatum were isolated. Tissues were clarified using the X-Clarity system (Logos Biosystem) according to manufacturer instructions. Briefly, tissues were incubated in embedding solution (Logos Biosystems, C13104) at 4°C for 24 h and then transferred in the X-CLARITY™ Polymerization System at 37°C for 3 hours under vacuum condition (-90kPa). To clarify tissues, slices were rinsed with Electrophoretic Tissue Clearing (ETC) Solution (Logos Biosystems, C13001) and incubated into the X-CLARITY™ Tissue Clearing System II (Logos Biosystems, C30001) chamber at 1.5

A at 37°C for 2-3 hours.

The endogenous signal (GFP) was acquired by using an A1 MP+ microscope (Nikon) in collaboration with Alembic (San Raffaele Institute). Images (approximately 400 µm of z-stack with a z-step size of 5 µm) were acquired at 25x. For each slice, 2-3 images were acquired. To quantify DRD2-positive neurons, images were analyzed using the software NIS-Elements (Nikon): a mask was applied using a plugin for 3D reconstruction. For each image, the number of cells expressing GFP was normalized on the z-stack acquired.

4.11 Behavioral tests

Animals were assigned randomly, and sex was balanced in the various experimental groups. All the behavioral analyses were performed in blind.

Activity cage and novel object recognition test was performed as described in 220.

Grip strength test: mice were lifted by the lower back and tail and lowered towards the grip (Ugo Basile) until the animal grabbed it with both front paws. The animal was then lowered toward the platform and gently pulled straight back with consistent force until it released its grip. The forelimb grip force, measured in grams, was recorded. The test was repeated for 5 times, and measures were averaged. After testing, animals were placed

back into their home cage.

Paw clasping test: mice were suspended by the tail for 30 seconds and the clasping phenotype was graded according to the following scale: level 0, no clasping; level 1, one hindlimb retracted toward the abdomen; level 2, both hindlimbs retracted toward the abdomen; level 3, both hindlimbs entirely retracted and touching the abdomen. After testing, animals were placed back into their home cage.

4.12 Electrophysiological analysis

Experiments were performed in collaboration with G. Biella (University of Pavia) on submerged brain slices obtained from adult mice (12 weeks of age) 4 weeks after the infection into the right striatum as described in 220.

4.13 Statistics

To pre-determine sample sizes, we used G-power analysis based on pilot or previous studies. Table 4.7 summarizes all the trials and read-outs performed. Before analyzing data, Grubbs' test was applied to identify outliers. Statistical analyses were performed using Prism 8 (GraphPad software).

Data are presented as means \pm standard error of the mean (SEM). For each set of data to be compared, we determined whether data were normally distributed or not to select parametric or not parametric statistical tests. The specific statistical test used is indicated in the legend of all results figures. Differences were considered statistically if the p-value was less than 0.05.

Trial number and date	Experimental groups	NPs Bio-distribution analysis	Chol release: quantitative analysis	Chol release: quantitative analysis	Mass spectrometry analysis	Behavioral analysis	Bioplex analysis
		N mice	N mice	N mice	N mice	N mice	N mice
1 - September 2017	wt + cy5-g7-NPs-cholesterol 2.0 MIX-1	10					
	wt + cy5-g7-NPs-cholesterol 2.0 MIX-2	10					
2 - November 2017	wt + cy5-g7-NPs-cholesterol 2.0 MIX-1	10					
	wt + cy5-g7-NPs-cholesterol 2.0 MIX-2	10					
3 - February 2018	wt + cy5-g7-NPs-bodipy-cholesterol 2.0 MIX 1		9				
	wt + cy5-g7-NPs-bodipy-cholesterol 2.0 MIX 2		9				
	R6/2 + cy5-g7-NPs-bodipy-cholesterol 2.0 MIX 1		9				
	R6/2 + cy5-g7-NPs-bodipy-cholesterol 2.0 MIX 2		9				
4 - May 2018	R6/2 + g7-NPs-d6-cholesterol 2.0 MIX-1			21			
5 - January 2019	wt saline				3	10	
	R6/2 saline				3	8	
	R6/2 + g7-NPs-cholesterol 2.0				3	10	
6 - November 2019	wt saline					5	
	R6/2 saline					4	4
	R6/2 + g7-NPs-cholesterol 1.0					10	
	R6/2 + g7-NPs-cholesterol 2.0					7	5
7 - February 2020	wt saline					18	
	Q175 saline					17	
	Q175 + g7-NPs-cholesterol 2.0 (1 cycle)					9	
	Q175 + g7-NPs-cholesterol 2.0 (2 cycles)					9	

Trial number and date	Experimental groups	Viral spread and tropism	qRT-PCR analysis	Western blot analysis	Ephys analysis	Drd2 quantification analysis	muHTT analysis	Mass spectrometry analysis	Behavioral analysis
		N mice	N mice	N mice	N mice	N mice	N mice	N mice	N mice
1 - September 2017	wt-HSV	4							
	wt-Tom	3							
	R6/2-Tom	3							
	R6/2-hBP2	5							
2 - November 2017	wt		3						
	R6/2		3						
	R6/2-Tom	3	3						
	R6/2-hBP2	2	3						
3 - October 2018	wt-Tom			4					
	R6/2-Tom			4					
	R6/2-hBP2	3		4					
4 - December 2019	wt				5				
	R6/2-hBP2				5				
5 - January 2020	wt-Tom								8
	R6/2-Tom						3		8
	R6/2-hBP2						5		7
6 - February 2020	wt-Tom					5			
	R6/2-Tom					4			
	R6/2-hBP2					4			
7 - June 2020	wt-Tom				5			4	4
	R6/2-Tom				5			4	7
	R6/2-hBP2				3			4	6

Table 4.7 List of the animals used for the study

Summary of all the trial performed and the animals used for this study.

5. References

1. Björkhem, I., Meaney, S. & Fogelman, A. M. Brain Cholesterol: Long Secret Life behind a Barrier. *Arterioscler. Thromb. Vasc. Biol.* **24**, 806–815 (2004).
2. Dietschy, J. M. & Turley, S. D. Cholesterol metabolism in the central nervous system during early development and in the mature animal. *J. Lipid Res.* **45**, 1375–1397 (2004).
3. Dietschy, J. M. Central nervous system: Cholesterol turnover, brain development and neurodegeneration. *Biol. Chem.* **390**, 287–293 (2009).
4. Dietschy, J. M. & Turley, S. D. Cholesterol metabolism in the brain. *Lipids* **3**, 136–142 (1968).
5. Zhang, J. & Liu, Q. Cholesterol metabolism and homeostasis in the brain. *Protein Cell* **6**, 254–264 (2015).
6. Jurevics, H. & Morell, P. Cholesterol for synthesis of myelin is made locally, not imported into brain. *J Neurochem.* **64**, 895–901 (1995).
7. Björkhem, I. *et al.* Cholesterol homeostasis in human brain: Turnover of 24S- hydroxycholesterol and evidence for a cerebral origin of most of this oxysterol in the circulation. *J. Lipid Res.* **39**, 1594–1600 (1998).
8. Ikonen, E. Mechanisms for cellular cholesterol transport: Defects and human disease. *Physiol. Rev.* **86**, 1237–1261 (2006).
9. Compagnone, N. A. & Mellon, S. H. Neurosteroids: Biosynthesis and function of these novel neuromodulators. *Front. Neuroendocrinol.* **21**, 1–56 (2000).
10. Mauch, D. H. *et al.* CNS synaptogenesis promoted by glia-derived cholesterol. *Science.* **294**, 1354–1357 (2001).
11. Göritz, C., Mauch, D. H., Nägler, K. & Pfrieder, F. W. Role of glia-derived cholesterol in synaptogenesis: New revelations in the synapse-glia affair. *J. Physiol. Paris* **96**, 257–263 (2002).
12. Goritz, C., Mauch, D. H. & Pfrieder, F. W. Multiple mechanisms mediate cholesterol-induced synaptogenesis in a CNS neuron. *Mol. Cell. Neurosci.* **29**, 190–201 (2005).
13. Maxfield, F. R. & Tabas, I. Role of cholesterol and lipid organization in disease. *Nature* **438**, 612–621 (2005).
14. Pfrieder, F. W. Role of cholesterol in synapse formation and function. *Biochim. Biophys. Acta - Biomembr.* **1610**, 271–280 (2003).

15. Pfrieger, F. W. Cholesterol homeostasis and function in neurons of the central nervous system. *Cell. Mol. Life Sci.* **60**, 1158–1171 (2003).
16. Pfrieger, F. W. Outsourcing in the brain: Do neurons depend on cholesterol delivery by astrocytes? *BioEssays* **25**, 72–78 (2003).
17. Orth, M. & Bellosta, S. Cholesterol: Its regulation and role in central nervous system disorders. *Cholesterol* **2012**, (2012).
18. Leoni, V. & Caccia, C. The impairment of cholesterol metabolism in Huntington disease. *Biochim. Biophys. Acta - Mol. Cell Biol. Lipids* **1851**, 1095–1105 (2015).
19. Singh, P., Saxena, R., Srinivas, G., Pande, G. & Chattopadhyay, A. Cholesterol Biosynthesis and Homeostasis in Regulation of the Cell Cycle. *PLoS One* **8**, (2013).
20. Mitsche, M. A., McDonald, J. G., Hobbs, H. H. & Cohen, J. C. Flux analysis of cholesterol biosynthesis in vivo reveals multiple tissue and cell-type specific pathways. *Elife* **4**, 1–21 (2015).
21. Ye, J. & DeBose-Boyd, R. A. Regulation of cholesterol and fatty acid synthesis. *Cold Spring Harb. Perspect. Biol.* **3**, 1–13 (2011).
22. Jeon, T. II & Osborne, T. F. SREBPs: Metabolic integrators in physiology and metabolism. *Trends Endocrinol. Metab.* **23**, 65–72 (2012).
23. Eberlé, D., Hegarty, B., Bossard, P., Ferré, P. & Foufelle, F. SREBP transcription factors: Master regulators of lipid homeostasis. *Biochimie* **86**, 839–848 (2004).
24. Valenza, M. & Cattaneo, E. Emerging roles for cholesterol in Huntington's disease. *Trends Neurosci.* **34**, 474–486 (2011).
25. Yang, T. *et al.* Crucial step in cholesterol homeostasis: Sterols promote binding of SCAP to INSIG-1, a membrane protein that facilitates retention of SREBPs in ER. *Cell* **110**, 489–500 (2002).
26. Suzuki, R., Ferris, H. A., Chee, M. J., Maratos-Flier, E. & Kahn, C. R. Reduction of the Cholesterol Sensor SCAP in the Brains of Mice Causes Impaired Synaptic Transmission and Altered Cognitive Function. *PLoS Biol.* **11**, (2013).
27. Camargo, N. *et al.* Oligodendroglial myelination requires astrocyte-derived lipids. *PLoS Biol.* **15**, 1–24 (2017).
28. Camargo, N. *et al.* High-fat diet ameliorates neurological deficits caused by defective astrocyte lipid metabolism. *FASEB J.* **26**, 4302–4315 (2012).
29. Ferris, H. A. *et al.* Loss of astrocyte cholesterol synthesis disrupts neuronal function and alters whole-body metabolism. *Proc. Natl. Acad.*

- Sci. U. S. A.* **114**, 1189–1194 (2017).
30. Hayashi, H. Lipid metabolism and glial lipoproteins in the central nervous system. *Biol. Pharm. Bull.* **34**, 453–461 (2011).
 31. Thiele, C., Hannah, M. J., Fahrenholz, F. & Huttner, W. B. Cholesterol binds to synaptophysin and is required for biogenesis of synaptic vesicles. *Nat. Cell Biol.* **2**, 42–49 (2000).
 32. Liu, Q. *et al.* Neuronal LRP1 knockout in adult mice leads to impaired brain lipid metabolism and progressive, age-dependent synapse loss and neurodegeneration. *J. Neurosci.* **30**, 17068–17078 (2010).
 33. Pfrieger, F. W. & Ungerer, N. Cholesterol metabolism in neurons and astrocytes. *Prog. Lipid Res.* **50**, 357–371 (2011).
 34. Mahley, R. W., Weisgraber, K. H. & Huang, Y. Apolipoprotein E4: A causative factor and therapeutic target in neuropathology, including Alzheimer's disease. *Proc. Natl. Acad. Sci. U. S. A.* **103**, 5644–5651 (2006).
 35. Lahiri, D. K. Apolipoprotein E as a target for developing new therapeutics for Alzheimer's disease based on studies from protein, RNA, and regulatory region of the gene. *J. Mol. Neurosci.* **23**, 225–233 (2004).
 36. Hirsch-Reinshagen, V. *et al.* Deficiency of ABCA1 impairs apolipoprotein E metabolism in brain. *J. Biol. Chem.* **279**, 41197–41207 (2004).
 37. Wahrle, S. E. *et al.* ABCA1 is required for normal central nervous system apoE levels and for lipidation of astrocyte-secreted apoE. *J. Biol. Chem.* **279**, 40987–40993 (2004).
 38. Karasinska, J. M. *et al.* ABCA1 influences neuroinflammation and neuronal death. *Neurobiol. Dis.* **54**, 445–455 (2013).
 39. Rebeck, G. W., Reiter, J. S., Strickland, D. K. & Hyman, B. T. Apolipoprotein E in sporadic Alzheimer's disease: allelic variation and receptor interactions. *Neuron* **11**, 575–580 (1993).
 40. Bu, G. Apolipoprotein E and Apolipoprotein in Alzheimer Disease: pathways, pathogenesis and therapy. *Nat Rev Neurosci.* **10**, 333–344 (2009).
 41. Holtzman, D. M., Herz, J. & Bu, G. Apolipoprotein E and Apolipoprotein E Receptors: Normal Biology and Roles in Alzheimer Disease. *Cold Spring Harb Perspect Med.* **2**, a006312 (2012).
 42. Lane-Donovan, C. E., Phillips, G. T. & Herz, J. More than cholesterol transporters: lipoprotein receptors in CNS function and neurodegeneration. *Neuron.* **83**, 771–787 (2015).

43. Lund, E. G. *et al.* Knockout of the cholesterol 24-hydroxylase gene in mice reveals a brain-specific mechanism of cholesterol turnover. *J. Biol. Chem.* **278**, 22980–22988 (2003).
44. Ramirez, D. M. O., Andersson, S. & Russel, D. W. Neuronal Expression and Subcellular Localization of Cholesterol 24-Hydroxylase in the Mouse Brain. *J Comp Neurol.* **507**, 1676–1693 (2008).
45. Lütjohann, D. *et al.* Cholesterol homeostasis in human brain: Evidence for an age-dependent flux of 24S-hydroxycholesterol from the brain into the circulation. *Proc. Natl. Acad. Sci. U. S. A.* **93**, 9799–9804 (1996).
46. Russell, D. W., Halford, R. W., Ramirez, D. M. O., Shah, R. & Kotti, T. Cholesterol 24-hydroxylase: An enzyme of cholesterol turnover in the brain. *Annu. Rev. Biochem.* **78**, 1017–1040 (2009).
47. Lund, E. G., Guileyardo, J. M. & Russell, D. W. cDNA cloning of cholesterol 24-hydroxylase, a mediator of cholesterol homeostasis in the brain. *Proc. Natl. Acad. Sci. U. S. A.* **96**, 7238–7243 (1999).
48. Björkhem, I. Crossing the barrier: Oxysterols as cholesterol transporters and metabolic modulators in the brain. *J. Intern. Med.* **260**, 493–508 (2006).
49. Leoni, V., Long, J. D., Mills, J. A., Di Donato, S. & Paulsen, J. S. Plasma 24S-hydroxycholesterol correlation with markers of Huntington disease progression. *Neurobiol. Dis.* **55**, 37–43 (2013).
50. Leoni, V. & Caccia, C. 24S-hydroxycholesterol in plasma: A marker of cholesterol turnover in neurodegenerative diseases. *Biochimie* **95**, 595–612 (2013).
51. Abildayeva, K. *et al.* 24(S)-hydroxycholesterol participates in a liver X receptor-controlled pathway in astrocytes that regulates apolipoprotein E-mediated cholesterol efflux. *J. Biol. Chem.* **281**, 12799–12808 (2006).
52. Rawlins, M. D. *et al.* The prevalence of Huntington's disease. *Neuroepidemiology* **46**, 144–153 (2016).
53. Martin, J. B. & Gusella, J. F. Huntington's disease. Pathogenesis and management. *N. Engl. J. Med.* **315**, 1267–1276 (1986).
54. Rosenberg, N. K., Sørensen, S. A. & Christensen, A. L. Neuropsychological characteristics of Huntington's disease carriers: A double blind study. *J. Med. Genet.* **32**, 600–604 (1995).
55. Deffains, M. & Bergman, H. Striatal cholinergic interneurons and cortico-striatal synaptic plasticity in health and disease. *Mov. Disord.* **30**, 1014–1025 (2015).
56. Van der Burg, J. M., Björkqvist, M. & Brundin, P. Beyond the brain:

- widespread pathology in Huntington's disease. *Lancet Neurol.* **8**, 765–774 (2009).
57. HD Collaborative Research Group. A novel gene containing a trinucleotide repeat that is expanded and unstable on Huntington's disease chromosomes. The Huntington's Disease Collaborative Research Group. *Cell.* **72**, 971–983 (1993).
 58. Kremer, B. *et al.* A worldwide study of the Huntington's disease mutation. *New English J. Med.* **330**, 1401–1406 (1994).
 59. Rubinsztein, D. C. *et al.* Phenotypic characterization of individuals with 30-40 CAG repeats in the Huntington disease (HD) gene reveals HD cases with 36 repeats and apparently normal elderly individuals with 36-39 repeats. *Am. J. Hum. Genet.* **59**, 16–22 (1996).
 60. Semaka, A., Collins, J. A. & Hayden, M. R. Unstable familial transmissions of huntington disease alleles with 27-35 CAG repeats (intermediate alleles). *Am. J. Med. Genet. Part B Neuropsychiatr. Genet.* **153**, 314–320 (2010).
 61. Ranen, N. G. *et al.* Anticipation and instability of IT-15 (CAG)(N) repeats in parent-offspring pairs with Huntington disease. *Am. J. Hum. Genet.* **57**, 593–602 (1995).
 62. Langbehn, D. R., Hayden, M., Paulsen, J. S. & the PREDICT-HD Investigators of the Huntington Study Group. CAG-Repeat Length and the Age of Onset in Huntington Disease (HD): A Review and Validation Study of Statistical Approaches. *Am J Med Genet B Neuropsychiatr Genet.* **153**, 397–408 (2010).
 63. Ross, C. A. & Tabrizi, S. J. Huntington's disease: From molecular pathogenesis to clinical treatment. *Lancet Neurol.* **10**, 83–98 (2011).
 64. Lee, J. M. *et al.* CAG repeat expansion in Huntington disease determines age at onset in a fully dominant fashion. *Neurology* **78**, 690–695 (2012).
 65. Vonsattel, J. P. & DiFiglia, M. Huntington disease. *J. Neuropathol. Exp. Neurol. Neuropathol Exp Neurol.* **57**, 369–384 (1998).
 66. Aylward, E. H. *et al.* Association between Age and Striatal Volume Stratified by CAG Repeat Length in Prodromal Huntington Disease. *PLoS Curr.* **82**, 405–410 (2011).
 67. Vonsattel, J. P. *et al.* Neuropathological classification of Huntington's disease. *J. Neuropathol. Exp. Neurol.* **44**, 559–577 (1985).
 68. Sotrel, A. *et al.* Morphometric analysis of the prefrontal cortex in Huntington's disease. *Neurology.* **41**, 1117–1123 (1991).
 69. Vonsattel, J. P. G. Huntington disease models and human

- neuropathology: similarities and differences. *Acta Neuropathol.* **115**, 55–69 (2008).
70. Ariano, M. A. *et al.* Striatal neurochemical changes in transgenic models of Huntington's disease. *J. Neurosci. Res.* **68**, 716–729 (2002).
71. Gerfen, C. R. *et al.* D1 and D2 Dopamine receptor-regulated gene expression of striatonigral and striatopallidal neurons. *Science.* **250**, 1429–1432 (2018).
72. Calabresi, P., Picconi, B., Tozzi, A., Ghiglieri, V. & Di Filippo, M. Direct and indirect pathways of basal ganglia: A critical reappraisal. *Nat. Neurosci.* **17**, 1022–1030 (2014).
73. Reiner, A. *et al.* Differential loss of striatal projection neurons in Huntington disease. *Proc. Natl. Acad. Sci. U. S. A.* **85**, 5733–5737 (1988).
74. Albin, R. L., Young, A. B. & Penney, J. B. The functional anatomy of basal ganglia disorders. *Trends Neurosci.* **12**, 366–375 (1989).
75. Reiner, A. *et al.* Striatal parvalbuminergic neurons are lost in Huntington's disease: Implications for dystonia. *Mov. Disord.* **28**, 1691–1699 (2013).
76. Albin, R. L. *et al.* Abnormalities of striatal projection neurons and N-methyl-D-aspartate receptors in presymptomatic Huntington's disease. *N Engl J Med.* **322**, 1293–1298 (1990).
77. Arrasate, M. & Finkbeiner, S. Protein aggregates in Huntington's disease. *Exp. Neurol.* **238**, 1–11 (2012).
78. DiFiglia, M. *et al.* Aggregation of huntingtin in neuronal intranuclear inclusions and dystrophic neurites in brain. *Science.* **277**, 1990–1993 (1997).
79. Takahashi, T. *et al.* Soluble polyglutamine oligomers formed prior to inclusion body formation are cytotoxic. *Hum. Mol. Genet.* **17**, 345–356 (2008).
80. Lajoie, P. & Snapp, E. L. Formation and toxicity of soluble polyglutamine oligomers in living cells. *PLoS One* **5**, (2010).
81. Leitman, J., Ulrich Hartl, F. & Lederkremer, G. Z. Soluble forms of polyQ-expanded huntingtin rather than large aggregates cause endoplasmic reticulum stress. *Nat. Commun.* **4**, 1–10 (2013).
82. Saudou, F., Finkbeiner, S., Devys, D. & Greenberg, M. E. Huntingtin acts in the nucleus to induce apoptosis but death does not correlate with the formation of intranuclear inclusions. *Cell.* **95**, 55–66 (1998).
83. Mastroberardino, P. G. *et al.* 'Tissue' transglutaminase ablation reduces neuronal death and prolongs survival in a mouse model of Huntington's

- disease. *Cell Death Differ.* **9**, 873–880 (2002).
84. Arrasate, M., Mitra, S., Schweitzer, E. S., Segal, M. R. & Finkbeiner, S. Inclusion body formation reduces levels of mutant huntingtin and the risk of neuronal death. *Nature* **431**, 805–810 (2004).
 85. Nucifora, L. G. *et al.* Identification of novel potentially toxic oligomers formed in vitro from mammalian-derived expanded huntingtin exon-1 protein. *J. Biol. Chem.* **287**, 16017–16028 (2012).
 86. DiFiglia, M. *et al.* Huntingtin is a cytoplasmic protein associated with vesicles in human and rat brain neurons. *Neuron* **14**, 1075–1081 (1995).
 87. Ferrante, R. J. *et al.* Neuroprotective effects of creatine in a transgenic Mouse model of Huntington's disease. *J. Neurosci.* **20**, 4389–4397 (2000).
 88. Guo, Q. *et al.* The cryo-electron microscopy structure of huntingtin. *Nature* **555**, 117–120 (2018).
 89. Zuccato, C., Valenza, M. & Cattaneo, E. Molecular mechanisms and potential therapeutical targets in Huntington's disease. *Physiol. Rev.* **90**, 905–981 (2010).
 90. Duyao, M. P. *et al.* Inactivation of the Mouse Huntington's Disease Gene Homolog Hdh. *Cell.* **269**, 407–410 (2017).
 91. Nasir, J. *et al.* Targeted disruption of the Huntington's disease gene results in embryonic lethality and behavioral and morphological changes in heterozygotes. *Cell* **81**, 811–823 (1995).
 92. Zeitlin, S., Liu, J., Chapman, D. L. & Papaioannou, V. E. article nullizygous for the Huntington's disease gene homo logue. **11**, 155–163 (1995).
 93. White, J. K. *et al.* CAG expansion. *Nat. Genet.* **17**, 404–410 (1997).
 94. Auerbach, W. *et al.* The HD mutation causes progressive lethal neurological disease in mice expressing reduced levels of huntingtin. *Hum. Mol. Genet.* **10**, 2515–2523 (2001).
 95. Reiner, A. *et al.* Neurons lacking huntingtin differentially colonize brain and survive in chimeric mice. *J. Neurosci.* **21**, 7608–7619 (2001).
 96. Rigamonti, D. *et al.* Wild-Type Huntingtin protects from apoptosis upstream of Caspase-3. *J. Neurosci.* **20**, 3705–3713 (2000).
 97. Rigamonti, D. *et al.* Huntingtin's neuroprotective activity occurs via inhibition of Procaspase-9 processing. *J. Biol. Chem.* **276**, 14545–14548 (2001).

98. McKinstry, S. U. *et al.* Huntingtin is required for normal excitatory synapse development in cortical and striatal circuits. *J. Neurosci.* **34**, 9455–9472 (2014).
99. Zuccato, C. & Cattaneo, E. Role of brain-derived neurotrophic factor in Huntington's disease. *Prog. Neurobiol.* **81**, 294–330 (2007).
100. Cattaneo, E., Zuccato, C. & Tartari, M. Normal huntingtin function: An alternative approach to Huntington's disease. *Nat. Rev. Neurosci.* **6**, 919–930 (2005).
101. Caviston, J. P., Ross, J. L., Antony, S. M., Tokito, M. & Holzbaur, E. L. F. Huntingtin facilitates dynein/dynactin-mediated vesicle transport. *Proc. Natl. Acad. Sci. U. S. A.* **104**, 10045–10050 (2007).
102. Gauthier, L. R. *et al.* Huntingtin controls neurotrophic support and survival of neurons by enhancing BDNF vesicular transport along microtubules. *Cell* **118**, 127–138 (2004).
103. Pla, P. *et al.* Huntingtin acts non cell-autonomously on hippocampal neurogenesis and controls anxiety-related behaviors in adult mouse. *PLoS One* **8**, 1–12 (2013).
104. Poirier, M. A. *et al.* Huntingtin spheroids and protofibrils as precursors in polyglutamine fibrilization. *J. Biol. Chem.* **277**, 41032–41037 (2002).
105. Legleiter, J. *et al.* Mutant huntingtin fragments form oligomers in a polyglutamine length-dependent manner in Vitro and in Vivo. *J. Biol. Chem.* **285**, 14777–14790 (2010).
106. Gu, M. *et al.* Mitochondrial defect in Huntington's disease caudate nucleus. *Ann. Neurol.* **39**, 385–389 (1996).
107. Panov, A. V. *et al.* Early mitochondrial calcium defects in Huntington's disease are a direct effect of polyglutamines. *Nat. Neurosci.* **5**, 731–736 (2002).
108. Browne, S. E. Mitochondria and Huntington's disease pathogenesis: Insight from genetic and chemical models. *Ann. N. Y. Acad. Sci.* **1147**, 358–382 (2008).
109. Bennett, E. J. *et al.* Global changes to the ubiquitin system in Huntington's disease. *Nature* **448**, 704–708 (2007).
110. Martinez-Vicente, M. *et al.* Cargo recognition failure is responsible for inefficient autophagy in Huntington's disease. *Nat. Neurosci.* **13**, 567–576 (2010).
111. Zuccato, C. *et al.* Systematic assessment of BDNF and its receptor levels in human cortices affected by Huntington's disease. *Brain Pathol.* **18**, 225–238 (2008).

112. Sun, Y., Savanenin, A., Reddy, P. H. & Liu, Y. F. Polyglutamine-expanded Huntingtin Promotes Sensitization of N-Methyl-D-aspartate Receptors via Post-synaptic Density 95. *J. Biol. Chem.* **276**, 24713–24718 (2001).
113. Cha, J. H. J. *et al.* Altered brain neurotransmitter receptors in transgenic mice expressing a portion of an abnormal human Huntington disease gene. *Proc. Natl. Acad. Sci. U. S. A.* **95**, 6480–6485 (1998).
114. Cha, J. H. J. *et al.* Altered neurotransmitter receptor expression in transgenic mouse models of Huntington's disease. *Philos. Trans. R. Soc. B Biol. Sci.* **354**, 981–989 (1999).
115. Luthi-Carter, R. *et al.* Decreased expression of striatal signaling genes in a mouse model of Huntington's disease. *Hum. Mol. Genet.* **9**, 1259–1271 (2000).
116. Luthi-Carter, R. *et al.* Complex alteration of NMDA receptors in transgenic Huntington's disease mouse brain: Analysis of mRNA and protein expression, plasma membrane association, interacting proteins, and phosphorylation. *Neurobiol. Dis.* **14**, 624–636 (2003).
117. Song, C., Zhang, Y., Parsons, C. G. & Liu, Y. F. Expression of polyglutamine-expanded huntingtin induces tyrosine phosphorylation of N-methyl-D-aspartate receptors. *J. Biol. Chem.* **278**, 33364–33369 (2003).
118. Fan, M. M. Y., Fernandes, H. B., Zhang, L. Y. J., Hayden, M. R. & Raymond, L. A. Altered NMDA receptor trafficking in a yeast artificial chromosome transgenic mouse model of Huntington's disease. *J. Neurosci.* **27**, 3768–3779 (2007).
119. Fan, M. M. Y. & Raymond, L. A. N-Methyl-d-aspartate (NMDA) receptor function and excitotoxicity in Huntington's disease. *Prog. Neurobiol.* **81**, 272–293 (2007).
120. Crotti, A. & Glass, C. K. The choreography of neuroinflammation in Huntington's disease. *Trends Immunol.* **36**, 364–373 (2015).
121. Pecho-Vrieseling, E. *et al.* Transneuronal propagation of mutant huntingtin contributes to non-cell autonomous pathology in neurons. *Nat. Neurosci.* **17**, 1064–1072 (2014).
122. Behrens, P. F., Franz, P., Woodman, B., Lindenberg, K. S. & Landwehrmeyer, G. B. Impaired glutamate transport and glutamate - Glutamine cycling: Downstream effects of the Huntington mutation. *Brain* **125**, 1908–1922 (2002).
123. Estrada-Sánchez, A. M., Montiel, T., Segovia, J. & Massieu, L. Glutamate toxicity in the striatum of the R6/2 Huntington's disease transgenic mice is age-dependent and correlates with decreased levels of glutamate

- transporters. *Neurobiol. Dis.* **34**, 78–86 (2009).
124. Tong, X. *et al.* Astrocyte Kir4.1 ion channel deficits contribute to neuronal dysfunction in Huntington's disease model mice. *Nat. Neurosci.* **17**, 694–703 (2014).
125. Jiang, R., Diaz-Castro, B., Looger, L. L. & Khakh, B. S. Dysfunctional calcium and glutamate signaling in striatal astrocytes from Huntington's disease model mice. *J. Neurosci.* **36**, 3453–3470 (2016).
126. Caron, N. S., Dorsey, E. R. & Hayden, M. R. Therapeutic approaches to Huntington disease: From the bench to the clinic. *Nat. Rev. Drug Discov.* **17**, 729–750 (2018).
127. Rodrigues, F. B., Quinn, L. & Wild, E. J. Huntington's disease clinical trials corner: January 2019. *J. Huntingtons. Dis.* **8**, 115–125 (2019).
128. Rocha, B. N. P., Colpo, G. D., Teixeira, A. L. & Stimming, E. F. Clinical Trials for Huntington Disease. 69–74 (2020).
129. Tabrizi, S. J. *et al.* Targeting huntingtin expression in patients with Huntington's disease. *N. Engl. J. Med.* **380**, 2307–2316 (2019).
130. Sipione, S. *et al.* Early transcriptional profiles in huntingtin-inducible striatal cells by microarray analyses. *Hum. Mol. Genet.* **25**, 210–210 (2002).
131. Mangiarini, L. *et al.* Exon 1 of the HD Gene with an Expanded CAG Repeat Is Sufficient to Cause a Progressive Neurological Phenotype in Transgenic Mice. *Cell* **87**, 493–506 (1996).
132. Valenza, M. *et al.* Dysfunction of the cholesterol biosynthetic pathway in Huntington's disease. *J. Neurosci.* **25**, 9932–9939 (2005).
133. Valenza, M. *et al.* Progressive dysfunction of the cholesterol biosynthesis pathway in the R6/2 mouse model of Huntington's disease. *Neurobiol. Dis.* **28**, 133–142 (2007).
134. Valenza, M. *et al.* Cholesterol biosynthesis pathway is disturbed in YAC128 mice and is modulated by huntingtin mutation. *Hum. Mol. Genet.* **16**, 2187–2198 (2007).
135. Valenza, M. *et al.* Cholesterol defect is marked across multiple rodent models of Huntington's disease and is manifest in astrocytes. *J. Neurosci.* **30**, 10844–10850 (2010).
136. Hodgson, J. G. *et al.* A YAC mouse model for Huntington's disease with full-length mutant huntingtin, cytoplasmic toxicity, and selective striatal neurodegeneration. *Neuron* **23**, 181–192 (1999).
137. Von Hörsten, S. *et al.* Transgenic rat model of Huntington's disease. *Hum.*

- Mol. Genet.* **12**, 617–624 (2003).
138. Shankaran, M. *et al.* Early and brain region-specific decrease of de novo cholesterol biosynthesis in Huntington's disease: A cross-validation study in Q175 knock-in mice. *Neurobiol. Dis.* **98**, 66–76 (2017).
 139. Trushina, E. *et al.* Mutant huntingtin inhibits clathrin-independent endocytosis and causes accumulation of cholesterol in vitro and in vivo. *Hum. Mol. Genet.* **15**, 3578–3591 (2006).
 140. Del Toro, D. *et al.* Altered cholesterol homeostasis contributes to enhanced excitotoxicity in Huntington's disease. *J. Neurochem.* **115**, 153–167 (2010).
 141. Boussicault, L. *et al.* CYP46A1, the rate-limiting enzyme for cholesterol degradation, is neuroprotective in Huntington's disease. *Brain* **139**, 953–970 (2016).
 142. Marullo, M. *et al.* Pitfalls in the detection of cholesterol in Huntington's disease models. *PLoS Curr.* 1–21 (2012) doi:10.1371/505886e9a1968.
 143. Menalled, L. B. *et al.* Comprehensive Behavioral and Molecular Characterization of a New Knock-In Mouse Model of Huntington's Disease: ZQ175. *PLoS One* **7**, (2012).
 144. Kacher, R. *et al.* CYP46A1 gene therapy deciphers the role of brain cholesterol metabolism in Huntington's disease. *Brain* **142**, 2432–2450 (2019).
 145. Leoni, V. *et al.* Whole body cholesterol metabolism is impaired in Huntington's disease. *Neurosci. Lett.* **494**, 245–249 (2011).
 146. Wang, R. *et al.* Metabolic and hormonal signatures in pre-manifest and manifest Huntington's disease patients. *Front. Physiol.* **5**, 1–10 (2014).
 147. Leoni, V. *et al.* Plasma 24S-hydroxycholesterol and caudate MRI in pre-manifest and early Huntington's disease. *Brain* **131**, 2851–2859 (2008).
 148. Lütjohann, D. & von Bergmann, K. 24S-hydroxycholesterol: a marker of brain cholesterol metabolism. *Pharmacopsychiatry* **36**, 102–106 (2003).
 149. Di Pardo, A. *et al.* Mutant huntingtin interacts with the sterol regulatory element-binding proteins and impairs their nuclear import. *Hum. Mol. Genet.* **29**, 418–431 (2020).
 150. Valenza, M. *et al.* Disruption of astrocyte-neuron cholesterol cross talk affects neuronal function in Huntington's disease. *Cell Death Differ.* **22**, 690–702 (2015).
 151. Vanier, T. M. Niemann-Pick disease type C. *Orphanet J Rare Dis* **5**, 1–18 (2010).

152. Karten, B., Vance, D. E., Campenot, R. B. & Vance, J. E. Cholesterol accumulates in cell bodies, but is decreased in distal axons, of Niemann-Pick C1-deficient neurons. *J. Neurochem.* **83**, 1154–1163 (2002).
153. Rosenbaum, A. I., Zhang, G., Warren, J. D. & Maxfield, F. R. Endocytosis of beta-cyclodextrins is responsible for cholesterol reduction in Niemann-Pick type C mutant cells. *Proc. Natl. Acad. Sci. U. S. A.* **107**, 5477–5482 (2010).
154. Aqul, A. *et al.* Unesterified cholesterol accumulation in late endosomes/lysosomes causes neurodegeneration and is prevented by driving cholesterol export from this compartment. *J. Neurosci.* **31**, 9404–9413 (2011).
155. Peake, K. B. & Vance, J. E. Normalization of cholesterol homeostasis by 2-hydroxypropyl- β -cyclodextrin in neurons and glia from Niemann-Pick C1 (NPC1)-deficient mice. *J. Biol. Chem.* **287**, 9290–9298 (2012).
156. Xie, C., Gong, X. M., Luo, J., Li, B. L. & Song, B. L. AAV9-NPC1 significantly ameliorates Purkinje cell death and behavioral abnormalities in mouse NPC disease. *J. Lipid Res.* **58**, 512–518 (2017).
157. Porter, F. D. Cholesterol precursors and facial clefting. *J. Clin. Invest.* **116**, 2322–2325 (2006).
158. Porter, F. D. & Herman, G. E. Malformation syndromes caused by disorders of cholesterol synthesis. *J. Lipid Res.* **52**, 6–34 (2011).
159. DeBarber, A. E. *et al.* Smith-Lemli-Opitz Syndrome. *Expert Rev Mol Med.* **13**, e24 (2011).
160. Nowaczyk, M. J. M. & Irons, M. B. Smith – Lemli – Opitz Syndrome: phenotype, natural history, and epidemiology. **262**, 250–262 (2012).
161. Svoboda, M. D. *et al.* Treatment of Smith-Lemli-Opitz Syndrome and Other Sterol Disorders. *Am J Med Genet C Semin Med Genet.* **0**, 285–294 (2012).
162. Selkoe, D. J. Alzheimer's disease is a synaptic failure. *Science.* **298**, 789–791 (2002).
163. Lane, C. A., Hardy, J. & Schott, J. M. Alzheimer's disease. *Eur. J. Neurol.* **25**, 59–70 (2018).
164. Ballard, C. *et al.* The progression of cognitive impairment in dementia with Lewy bodies, vascular dementia and Alzheimer's disease. *Int. J. Geriatr. Psychiatry* **16**, 499–503 (2001).
165. Strittmatter, W. J. *et al.* Apolipoprotein E: High-avidity binding to β -amyloid and increased frequency of type 4 allele in late-onset familial Alzheimer disease. *Proc. Natl. Acad. Sci. U. S. A.* **90**, 1977–1981 (1993).

166. Martín, M. G., Pfrieder, F. & Dotti, C. G. Cholesterol in brain disease: sometimes determinant and frequently implicated. *EMBO Rep.* **15**, 1036–1052 (2014).
167. Chang, T. Y., Yamauchi, Y., Hasan, M. T. & Chang, C. Cellular cholesterol homeostasis and Alzheimer's disease. *J. Lipid Res.* **58**, 2239–2254 (2017).
168. Wahrle, S. E. *et al.* Deletion of *Abca1* increases A β deposition in the PDAPP transgenic mouse model of Alzheimer disease. *J. Biol. Chem.* **280**, 43236–43242 (2005).
169. Wahrle, S. E. *et al.* Overexpression of ABCA1 reduces amyloid deposition in the PDAPP mouse model of Alzheimer disease. *J. Clin. Invest.* **118**, 671–682 (2008).
170. Longenberger, J. & Shah, Z. A. Simvastatin and other HMG-CoA reductase inhibitors on brain cholesterol levels in Alzheimer's disease. *Curr Alzheimer Res.* **8**, 434–442 (2011).
171. Sveinbjornsdottir, S. The clinical symptoms of Parkinson's disease. *J. Neurochem.* **139**, 318–324 (2016).
172. Kalia, L. V. & Lang, A. E. Parkinson's disease. *Lancet* **386**, 896–912 (2015).
173. Davie, C. A. A review of Parkinson's disease. *Br Med Bull.* **86**, 109–127 (2008).
174. Musanti, R., Parati, E., Lamperti, E. & Ghiselli, G. Decreased cholesterol biosynthesis in fibroblasts from patients with Parkinson disease. *Biochem Med Metab Biol.* **49**, 133–142 (1993).
175. Fabelo, N. *et al.* Severe alterations in lipid composition of frontal cortex lipid rafts from Parkinson's disease and incidental Parkinson's disease. *Mol. Med.* **17**, 1107–1118 (2011).
176. Paul, R. *et al.* Cholesterol contributes to dopaminergic neuronal loss in MPTP mouse model of Parkinson's disease: Involvement of mitochondrial dysfunctions and oxidative stress. *PLoS One* **12**, 1–22 (2017).
177. Jin, U., Park, S. J. & Park, S. M. Cholesterol metabolism in the brain and its association with Parkinson's disease. *Exp. Neurobiol.* **28**, 554–567 (2019).
178. Lee, C. Y. J., Seet, R. C. S., Huang, S. H., Long, L. H. & Halliwell, B. Different patterns of oxidized lipid products in plasma and urine of dengue fever, stroke, and parkinson's disease patients: Cautions in the use of biomarkers of oxidative stress. *Antioxidants Redox Signal.* **11**, 407–420 (2009).

179. Huang, X. *et al.* Brain cholesterol metabolism and Parkinson's disease. *Mov. Disord.* **34**, 386–395 (2019).
180. Van Maarschalkerweerd, A., Vetri, V. & Vestergaard, B. Cholesterol facilitates interactions between α -synuclein oligomers and charge-neutral membranes. *FEBS Lett.* **589**, 2661–2667 (2015).
181. Bosco, D. A. *et al.* Elevated levels of oxidized cholesterol metabolites in Lewy body disease brains accelerate alpha-synuclein fibrilization. *Nat Chem Biol.* **2**, 249–253 (2006).
182. Koob, A. O. *et al.* Lovastatin ameliorates α -synuclein accumulation and oxidation in transgenic mouse models of α -synucleinopathies. *Exp. Neurol.* **221**, 267–274 (2010).
183. Bar-On, P. *et al.* Effects of the cholesterol-lowering compound methyl- β -cyclodextrin in models of α -synucleinopathy. *J. Neurochem.* **98**, 1032–1045 (2006).
184. Ghosh, A. *et al.* Simvastatin inhibits the activation of p21ras and prevents the loss of dopaminergic neurons in a mouse model of Parkinson's disease. *J. Neurosci.* **29**, 13543–13556 (2009).
185. Figiel, M., Szlachcic, W. J., Switonski, P. M., Gabka, A. & Krzyzosiak, W. J. Mouse models of polyglutamine diseases: Review and data table. Part I. *Mol. Neurobiol.* **46**, 393–429 (2012).
186. Heng, M. Y., Detloff, P. J. & Albin, R. L. Rodent genetic models of Huntington disease. *Neurobiol. Dis.* **32**, 1–9 (2008).
187. Pouladi, M. A., Morton, A. J. & Hayden, M. R. Choosing an animal model for the study of Huntington's disease. *Nat. Rev. Neurosci.* **14**, 708–721 (2013).
188. Crook, Z. R. & Housman, D. Huntington's Disease: Can Mice Lead the Way to Treatment? *Neuron* **69**, 423–435 (2011).
189. Gil, J. M. & Rego, A. C. The R6 lines of transgenic mice: A model for screening new therapies for Huntington's disease. *Brain Res. Rev.* **59**, 410–431 (2009).
190. Li, J. Y., Popovic, N. & Brundin, P. The use of the R6 transgenic mouse models of Huntington's disease in attempts to develop novel therapeutic strategies. *NeuroRx* **2**, 447–464 (2005).
191. Switonski, P. M., Szlachcic, W. J., Gabka, A., Krzyzosiak, W. J. & Figiel, M. Mouse models of polyglutamine diseases in therapeutic approaches: Review and data table. Part II. *Mol. Neurobiol.* **46**, 430–466 (2012).
192. Cummings, D. M. *et al.* A critical window of CAG repeat-length correlates with phenotype severity in the r6/2 mouse model of Huntington's disease.

- J. Neurophysiol.* **107**, 677–691 (2012).
193. Dragatsis, I. *et al.* Healthy food access for urban food desert residents: examination of the food environment, food purchasing practices, diet, and body mass index. *Neurobiol. Dis.* **33**, 315–330 (2009).
194. Morton, A. J. *et al.* Paradoxical delay in the onset of disease caused by super-long CAG repeat expansions in R6/2 mice. *Neurobiol. Dis.* **33**, 331–341 (2009).
195. Stack, E. C. *et al.* Chronology of behavioral symptoms and neuropathological sequela in R6/2 Huntington’s disease transgenic mice. *J. Comp. Neurol.* **490**, 354–370 (2005).
196. Lüsse, H. G. *et al.* Evaluation of R6/2 HD transgenic mice for therapeutic studies in Huntington’s disease: Behavioral testing and impact of diabetes mellitus. *Behav. Brain Res.* **126**, 185–195 (2001).
197. Carter, R. J. *et al.* Characterization of progressive motor deficits in mice transgenic for the human Huntington’s disease mutation. *J. Neurosci.* **19**, 3248–3257 (1999).
198. Lione, L. A. *et al.* Selective discrimination learning impairments in mice expressing the human Huntington’s disease mutation. *J. Neurosci.* **19**, 10428–10437 (1999).
199. Murphy, K. P. S. J. *et al.* Abnormal synaptic plasticity and impaired spatial cognition in mice transgenic for exon 1 of the human Huntington’s disease mutation. *J. Neurosci.* **20**, 5115–5123 (2000).
200. Giralt, A. *et al.* Increased PKA signaling disrupts recognition memory and spatial memory: Role in Huntington’s disease. *Hum. Mol. Genet.* **20**, 4232–4247 (2011).
201. Antunes, M. & Biala, G. The novel object recognition memory: Neurobiology, test procedure, and its modifications. *Cogn. Process.* **13**, 93–110 (2012).
202. Dodds, L., Chen, J., Berggren, K. & Fox, J. Characterization of striatal neuronal loss and atrophy in the R6/2 mouse model of Huntington’s Disease. *PLoS Curr.* **6** (2014).
203. Davies, S. W. *et al.* Formation of neuronal intranuclear inclusions underlies the neurological dysfunction in mice transgenic for the HD mutation. *Cell* **90**, 537–548 (1997).
204. Rattray, I. *et al.* Correlations of Behavioral Deficits with Brain Pathology Assessed through Longitudinal MRI and Histopathology in the R6/2 Mouse Model of HD. *PLoS One* **8**, (2013).
205. Meade, C. A. *et al.* Cellular localization and development of neuronal

- intranuclear inclusions in striatal and cortical neurons in R6/2 transgenic mice. *J. Comp. Neurol.* **449**, 241–269 (2002).
206. Cepeda, C. *et al.* Transient and progressive electrophysiological alterations in the corticostriatal pathway in a mouse model of Huntington's disease. *J. Neurosci.* **23**, 961–969 (2003).
207. Cepeda, C. *et al.* Increased GABAergic function in mouse models of Huntington's disease: Reversal by BDNF. *J. Neurosci. Res.* **78**, 855–867 (2004).
208. Farrer, L. A. *et al.* The normal Huntington disease (HD) allele, or a closely linked gene, influences age at onset of HD. *Am. J. Hum. Genet.* **53**, 125–130 (1993).
209. Djoussé, L. *et al.* Interaction of normal and expanded CAG repeat sizes influences age at onset of Huntington disease. *Am. J. Med. Genet.* **119 A**, 279–282 (2003).
210. Aziz, N. A. *et al.* Normal and mutant HTT interact to affect clinical severity and progression in Huntington disease. *Neurology* **73**, 1280–1285 (2009).
211. Heikkinen, T. *et al.* Characterization of neurophysiological and behavioral changes, MRI brain volumetry and 1H MRS in zQ175 knock-in mouse model of Huntington's Disease. *PLoS One* **7**, (2012).
212. Peng, Q. *et al.* Characterization of behavioral, neuropathological, brain metabolic and key molecular changes in zQ175 knock-in mouse model of Huntington's disease. *PLoS One* **11**, (2016).
213. Southwell, A. L. *et al.* An enhanced Q175 knock-in mouse model of Huntington disease with higher mutant huntingtin levels and accelerated disease phenotypes. *Hum. Mol. Genet.* **25**, 3654–3675 (2016).
214. Valenza, M. *et al.* Cholesterol-loaded nanoparticles ameliorate synaptic and cognitive function in Huntington's disease mice. *EMBO Mol. Med.* **7**, 1547–1564 (2015).
215. Mundargi, R. C., Babu, V. R., Rangaswamy, V., Patel, P. & Aminabhavi, T. M. Nano/micro technologies for delivering macromolecular therapeutics using poly(D,L-lactide-co-glycolide) and its derivatives. *J. Control. Release* **125**, 193–209 (2008).
216. Costantino, L. *et al.* Peptide-derivatized biodegradable nanoparticles able to cross the blood-brain barrier. *J. Control. Release* **108**, 84–96 (2005).
217. Tosi, G. *et al.* Targeting the central nervous system: In vivo experiments with peptide-derivatized nanoparticles loaded with Loperamide and Rhodamine-123. *J. Control. Release* **122**, 1–9 (2007).
218. Tosi, G. *et al.* Investigation on mechanisms of glycopeptide nanoparticles

- for drug delivery across the blood-brain barrier. *Nanomedicine* **6**, 423–436 (2011).
219. Tosi, G. *et al.* NIR-labeled nanoparticles engineered for brain targeting: In vivo optical imaging application and fluorescent microscopy evidences. *J. Neural Transm.* **118**, 145–153 (2011).
220. Birolini, G. *et al.* Striatal infusion of cholesterol promotes dose-dependent behavioral benefits and exerts disease-modifying effects in Huntington's disease mice. *EMBO Mol. Med.* **e12519** (2020).
221. Pardeshi, C. V. & Belgamwar, V. S. Direct nose to brain drug delivery via integrated nerve pathways bypassing the blood-brain barrier: An excellent platform for brain targeting. *Expert Opin. Drug Deliv.* **10**, 957–972 (2013).
222. Crowe, T. P., Greenlee, M. H. W., Kanthasamy, A. G. & Hsu, W. H. Mechanism of intranasal drug delivery directly to the brain. *Life Sci.* **195**, 44–52 (2018).
223. Selvaraj, K., Gowthamarajan, K. & Karri, V. V. S. R. Nose to brain transport pathways an overview: potential of nanostructured lipid carriers in nose to brain targeting. *Artif. Cells, Nanomedicine Biotechnol.* **46**, 2088–2095 (2018).
224. Passoni, A. *et al.* Efficacy of Cholesterol Nose-to-Brain Delivery for Brain Targeting in Huntington's Disease. *ACS Chem. Neurosci.* **11**, 367–372 (2020).
225. Bozzuto, G. & Molinari, A. Liposomes as nanomedical devices. *Int. J. Nanomedicine* **10**, 975–999 (2015).
226. Belletti, D. *et al.* Hybrid nanoparticles as a new technological approach to enhance the delivery of cholesterol into the brain. *Int. J. Pharm.* **543**, 300–310 (2018).
227. Tosi, G. *et al.* Conjugated poly(D,L-lactide-co-glycolide) for the preparation of in vivo detectable nanoparticles. *Biomaterials* **26**, 4189–4195 (2005).
228. Vilella, A. *et al.* Insight on the fate of CNS-targeted nanoparticles. Part I: Rab5-dependent cell-specific uptake and distribution. *J. Control. Release* **174**, 195–201 (2014).
229. Tosi, G. *et al.* Insight on the fate of CNS-targeted nanoparticles. Part II: Intercellular neuronal cell-to-cell transport. *J. Control. Release* **177**, 96–107 (2014).
230. Wüstner, D. *et al.* Quantitative assessment of sterol traffic in living cells by dual labeling with dehydroergosterol and BODIPY-cholesterol. *Chem. Phys. Lipids* **164**, 221–235 (2011).

231. Villeda, S. A. *et al.* The aging systemic milieu negatively regulates neurogenesis and cognitive function. *Nature*. **477**, 90–94 (2011).
232. Verlengia, G. *et al.* Engineered HSV vector achieves safe long-term transgene expression in the central nervous system. *Sci. Rep.* **7**, 1–11 (2017).
233. Miyagawa, Y. *et al.* Deletion of the Virion Host Shut-off Gene Enhances Neuronal-Selective Transgene Expression from an HSV Vector Lacking Functional IE Genes. *Mol. Ther. - Methods Clin. Dev.* **6**, 79–90 (2017).
234. Daya, S. & Berns, K. I. Gene therapy using adeno-associated virus vectors. *Clin. Microbiol. Rev.* **21**, 583–593 (2008).
235. Slezak, M. & Pfriege, F. W. New roles for astrocytes: regulation of CNS synaptogenesis. *Trends Neurosci.* **26**, 531–535 (2003).
236. Lim, K. L., Ng, X. H., Grace, L. G. Y. & Yao, T. P. Mitochondrial dynamics and Parkinson's disease: Focus on parkin. *Antioxidants Redox Signal.* **16**, 935–949 (2012).
237. Zhao, L. *et al.* Lanosterol reverses protein aggregation in cataracts. *Nature* **523**, 607–611 (2015).
238. Upadhyay, A., Amanullah, A., Mishra, R., Kumar, A. & Mishra, A. Lanosterol Suppresses the Aggregation and Cytotoxicity of Misfolded Proteins Linked with Neurodegenerative Diseases. *Mol. Neurobiol.* **55**, 1169–1182 (2018).
239. Crook, Z. R. & Housman, D. E. Dysregulation of dopamine receptor D2 as a sensitive measure for Huntington disease pathology in model mice. *Proc. Natl. Acad. Sci. U. S. A.* **109**, 7487–7492 (2012).
240. Valenza, M. & Cattaneo, E. Cholesterol dysfunction in neurodegenerative diseases: Is Huntington's disease in the list? *Prog. Neurobiol.* **80**, 165–176 (2006).
241. Araque, A. *et al.* Gliotransmitters travel in time and space. *Neuron* **81**, 728–739 (2014).
242. Adamsky, A. *et al.* Astrocytic Activation Generates De Novo Neuronal Potentiation and Memory Enhancement. *Cell* **174**, 59–71 (2018).
243. Frank, C., Giammarioli, A. M., Pepponi, R., Fiorentini, C. & Rufini, S. Cholesterol perturbing agents inhibit NMDA-dependent calcium influx in rat hippocampal primary culture. *FEBS Lett.* **566**, 25–29 (2004).
244. Frank, C. *et al.* Cholesterol depletion inhibits synaptic transmission and synaptic plasticity in rat hippocampus. *Exp. Neurol.* **212**, 407–414 (2008).
245. Lee, J. H. *et al.* Reinstating aberrant mTORC1 activity in Huntington's

- disease mice improves disease phenotypes. *Neuron* **85**, 303–315 (2015).
246. Ochteau, J. C. *et al.* An optical neuron-astrocyte proximity assay at synaptic distance scales. *Neuron* **98**, 49–66 (2018).
247. Gong, S. *et al.* A gene expression atlas of the central nervous system based on bacterial artificial chromosomes. *Nature* **425**, 917–925 (2003).
248. Paolone, G. *et al.* Personalized needles for microinjections in the rodent brain. *J. Vis. Exp.* **2018**, 1–8 (2018).
249. Lloyd, M. H. & Wolfensohn, S. E. Practical use of distress scoring systems in the application of humane endpoints. *Int. Conf. Hum. endpoints Anim. Exp. Biomed. Res.* **36**, 22–25 (1998).

6. Appendix

6.1 Contribution to published articles

6.1.1 Efficacy of Cholesterol Nose-to-Brain Delivery for Brain Targeting in Huntington's disease

Alice Passoni, Monica Favagrossa, Laura Colombo, Renzo Bagnati, Marco Gobbi, Luisa Diomede, **Giulia Birolini**, Eleonora Di Paolo, Marta Valenza, Elena Cattaneo, and Mario Salmona

ACS Chemical Neuroscience **2020** 11 (3), 367-372

DOI: 10.1021/acscemneuro.9b00581

The aim of this paper is to study the feasibility of intranasal delivery to supply cholesterol to the brain of a transgenic mouse model of Huntington's disease (e.g. R6/2 mice). Nose-to-brain delivery is a non-invasive strategy that is already used in humans to deliver drugs to the brain bypassing the blood-brain barrier. Here, we treated wild-type mice with a single/multiple intranasal dose of liposomes loaded with cholesterol and we measured the exogenous cholesterol by mass spectrometry in different brain areas and in mice plasma at different time point.

My contribution in this work included:

- maintenance of the R6/2 mice colony by mating, weaning and genotyping the animals;
- intranasal administration of liposomes together with E.D.P and L.C.;
- mice sacrifice through intra-cardiac perfusion with saline solution;
- collection of plasma, striatum, cortex and cerebellum to perform mass spectrometry analysis (Figures 1, 2 and 3).

6.1.2 Striatal infusion of cholesterol promotes a dose-dependent behavioral benefit and exerts disease-modifying effects in Huntington's disease mice

Giulia Birolini, Marta Valenza, Eleonora Di Paolo, Elena Vezzoli, Francesca Talpo, Claudia Maniezzi, Claudio Caccia, Valerio Leoni, Vittoria D. Bocchi, Paola Conforti, Elisa Sogne, Lara Petricca, Cristina Cariulo, Margherita Verani, Andrea Caricasole, Andrea Falqui, Gerardo Biella, Elena Cattaneo

EMBO Mol Med (accepted)

DOI: 10.15252/emmm.202012519

The aim of this paper is to identify an appropriate regimen to deliver cholesterol to brain of HD mice to recover HD-related parameters. Accordingly, we used osmotic-minipumps to infuse three escalating doses of cholesterol directly into the striatum of HD mice in a continuous and rate-controlled manner and we performed behavioral, functional and biochemical assays to study HD phenotypes.

My contribution in this work included:

- maintenance of the R6/2 mice colony by mating, weaning and genotyping the animals;
- surgical implantation of osmotic minipumps together with E.D.P.;
- behavioral analysis including rotarod test, novel object recognition test and activity cage test together with E.D.P. (Figure 1);
- mice sacrifice to perform subsequent analysis;
- preparation of brain slices to perform immuno-histochemical experiments;
- IHC for SREBP2, muHTT, p62 and LAMP1 (Figures 4, 5 and 6);
- acquisition of all the confocal images in the paper (SREBP2 translocation analysis, muHTT aggregation analysis, p62/LAMP 1 analysis) with relative quantification (Figures 4, 5 and 6).

6.2 Contribution to *in progress* articles

6.2.1 SREBP2 delivery to striatal astrocytes enhances brain cholesterol biosynthesis defect and ameliorates pathological features in Huntington's disease

Giulia Birolini, Gianluca Verlengia, Francesca Talpo, Claudia Maniezzi, Lorena Zentilin, Mauro Giacca, Paola Conforti, Claudio Caccia, Valerio Leoni, Franco Taroni, Gerardo Biella, Michele Simonato, Elena Cattaneo, Marta Valenza
Manuscript ready to be submitted

The aim of this paper is to demonstrate *in vivo* the importance of SREBP2 for brain cholesterol synthesis. Accordingly, we over-expressed the N-terminal active fragment of hSREBP2 in striatal astrocytes of R6/2 mice using a recombinant adeno-associated virus 2/5 (AAV2/5) to enhance *in vivo* endogenous cholesterol biosynthesis.

My contribution in this work included:

- maintenance of the R6/2 mice colony by mating, weaning and genotyping the animals;
- intra-striatal surgical infection of mice with AAV2/5 and HSV;
- behavioral analysis including rotarod test, novel object recognition test, activity cage test, paw clasp test and grip strength test (Figure 5) together with M.V.;
- mice sacrifice and tissues isolation for subsequent experiments;
- brain slices preparation to performed immuno-histochemical experiments and tissue clarification;
- IHC for viral spread and tropism and muHTT aggregates (Figures 1 and 4);
- acquisition of all the confocal images in the paper (viral spread and tropism, muHTT aggregates analysis) with relative quantification (Figure 1 and 4);
- preparation of synaptosomes from cortico-striatal tissues and western blot analysis to study the level of pre and postsynaptic proteins (Figure 2).

6.2.2 Brain-targeted hybrid nanoparticles boost cholesterol delivery to the central nervous system and rescues behavioral phenotypes in Huntington's disease

Giulia Birolini, Ilaria Ottonelli, Jason T. Duskey, Alice Passoni, Monica Favagrossa, Claudio Caccia, Valerio Leoni, Laura Colombo, Mauro Bombaci, Renzo Bagnati, Franco Taroni, Maria Angela Vandelli, Flavio Forni, Barbara Ruozi, Mario Salmona, Giovanni Tosi, Marta Valenza, Elena Cattaneo
Manuscript ready to be submitted

The aim of this paper is to characterize *in vivo* g7-NPs-chol_2.0 and compare them to g7-NPs-chol_1.0 used in Valenza *et al. EMBO Mol Med*, 2015. First of all, nanoparticles distribution and cholesterol release have been studied. Then, we evaluated the effect of the delivered cholesterol on the behavior of HD mice and on the endogenous synthesis of cholesterol in their brain. Finally, we checked central and systemic inflammation following chronic treatment.

My contribution in this work included:

- maintenance of the R6/2 mice colony by mating, weaning and genotyping the animals;
- intraperitoneal injection of nanoparticles in R6/2 mice;
- behavioral analysis including rotarod test, novel object recognition test, activity cage test, paw clasp test and grip strength test (Figure 5) together with M.V.;
- mice sacrifice and tissues isolation for subsequent experiments;
- brain slices preparation to performed immuno-histochemical experiments;
- IHC for nanoparticles biodistribution and cholesterol release (Figures 1 and 2);
- acquisition of all the confocal images in the paper (nanoparticles distribution and cholesterol release) with relative quantification (Figures 1 and 2);
- preparation of samples (striatum, cortex, liver, and plasma) for Bioplex analysis and relative quantification together with M.V. (Figure 6).

Efficacy of Cholesterol Nose-to-Brain Delivery for Brain Targeting in Huntington's Disease

Alice Passoni,^{†,‡,§} Monica Favagrossa,^{†,‡,§} Laura Colombo,[†] Renzo Bagnati,^{†,§} Marco Gobbi,[†] Luisa Diomede,^{†,§} Giulia Birolini,^{‡,§} Eleonora Di Paolo,^{‡,§} Marta Valenza,^{‡,§} Elena Cattaneo,^{‡,§} and Mario Salmons^{*,†,§}

[†]Istituto di Ricerche Farmacologiche Mario Negri IRCCS, via Mario Negri 2, 20156 Milan, Italy

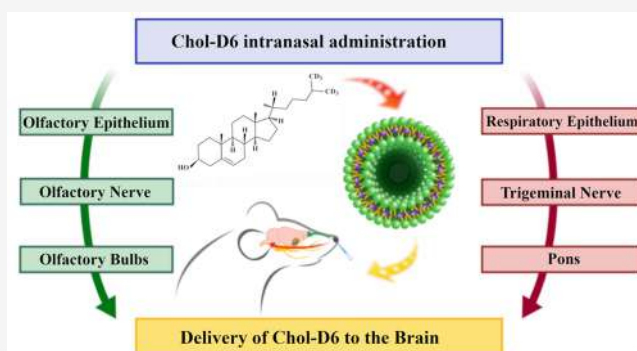
[‡]Department of Biosciences, University of Milan, via G. Celoria 26, 20133, Milan, Italy

[§]Istituto Nazionale di Genetica Molecolare "Romeo ed Enrica Invernizzi," via F. Sforza 35, 20122, Milan, Italy

Supporting Information

ABSTRACT: The current pharmacological treatment of Huntington's disease (HD) is palliative, and therapies to restore functions in patients are needed. One of the pathways affected in HD involves brain cholesterol (Chol) synthesis, which is essential for optimal synaptic transmission. Recently, it was reported that in a HD mouse model, the delivery of exogenous Chol to the brain with brain-permeable nanoparticles protected animals from cognitive decline and rescued synaptic communication, indicating Chol as a therapeutic candidate. We examined whether nose-to-brain delivery, already used in human therapy, could be an alternative, noninvasive strategy to deliver Chol to the adult brain and, in the future, replenish Chol in the HD brain. We gave wild-type (WT) mice a single intranasal (IN) dose of liposomes loaded with deuterium-labeled cholesterol (Chol-D6, to distinguish and quantify the exogenous cholesterol from the native one) (200 μ g Chol-D6/dose). After different intervals, Chol-D6 levels, determined by LC-MS in plasma, striatum, cortex, and cerebellum, reached a steady-state concentration of 0.400 ng/mg between 24 and 72 h. A subsequent acute study confirmed the kinetic profiles of Chol-D6 in all tissues, indicating correspondence between the dose (two doses of 200 μ g Chol-D6/dose) and the calculated brain area concentration (0.660 ng/mg). Finally, in WT mice given repeated IN doses, the average Chol-D6 level after 24 h was about 1.5 ng/mg in all brain areas. Our data indicate the effectiveness of IN Chol-loaded liposomes to deliver Chol in different brain regions, opening the way to future investigations in HD mice.

KEYWORDS: Huntington's disease, brain cholesterol, nose-to-brain delivery, intranasal administration, LC-MS analysis, liposomes



1. INTRODUCTION

The brain is the most cholesterol-rich organ as more than 70% of cholesterol (Chol) is located in myelin sheaths, and the remainder is a structural and functional component of glial and neuronal membranes. Chol is located in specific membrane microdomains, known as lipid rafts, that initiate, propagate, and maintain signal transduction.¹ In the adult brain, Chol levels are maintained by local de novo synthesis because the blood-brain barrier (BBB) prevents its uptake from the circulation.² Synaptic transmission is sensitive to newly synthesized Chol, so changes in Chol biosynthesis affect vesicle formation, recycling, and fusion, as well as the activity of neurotransmitter receptors.^{3–5}

Several diseases have been linked to dyshomeostasis of brain Chol production and degradation, including Huntington's disease (HD). HD is a dominantly inherited neurodegenerative disorder caused by an abnormal expansion of cytosine-adenosine-guanine (CAG) repeats in the first exon of the IT15

gene, leading to the formation of a pathological polyQ tract (Q > 40) in huntingtin (HTT) protein (The Huntington's Disease Collaborative Research Group, 1993). As a consequence, neurons become dysfunctional and eventually die, leading to choreiform movements, cognitive decline, and psychiatric disturbance.^{6–8} Different molecular and cellular dysfunctions have been reported in HD cells and mouse models and in human post-mortem material,^{9,10} including alterations of brain Chol biosynthesis.^{11,12} Chol precursors such as lanosterol, lathosterol, and desmosterol and the enzymatic activity of 3-hydroxy-3-methylglutaryl-coenzyme A reductase (HMGCR) were found downregulated in the brain of several HD animal models, already in the presymptomatic stage of the disease, leading to a significantly lower Chol content at later

Received: October 28, 2019

Accepted: December 20, 2019

Published: December 20, 2019

times.^{13–15} Chol treatment ameliorates neurite outgrowth defects in HD neurons *in vitro*¹⁶ and brain-permeable nanoparticles loaded with Chol prevent cognitive decline and rescue synaptic dysfunction in HD mice,¹⁷ indicating a relationship between neuronal function and exogenous Chol.

Targeting the brain with drugs or molecules that do not pass the BBB (such as Chol) has always been challenging, and noninvasive strategies are attractive. Most treatments for central nervous system (CNS) disorders employ peripheral drug administration, which is limited by the difficulty of drug access to the CNS from the blood. Moreover, drugs given by these routes incur the first-pass metabolism and systemic clearance, which reduce their bioavailability.¹⁸

An alternative strategy for targeting CNS is nose-to-brain delivery, which can overcome the BBB. The neuroepithelium of the olfactory region is the only part of the body where the peripheral environment is in direct contact with the brain.¹⁹ Olfactory and trigeminal nerve pathways mostly mediate drug transport from the nasal cavity to the CNS. Through the olfactory nerve pathway, a drug crosses the cribriform plate and reaches the olfactory bulbs and the deeper part of the brain. Meanwhile, through the trigeminal nerve pathway, the drug is transported mostly to the pons and cerebrum, and to a lesser extent to the frontal and olfactory brain. Pathways involving vasculature, cerebrospinal fluid and lymphatic system all enrich the transport of molecules from the nasal cavity to the CNS.^{20,21}

Thus, the aim of this work was to explore the potential of intranasal (IN) Chol-D6-loaded liposomes as a noninvasive strategy for Chol delivery into the HD brain. We report quantifiable levels of Chol-D6 after acute and repeated IN treatments. We also found that Chol-D6 distributes evenly and accumulates in the brain of WT and HD mice, paving the way for further preclinical investigations. In addition, to quantify the brain distribution of exogenous Chol, we developed a liquid chromatography mass spectrometry (LC-MS)-based method, validated according to the European Medicine Agency (EMA) guidelines,²² in plasma and brain.

2. RESULTS AND DISCUSSION

2.1. Development and Validation of the LC-MS Method.

Validation data are reported in detail in the [Supplementary Results](#).

2.2. Acute Treatments of 8-Week-Old WT and HD Mice.

To assess the efficacy of IN delivery of Chol into the brain, we initially gave 8-week-old WT mice an acute dose of Chol-D6-loaded liposomes (200 $\mu\text{g}/\text{mouse}$); animals were then euthanized after 1, 3, 6, 24, 48, and 72 h (3 animals/time-point). Chol-D6 concentrations were measured in plasma and three brain areas (Figure 1). Plasma concentrations reached a maximum of 2417 ± 313 ng/mL (mean \pm SD) after 24 h, declining to 839 ± 76 ng/mL (mean \pm SD) at 72 h. In the brain areas, Chol-D6 levels rose in the first 24 h but, unlike in plasma, did not decline, and they remained stable until 72 h. These data suggest a slow elimination rate in the brain.

We then ran an acute study to confirm the passage of the BBB and assess the relationship between administered dose and concentrations in plasma and different brain areas in WT and HD mice. Eight-week-old WT and HD mice were treated with two IN doses of 200 $\mu\text{g}/\text{mouse}$ of Chol-D6, 5 h apart (5 mice/time point/genotype), and were euthanized 3, 24, 48, and 72 h after the second dose. Plasma concentrations reached a maximum of 4350 ± 1207 ng/mL (mean \pm SD) and $4760 \pm$

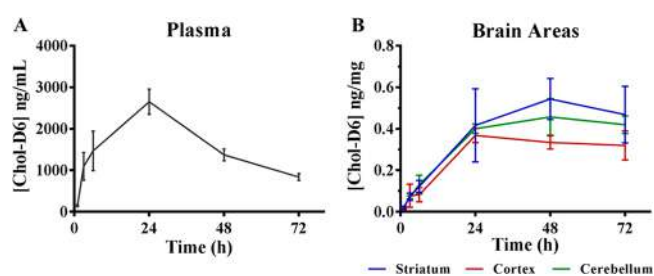


Figure 1. Chol-D6 levels in plasma (gray) (A), striatum (blue), cortex (red) and cerebellum (green) (B) of WT mice after single intranasal doses (connecting lines with error bars, mean \pm SD; $n = 3/\text{time point}$).

703 ng/mL (mean \pm SD) after 24 h in HD and WT mice, respectively. Plasma levels declined with similar kinetic profiles in HD and WT mice to 1698 ± 295 ng/mL (mean \pm SD; $n = 7$) after 72 h. There were no significant differences between WT and HD mice since Chol-D6 had the same time-course profiles (Figure 2).

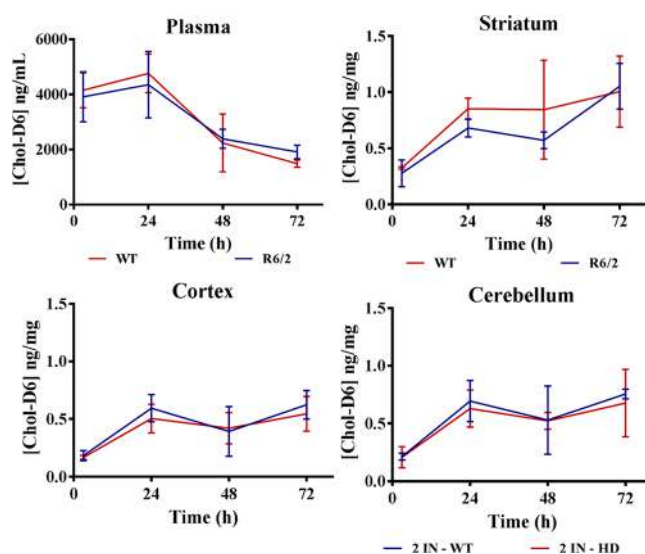


Figure 2. Chol-D6 levels in plasma (A), striatum (B), cortex (C), and cerebellum (D) of WT and HD mice after two intranasal doses, each with 200 $\mu\text{g}/\text{mouse}$, 5 h apart (means \pm SD; $n = 5/\text{time-point/genotype}$; blue, WT; red, HD).

Finally, we compared Chol-D6 levels at 24 h for single and double IN doses in plasma and brain areas of WT mice. Chol-D6 levels rose at least 61% after two IN doses, suggesting a linear relationship with the dose. Interestingly, Chol-D6 levels in the striatum rose 105% after two doses, confirming the effectiveness of nose-to-brain delivery to the target tissue of HD (Table 1).

2.3. Repeated Treatment in WT Mice.

To assess the accumulation of Chol-D6 in the brain after multiple IN doses, we repeated the treatments of WT mice at 8 weeks of age with Chol-D6-loaded liposomes (200 $\mu\text{g}/\text{dose}$). Chol-D6 levels in the striatum, cortex, and cerebellum were markedly higher after a single dose, indicating accumulation in the brain (Figure 3). With this schedule, Chol-D6 reached at least 1.5 ng/mg tissue in all the brain areas. Statistical analysis showed no significant differences in Chol-D6 levels in the brain areas after repeated dosing, confirming homogeneous distribution of Chol-D6 in

Table 1. Chol-D6 Levels 24 h after the Last IN Dose in WT Mice Given One or Two IN Doses

tissues	1 IN	2 IN	% increase 2 IN over 1 IN
plasma (ng/mL)	2650 ± 305	4760 ± 703	79.6
striatum (ng/mg)	0.416 ± 0.176	0.853 ± 0.095	105.0
cortex (ng/mg)	0.368 ± 0.034	0.594 ± 0.118	61.4
cerebellum (ng/mg)	0.400 ± 0.022	0.694 ± 0.179	73.5

^a1 IN = one dose, 200 μg/dose; 2 IN = two doses, 5 h apart, 200 μg/dose; mean ± SD.

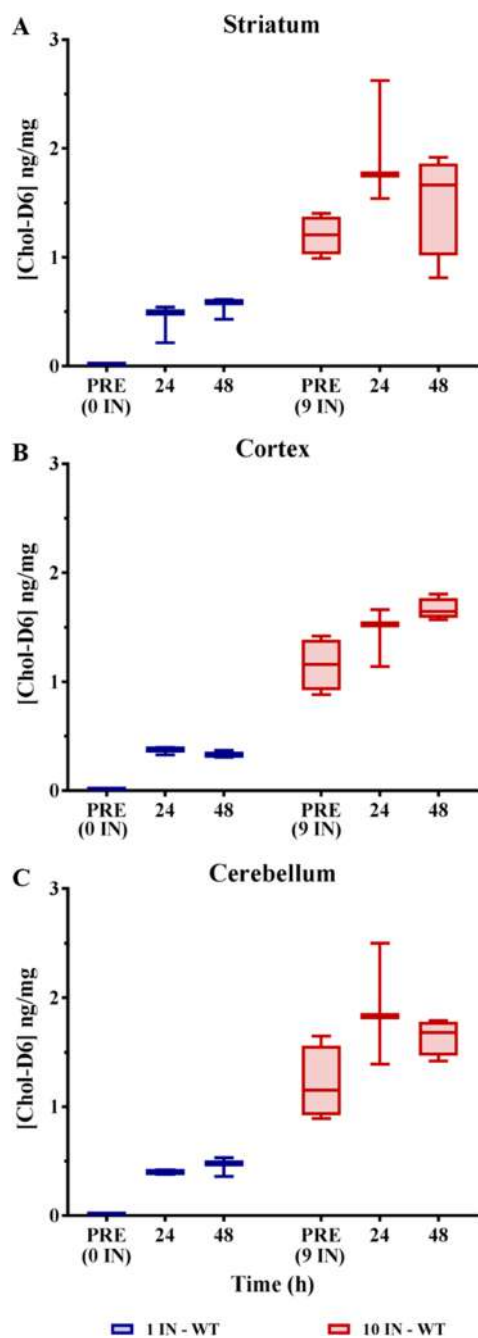


Figure 3. Chol-D6 levels in the striatum (A), cortex (B) and cerebellum (C) in WT mice after acute or repeated intranasal treatments. WT mice were treated every 2 days for 19 days (10 IN). Two days after the ninth dose, four mice/genotype were euthanized before the tenth treatment (PRE 9 IN). The remaining mice received the tenth IN and were euthanized at 24 and 48 h after the treatment.

the whole brain, suggesting both olfactory and trigeminal pathways are involved. The connections between the nasal cavity and the CNS through olfactory and trigeminal neurons have already been described.^{19,21,23} From the nasal olfactory epithelium, drugs are taken up into neuronal cells and transported to the olfactory bulb and the cerebrospinal fluid through the olfactory nerve pathways. The trigeminal nerve innervates both the olfactory and respiratory epithelium and enters the CNS in the pons, leading the distribution of drugs in the rostral brain.^{19,24} These two pathways permit the distribution of drugs to all brain areas. Our observations confirm the efficacy of nose-to-brain Chol delivery as a potential noninvasive approach to increase Chol availability in the HD brain.

3. CONCLUSIONS

To develop a new therapeutic strategy for HD based on Chol delivery to the brain, we set up an experimental approach to investigate the efficacy of exogenous IN Chol. We based our assumption on evidence that Chol biosynthesis is reduced in HD mouse brains^{11,13–15} and that exogenous Chol can rescue the HD phenotypes (ref 17 and unpublished data). Importantly, nose-to-brain delivery is safe and noninvasive and avoids hepatic first-pass metabolism. The nasal route for delivery of drugs that otherwise could not cross the BBB could be beneficial if translatable to clinical practice, and there are already examples in the literature.^{25–28}

In the present study, we also developed and validated according to EMA guidelines, a new LC-MS method to quantify the levels of exogenous Chol-D6 in brain areas and plasma after single or repeated IN doses. Chol-D6 reached measurable levels in the brain and persisted at least 72 h thanks to its slow elimination rate (Figure 1). After two doses HD and WT mice did not present any significant differences in Chol-D6 distribution and accumulation. The final comparison of the two acute treatments showed increases in Chol-D6 in plasma and the brain areas, from 61% in cortex up to 105% in the striatum. These results confirmed the effectiveness of nose-to-brain delivery. The Chol-D6 levels rose most in the striatum, the target tissue of HD (Table 1). Finally, Chol-D6 distributed and accumulated without differences after 10 IN doses in striatum, cortex, and cerebellum (Figure 3), indicating the involvement of both olfactory and trigeminal pathways.

The experimental design in this initial approach provides a detailed view of the effectiveness of the nose-to-brain delivery of Chol. It could also help lay the basis for further preclinical studies for evaluating the therapeutic potential of this approach to supply Chol to neurons affected in HD.

4. MATERIALS AND METHODS

4.1. Standard and Chemicals. Deuterated cholesterol (Chol-D6) (isotopic purity: 97 atom % D), phosphatidylcholine (PC), and β-sitosterol were obtained from Sigma-Aldrich (St Louis, MO, U.S.A.). LC-MS grade acetonitrile and formic acid were from Carlo

Erba, Milan, Italy. LC-MS grade deionized water was obtained from Milli-Ro 60 Water System, Millipore, Milford, MA, U.S.A. Chol-D6 and β -sitosterol, used as the internal standard (IS), were prepared as stock solutions in methanol (MeOH) at 1 mg/mL. The Chol-D6 stock solution was diluted in MeOH to obtain a series of seven working solutions for the construction of calibration curves, validation and sample analysis. The IS stock solution was diluted to 5 μ g/mL in the same organic solvent. All solutions were stored at -20 °C until use.

4.2. Liposomes. Chol-D6 was entrapped in oligolamellar, 280–300 nm-wide liposomes, following the dehydration–rehydration method.^{29,30} Briefly, Chol-D6 and PC were dissolved in chloroform at a 1:1 molar ratio. After solvent evaporation, the lipid film was rehydrated with phosphate buffer solution (PBS) and ultracentrifuged at 100 000g for 35 min at 4 °C to separate residual lipids. Liposomes were resuspended with 10 mM phosphate-buffered saline, pH 7.4. The concentration of Chol-D6 entrapped in liposomes was determined by HPLC (System Gold instrument – Beckman) equipped with an Eco Cart-LiChrospher 60 RP-select B column (125 \times 3 mm, particle size 5 μ m, pore size 60 Å, Merck) at 214 nm. Separation was done with isocratic elution at 100% methanol:isopropanol:NH₄OH (70%:30%, 5 mM) for 12 min. The flow rate was 0.6 mL/min. Entrapment efficacy was $\pm 90\%$, and liposomes were diluted to a final Chol-D6 concentration of 5.6 mg/mL.

4.3. Animal Model and Treatment Schedules. We used an R6/2 colony generated to overexpress the first exon of the human mutant huntingtin gene with approximately 144–150 CAG repeats. The R6/2 line was genotyped by polymerase chain reaction (PCR) on DNA from tail samples at weaning.⁵¹

The IRFMN adheres to the principles set out in the following laws, regulations, and policies governing the care and use of laboratory animals: Italian Governing Law (D.lgs 26/2014; Authorisation n.19/2008-A issued March 6, 2008 by Ministry of Health); Mario Negri Institutional Regulations and Policies providing internal authorization for persons conducting animal experiments (Quality Management System Certificate – UNI EN ISO 9001:2015 – Reg. No. 6121); the NIH Guide for the Care and Use of Laboratory Animals (2011 edition) and EU directives and guidelines (EEC Council Directive 2010/63/UE).

Liposomes were administered to mice by applying 6 μ L of a 5.6 mg/mL solution three times to the inner surface of each nostril for a total of 36 μ L, corresponding to a final dose of 200 μ g of Chol-D6/mouse.³² For the first acute studies, 8-week-old wild-type (WT) mice were euthanized 1, 3, 6, 24, 48, and 72 h after a single IN dose (3 mice/time point). For the acute study, 8-week-old WT and R6/2 mice were given two doses of 200 μ g/mouse of Chol-D6, 5 h apart (5 mice/time point/genotype). Mice were euthanized 3, 24, 48, and 72 h from the second IN treatment. For repeated treatments, 8-week-old WT mice received 9 or 10 IN doses, once every 2 days (4 mice/time point). One group of animals was euthanized 2 days after the ninth IN treatment, while the others received the tenth IN dose and were euthanized 24 and 48 h later. Blood samples were collected with the anticoagulant K₃EDTA, and plasma samples were obtained by centrifugation at 2000g for 15 min. Brains were immediately removed and striatum, cortex, and cerebellum were collected separately. All samples were stored at -80 °C until LC-MS analysis.

4.4. LC-MS. Chol-D6 levels were determined using a 1200 Series HPLC system (Agilent Technologies, Santa Clara, CA, U.S.A.) interfaced to an API 5500 triple quadrupole mass spectrometer (Sciex, Thornhill, Ontario, Canada). The mass spectrometer was equipped with an atmospheric pressure chemical ionization (APCI) source operating in positive ion and selected reaction monitoring (SRM) mode to measure the product ions obtained in a collision cell from the protonated $[M - H_2O]^+$ ions of the analytes. The transitions identified during the optimization of the method were m/z 375.3–152.1 (quantification transition) and m/z 375.3–167.1 (qualification transition) for Chol-D6; m/z 397.3–147.1 (quantification transition) and m/z 397.3–161.1 (qualification transition) for β -sitosterol as IS. The ion source settings were as follows: nebulized current (NC) 3; curtain gas (CUR) 30; collision gas (CAD) 7; source temperature 400

°C; ion source gas 1 (GS1) 60 and gas 2 (GS2) 30. Chol-D6 and β -sitosterol were separated on a Gemini C18 column (50 \times 2 mm; 5 μ m particle size), using an isocratic gradient in methanol at 35 °C.

4.4.1. Sample Preparation. Plasma. Fifty microliters of plasma was diluted with 200 μ L of ethanol containing 200 ng of IS. Samples were vortexed and centrifuged at 13 200 rpm for 15 min; 4 μ L aliquots of the supernatants were injected directly into the LC-MS system.

Striatum, Cortex, and Cerebellum. Forty milligrams of each brain area was homogenized in 1 mL of ethanol/water 4:1 (v/v), containing 500 ng of IS. Homogenates were centrifuged for 15 min at 13 200 rpm at 4 °C, and the supernatants were injected into the LC-MS apparatus.

4.4.2. Validation. The LC-MS method was validated in mouse plasma and brain tissue following EMA guidelines²² (EMA). Accuracy was determined by expressing the calculated concentration as a percentage of the nominal concentration. Accuracy had to be within 15% of the nominal value for each concentration ($\pm 20\%$ of the nominal value for the lower limit of quantification (LLOQ) as an exception); the precision, expressed by the CV (%), had not to exceed 15% for all concentrations, except 20% for the LLOQ. A freshly prepared calibration curve was analyzed during each validation run.

Calibration Curves. All calibration curves during the validation included one zero point and six calibration points at the concentrations of 50, 100, 250, 500, 1000, 2500, and 5000 ng/mL and 0.030, 0.100, 0.300, 1.00, 3.00, and 10.0 ng/mg of Chol-D6 respectively for plasma and brain samples. The IS concentration was 100 ng/mL in plasma and 0.010 ng/mg in brain homogenates. Responses, expressed as the peak area ratio of the analyte to the IS, were plotted against the corresponding Chol-D6 concentration, and the data were fitted with a linear regression curve. The quality of calibration curves was evaluated from the determination coefficient (r^2) and by comparing the back-calculated concentrations of calibrators with the corresponding nominal values.

Carry-over. The carry-over of the analytical instrumentation was checked by injecting Chol-D6 at the highest concentration (upper limit of quantitation, ULOQ), followed by repeated injections of blank samples. The carry-over was considered absent if the Chol-D6 signal measured in the blank samples immediately after the ULOQ was $< 20\%$ of the LLOQ signal.

Recovery. Recovery was determined by comparing the peak area of Chol-D6 spiked to plasma and brain samples before extraction (C) and the peak area of the analyte spiked to the same samples after extraction (A). The same method was used to calculate the recovery of IS, as follows $\% \text{ Rec} = C/A \times 100$

4.5. Statistical Analysis. Data were analyzed by ANOVA multiple comparisons and Tukey's tests, using GraphPad v7 (GraphPad Software Inc.). The limit of statistical significance was set at $p < 0.05$.

■ ASSOCIATED CONTENT

📄 Supporting Information

The Supporting Information is available free of charge at <https://pubs.acs.org/doi/10.1021/acschemneuro.9b00581>.

Supporting material, including tables and figures, describes in detail the validation of the analytical method in plasma and brain samples (PDF)

■ AUTHOR INFORMATION

Corresponding Author

*E-mail: mario.salmona@marionegri.it

ORCID

Alice Passoni: 0000-0001-6003-5932

Renzo Bagnati: 0000-0002-6535-2686

Luisa Diomede: 0000-0002-2258-0531

Mario Salmona: 0000-0002-9098-9873

Author Contributions

#A.P. and M.F. contributed equally to this paper. M.S., L.C., and E.C. designed the experiments and supervised the scientific work; A.P. and R.B. set up the analytical method, designed the validation experiments and analyzed data; M.F. and L.D. prepared Chol-D6 loaded liposomes; M.V. and G.B. maintained and genotyped the R6/2 colony and contributed to design the *in vivo* experiments; M.F., L.C., E.D.P., and G.B. conducted the *in vivo* experiments; A.P. and M.F. prepared samples for LC-MS analysis and wrote the manuscript; M.G. revised the statistical analysis. All authors reviewed the manuscript.

Notes

The authors declare no competing financial interest.

ACKNOWLEDGMENTS

This paper was supported by a grant of the Italian Ministry of Health entitled “Innovative therapeutic strategy targeting neurons with cholesterol in Huntington disease: from preclinical studies to clinical trial readiness” (RF-2016-02361928), and partially by Telethon (GGP17102).

ABBREVIATIONS

Chol-D6, deuterium-labeled cholesterol
IN, intranasal
HMGCR, 3-hydroxy-3-methylglutaryl-coenzyme A reductase
CNS, central nervous system
LC-MS, liquid chromatography–mass spectrometry
HTT, Huntingtin
HD, Huntington’s disease
BBB, blood-brain barrier
EMA, European Medicine Agency
WT, wild type
LLOQ, lower limit of quantitation
ULOQ, upper limit of quantitation
MeOH, methanol
PBS, phosphate buffer solution

REFERENCES

- (1) Lingwood, D., and Simons, K. (2010) Lipid Rafts as a Membrane-Organizing Principle. *Science* 327 (5961), 46–50.
- (2) Bjorkhem, I., and Meaney, S. (2004) Brain Cholesterol: Long Secret Life behind a Barrier. *Arterioscler., Thromb., Vasc. Biol.* 24 (5), 806–815.
- (3) Pfrieger, F. W. (2003) Role of Cholesterol in Synapse Formation and Function. *Biochim. Biophys. Acta, Biomembr.* 1610 (2), 271–280.
- (4) Orth, M., and Bellosta, S. (2012) Cholesterol: Its Regulation and Role in Central Nervous System Disorders. *Cholesterol* 2012, 1.
- (5) Zhang, J., and Liu, Q. (2015) Cholesterol Metabolism and Homeostasis in the Brain. *Protein Cell* 6 (4), 254–264.
- (6) Bohanna, I., Georgiou-Karistianis, N., Hannan, A. J., and Egan, G. F. (2008) Magnetic Resonance Imaging as an Approach towards Identifying Neuropathological Biomarkers for Huntington’s Disease. *Brain Res. Rev.* 58 (1), 209–225.
- (7) Rosas, H. D., Salat, D. H., Lee, S. Y., Zaleta, A. K., Pappu, V., Fischl, B., Greve, D., Hevelone, N., and Hersch, S. M. (2008) Cerebral Cortex and the Clinical Expression of Huntington’s Disease: Complexity and Heterogeneity. *Brain* 131 (4), 1057–1068.
- (8) Waldvogel, H. J., Kim, E. H., Tippett, L. J., Vonsattel, J.-P. G., and Faull, R. L. (2014) The Neuropathology of Huntington’s Disease. *Curr. Top. Behav. Neurosci.* 22, 33–80.

- (9) Zuccato, C., Valenza, M., and Cattaneo, E. (2010) Molecular Mechanisms and Potential Therapeutic Targets in Huntington’s Disease. *Physiol. Rev.* 90 (3), 905–981.

- (10) McColgan, P., and Tabrizi, S. J. (2018) Huntington’s Disease: A Clinical Review. *Eur. J. Neurol.* 25 (1), 24–34.

- (11) Valenza, M., Leoni, V., Karasinska, J. M., Petricca, L., Fan, J., Carroll, J., Pouladi, M. A., Fossale, E., Nguyen, H. P., Riess, O., et al. (2010) Cholesterol Defect Is Marked across Multiple Rodent Models of Huntington’s Disease and Is Manifest in Astrocytes. *J. Neurosci.* 30 (32), 10844–10850.

- (12) Karasinska, J. M., and Hayden, M. R. (2011) Cholesterol Metabolism in Huntington Disease. *Nat. Rev. Neurol.* 7 (10), 561–572.

- (13) Valenza, M., Carroll, J. B., Leoni, V., Bertram, L. N., Björkhem, I., Singaraja, R. R., Di Donato, S., Lutjohann, D., Hayden, M. R., and Cattaneo, E. (2007) Cholesterol Biosynthesis Pathway Is Disturbed in YAC128 Mice and Is Modulated by Huntingtin Mutation. *Hum. Mol. Genet.* 16 (18), 2187–2198.

- (14) Valenza, M., Leoni, V., Tarditi, A., Mariotti, C., Björkhem, I., Di Donato, S., and Cattaneo, E. (2007) Progressive Dysfunction of the Cholesterol Biosynthesis Pathway in the R6/2 Mouse Model of Huntington’s Disease. *Neurobiol. Dis.* 28 (1), 133–142.

- (15) Shankaran, M., Di Paolo, E., Leoni, V., Caccia, C., Ferrari Bardile, C., Mohammed, H., Di Donato, S., Kwak, S., Marchionini, D., Turner, S., et al. (2017) Early and Brain Region-Specific Decrease of de Novo Cholesterol Biosynthesis in Huntington’s Disease: A Cross-Validation Study in Q175 Knock-in Mice. *Neurobiol. Dis.* 98, 66–76.

- (16) Valenza, M., Marullo, M., Di Paolo, E., Cesana, E., Zuccato, C., Biella, G., and Cattaneo, E. (2015) Disruption of Astrocyte-Neuron Cholesterol Cross Talk Affects Neuronal Function in Huntington’s Disease. *Cell Death Differ.* 22 (4), 690–702.

- (17) Valenza, M., Chen, J. Y., Di Paolo, E., Ruozi, B., Belletti, D., Ferrari Bardile, C., Leoni, V., Caccia, C., Brill, E., Di Donato, S., et al. (2015) Cholesterol-Loaded Nanoparticles Ameliorate Synaptic and Cognitive Function in Huntington’s Disease Mice. *EMBO Mol. Med.* 7 (12), 1547–1564.

- (18) Agrawal, M., Saraf, S., Saraf, S., Antimisiaris, S. G., Chougule, M. B., Shoye, S. A., and Alexander, A. (2018) Nose-to-Brain Drug Delivery: An Update on Clinical Challenges and Progress towards Approval of Anti-Alzheimer Drugs. *J. Controlled Release* 281 (May), 139–177.

- (19) Selvaraj, K., Gowthamarajan, K., and Karri, V. V. S. R. (2017) Nose to Brain Transport Pathways an Overview: Potential of Nanostructured Lipid Carriers in Nose to Brain Targeting. *Artif. Cells, Nanomed., Biotechnol.* 46 (8), 2088–2095.

- (20) Crowe, T. P., Greenlee, M. H. W., Kanthasamy, A. G., and Hsu, W. H. (2018) Mechanism of Intranasal Drug Delivery Directly to the Brain. *Life Sci.* 195 (September 2017), 44–52.

- (21) Pardeshi, C. V., and Belgamwar, V. S. (2013) Direct Nose to Brain Drug Delivery via Integrated Nerve Pathways Bypassing the Blood–Brain Barrier: An Excellent Platform for Brain Targeting. *Expert Opin. Drug Delivery* 10 (7), 957–972.

- (22) EMEA (2015) Guideline on Bioanalytical Method Validation. *Eur. Med. Agency. Comm. Med. Prod. Hum. Use* 44 (July 2011), 1–23.

- (23) Khan, A. R., Liu, M., Khan, M. W., and Zhai, G. (2017) Progress in Brain Targeting Drug Delivery System by Nasal Route. *J. Controlled Release* 268, 364–389.

- (24) Dhuria, S. V., Hanson, L. R., and Frey, W. H. (2010) Intranasal Delivery to the Central Nervous System: Mechanisms and Experimental Considerations. *J. Pharm. Sci.* 99 (4), 1654–63.

- (25) Claxton, A., Baker, L. D., Hanson, A., Trittschuh, E. H., Cholerton, B., Morgan, A., Callaghan, M., Ar buckle, M., Behl, C., and Craft, S. (2015) Long-Acting Intranasal Insulin Detemir Improves Cognition for Adults with Mild Cognitive Impairment or Early-Stage Alzheimer’s Disease Dementia. *J. Alzheimer’s Dis.* 44 (3), 897–906.

- (26) Mischley, L. K., Conley, K. E., Shankland, E. G., Kavanagh, T. J., Rosenfeld, M. E., Duda, J. E., White, C. C., Wilbur, T. K., De La Torre, P. U., and Padowski, J. M. (2016) Central Nervous System

Uptake of Intranasal Glutathione in Parkinson's Disease. *npj Park. Dis.* 2 (1), Article No. 16002.

(27) Novak, V., Milberg, W., Hao, Y., Munshi, M., Novak, P., Galica, A., Manor, B., Roberson, P., Craft, S., and Abduljalil, A. (2014) Enhancement of Vasoreactivity And cognition by Intranasal Insulin in Type 2 Diabetes. *Diabetes Care* 37 (3), 751–759.

(28) Reger, M. A., Watson, G. S., Green, P. S., Baker, L. D., Cholerton, B., Fishel, M. A., Plymate, S. R., Cherrier, M. M., Schellenberg, G. D., Frey II, W. H., and Craft, S. (2008) Intranasal Insulin Administration Dose-Dependently Modulates Verbal Memory and Plasma β -Amyloid in Memory-Impaired Older Adults. *J. Alzheimer's Dis.* 13 (3), 323–331.

(29) De Luigi, A., Colombo, L., Diomede, L., Capobianco, R., Mangieri, M., Miccolo, C., Limido, L., Forloni, G., Tagliavini, F., and Salmona, M. (2008) The Efficacy of Tetracyclines in Peripheral and Intracerebral Prion Infection. *PLoS One* 3 (3), Article No. e1888.

(30) Kirby, C. J., and Gregoriadis, G. (1984) Preparation of Liposomes Containing Factor VIII for Oral Treatment of Haemophilia. *J. Microencapsulation* 1 (1), 33–45.

(31) Mangiarini, L., Sathasivam, K., Seller, M., Cozens, B., Harper, A., Hetherington, C., Davies, S. W., and Bates, G. P. (1996) Exon 1 of the HD Gene with an Expanded CAG Repeat Is Sufficient to Cause a Progressive Neurological Phenotype in Transgenic Mice. *Cell* 87, 493–506.

(32) Hanson, L. R., Fine, J. M., Svitak, A. L., and Faltese, K. A. (2013) Intranasal Administration of CNS Therapeutics to Awake Mice. *J. Visualized Exp.* 74, 1–7.

SUPPORTING INFORMATION

EFFICACY OF CHOLESTEROL NOSE-TO-BRAIN DELIVERY FOR BRAIN TARGETING IN HUNTINGTON'S DISEASE

Alice Passoni^{1,#}, Monica Favagrossa^{1,#}, Laura Colombo¹, Renzo Bagnati¹, Marco Gobbi¹, Luisa Diomedea¹,
Giulia Birolini^{2,3}, Eleonora Di Paolo^{2,3}, Marta Valenza^{2,3}, Elena Cattaneo^{2,3}, Mario Salmona^{1,*}

#contributed equally to this paper

*corresponding author:

Mario Salmona,

mario.salmona@marionegri.it

ORCID: 0000-0002-9098-9873

¹ Istituto di Ricerche Farmacologiche Mario Negri IRCCS, via Mario Negri 2, 20156 Milan, Italy

² Department of Biosciences, University of Milan, via G. Celoria 26, 20133, Milan, Italy

³ Istituto Nazionale di Genetica Molecolare "Romeo ed Enrica Invernizzi," via F. Sforza 35, 20122, Milan, Italy

Keywords: Huntington's disease, brain cholesterol, nose-to-brain delivery, intranasal administration, LC-MS analysis, liposomes

TABLE OF CONTENTS

1. Validation of the LC-MS method for Chol-D6 quantitation

1.1. Calibration curve

1.2. Carry-over

1.3. Accuracy and precision

1.4. Recovery

1.5. Stability

34 **VALIDATION OF THE LC-MS METHOD FOR CHOL-D6 QUANTITATION**

35 **1.1. Calibration curve**

36 The calibration curve was linear in the selected range of Chol-D6 concentrations. In five different analytical
 37 sessions, the determination coefficients (r^2) and linear regression analysis gave averages of 0.998 and 0.997 in
 38 plasma and brain, respectively. The slope values were highly reproducible among different analytical sessions
 39 (Tables 1 and 2). The mean accuracy of the back-calculated concentrations ranged from 99% to 102% in
 40 plasma samples. The mean accuracy was varied slightly more in brain samples, from 93% to 108%. The
 41 precision of back-calculated concentrations was expressed as coefficient of variation (CV%) and was
 42 acceptable for all calibration points in both matrices. Figure 1 presents representative calibration curves in
 43 plasma (1A) and brain (1B).

44

45 **Table 1. Linearity and LLOQ of Chol-D6 in plasma**

Linearity and LLOQ (50 ng/mL) of Chol-D6 in mouse plasma										
Mouse plasma	5 runs	Nominal concentration (ng/mL)							Calibration curve	
		50.00	100.0	250.0	500.0	1000	2500	5000	slope	r^2
		Calculated concentration (ng/mL)								
	Mean	50.44	98.10	251.2	494.0	1009	2466	5118	0.00014	0.9980
	± SD	0.8591	2.146	8.258	18.14	59.83	89.33	536.5	0.00002	0.0031
Accuracy (%)	101%	98%	100%	99%	101%	99%	102%			
Precision (CV%)	2%	2%	3%	4%	6%	4%	10%			

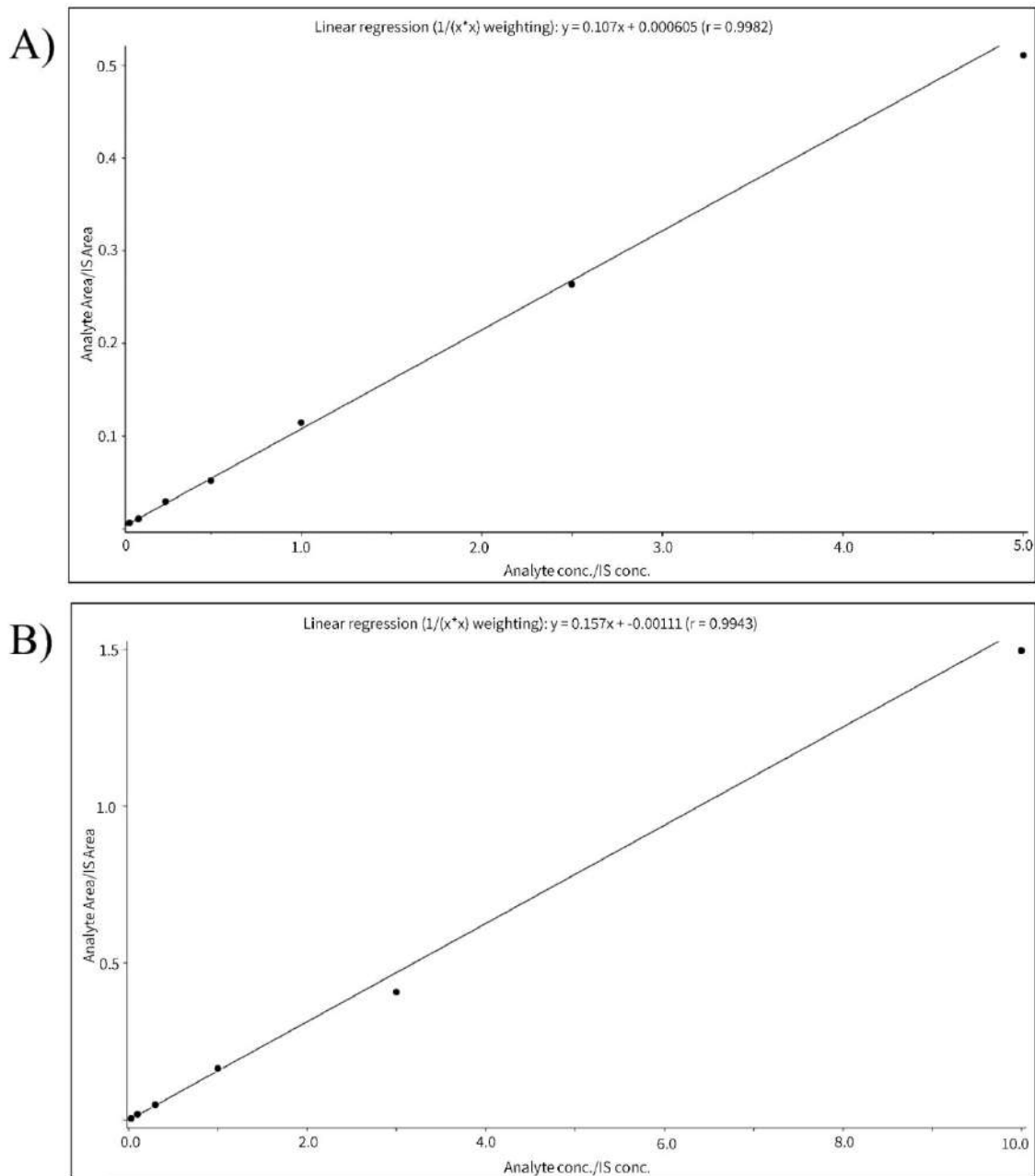
46

47 **Table 2. Linearity and LLOQ of Chol-D6 in brain**

Linearity and LLOQ (0.03 ng/mg) of Chol-D6 in mouse brain									
Mouse brain	5 runs	Nominal concentration (ng/mg)						Calibration curve	
		0.0300	0.1000	0.3000	1.000	3.000	10.00	slope	r^2
		Calculated concentration (ng/mg)							
	Mean	0.0298	0.1019	0.3038	1.007	2.740	10.57	0.09286	0.9971
	± SD	0.0003	0.0045	0.0106	0.0471	0.1598	0.4949	0.01633	0.0020
Accuracy (%)	100%	101%	99%	100%	93%	108%			
Precision (CV%)	2%	5%	6%	5%	6%	6%			

48

49



50

51 **Figure 1A.** Representative calibration curve in plasma, from 0.05 to 5 $\mu\text{g/mL}$ **1B.** Representative calibration curve in

52 brain homogenate, from 0.03 ng/mg and 10 ng/mg

53 1.2. Carry-over

54 The carry-over effect was investigated by examining the Chol-D6 signal in blank plasma and brain samples

55 after injection of the highest Chol-D6 concentration. The residual signals were about 4% and 40% of the LLOQ

56 signal in plasma and brain samples, respectively. After injection of samples containing concentrations higher

57 than 3 ng/mg for the brain, blank samples were injected in order to reduce interference (up to 10%).

58 **1.3. Accuracy and precision**

59 In mouse plasma the mean intra-day accuracy ranged from 87 to 98%, with mean precision 5% (Table 3).

60 Intra-day accuracy for brain homogenates ranged from 93% and 108%, with slightly higher mean precision

61 (7.5 %) (Table 4). The mean inter-day accuracy of plasma samples was similar to the mean intra-day accuracy,

62 from 93% to 98% with the same mean inter-day precision (Table 5). The mean inter-day accuracy and precision

63 of brain homogenates were higher than intra-day results but within EMA guideline limits for all concentrations

64 (Table 6).

65

66 **Table 3. Intra-day accuracy and precision of Chol-D6 in plasma**

Intra-day accuracy and precision of Chol-D6 in mouse plasma											
Nominal concentration (ng/mL)		Calculated concentration (ng/mL)						Mean (ng/mL)	± SD	Accuracy (%)	Precision (CV%)
Mouse Plasma	50.00	45.72	48.43	48.63	48.31	50.81	50.14	48.67	1.768	97%	4%
	150.0	142.3	138.4	153.4	143.2	157.2	145.1	146.6	7.185	98%	5%
	1000	897.1	897.1	886.3	772.4	900.3	757.3	851.8	67.65	87%	6%
	3000	2970	2870	3010	2720	2780	2730	2847	123.7	95%	4%

67

68 **Table 4. Intra-day accuracy and precision of Chol-D6 in brain**

Intra-day accuracy and precision of Chol-D6 in mouse brain											
Nominal concentration (ng/mg)		Calculated concentration (ng/mg)						Mean (ng/mg)	± SD	Accuracy (%)	Precision (CV%)
Mouse Brain	0.0300	0.0322	0.0334	0.0382	0.0271	0.0312	0.0315	0.0320	0.0036	108%	11%
	0.2000	0.1871	0.1900	0.1712	0.2322	0.1774	0.2014	0.1930	0.0218	97%	11%
	2.000	1.610	1.811	1.720	1.371	1.940	2.093	1.758	0.2534	88%	14%
	6.000	5.443	5.731	5.831	6.022	6.413	5.850	5.882	0.3229	98%	5%

69

70

71

72

73

74

75 **Table 5.** Inter-day accuracy and precision of Chol-D6 in plasma

Inter-day accuracy and precision of Chol-D6 in mouse plasma											
Nominal concentration (ng/mL)		Calculated concentration (ng/mL)						Mean (ng/mL)	± SD	Accuracy (%)	Precision (CV%)
		day 1		day 2		day 3					
Mouse Plasma	50.00	48.24	48.45	46.43	51.23	52.11	49.39	49.31	2.084	98%	4%
	150.0	157.4	145.4	141.2	138.1	149.1	152.0	147.2	7.110	98%	5%
	1000	897.1	900.0	883.4	970.3	948.5	980.2	929.8	41.65	93%	4%
	3000	3010	2720	2480	2700	2860	2930	2783	190.6	93%	7%

76

77

78 **Table 6.** Inter-day accuracy and precision of Chol-D6 in brain

Inter-day accuracy and precision of Chol-D6 in mouse brain											
Nominal concentration (ng/mg)		Calculated concentration (ng/mg)						Mean (ng/mg)	± SD	Accuracy (%)	Precision (CV%)
		day 1		day 2		day 3					
Mouse Brain	0.0300	0.0321	0.0322	0.0343	0.0314	0.0241	0.0374	0.0319	0.0044	102%	14%
	0.2000	0.1822	0.2021	0.2384	0.2371	0.2283	0.1773	0.2109	0.0275	105%	13%
	2.000	1.930	1.800	1.980	2.440	1.730	1.920	1.967	0.2496	98%	13%
	6.000	5.780	5.670	5.820	6.010	6.130	5.410	5.803	0.2541	97%	4%

79

80

81 **1.4. Recovery**

82 The analyte recovery of the extraction procedure was evaluated for Chol-D6 in six independent plasma samples
 83 and brain homogenates at LQC and HQC concentrations. In plasma, Chol-D6 recoveries were 98% and 95%
 84 for LQC and HQC samples, respectively. In brain homogenates, the recoveries were slightly lower (57% and
 85 43% for LQC and HQC samples) because of the more complicated extraction procedure and the higher matrix
 86 effect (Table 7).

87 **Table 7.** Recovery of Chol-D6 in plasma and brain

Recovery of Chol-D6 in plasma and brain matrices							
Recovery (%)							
Nominal conc. (ng/mL)	Chol-D6 in plasma			Nominal conc. (ng/mg)	Chol-D6 in brain		
	Mean	± SD	CV (%)		Mean	± SD	CV (%)
LQC (150.0 ng/mL)	98%	4%	4%	LQC (0.2000 ng/mg)	57%	8%	14%
HQC (3000 ng/mL)	95%	3%	4%	HQC (6.000 ng/mg)	43%	6%	13%

88

89

90 **1.5. Stability**

91 We examined Chol-D6 stability in plasma and brain homogenates under three conditions in order to simulate
 92 the working conditions of the analytical sessions. We checked bench-top stability, long-term storage stability
 93 and stability after freeze-thaw cycles. These studies were done on the mouse plasma QC samples at LQC (50
 94 ng/mL) and HQC (3000 ng/mL) in six replicates; QC sample concentrations were obtained against a freshly
 95 prepared calibration curve. All the results indicated Chol-D6 stability in plasma and brain homogenates in the
 96 conditions used (Tables 8 and 9).

97 **Table 8.** Stability of Chol-D6 in plasma in different analytical conditions: bench top stability, long-term storage and
 98 freeze and thaw stability

Stability of cholesterol-D6 in mouse plasma										
Stability test conditions	LQC – 150.0 ng/mL					HQC – 3000 ng/mL				
	Mean (ng/mL)	± SD	Mean Accuracy (%)	Deviation (%)	CV (%)	Mean (ng/mL)	± SD	Mean Accuracy (%)	Deviation (%)	CV (%)
Freshly prepared	146.3	7.202	98%		5%	2847	123.7	95%		4%
Bench top (2h RT)	145.5	8.167	97%	-0.6%	6%	3037	249.3	101%	6.7%	8%
2 weeks (-20° C)	143.5	7.007	96%	-1.9%	5%	2762	118.7	92%	-3.0%	4%
Freeze-thaw 1st cycle	146.5	7.791	98%	0.1%	5%	2860	77.97	95%	0.5%	3%

99




100 **Table 9.** Stability of Chol-D6 in brain homogenate in different analytical conditions: bench top stability, long-term
 101 storage and freeze and thaw stability

Stability of cholesterol-D6 in mouse brain										
Stability test conditions	LQC - 0.2 ng/mg					HQC - 6 ng/mg				
	Mean (ng/mL)	± SD	Mean Accuracy (%)	Deviation (%)	CV (%)	Mean (ng/mL)	± SD	Mean Accuracy (%)	Deviation (%)	CV (%)
Freshly prepared	0.1900	0.0262	95%		14%	5.790	0.4144	96%		7%
Bench top (2h RT)	0.2200	0.0105	110%	16%	5%	6.550	0.2259	109%	13.2%	3%
2 weeks (-20° C)	0.1867	0.0187	93%	-2%	10%	5.852	0.1829	98%	1.1%	3%
Freeze-thaw 1st cycle	0.2225	0.0264	111%	17%	12%	5.982	0.4912	100%	3.4%	8%

102



Striatal infusion of cholesterol promotes dose-dependent behavioral benefits and exerts disease-modifying effects in Huntington's disease mice

Giulia Birolini^{1,2,‡}, Marta Valenza^{1,2,‡,*} , Eleonora Di Paolo^{1,2,‡}, Elena Vezzoli^{1,2,†}, Francesca Talpo³, Claudia Maniezzi³, Claudio Caccia⁴, Valerio Leoni⁵, Franco Taroni⁴, Vittoria D Bocchi^{1,2}, Paola Conforti^{1,2}, Elisa Sogne⁶, Lara Petricca⁷, Cristina Cariulo⁷, Margherita Verani⁷, Andrea Caricasole⁷, Andrea Falqui⁶ , Gerardo Biella³ & Elena Cattaneo^{1,2,**} 

Abstract

A variety of pathophysiological mechanisms are implicated in Huntington's disease (HD). Among them, reduced cholesterol biosynthesis has been detected in the HD mouse brain from pre-symptomatic stages, leading to diminished cholesterol synthesis, particularly in the striatum. In addition, systemic injection of cholesterol-loaded brain-permeable nanoparticles ameliorates synaptic and cognitive function in a transgenic mouse model of HD. To identify an appropriate treatment regimen and gain mechanistic insights into the beneficial activity of exogenous cholesterol in the HD brain, we employed osmotic mini-pumps to infuse three escalating doses of cholesterol directly into the striatum of HD mice in a continuous and rate-controlled manner. All tested doses prevented cognitive decline, while amelioration of disease-related motor defects was dose-dependent. In parallel, we found morphological and functional recovery of synaptic transmission involving both excitatory and inhibitory synapses of striatal medium spiny neurons. The treatment also enhanced endogenous cholesterol biosynthesis and clearance of mutant Huntingtin aggregates. These results indicate that cholesterol infusion to the striatum can exert a dose-dependent, disease-modifying effect and may be therapeutically relevant in HD.

Keywords aggregates; behavior; cholesterol; Huntington's disease; synapses

Subject Categories Genetics, Gene Therapy & Genetic Disease; Neuroscience

DOI 10.15252/emmm.202012519 | Received 15 April 2020 | Revised 13 August 2020 | Accepted 26 August 2020

EMBO Mol Med (2020) e12519

Introduction

The brain is the most cholesterol-rich organ, accounting for about 25% of the whole body's cholesterol (Dietschy & Turley, 2004; Dietschy, 2009). Its biosynthesis occurs through a stepwise cascade involving several enzymes under transcriptional regulation by sterol regulatory element binding protein 2 (SREBP2) transcription factor (Seo *et al*, 2012). In the adult brain, a small amount of cholesterol continues to be synthesized locally, where it regulates multiple processes including synapse formation and maintenance, synaptic vesicle (SV) recycling, and optimal release of neurotransmitters for downstream intracellular signaling pathways (Mauch *et al*, 2001; Rohrbough & Broadie, 2005; Fukui *et al*, 2015; Postila & Róg, 2020). Consequently, dysregulation of brain cholesterol homeostasis is linked to several chronic neurological and neurodegenerative diseases (Valenza & Cattaneo, 2011; Martin *et al*, 2014). Among these conditions is Huntington's disease (HD), an adult-onset disorder characterized by motor, cognitive, and psychiatric features.

The basis of HD is expansion of a CAG trinucleotide repeat in the gene encoding the Huntingtin protein (HTT; Saudou & Humbert, 2016). In HD, the striatal medium spiny neurons (MSNs) and

1 Department of Biosciences, University of Milan, Milan, Italy

2 Istituto Nazionale di Genetica Molecolare "Romeo ed Enrica Invernizzi", Milan, Italy

3 Department of Biology and Biotechnologies, University of Pavia, Pavia, Italy

4 Unit of Medical Genetics and Neurogenetics, Fondazione I.R.C.C.S. Istituto Neurologico Carlo Besta, Milan, Italy

5 School of Medicine and Surgery, Monza and Laboratory of Clinical Pathology, Hospital of Desio, ASST-Monza, University of Milano-Bicocca, Milan, Italy

6 Biological and Environmental Science & Engineering (BESE) Division, NABLA Lab, King Abdullah University of Science and Technology (KAUST), Thuwal, Saudi Arabia

7 Neuroscience Unit, Translational and Discovery Research Department, IRBM S.p.A, Rome, Italy

*Corresponding author. Tel: +39 02 50325851; E-mail: marta.valenza@unimi.it

**Corresponding author. Tel: +39 02 5032 5846; E-mail: elena.cattaneo@unimi.it

†Present address: Department of Biomedical Sciences for Health, University of Milan, Milan, Italy

‡These authors contributed equally to this work

cortical pyramidal neurons projecting to the striatum are primarily affected and degenerate (Zuccato *et al*, 2010; Rüb *et al*, 2016). One of the underlying pathophysiological mechanisms is disruption of brain cholesterol biosynthesis due to reduced nuclear translocation of SREBP2 and diminished expression of its downstream target genes in the cholesterol biosynthesis pathway (Valenza *et al*, 2005, 2015a; Di Pardo *et al*, 2020). This defect occurs in astrocytes, which are the major producers of cholesterol in the adult brain, with consequent reduction of newly synthesized cholesterol available for neuronal function (Valenza *et al*, 2010, 2015a). This compromised process is manifested in reduced mRNA levels of key enzymes in the cholesterol synthesis pathway in HD cells, HD mouse models, and post-mortem brain from HD patients (Sipione *et al*, 2002; Valenza *et al*, 2005, 2015a; Bobrowska *et al*, 2012; Lee *et al*, 2015). Also evident is a reduction in cholesterol precursors, in particular lathosterol and lanosterol, as judged by isotopic dilution mass spectrometry (ID-MS) in HD cells (Ritch *et al*, 2012) and in seven rodent HD models (Valenza *et al*, 2007a,b, 2010; Shankaran *et al*, 2017); moreover, striatal level of lathosterol is inversely correlated with CAG repeat number (Shankaran *et al*, 2017). In addition, the striatum of knock-in zQ175 mice (Shankaran *et al*, 2017) shows reduced synthesis of new cholesterol after administration of deuterated water *in vivo* at the pre-symptomatic stage (Shankaran *et al*, 2017) and decreased cholesterol at late time points, as measured by gas chromatography–mass spectrometry (GC-MS). Finally, levels of the brain-derived cholesterol catabolite 24S-hydroxycholesterol (24S-OHC) are decreased in brain and blood from HD mice (Valenza *et al*, 2007b, 2010; Shankaran *et al*, 2017), post-mortem caudate (Boussicault *et al*, 2016), plasma of HD patients (Leoni *et al*, 2008, 2011), as well as in pre-HD manifesting patients who are close to the disease onset (Leoni *et al*, 2013).

All of these findings support the idea that the primary event of cholesterol dysfunction in the HD brain is decreased synthesis, followed by reduced conversion of cholesterol into 24S-OHC, ultimately leading to reduced cholesterol content at the late-symptomatic stages (Shankaran *et al*, 2017). In two studies conducted in two HD animal models (R6/2 and zQ175 mice), enhancement of cholesterol catabolism in the striatum via neuronal overexpression of cholesterol 24-hydroxylase (Cyp46A1) increased striatal levels of 24S-OHC and endogenous cholesterol biosynthesis and rescued several disease phenotypes (Boussicault *et al*, 2016; Kacher *et al*, 2019). Despite conflicting data regarding the amount of striatal cholesterol measured in the two studies in R6/2 and zQ175 adult mice (Boussicault *et al*, 2016; Kacher *et al*, 2019), this strategy proved to be of therapeutic relevance in targeting cholesterol biosynthesis in HD brain.

We previously reported that systemic administration of brain-permeable polymeric nanoparticles loaded with cholesterol (g7-NPs-cho) reversed synaptic alterations and prevented cognitive defects in a HD transgenic mouse model (Valenza *et al*, 2015b). This work provided the first proof-of-concept that cholesterol delivery to the HD brain is beneficial, but the low cholesterol content of g7-NPs-cho did not allow for full characterization of a target therapeutic dose or its effects on motor and cognitive capacity.

Here we sought to evaluate the dose-dependent effects of cholesterol infusion on molecular, functional, and behavioral parameters. For this purpose, we took advantage of osmotic mini-pumps to infuse three escalating doses of cholesterol directly into

the striatum of HD mice, in a continuous and rate-controlled manner. In this model, all three doses prevented cognitive defects, and the highest dose attenuated also disease-related motor phenotypes. In parallel with these behavioral benefits, we detected morphological and functional recovery of synaptic transmission that involved both excitatory and inhibitory synapses on striatal MSNs. Striatal infusion of cholesterol in HD mice also increased levels of the brain-specific cholesterol catabolite 24S-OHC and enhanced endogenous cholesterol biosynthesis, restoring the primary cholesterol defect in HD. At the cellular level, we show that striatal infusion of cholesterol reduced muHTT aggregates by reducing lysosome accumulation.

Results

Striatal infusion of cholesterol prevents motor and cognitive deficits in HD mice

To identify the target therapeutic dose of cholesterol to administer, we infused three escalating doses of cholesterol—15 µg (chol-low), 185 µg (chol-medium), and 369 µg (chol-high)—directly into one hemi-striatum of the R6/2 transgenic model of HD (Mangiarini *et al*, 1996). For this purpose, we used miniature infusion osmotic pumps implanted subcutaneously on the back and connected to a catheter. We targeted the striatum as the most affected brain region in HD and the earliest and most obvious site of decreased cholesterol biosynthesis (Shankaran *et al*, 2017). Mice were operated at age 7 weeks, and motor and cognitive tests were performed over a 4-week infusion period (Fig 1A).

Before testing HD mice and to reduce the number of animals in the main study without compromising statistical power, we performed a pilot experiment with healthy wild-type (wt) mice to assess the behavioral influence of osmotic mini-pump implantation and 4 weeks of high-dose cholesterol administration. Mini-pumps filled with artificial cerebrospinal fluid (ACSF) or high-dose cholesterol were implanted in wt mice, and behavioral tests were performed. Coordination, motor activity, and memory recognition were similar among unoperated wt, wt ACSF, and wt chol-high mice (Fig EV1A–F). Using GC-MS, we verified increased cholesterol content in the infused striatum and ipsilateral cortex of wt chol-high mice compared to wt ACSF animals (Fig EV1G and H). These results allowed us to include only unoperated wt mice as controls in subsequent studies.

To visualize the spread of exogenous cholesterol and study its partition in striatum, we tested an analogue of cholesterol tagged with a fluorescent BODIPY group at carbon 24 (BODIPY-cho), using the experimental paradigm described in Fig 1A. After a 4-week infusion period, BODIPY-cho covered 39.7% ± 5.9% of the infused hemi-striatum of R6/2 mice, whereas we found no signal in the contralateral hemisphere (Fig 1B). Within the striatum, BODIPY-cholesterol did not localize with TGN46, a marker of Golgi or with calnexin, a marker of endoplasmic reticulum (ER) (Fig EV1I–J). Instead, BODIPY-cholesterol partially co-localized with late endosome marker Rab9A and with plasma membrane marker PMCA-ATPase (Fig EV1K–L) while complete co-localization was found with LAMP1, a marker of lysosomes (Fig EV1M).

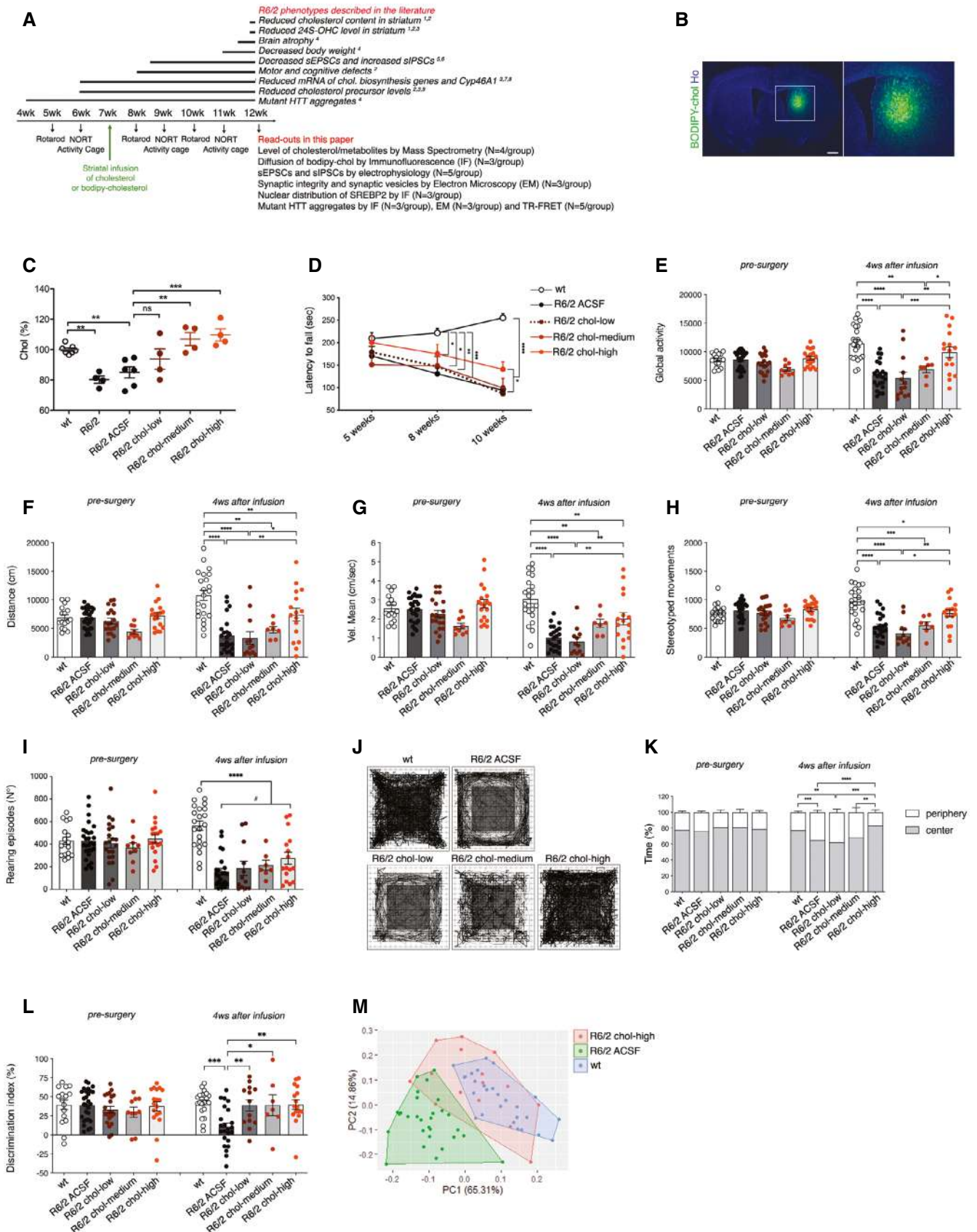


Figure 1.

Figure 1. Striatal infusion of three escalating doses of cholesterol ameliorates cognitive and motor deficits in HD mice.

- A Experimental paradigm performed in all the trials: Mini-pumps were implanted in the striatum of 7-week-old mice. A battery of behavioral tests was performed before and after mini-pump implantation. In bold, a list of R6/2 phenotypes (above) and read-outs analyzed following cholesterol (chol) infusion (below). References: (1) Valenza (2010); (2) Valenza et al (2015a,b); (3) Boussicault et al (2016); (4) Mangiarini et al (1996); (5) Cepeda et al (2003); (6) Cepeda et al (2004); (7) Valenza et al (2005); (8) Bobrowska et al (2012); (9) Valenza et al (2007a,b).
- B Representative large image of a brain slice from R6/2 mice after 4-week striatal infusion of fluorescent cholesterol (BODIPY-chol, green). In the inlet, infused striatum is shown. Hoechst (Ho, blue) was used to counterstain nuclei. Scale bar: 1000 μ m.
- C Cholesterol content measured by mass spectrometry in infused striatum of untreated wt ($N = 7$) and R6/2 ($N = 4$), R6/2 ACSF ($N = 5$), R6/2 chol-low ($N = 5$), R6/2 chol-medium ($N = 5$), and R6/2 chol-high ($N = 5$) mice at 12 weeks of age after 4-week striatal cholesterol infusion. The low, medium, and high doses, respectively, correspond to 15 μ g, 185 μ g, and 369 μ g of cholesterol infused in the striatum after 4 weeks.
- D Latency to fall (seconds) from an accelerating rotarod from 5 weeks (pre-surgery; i.e., before pump implantation) to 10 weeks of age in wt ($N = 23$ at 5 weeks, $N = 28$ at 8 and 10 weeks), R6/2 ACSF ($N = 35$ at 5 weeks, $N = 31$ at 8 weeks and $N = 30$ at 10 weeks), R6/2 chol-low ($N = 22$ at 5 weeks, $N = 14$ at 8 weeks and $N = 13$), R6/2 chol-medium ($N = 13$ at 5 weeks, $N = 9$ at 8 weeks and $N = 8$ at 10 weeks), and R6/2 chol-high ($N = 19$ at 5 weeks, $N = 17$ at 8 and 10 weeks) mice. The graph shows means \pm standard error for each time point.
- E–I Global motor activity (E), total distance traveled (F), mean velocity (G), stereotyped movements (H), and number of rearings (I) in an open-field test at 6 weeks of age (pre-surgery) and 11 weeks of age (4 weeks after infusion) of wt ($N = 16$ at 9 weeks, $N = 22$ at 11 weeks), R6/2 ACSF ($N = 27$ at 9 weeks, $N = 23$ at 11 weeks), R6/2 chol-low ($N = 20$ at 9 weeks, $N = 13$ at 11 weeks), R6/2 chol-medium ($N = 9$ at 9 weeks, $N = 7$ at 11 weeks), and R6/2 chol-high ($N = 18$ at 9 weeks, $N = 16$ at 11 weeks) mice.
- J, K Representative track plots (J) generated from the open-field test from wt ($N = 16$ at 9 weeks, $N = 22$ at 11 weeks), R6/2 ACSF ($N = 26$ at 9 weeks, $N = 23$ at 11 weeks), R6/2 chol-low ($N = 11$ at 9 weeks, $N = 7$ at 11 weeks), R6/2 chol-medium ($N = 11$ at 9 weeks, $N = 7$ at 11 weeks), and the R6/2 chol-high mice ($N = 18$ at 9 weeks, $N = 16$ at 11 weeks) and relative quantification (K) of the time spent in the center and in the periphery (%) of the arena.
- L Discrimination index (DI; %) in the novel object recognition test at 6 weeks of age (before pump implantation) and 11 weeks of age (4 weeks after cholesterol infusion) of wt ($N = 16$ at 9 weeks, $N = 21$ at 11 weeks), R6/2 ACSF ($N = 28$ at 9 weeks, $N = 23$ at 11 weeks), R6/2 chol-low ($N = 21$ at 9 weeks, $N = 13$ at 11 weeks), R6/2 chol-medium ($N = 10$ at 9 weeks, $N = 7$ at 11 weeks), and R6/2 chol-high mice ($N = 18$ at 9 weeks, $N = 16$ at 11 weeks). DI above zero indicates a preference for the novel object; DI below zero indicates a preference for the familiar object.
- M Principal component analysis by combining all the values related to motor and cognitive tasks from wt mice (blue dots), R6/2 ACSF mice (green dots), and R6/2 chol-high mice (red dots).

Data information: The data in (C–L) are from five independent trials and shown as scatterplot graphs with means \pm standard error. Each dot (C, E–I, L) corresponds to the value obtained from each animal. Statistics: one-way ANOVA with Newman–Keuls *post hoc* test (* $P < 0.05$; ** $P < 0.01$; *** $P < 0.001$; **** $P < 0.0001$).

In all trials, with the aim of obtaining the maximum solubility and diffusion of the exogenous cholesterol (Loftsson et al, 2005), we used water-soluble methyl- β -cyclodextrin (M β CD)-balanced cholesterol. To exclude any potential effect of M β CD, we performed motor and cognitive tests in an additional control group, comparing R6/2 ACSF and R6/2 mice with mini-pumps containing ACSF and the equivalent quantity of M β CD to be used with chol-high (R6/2 ACSF-M β CD). We found that the presence of M β CD in ACSF did not influence outcomes in the motor and cognitive tasks (Fig EV2A–F). Furthermore, cholesterol content and levels of cholesterol precursors and 24S-OHC were not influenced by M β CD (Fig EV2G–K).

We next tested three doses of exogenous cholesterol in R6/2 mice. We used GC-MS to quantify cholesterol content in the striatum and cortex of R6/2 mice and verify the success of chronic cholesterol infusion. Compared to animals implanted with osmotic mini-pumps filled with ACSF, R6/2 mice infused with the three doses of cholesterol showed a dose-dependent increase in cholesterol content in the striatum (Fig 1C). The increase was significant with the chol-medium and chol-high doses (Fig 1C). Of note, striatal cholesterol content was consistently decreased in late-symptomatic R6/2 and R6/2 ACSF mice (for a total of 20 MS measurements performed in 10 mice) compared to wt mice (14 MS measurements in 7 mice; Figs 1C and EV3B; Valenza et al, 2010). A significant increase in cholesterol content was also observed in the ipsilateral cortex of R6/2 chol-high groups (Fig EV3A) but not in the contralateral striatum and cortex of these animals compared to R6/2 ACSF mice (Fig EV3B and C). These results demonstrate the efficiency of osmotic mini-pumps in releasing exogenous cholesterol around the site of infusion and partially into the surrounding cortex in HD animals.

For all the experiments, the body weight of mice was monitored over time. Before the surgery, at 7 weeks of age, body

weight was similar across all groups (Fig EV3D and E). At 12 weeks of age, R6/2-ACSF males, as well as R6/2 chol-low and R6/2 chol-high males, lost body weight compared to wt males. Of note, R6/2 chol-high males did not lose body weight over time as they were comparable to that of wt mice (Fig EV3F). No significant changes were observed in all female groups regardless of genotype or treatment (Fig EV3G).

Compared to wt mice, R6/2 ACSF animals showed a progressive deterioration in fine motor coordination, as assessed by an accelerating rotarod test, from the early-symptomatic (8 weeks of age) to late-symptomatic stages (10 weeks of age; Fig 1D). In contrast, R6/2 chol-high mice presented a partial but significant amelioration in rotarod performance at 10 weeks compared to R6/2 chol-medium and R6/2 chol-low groups (Fig 1D).

To further test motor abilities, we evaluated spontaneous locomotor activity in the activity cage test. R6/2 ACSF mice exhibited a severe hypokinetic phenotype with disease progression, i.e., at 11 weeks (Fig 1E, right panel) compared to 6 weeks (Fig 1E, left panel; Fig 1E). Of note, global activity deficits were normalized in R6/2 chol-high mice, while the low and medium dose of cholesterol did not produce any effect (Fig 1E). Other parameters, such as distance traveled (Fig 1F), mean velocity (Fig 1G), and stereotyped movements (Fig 1H), significantly improved in R6/2 chol-high mice compared to R6/2 ACSF mice. An ANOVA multiple comparison test revealed a significant decrease in the number of vertical movements (rearings) in all R6/2 groups (Fig 1I). However, a significant increase in rearings was found only in R6/2 chol-high group ($P = 0.0419$, unpaired *t*-test), indicating an effect of exogenous cholesterol on this parameter only at the highest dose. By comparing among R6/2 groups treated with the three doses of cholesterol, we identified a dose-dependent effect, with a progressive increase in

all activity-related values from low to medium to high doses of cholesterol (Table EV1).

As a measure of anxiety-like behavior, we also evaluated the time that mice spent exploring the periphery or center area of the arena during the activity cage test (Fig 1J). R6/2 ACSF animals spent more time in the periphery compared to wt mice, indicating anxiety-related behavior. R6/2 chol-high mice spent more time in the center compared to R6/2 ACSF mice, with animals performing similarly to the wt group (Fig 1K), indicating a normalization of anxiety-related behavior.

To assess if striatal infusion of cholesterol influences also cognitive abilities, we used the novel object recognition test (NORT). Long-term memory declined during disease progression in R6/2 ACSF mice, with a marked impairment in the ability to discriminate novel and familiar objects at age 11 weeks (Fig 1L). R6/2 mice in all cholesterol-dose groups performed similarly to wt mice (Fig 1L). Finally, principal component analysis (PCA) of all values related to motor and cognitive tests for chol-high animals identified two distinguishable groups (wt and R6/2 ACSF) that separated in the first principal component, with the R6/2 chol-high mice displaying a greater overlap with wt group than R6/2 ACSF mice (Fig 1M).

Taken together, these results indicate that extensive behavioral recovery occurs in HD mice after striatal infusion of cholesterol.

Striatal infusion of cholesterol rescues excitatory synaptic defects in HD mice

Cholesterol is involved in synaptic function (Pfrieger, 2003), and functionality and morphology of excitatory and inhibitory synapses are both altered in HD (Cepeda *et al*, 2003, 2004). For this reason, we adopted a combination of techniques to explore whether and how exogenous cholesterol can influence on synaptic function and morphology. The analyses were performed in R6/2 chol-high mice and relevant controls.

We first compared whole-cell patch-clamp recordings of striatal MSNs from brain slices of wt, R6/2 ACSF, and R6/2 chol-high mice (Fig 2A). The membrane capacitance, which is proportional to cell size, was significantly lower in R6/2 ACSF compared to wt MSNs and unaffected in R6/2 chol-high mice (Table EV2). Similarly, input resistance, reflecting the number of ion channels expressed by the cell, was significantly increased in both R6/2 ACSF and R6/2 chol-high compared to wt cells, but unaffected by cholesterol administration (Table EV2).

To evaluate the effect of cholesterol on excitatory transmission, we recorded spontaneous excitatory postsynaptic currents (sEPSC) in MSNs at a holding potential of -70 mV (Fig 2B). We did not find any significant differences in the average amplitude of sEPSCs between groups (Fig 2C). In agreement with previous studies (Cepeda *et al*, 2003), we found a significant reduction in frequency of sEPSCs in R6/2 MSNs compared to wt MSNs (Fig 2D). Of note, striatal infusion of cholesterol led to a significant increase in the frequency of sEPSCs in R6/2 chol-high compared to R6/2 ACSF mice, partially rescuing this defect (Fig 2D).

To identify the structural bases underlying the functional recovery of excitatory synapses after striatal infusion of cholesterol, we undertook a series of morphological studies by electron microscopy. We employed the combination of focused ion beam milling and scanning electron microscopy (FIB/SEM) followed by the 3D

reconstruction of complete synaptic junctions in large volumes of tissue (Fig 2E and F). The high spatial resolution of the FIB/SEM images and long series of serial sections allowed for classification of all synapses as asymmetric or symmetric using morphological criteria (Merchán-Pérez *et al*, 2009), providing the actual number of synapses per volume of the striatal region. Fig 2F shows an example of the 3D reconstruction of excitatory synapses (in yellow) in a large portion of the tissue blocks used for the analysis ($10\ \mu\text{m} \times 5\ \mu\text{m} \times 10\ \mu\text{m}$) from wt, R6/2, R6/2 ACSF, and R6/2 chol-high mice. The density of excitatory synapses was reduced in the striatal neurons of R6/2 compared to wt mice, but cholesterol infusion did not rescue this defect (Fig 2G). We then tested whether cholesterol could influence synaptic parameters at the active site of excitatory synapses. Using transmission electron microscopy (TEM), we visualized the synaptic vesicles (SVs) to quantify their density (Fig 2H and I). The number of total and docked SVs was reduced in R6/2 and R6/2 ACSF mice compared to wt mice (Fig 2J and K). These structural defects were completely rescued by striatal infusion of cholesterol in R6/2 chol-high mice (Fig 2J and K). Instead, postsynaptic density (PSD) area and length (Fig EV4A and B), pre-synaptic area, and active zone (AZ) length (Fig EV4C and D) were not altered in R6/2 groups compared to wt mice.

Collectively, these findings indicate that cholesterol partially rescues excitatory synaptic transmission by enhancing the formation and/or release of SVs at the pre-synaptic site, but not by increasing the number of excitatory synapses.

Striatal infusion of cholesterol rescues GABAergic inhibitory synaptic defects in HD mice

To test the effect of exogenous cholesterol at the inhibitory synapses, we recorded spontaneous inhibitory synaptic currents (sIPSCs) in brain slices from wt, R6/2 ACSF, and R6/2 chol-high mice at a holding potential of 0 mV (Fig 3A). The average amplitude of sIPSCs was similar between wt and R6/2 ACSF MSNs and was unaffected by cholesterol (Fig 3B). However, the average frequency of sIPSCs was significantly increased in R6/2 ACSF compared to wt cells (Fig 3C) as known in the literature (Cepeda *et al*, 2004). Of note, striatal infusion of cholesterol led to a significant reduction in the average frequency of sIPSCs, bringing this parameter close to what we observed in wt MSNs (Fig 3C) and indicating that exogenous cholesterol contributes to restoring GABAergic inhibitory synaptic defects.

To identify the structural changes underlying the functional recovery of inhibitory synaptic transmission after striatal infusion of cholesterol, we first analyzed the number of inhibitory synapses per volume of striatal tissue, looking at the serial sections obtained by FIB/SEM. We identified symmetric junctions by the presence of a thin postsynaptic density and performed 3D reconstruction for all groups (Fig 3D). The density of inhibitory synapses was significantly increased in striatal neurons in both R6/2 and R6/2 ACSF mice compared to wt mice (Fig 3E), in agreement with the electrophysiological findings of increased frequency. Cholesterol striatal infusion reduced the density of inhibitory synapses, rescuing the morphological defect (Fig 3E). TEM analysis of inhibitory synapses showed no alterations in SVs density in R6/2 and R6/2 chol-high mice compared to wt animals (Fig EV4E and F).

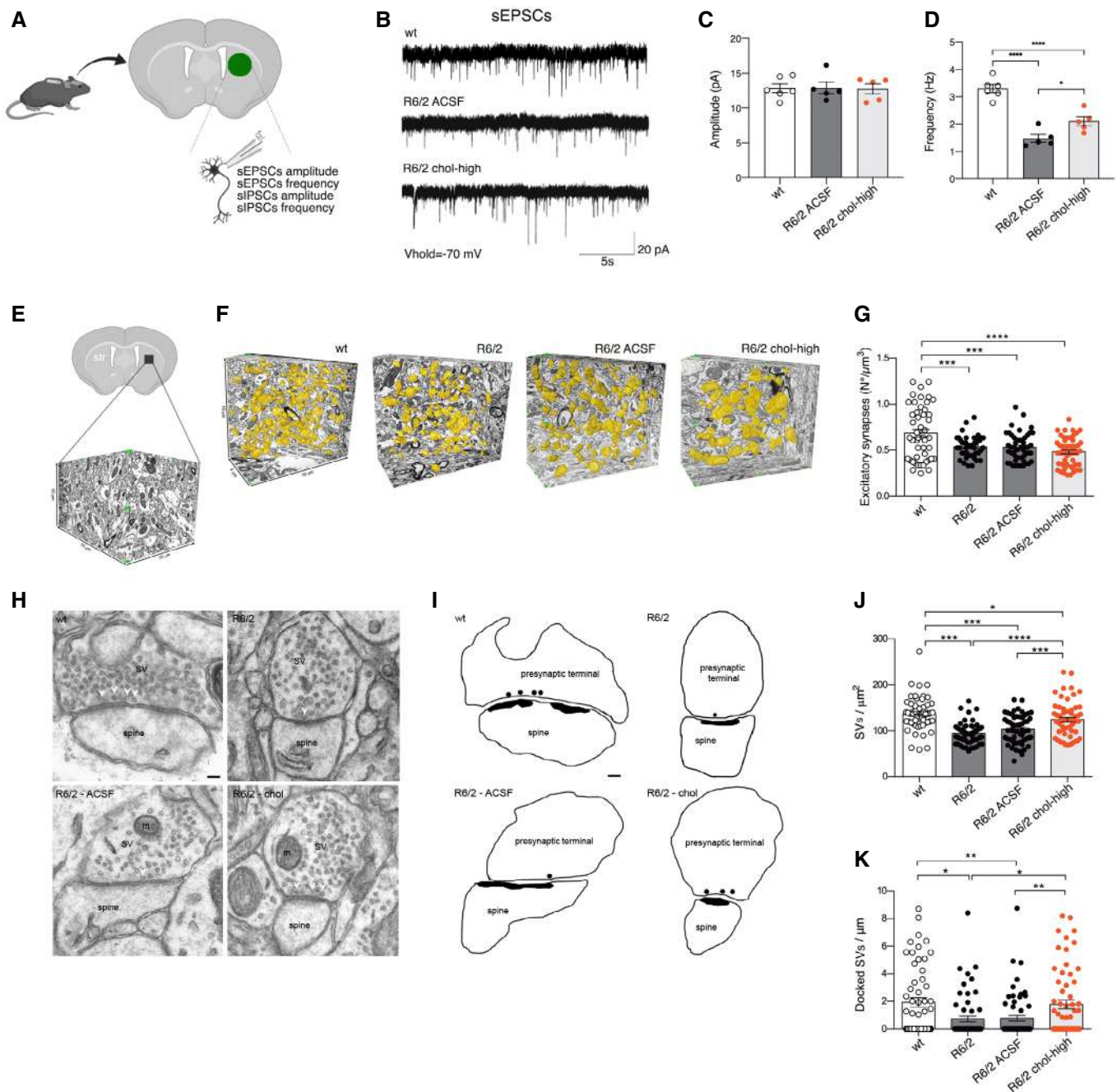


Figure 2. Striatal infusion of the high dose of cholesterol partially rescues synaptic activity and ultrastructure of excitatory synapses in HD MSNs.

A Schematic representation of the electrophysiological parameters analyzed in the infused striatum of 12-week-old mice following 4 weeks of striatal infusion of cholesterol.

B Spontaneous EPSCs were recorded from striatal MSNs (wt = 6; R6/2 ACSF = 5; R6/2 chol-high = 5) at a holding potential of -70 mV.

C, D Average amplitude (C) and average frequency (D) of EPSCs from wt, R6/2 ACSF, and R6/2 chol-high MSNs.

E–G Number of excitatory synapses per volume of striatum by using FIB/SEM followed by 3D reconstruction. (E) Representative tissue block of striatum ($10 \mu\text{m} \times 15 \mu\text{m} \times 10 \mu\text{m}$) used for the 3D analysis. (F) Representative FIB-SEM segmentation and reconstruction of excitatory synapses (yellow) in 200 serial sections of striatum for a total volume of $500 \mu\text{m}^3$, of wt, R6/2, R6/2 ACSF, and R6/2 chol-high mice. (G) Density of excitatory synapses in at least $1,500 \mu\text{m}^3$ of striatal tissue from wt, R6/2, R6/2 ACSF, and R6/2 chol-high mice ($N = 3$ animals/group).

H, I TEM images (H) and 2D profile (I) of pre-synaptic terminal sections contain SVs and mitochondria (m). Docked vesicles are indicated by a white arrowhead (H) and black circle (I) and are defined as a vesicle with its center located within 20 nm from the pre-synaptic membrane. Scale bar: 100 nm.

J, K Quantification showing the total SVs/ μm^2 (J) and the docked SVs/ μm (K) in R6/2, R6/2 ACSF, and wt striatal synapses ($N = 3$ animals/group). $N = 60$ excitatory synapses/group were counted.

Data information: The data in (C, D, G, J, and K) are shown as scatterplot graphs with means \pm standard error. Each dot corresponds to the value of each cell recorded (C and D), the number of synapses counted/ μm^3 in different blocks of striatal tissue (G), and the number of total SVs/ μm^2 (J) and docked SVs/ μm of active zone (K) counted in each synapse. Statistics: one-way ANOVA with Newman–Keuls *post hoc* test ($*P < 0.05$; $**P < 0.01$; $***P < 0.001$; $****P < 0.0001$).

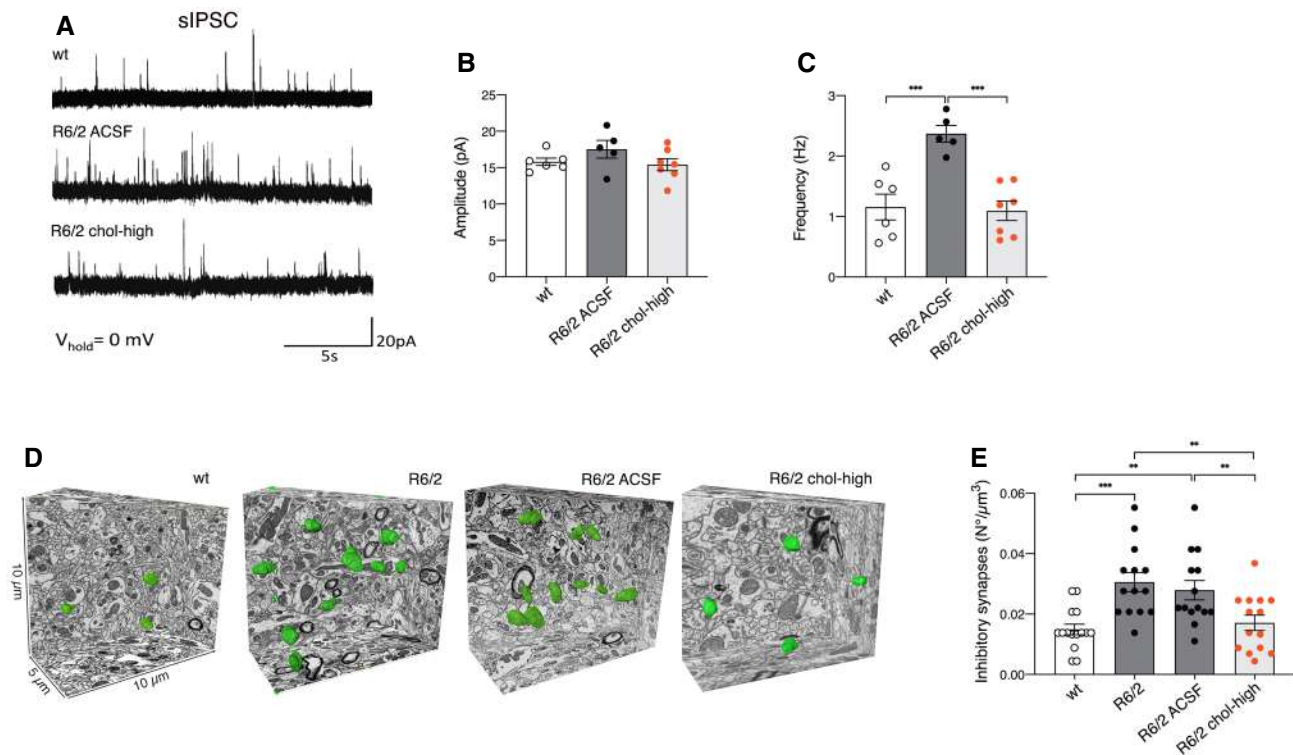


Figure 3. Striatal infusion of the high dose of cholesterol rescues synaptic activity and ultrastructure of inhibitory synapses in MSNs of HD mice.

A Spontaneous IPSCs were recorded from striatal MSNs (wt = 6; R6/2 ACSF = 5; R6/2 chol-high = 5) at a holding potential of 0 mV.

B, C Average amplitude (B) and average frequency (C) of IPSCs from wt, R6/2 ACSF, and R6/2 chol-high MSNs.

D, E Evaluation of the number of inhibitory synapses per volume of striatum by using FIB/SEM followed by 3D reconstruction. (D) Representative FIB-SEM segmentation and reconstruction of inhibitory synapses (green) in 200 serial sections of striatum for a total volume of 500 μm^3 in wt, R6/2, R6/2 ACSF, and R6/2 chol-high mice.

(E) Density of inhibitory synapses in at least 2000 μm^3 of striatal tissue of wt, R6/2, R6/2 ACSF, and R6/2 chol-high mice ($N = 3$ mice/group).

Data information: The data in (B, C, and E) are shown as scatterplot graphs with means \pm standard error. Each dot corresponds to the value of each cell recorded (B, C) and to the number of synapses counted/ μm^3 in different blocks of tissue for each group of animals ($N = 3$ animals/group) (E). Statistics: one-way ANOVA with Newman–Keuls *post hoc* test (** $P < 0.01$; *** $P < 0.001$).

These findings indicate that striatal infusion of cholesterol acts differentially on excitatory and inhibitory synapses and rescues alterations in inhibitory synaptic transmission by reducing the number of inhibitory synapses.

Striatal infusion of cholesterol does not rescue myelin defects in HD mice

Cholesterol influences myelin membrane biogenesis and the functionality of mature myelin (Saher & Stumpf, 2015). To evaluate whether striatal infusion of cholesterol counteracts myelin deficits in HD mice, we examined myelin in the striatum and corpus callosum of wt, R6/2, R6/2 ACSF, and R6/2 chol-high mice at age 12 weeks. The G-ratio of myelinated axons, a measure of myelin sheath thickness as evaluated by electron microscopy, was increased in both the striatum and corpus callosum of all R6/2 groups compared to wt mice (Appendix Fig S1A–F), indicating thinner myelin sheaths in HD mice even after striatal infusion of cholesterol. Periodicity, a measure of myelin compaction calculated as the mean distance between two major dense lines was similar in the striatum and in the corpus callosum among all groups (Appendix Fig S1G–I). These data suggest the presence of a thinner myelin sheath in the striatum

and corpus callosum of R6/2 mice and that cholesterol treatment did not rescue this defect.

Striatal infusion of cholesterol induces changes in sterol metabolism in HD mice

The synthesis of new cholesterol and production of its neuronal-specific catabolite 24S-OHC are closely related (Lund *et al*, 2003). To maintain constant levels of cholesterol in the brain, any excess of cholesterol is catabolized into 24S-OHC that can cross the blood–brain barrier and enter the circulation (Björkhem *et al*, 1997; Leoni *et al*, 2008, 2013).

Figure 4A shows a schematic representation of the enzymes involved in cholesterol biosynthesis and catabolism and how they are affected in HD. In this study, we first measured 24S-OHC level by ID-MS and found reductions in the contralateral and ipsilateral striatum of R6/2 ACSF compared to wt mice (Fig 4B). 24S-OHC level was increased in the infused striatum of R6/2 chol-high mice compared to R6/2 ACSF mice, with higher levels compared to wt mice (Fig 4B). Student's *t*-test analysis revealed a significant increase in 24S-OHC level in the infused striatum of wt mice treated with the high dose of cholesterol compared to wt ACSF mice,

suggesting a genotype-independent effect on 24S-OHC level (Fig EV5A). The low dose of cholesterol did not affect striatal level of 24S-OHC in either wt or R6/2 mice (Fig EV5A and B).

Exogenous cholesterol might operate in negative feedback on endogenous cholesterol biosynthesis, which is already compromised in HD mice. A robust deficit in levels of the key cholesterol precursors lanosterol and lathosterol was found in the striatum of R6/2 and R6/2 ACSF mice compared to wt animals (Fig 4C and D), confirming previous results (Valenza *et al*, 2007b, 2010). Unexpectedly, we also found a significant increase in striatal levels of lanosterol, lathosterol, and desmosterol in R6/2 chol-high mice compared R6/2 or R6/2 ACSF animals (Fig 4C–E), indicating enhancement of endogenous cholesterol biosynthesis following striatal cholesterol infusion. This increase was specific for the infused striatum and was not observed in the contralateral striatum of the same mice (Fig 4C–E). Increased levels of all cholesterol precursors were also found in wt mice treated with the high dose of cholesterol compared to wt ACSF mice (Fig EV5C, E, G), whereas we observed no changes in wt or R6/2 mice treated with the low dose of cholesterol (Fig EV5C–H).

Translocation into the nucleus of the N-terminal (active) fragment of SREBP2 triggers expression of genes involved in cholesterol biosynthesis (Brown & Goldstein, 1997). We sought to assess whether nuclear translocation of SREBP2 mediates the increase in endogenous cholesterol biosynthesis after striatal cholesterol infusion. For this purpose, we performed immunofluorescence staining with a specific antibody that targets the N-terminal fragment of this protein. As expected, SREBP2 localization was both nuclear and perinuclear in the striatum of wt mice (Fig 4F and G). On the contrary, reduced nuclear distribution of SREBP2 was found in the striatum of untreated R6/2 mice compared to wt mice (Fig 4F and G), as expected on the basis of the evidence of reduced cholesterol synthesis in R6/2 striatum. As shown in Fig 4H, we found a marked increase in nuclear distribution of SREBP2 in the infused striatum compared to the contralateral striatum of R6/2 chol-high mice, as confirmed by the relative quantification (Fig 4I). Specifically, by coupling the antibody against SREBP2 with a neuronal or an astrocytic marker (NeuN and GFAP, respectively), we found that the increased nuclear localization of SREBP2 was specific for glial cells

(Fig 4J and K), the major producers of cholesterol in the adult brain (Mauch *et al*, 2001; Camargo *et al*, 2012; Ferris *et al*, 2017).

Taken together, these findings indicate that the high dose of cholesterol enhances 24S-OHC availability and that increased endogenous cholesterol biosynthesis may occur through nuclear translocation of SREBP2 in glial cells.

Striatal infusion of cholesterol induces clearance of muHTT aggregates in R6/2 mice

A hallmark of HD is the presence of intracellular aggregates of muHTT (DiFiglia *et al*, 1997; Gutekunst *et al*, 1999; Maat-Schieman *et al*, 1999; Herndon *et al*, 2009). To test whether striatal infusion of cholesterol influences muHTT aggregation, we employed different methods to visualize and quantify different forms of muHTT during the process of aggregation. We first performed immunofluorescence staining on brain sections of R6/2 ACSF and R6/2 chol-high mice by using the EM48 antibody, which is specific for the expanded polyQ tract prone to aggregate (Fig 5A). The number and size of EM48-positive aggregates (size aggregates $\approx 2 \mu\text{m}$) was similar in the striatum of both hemispheres in R6/2 ACSF mice but significantly reduced in the infused striatum compared to the contralateral striatum in R6/2 chol-high mice (Fig 5B and C; Appendix Fig S2A and B). Evidence of reduced muHTT aggregates in cortical tissues of R6/2 mice, however, was variable among the animals (Appendix Fig S2C and D), likely depending on a heterogeneous diffusion of cholesterol into the cortex. We did not observe fewer aggregates in the hippocampus of the same animals (Appendix Fig S2E and F).

Double immunofluorescence staining with EM48 antibody in combination with an antibody against DARPP32 (MSN marker) or GFAP (astrocyte marker) allowed us to count the number of muHTT nuclear aggregates in the striatum of R6/2 chol-high mice in different cell types. In the infused compared to the contralateral striatum of R6/2 chol-high mice, the number of nuclear aggregates was reduced 6-fold in neurons (Fig 5D and E) and 2-fold in astrocytes (Fig 5F and G).

To investigate the morphology and localization of muHTT aggregates after striatal infusion of cholesterol, we employed electron

Figure 4. Striatal infusion of the high dose of cholesterol increases endogenous cholesterol catabolism and synthesis in the striatum of HD mice.

- A Schematic pathway of cholesterol synthesis and cholesterol precursors and catabolites in the brain. Green arrows indicate enzymes with downregulated mRNA in HD, and red arrows indicate cholesterol precursors or metabolites that were decreased per ID-MS; SREBP2-dependent genes are in bold. Here, lanosterol, 7-lathosterol, desmosterol, and 24S-OHC (highlighted in the boxes) were measured by ID-MS. References: (1) Bobrowska *et al* (2012); (2) Lee *et al* (2015); (3) Valenza *et al* (2005); (4) Samara *et al* (2014); (5) Boussicault *et al* (2016); (6) Kacher *et al* (2019); (7) Valenza *et al* (2007a); (8) Valenza *et al* (2007b); (9) Shankaran *et al* (2017); (10) Valenza *et al*, 2010; (11) Valenza *et al* (2015a,b).
- B 24S-OHC level measured by mass spectrometry in the infused and contralateral striatum of wt, R6/2-ACSF, and R6/2 chol-high mice at 12 weeks of age after a 4-week striatal infusion of cholesterol ($N = 4/\text{group}$). All values are expressed as % above the mean of wt, and these data are shown as scatterplots with means \pm standard error. Each dot corresponds to the value obtained from each animal.
- C–E Lanosterol (C), lathosterol (D), and desmosterol (E) level measured by mass spectrometry in the infused and contralateral striatum of wt, R6/2 ACSF, and R6/2 chol-high mice at 12 weeks of age after 4-week striatal infusion of cholesterol ($N = 4/\text{group}$). All values are expressed as % above the mean of wt, and these data are shown as scatterplots with means \pm standard error. Each dot corresponds to the value obtained from each animal.
- F–I Nuclear (white arrows) and perinuclear (yellow arrows) localization of endogenous SREBP2 in the striatum of wt, R6/2, and R6/2-chol mice. Representative confocal image (F and H) and relative quantification (G and I) of SREBP2 (red) in wt and R6/2 mice and in the infused and contralateral striatum of R6/2 chol-high mice ($N = 4$). Hoechst (Ho, blue) was used to counterstain nuclei. Scale bar in F and H: $10 \mu\text{m}$. Graphs in (G and I) represent the intensity of SREBP2 normalized on nuclei (%). Data are shown as scatterplots with means \pm standard error. Each dot corresponds to the value obtained from each image. Statistics: Student's *t*-test (** $P < 0.01$; **** $P < 0.0001$).
- J, K Representative high-magnification confocal images of immunostaining against SREBP2 (red) and NeuN (J) or GFAP (K) (green) on coronal sections of brains from R6/2 chol-high mice. A cell in the infused striatum, positive for NeuN and GFAP, respectively, is shown. Hoechst (Ho, blue) was used to counterstain nuclei. Scale bars: $1 \mu\text{m}$.

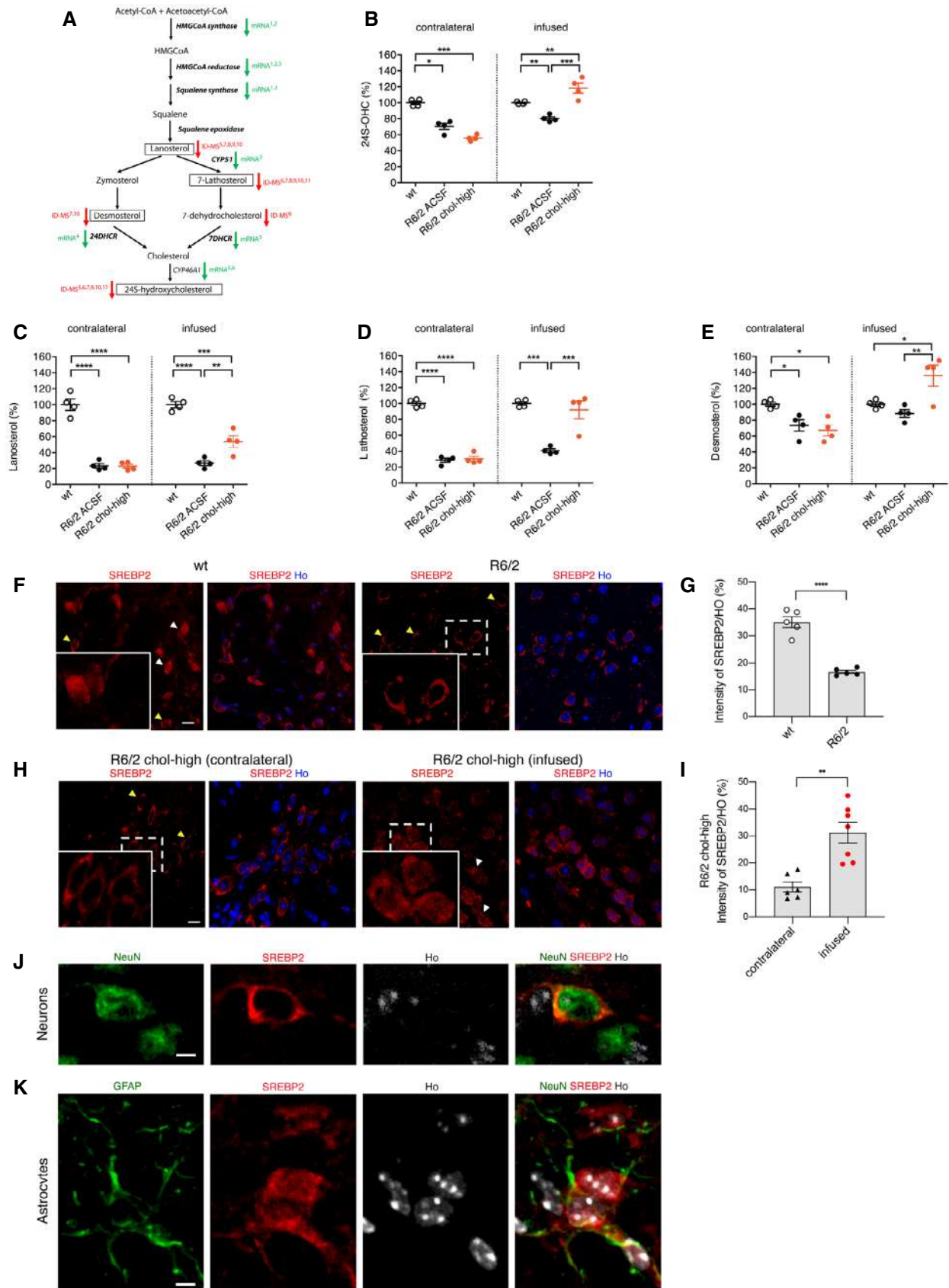


Figure 4.

microscopy using pre-embedded immunogold labeling for EM48 to visualize muHTT in striatal neurons of wt, R6/2, R6/2 ACSF, and R6/2 chol-high mice. Immunogold-labeled HTT fragments were

found either as protofibril-like structures of about 300 nm or dispersed in the cytoplasm and nucleus of striatal neurons from R6/2 ACSF mice (Fig 5H). In contrast, muHTT was found dispersed and

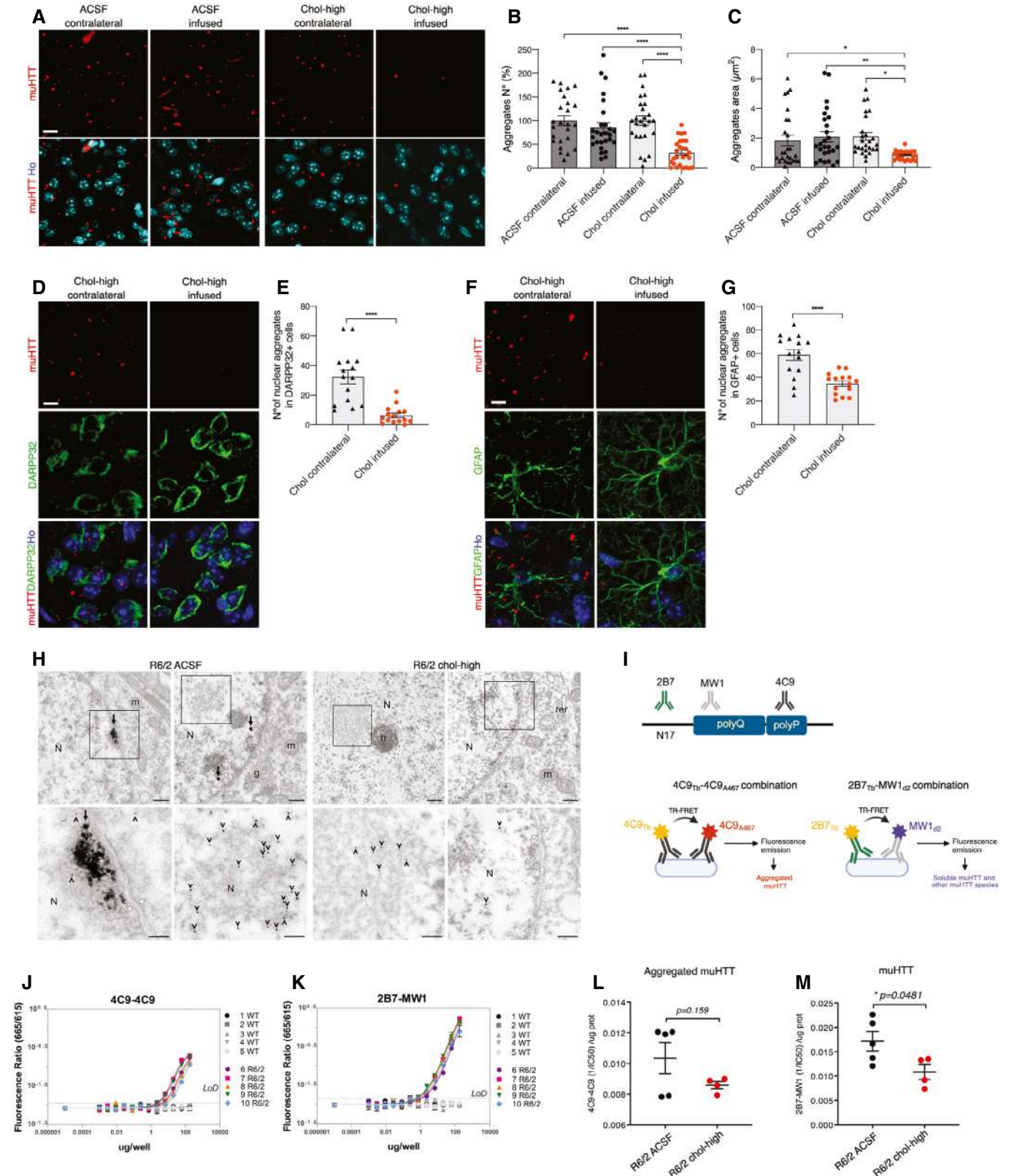


Figure 5.

Figure 5. Striatal infusion of the high dose of cholesterol rescues muHTT aggregation in the striatum of HD mice.

- A–G Immunolabeling of muHTT aggregates (red) in R6/2 ACSF and R6/2 chol-high mice ($N = 3/\text{group}$). Zoom of representative confocal images of immunostaining against muHTT aggregates (red) showing muHTT aggregates positive for EM48 antibody in the infused and contralateral striatum (A) and relative quantification of number (B) and size (C) of aggregates. Hoechst (Ho, blue) was used to counterstain nuclei. 18 images/animal were analyzed from 9 sections throughout the entire striatum. Representative confocal images of immunostaining against muHTT (red) and DARPP32 (D) or GFAP (F) (green) showing muHTT aggregates positive for EM48 antibody in the infused striatum in neurons or astrocytes and relative quantification (E, G). Hoechst (Ho, blue) was used to counterstain nuclei. All values are expressed as % above the mean of aggregates in the contralateral striatum of R6/2 ACSF or of R6/2 chol-high. The data in (B, C, E, and G) are shown as scatterplots with means \pm standard error. Each dot corresponds to aggregates counted in all the images from 3 animals. Scale bars: 10 μm (A) and 5 μm (D, F). Statistics: one-way ANOVA followed by Newman–Keuls multiple comparison tests ($*P < 0.05$; $**P < 0.01$; $****P < 0.0001$).
- H TEM images of EM48 pre-embedding immunogold labeling showing muHTT aggregates in the striatal neuron cell bodies of R6/2 ACSF mice and R6/2 chol-high mice (upper panels). In the lower panels, muHTT aggregates are clearly visible and the magnifications show the area indicated by the black square in the upper images. Arrows indicate large muHTT aggregates with a fibrous structure in the nucleus, and arrowheads indicate single 10-nm gold particles in MSN. Nucleus (N), nucleolus (n), mitochondrion (m), rough endoplasmic reticulum (rer), Golgi apparatus (g), and white arrows indicate the nuclear envelope ($N = 3$ animals/group). Scale bars: 700 nm and 300 nm.
- I–M Quantification of aggregated and total muHTT in the infused striatum of HD mice after 4-week cholesterol infusion by TR-FRET analysis using different antibody pairs. Schematic representation of employed TR-FRET assay (I). Preliminary assessment of the sustainability of the assay in wt and R6/2 striata ($N = 5/\text{group}$) using 4C9-4C9 and 2B7-MW1 antibodies in combination to detect, respectively, muHTT aggregates (J), and total muHTT (K). Quantification of muHTT aggregates (L) and soluble and other muHTT species (M) in the infused striata of R6/2 ACSF and R6/2 chol-high mice. Data in (J–M) are shown as scatterplots with means \pm standard error. Each dot corresponds to the value obtained from one striatum. Statistics: Student's t -test ($*P < 0.05$).

never composed in a fibril network in striatal neurons from R6/2 chol-high animals (Fig 5H).

We next sought to apply a more reliable quantitative measure of muHTT oligomers during the early phases of aggregation process (Baldo *et al*, 2012; Weiss *et al*, 2012). For this purpose, we employed a time-resolved Förster resonance energy transfer (TR-FRET)-based immunoassay (Baldo *et al*, 2012) to quantify muHTT species in striatal tissues from R6/2 ACSF and R6/2 chol-high mice using specific antibodies. In particular, we used the 4C9-4C9 combination to detect specifically muHTT aggregates, while the 2B7-MW1 combination recognized soluble muHTT and other muHTT species (Fig 5I). First, we validated the feasibility and specificity of the assay in striatal samples of wt and R6/2 mice (Fig 5J and K). Then, we quantified TR-FRET detection of aggregated muHTT (4C9-4C9 combination) and found no difference between R6/2 chol-high and R6/2 ACSF mice (Fig 5L). In contrast, a significant decrease in soluble and other muHTT species (2B7-MW1 combination) was found in the striatum of R6/2 chol-high compared to R6/2 ACSF mice (Fig 5M). Collectively, these findings demonstrate that striatal infusion of cholesterol counteracts the aggregation of different muHTT species which may ultimately contribute to reduced toxicity in HD mice.

Striatal infusion of cholesterol reverses lysosomal accumulation in HD mice

We next sought to test whether striatal infusion of cholesterol can stimulate clearance pathways involving autophagy or lysosomal activity. For this purpose, we performed immunofluorescence staining on brain sections of wt, R6/2 ACSF, and R6/2 chol-high mice with antibodies against p62, a protein involved in the recognition and delivery of substrates to autophagosomes, and against the lysosomal-associated membrane protein LAMP1. p62 (red signal) was present in round bodies in the perinuclear area of wt cells but was present primarily as cellular dots in the contralateral and infused striatum of R6/2 ACSF and R6/2 chol-high mice (Fig 6A). Quantification analysis revealed an increase in p62 dots in all R6/2 animal groups compared to wt mice (Fig 6B), suggesting a high basal autophagy in the presence of muHTT, which cholesterol treatment did not significantly influence.

In contrast, immunofluorescence staining for LAMP1 (Fig 6C) and relative quantification (Fig 6D) showed increased LAMP1 density in

the striatum of R6/2 ACSF mice and in the contralateral striatum of R6/2 chol-high compared to wt mice, suggesting an accumulation of lysosomes in HD cells. Of note, LAMP1 density was restored to physiological levels in the infused striatum of R6/2 chol-high mice (Fig 6C).

Taken together, these results suggest that striatal infusion of cholesterol in HD mice may affect lysosome function and counteract muHTT aggregates by reducing their accumulation in HD cells.

Discussion

In this work, we identified the therapeutic dose of cholesterol that can prevent both motor and cognitive defects in HD mice and ameliorate synaptic transmission while reducing muHTT aggregate load in the brain. Moreover, we showed that all tested doses of infused cholesterol prevented cognitive decline. In particular, the lower dose of cholesterol used here (15 μg) is similar to that employed in our previous work in which we delivered cholesterol via brain-targeted polymeric nanoparticles (Valenza *et al*, 2015b). The success in preventing mouse cognitive decline in both studies using this cholesterol dose is in line with reports highlighting a link between cholesterol and cognitive impairments in adult patients (Martin *et al*, 2014; Segatto *et al*, 2014). In contrast, only the highest dose of cholesterol we used here could also counteract progression of motor defects, suggesting that restoration of motor circuit function may require a higher cholesterol dose.

Cholesterol infusion can exert these beneficial effects by several mechanisms. One is improving the function of residual synaptic circuits. In fact, we showed here that striatal infusion of cholesterol restored both glutamatergic activation and GABAergic inhibition in MSNs of HD mice. Accordingly, exogenous cholesterol increased the number of total and docked vesicles of glutamatergic synapses, accounting for the increasing probability of vesicle release demonstrated through partial normalization of glutamatergic spontaneous synaptic current frequency. Furthermore, exogenous cholesterol reduced the number of GABAergic inhibitory synapses, as also demonstrated by a reduced frequency of spontaneous inhibitory currents. The magnitude of rescue was more evident for inhibitory transmission/synapses, suggesting circuit-specific signaling mechanisms in which cholesterol may act differently. Specific proteins involved in

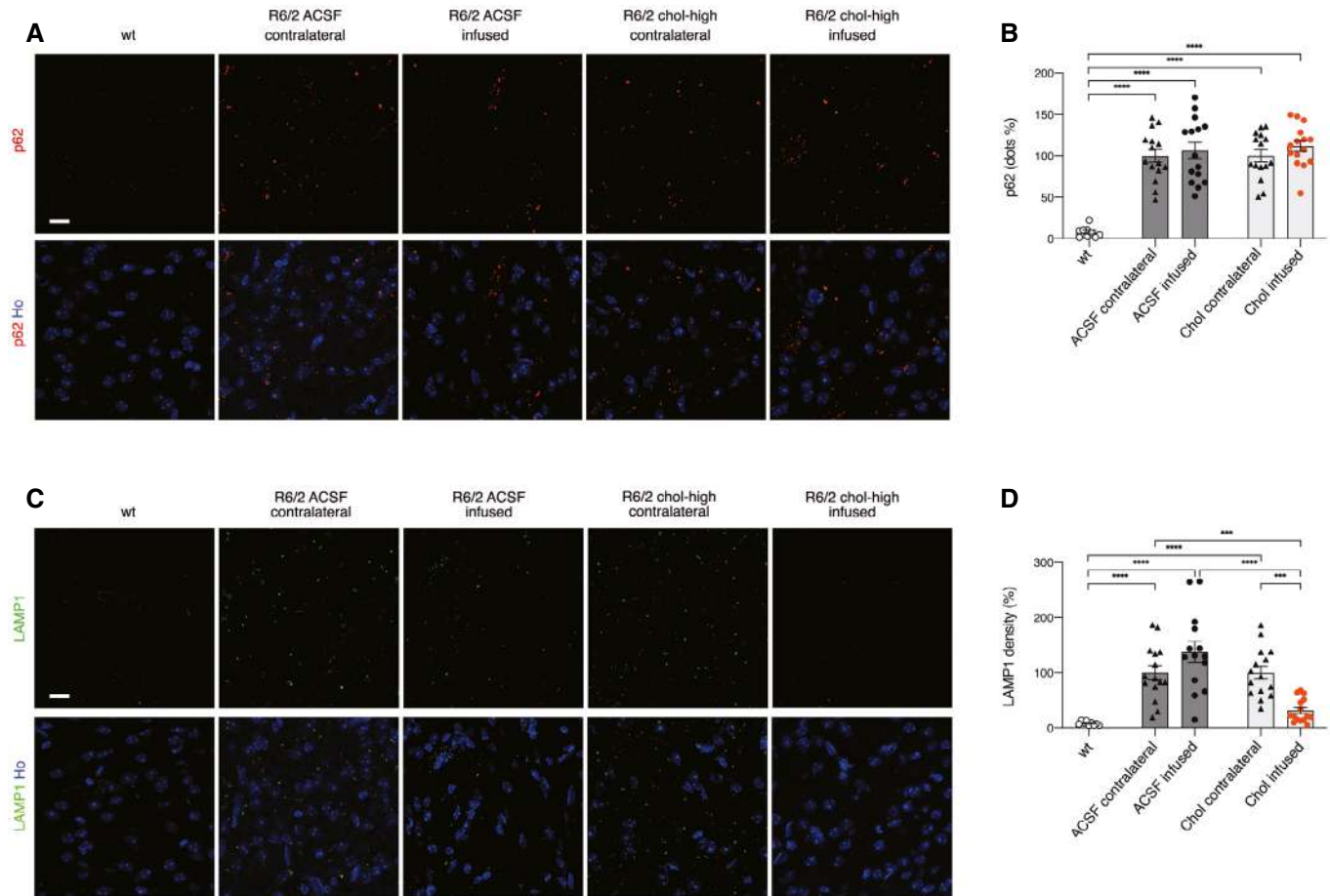


Figure 6. Striatal infusion of the high dose of cholesterol promotes lysosomal clearance and autophagy in the striatum of HD mice.

A–D Representative confocal images showing p62 (A, red) or LAMP1 (C, green) in the infused and contralateral striatum on brain coronal sections from wt, R6/2 ACSF, and R6/2 chol-high mice ($N = 3/\text{group}$). Hoechst (Ho, blue) was used to counterstain nuclei. Quantification of dots for p62 (B) and density for LAMP1 (D) in the contralateral and infused striatum of R6/2 ACSF and R6/2 chol-high mice. 20 images from 3 sections in the middle of the striatum for each animal were acquired and analyzed. The data in (B and D) are shown as scatterplots with means \pm standard error, and each dot corresponds to the value obtained from each image. Statistics: one-way ANOVA followed by Newman–Keuls multiple comparison tests ($***P < 0.001$; $****P < 0.0001$). Scale bars in (A, C): 10 μm .

Source data are available online for this figure.

inhibitory transmission might bind cholesterol for their function, exerting a major effect on this circuit with respect to the excitatory one.

Exogenous cholesterol may also act by partnering specifically with cellular proteins and influencing cell physiology. A recent proteome-wide mapping of cholesterol-interacting proteins in mammalian cells detected more than 250 proteins that bind cholesterol. These proteins are involved in vesicular transport, degradation pathways, and membrane structure and dynamics, and many of them are linked to neurological disorders (Hulce *et al*, 2013). Among them, several membrane receptors bind cholesterol in cholesterol-enriched lipid rafts at the plasma membrane, and their interaction determines their function (Oddi *et al*, 2011; Guixà-González *et al*, 2017; Rahbek-Clemmensen *et al*, 2017; preprint: Casarotto *et al*, 2020). Once infused, exogenous cholesterol localizes at the plasma membrane and it might renormalize the stoichiometry between plasma proteins and receptors and rescue the impaired intracellular and receptor signaling in HD.

Cholesterol supplementation in animal models of Pelizaeus–Merzbacher disease and of multiple sclerosis results in a permissive environment for myelin repair, preventing disease progression (Saher *et al*, 2012; Berghoff *et al*, 2017). Changes in myelin also occur in different HD animal models (Xiang *et al*, 2011; Teo *et al*, 2016) and in patients showing pre-HD signs (Rosas *et al*, 2018). In those studies, overexpression of muHTT in primary oligodendrocytes was accompanied by reduced expression of cholesterol biosynthesis genes and myelin-binding protein *in vitro* (Xiang *et al*, 2011), and muHTT interfered with oligodendrocyte maturation *in vivo* (Rosas *et al*, 2018). However, striatal infusion of cholesterol failed to promote myelin repair in the R6/2 HD mouse model used here. Although restoration of myelin defects in this rapid, aggressive HD model was not observed under our experimental conditions, cholesterol administration may normalize myelin phenotypes in less aggressive HD murine models such as the YAC128 and knock-in mice (Huang *et al*, 2015; Teo *et al*, 2016).

In this study, we also found that striatal infusion of the high dose of cholesterol restored the primary defect of brain cholesterol biosynthesis in HD mice. Cholesterol biosynthesis, as judged by cholesterol precursor levels (Valenza *et al*, 2007b, 2010) or its synthesis rate (Shankaran *et al*, 2017), is significantly reduced in the striatum of HD mice before disease onset, as we confirm here. The significant increase in levels of cholesterol precursors, along with increased nuclear translocation of SREBP2 mainly in astrocytes, is consonant with an enhanced endogenous cholesterol biosynthesis in the striatum of R6/2 chol-high mice. This outcome is specific for the infused striatum and the highest dose of cholesterol, possibly indicating that excess exogenous cholesterol is converted into 24S-OHC in neurons that in turn stimulates endogenous synthesis in astrocytes (Janowski *et al*, 1999; Abildayeva *et al*, 2006). Accordingly, the level of 24S-OHC was also increased in the infused striatum of R6/2 chol-high mice in this work, supporting evidence that synthesis and catabolism are closely related in the disease state as well, as previously reported (Shankaran *et al*, 2017). This connection is in agreement with two recent studies showing that adeno-associated virus over-expressing Cyp46A1, the neuronal-specific enzyme for cholesterol conversion to 24S-OHC, increased lanosterol and desmosterol levels in the striatum of R6/2 mice and zQ175 mice (Boussicault *et al*, 2016; Kacher *et al*, 2019). However, we cannot exclude that different and independent mechanisms participate to increase cholesterol precursors and 24S-OHC levels in HD striatum following striatal infusion of cholesterol.

The increase in cholesterol precursors may also explain the reduction that we observed in muHTT aggregates in R6/2 mice. Lanosterol reverses protein aggregation in cataracts (Zhao *et al*, 2015), suppresses the aggregation and cytotoxicity of misfolded proteins linked to neurodegenerative diseases (Upadhyay *et al*, 2018), and promotes autophagy in Parkinson's disease models (Lim *et al*, 2012). In our study, clearance of muHTT in R6/2 chol-high mice may have been secondary to stimulation of mTORC1 activity (Narita *et al*, 2011; Lee *et al*, 2015). Several studies have established links between mTORC1 activation and cholesterol metabolism. For example, the expression of the active form of the mTORC1 regulator, Rheb, in the HD mouse brain ameliorates aberrant cholesterol homeostasis and increases autophagy (Lee *et al*, 2015). In addition, mTORC1 activation increases nuclear translocation of SREBP2 and sterol synthesis (Yecies & Manning, 2011; Owen *et al*, 2012). Moreover, an increase in lysosomal cholesterol has been reported to activate mTORC1 (Castellano *et al*, 2017), and cholesterol is reduced in HD lysosomes (Koga *et al*, 2011). How exactly the increased nuclear translocation of SREBP2 and decreased muHTT aggregates observed here are linked to mTORC1 activity and lysosomes is currently unknown. Exogenous cholesterol, which partially co-localizes with late endosomes, may also act on the axonal transport, which is compromised in HD (Gunawardena *et al*, 2003; Gauthier *et al*, 2004; White *et al*, 2015), and contribute to diminish organelles accumulation (Ferguson, 2018).

The fact that we found no significant reduction in aggregated muHTT with the TR-FRET assay (4C9-4C9 combination) suggests that cholesterol is not sufficient to degrade muHTT oligomers at the beginning of aggregation process. However, the significant decrease in muHTT species (assessed by TR-FRET with B27-MW1 combination) coupled with the reduction in macro-aggregates (assessed by immunofluorescence) and the absence of amyloid-like fibers (by EM) supports the hypothesis that cholesterol mitigates different steps of

muHTT aggregation *in vivo* and that its targeted administration to the brain might be useful for reducing muHTT toxicity in HD.

In conclusion, we demonstrate a dose-dependent, disease-modifying effect of striatal infusion of cholesterol in HD mice. This work and our previous findings (Valenza *et al*, 2015b) support the hypothesis that reduced cholesterol biosynthesis contributes to disease pathogenesis and that cholesterol delivery to the HD brain is beneficial. Further studies will explore the potential for long-term cholesterol release in HD animal models with a longer lifespan and slower disease progression, enabling chronic treatment in older, symptomatic mice. In addition, with the aim of translating the delivery of cholesterol to the clinic, new brain-permeable nanoparticles have been developed (Belletti *et al*, 2018) that enable the controlled release of a higher cholesterol content to the brain. This advance may facilitate progress toward the goal of achieving the therapeutic dose identified here by systemic injection.

Materials and Methods

Colony management

All the *in vivo* experiments were carried out in accordance with Italian Governing Law (D.lgs 26/2014; Authorization n.324/2015-PR issued May 6, 2015 by Ministry of Health); the NIH Guide for the Care and Use of Laboratory Animals (2011 edition) and EU directives and guidelines (EEC Council Directive 2010/63/UE).

Our R6/2 colony lifespan was approximately of 13 weeks, and it was maintained through the male line exclusively (Mangiarini *et al*, 1996). Mice were weaned and then genotyped at 3 weeks of age (\pm 3 days). Transgenic R6/2 males were paired with non-carrier females (B6CBAF1/J, purchased from Charles River). CAG repeat length and changes that could affect strain productivity, general behavior, litter size, pup survival, genotype frequency, phenotype were constantly monitored with a range between 200 and 250 CAGs. Mice were housed under standard conditions ($22 \pm 1^\circ\text{C}$, 60% relative humidity, 12 h light/dark schedule, 3–4 mice/cage, with free access to food and water). After PCR genotyping (Mangiarini *et al*, 1996), male and female mice were included and randomly divided into experimental groups. Littermates were included as controls.

Surgical implantation of osmotic mini-pumps

Avertin 100% was prepared diluting 5 g of 2,2,2-Tribromoethanol (Sigma-Aldrich, #T48402-25G) in 5 ml of 2-methyl-2-butanol (Sigma-Aldrich, #240486). Mice were deeply anesthetized using 15 μl of Avertin 2.5% per gram of body weight. Once responses to tail/toe pinches and intactness of the ocular reflex were assessed, scalp was shaved and mice were placed into a stereotaxic apparatus (2-Biological Instrument). A subcutaneous pocket was made on the back of the animals, in the midscapular area, to insert the osmotic mini-pump (Alzet, pump model 1004, #0009922). The brain infusion microcannula (brain infusion kit n°3, Alzet, #0008851), connected to the mini-pump through a catheter, was stereotaxically implanted into mice right striatum (stereotaxic coordinates 1.75 mm mediolateral, 0.5 mm anteroposterior, 3 mm dorsoventral; from Paxinos G and Watson C. The Rat Brain in Stereotaxic Coordinates. Academic Press, San Diego).

Following surgery, mice were removed from the stereotaxic apparatus and placed on a warm cover to awaken from anesthesia. The mini-pump infused at constant rate (0.11 μ l/h) for 28 days a solution of artificial cerebrospinal fluid (ACSF); or methyl- β -cyclodextrin (Sigma-Aldrich, #M7439-1G) diluted in ACSF; or water-soluble methyl- β -cyclodextrin (M β CD)-balanced cholesterol (Sigma-Aldrich, #C4951-30MG) supplemented with 5 μ M free cholesterol, diluted in ACSF. ACSF was prepared mixing two solutions (A and B) in a 1:1 ratio. Solution A was prepared by diluting 8.66 g of NaCl (Sigma-Aldrich, #53014), 0.224 g of KCl (Sigma-Aldrich, #P9333), 0.206 g of CaCl₂ 2H₂O (Sigma-Aldrich, #C3881) and 0.163 g of MgCl₂ 6H₂O (Sigma-Aldrich, #M9272) in 500 ml of sigma water. Solution B was prepared by diluting 0.214 g of Na₂HPO₄ 7H₂O (Sigma-Aldrich, #59390) and 0.027 g of NaH₂PO₄ H₂O (Sigma-Aldrich, #59638) in 500 ml of sigma water.

Assessment of post-operative pain and distress was performed using a specific table for pain scoring based on behavioral indicators of well-being and monitoring mice body weight (Lloyd & Wolfensohn, 1998).

Behavioral tests

Mice behavior was evaluated from pre-symptomatic stages (5–6 weeks of age) until late-symptomatic stages of the disease (10–11 weeks of age). Animals were assigned randomly, and sex was balanced in the various experimental groups. All the behavioral analyses were performed in blind.

Rotarod

Motor coordination and balance were evaluated on the rotarod test. Mice were first trained to walk on a rotating bar at constant speed of 4 rpm (apparatus model 47600, Ugo Basile), for 300 s. 1 h after this training phase, mice motor performance was evaluated in an accelerating task (from 4 to 40 rpm) over a 300-s period. For three consecutive days, mice performed three daily trials, with an inter-trial interval of 30 min. Latency to fall was recorded for each trial and averaged.

Activity cage

Spontaneous locomotor activity was evaluated by the activity cage test, in presence of a low-intensity white light source. The animal was placed in the center of the testing, transparent, arena (25 cm \times 25 cm) (2Biological Instrument) and allowed to freely move for an hour. Following 15 minutes of habituation, both horizontal and vertical motor activities were assessed by an automated tracking system (Actitrack software, 2Biological Instrument) connected to infrared sensors surrounding the arena. Total distance travelled, mean velocity speed, stereotyped movements, and numbers of rearings were evaluated. The % of time that mice explored the periphery or the center area of the was evaluated as a measure of anxiety-like behavior.

Novel object recognition (NOR) test

Long-term memory was evaluated by the NOR test, using a gray-colored, non-reflective arena (44 \times 44 \times 44 cm). All phases of the test were conducted with a low-intensity white light source. In a first habituation phase, mice were placed into the empty arena for 10 min. The habituation phase was followed by the familiarization

one, in which two identical objects (A' and A'') were presented to each animal for 10 min. Twenty-four hours later, during the testing phase, the same animals were exposed to one familiar object (A'') and a new object (B) for 10 min. A measure of the spontaneous recognition memory was represented by the index of discrimination, calculated as (time exploring the novel object – time exploring the familiar object) / (time exploring both objects) \times 100. Mice exploring < 7 s were excluded from the analysis due to their inability to perform the task.

PCA analysis

Principal component analysis (PCA) was performed using the R package ade4 (Pavoine *et al*, 2004).

Gas chromatography–mass spectrometry (GC-MS) analysis for neutral sterols and 24S-hydroxycholesterol

To a screw-capped vial sealed with a Teflon-lined septum were added 50 μ l of homogenates together with 1,000 ng of D4-lathosterol (CDN Isotopes, Canada), 100 ng of D6-lanosterol (Avanti Polar Lipids, USA), 400 ng of D7-24S-hydroxycholesterol (Avanti Polar Lipids, USA), and 50 μ g of D6-cholesterol (CDN Isotopes, Canada) as internal standards, 50 μ l of butylated hydroxytoluene (BHT) (5 g/l), and 25 μ l of EDTA (10 g/l). Argon was flushed through to remove air. Alkaline hydrolysis was allowed to proceed at room temperature (22°C) for 1 h in the presence of 1 M ethanolic potassium hydroxide solution under magnetic stirring. After hydrolysis, the neutral sterols (cholesterol, lathosterol, and lanosterol) and oxysterols (24S-OHC) were extracted three times with 5 ml of hexane. The organic solvents were evaporated under a gentle stream of argon and converted into trimethylsilyl ethers with BSTFA-1% TMCS (Cerilliant, USA) at 70°C for 60 min. Analysis was performed by gas chromatography–mass spectrometry (GC-MS) on a Clarus 600 gas chromatograph (Perkin Elmer, USA) equipped with Elite-5MS capillary column (30 m, 0.32 mm, 0.25 μ m. Perkin Elmer, USA) connected to Clarus 600C mass spectrometer (Perkin Elmer, USA). The oven temperature program was as follows: initial temperature 180°C was held for 1 min, followed by a linear ramp of 20°C/min to 270°C, and then a linear ramp of 5°C/min to 290°C, which was held for 10 min. Helium was used as carrier gas at a flow rate of 1 ml/min and 1 μ l of sample was injected in splitless mode. Mass spectrometric data were acquired in selected ion monitoring mode. Peak integration was performed manually, and sterols were quantified against internal standards, using standard curves for the listed sterols (Leoni *et al*, 2017).

Electrophysiological analysis

Experiments were performed on submerged brain slices obtained from adult mice (12 weeks of age) after 4-week long infusion of ACSF or cholesterol directly into the striatum. Animals were anesthetized by inhalation of isoflurane and decapitated. The head was rapidly submerged in ice-cold (\sim 4°C) and oxygenated (95% O₂ – 5% CO₂) cutting solution containing: Sucrose 70 mM, NaCl 80 mM, KCl 2.5 mM, NaHCO₃ 26 mM, Glucose 15 mM, MgCl₂ 7 mM, CaCl₂ 1 mM and NaH₂PO₄ 1.25 mM. Striatal coronal slices (300- μ m-thick) were cut using a vibratome (DTK-1000, Dosaka EM, Kyoto, Japan) and allowed to equilibrate for at least 1 hour in a chamber filled

with oxygenated ACSF containing: NaCl 125 mM, KCl 2.5 mM, NaHCO₃ 26 mM, Glucose 15 mM, MgCl₂ 1.3 mM, CaCl₂ 2.3 mM and NaH₂PO₄ 1.25 mM. The slices collected from the hemisphere ipsilateral to the infusion site were transferred to a submerged-style recording chamber at room temperature (~ 23–25°C) and were continuously perfused at 1.4 ml/min with ACSF. The chamber was mounted on an E600FN microscope (Nikon) equipped with 4× and 40× water immersion objectives (Nikon) and connected to a near-infrared CCD camera for cells visualization.

Data were obtained from striatal projection medium spiny neurons (MSNs) using the whole-cell patch-clamp technique in both voltage- and current-clamp mode. The patch pipette was produced from borosilicate glass capillary tubes (Hilgenberg GmbH) using a horizontal puller (P-97, Sutter instruments) and filled with an intracellular solution containing: Cs-methanesulphonate 120 mM, KCl 5 mM, CaCl₂ 1 mM, MgCl₂ 2 mM, EGTA 10 mM, Na₂ATP 4 mM, Na₃GTP 0.3 mM, Hepes 8 mM and lidocaine N-ethyl bromide 5 mM (added to inhibit firing by blocking intracellularly the voltage-sensitive Na⁺ channels) (pH adjusted to 7.3 with KOH). Spontaneous excitatory postsynaptic currents (sEPSCs), mediated by the activation of ionotropic glutamate receptors, were recorded from MSNs at a holding potential of -70 mV, whereas spontaneous inhibitory postsynaptic currents (sIPSCs), elicited by the activation of GABA_A receptors, were assessed at a holding potential of 0 mV. The signals were amplified with a MultiClamp 700B amplifier (Molecular Devices) and digitized with a Digidata 1322 computer interface (Digitata, Axon Instruments Molecular Devices, Sunnyvale, CA). Data were acquired using the software Clampex 9.2 (Molecular Devices, Palo Alto, CA, U.S.A.), sampled at 20 kHz and filtered at 2 kHz.

The off-line detection of spontaneous postsynaptic currents (sPSCs) were performed manually using a custom-made software in Labview (National Instruments, Austin, TX, U.S.A.). The amplitudes of sPSCs obeyed a lognormal distribution. Accordingly, the mean amplitude was computed as the peak of the lognormal function used to fit the distribution. Intervals (measured as time between two consecutive sPSCs) for spontaneous events were distributed exponentially and the mean interval was computed as the tau (τ_{interval}) value of the mono-exponential function that best fitted this distribution. The reciprocal of τ ($1/\tau$) is the mean of the instantaneous frequencies of sPSCs. Furthermore, the analysis of the membrane capacitance (C_m) and the input resistance (R_{in}) was performed using Clampfit 10.2 (Molecular Devices, Palo Alto, CA, U.S.A.). C_m was estimated from the capacitive current evoked by a -10 mV pulse, whereas R_{in} was calculated from the linear portion of the I-V relationship obtained by measuring steady-state voltage responses to hyperpolarizing and depolarizing current steps.

Immunohistochemistry analysis

Mice were anesthetized by intraperitoneal injection of Avertin 2.5% and transcardially perfused with PFA 4%. Brains were post-fixed overnight in the same solution at 4°C and then in 30% sucrose to prevent ice crystal damage during freezing in OCT.

Immunohistochemistry was performed on 15 μm coronal sections. Epitopes were demasked at 98°C with NaCitrate 10 mM and then slices were incubated with the following primary antibodies for 3 h at RT: rabbit anti-SREBP2 (1:2,000; gift by T. Osborne) (Seo et al, 2012),

mouse anti-SREBP2 (1:100; Ls-Bio, LS-C179708), rabbit anti-DARPP32 (1:100; Cell Signalling, 2306), mouse anti-NeuN (1:100; Millipore, MAB377), rabbit anti-NeuN (1:500; Abcam, AB104225), rabbit anti-GFAP (1:250; Dako, Z0334), mouse anti-Huntingtin clone EM48 (1:100; Millipore, MAB5374), rabbit anti-p62 (1:100; Abcam, AB109012) or rat anti-LAMP1 (1:50; Santa Cruz, SC19992), rabbit anti-TGN46 (1:60; Abcam, ab16059), rabbit anti-Rab9A (1:50; EuroClone, BK5118S-CST), rabbit anti-calnexin (1:100; Life technologies, PA534754), mouse anti PMCA-ATPase (1:500; Thermo Fisher Scientific, MA3-914). Anti-rabbit or anti-mouse Alexa Fluor 568-conjugated goat secondary antibodies (1:500; Invitrogen), anti-rabbit Alexa Fluor 633-conjugated goat secondary antibodies (1:500; Invitrogen) or anti-mouse Alexa Fluor 488-conjugated goat secondary antibodies (1:500; Invitrogen) were used for detection (1 h at RT) depending on the primary antibodies. Sections were counterstained with the nuclear dye Hoechst 33258 (1:10,000, Invitrogen) and then mounted under cover slips using Vectashield (Vector Laboratories).

Image acquisition and quantification

Confocal images were acquired with a LEICA SP5 laser scanning confocal microscope. Laser intensity and detector gain were maintained constant for all images and 3–10-z steps images were acquired.

To count aggregates in the different brain areas 34 images/mice taken from three R6/2-ACSF and three R6/2-chol mice were made at 40×. For the striatum 18 images/animal were analyzed from 9 sections throughout the entire striatum. For the cortex, 10 images for each animal were analyzed from 3 sections and for the hippocampus, 6 images for each animal/condition were analyzed from 3 sections. To quantify the number of aggregates, ImageJ software was used to measure the fluorescence. Images were divided into three-color channels and the same global threshold was set. In both R6/2-ACSF and R6/2-chol mice, the total number of aggregates in the infused hemisphere was normalized to the total number of aggregates in the contralateral hemisphere. To count the number of aggregates in the nucleus of DARPP32 or GFAP-positive cells, the NIS software was used.

To quantify the amount of SREBP2 inside the nucleus, images were acquired at 40× and were segmented using the NIS software. A threshold was applied to both channels and the intensity ratio of SREBP2/Hoechst was measured.

To count the dots of p62 and LAMP1 in the different brain areas 20 images/mice taken from three R6/2-ACSF and three R6/2-chol mice were made at 40×. For the striatum 10 images/animal were analyzed from 3 sections in the middle of the striatum. For the cortex, 10 images for each animal were analyzed from 3 sections. To quantify the number of dots, ImageJ software was used to measure the fluorescence. Images were divided into three-color channels and the same global threshold was set. In both R6/2-ACSF and R6/2-chol mice, the total number of dots in the infused hemisphere was normalized to the total number of dots in the contralateral hemisphere.

Electron microscopy

Sample preparation

Mice were anesthetized by intraperitoneal injection of 10 mg/ml Avertin (Sigma) and transcardially perfused using a fixative solution

of: 2.5% glutaraldehyde (#16220 Electron Microscopy Sciences (EMS), Hartfield, PA), and 2% paraformaldehyde (P16148 EMS) in sodium cacodylate buffer 0.15 M (pH 7.4) (#12300 EMS). Brains were removed and post-fixed for additional 24 h at 4°C. Brains were cut in 100 μm -thick coronal slices by using a Leica VT1000S vibratome. Sections were collected in sodium cacodylate buffer 0.1 M and striatum, and corpus callosum were manually dissected for staining and embedding. Samples were then washed with cold sodium cacodylate buffer 0.1 M and then post-fixed in a reduced osmium solution (i.e., 1.5% potassium ferrocyanide (#20150 EMS) with 2% osmium tetroxide (#19170 EMS) in 0.15 M cacodylate buffer, for 1 h in ice. After the first heavy metal incubation, the tissues were washed with ddH₂O at room temperature and then placed in the 0.22 μm -Millipore-filtered 1% thiocarbohydrazide (TCH) (#21900 EMS) in ddH₂O solution for 20 min, at room temperature. Tissues were then rinsed again in ddH₂O and incubated in 2% osmium tetroxide in ddH₂O for 30 min, at room temperature. After several washings at room temperature in ddH₂O, they were then placed in 1% uranyl acetate (aqueous), overnight at 4°C. Samples were washed and then incubated *en-bloc* in Walton's lead aspartate solution (0.066 gr lead nitrate (#17900 EMS) dissolved in 10 ml of 0.003 M aspartic acid solution, pH 5.5) at 60°C for 30 min. The tissues were still washed and then dehydrated with an ethanol series and finally placed in anhydrous ice-cold acetone for 10 min. Infiltration was performed with acetone (#179124 Sigma-Aldrich)—Durcupan ACM[®] (#14040 EMS) mixture with 3:1 volume ratio for 2 h, then 1:1 overnight. The tissues were left for 2 h in pure resin and then embedded in Durcupan ACM[®] resin and placed in a 60°C oven for 48 h for polymerization.

TEM imaging

Ultrathin sections 70 nm-thick were prepared by an UltraCut E ultramicrotome (Reichert) and collected on TEM copper grids, which were then observed by a LEO 912AB microscope (Carl Zeiss), equipped with a thermionic W electron source and operating at an acceleration voltage of 100 kV. For quantitative analyses, images with a resolution of 1,024 \times 1,024 pixels were acquired using a bottom mount Esivision CCD-BM/1K system (ProScan Camera). Quantitative measurements were performed by ImageJ 1.47v, and measuring the following parameters: total SVs density as the number of SVs divided by the pre-synaptic area (μm^2), number of docked vesicles per active zone (AZ) length (μm), pre-synaptic area (μm^2), active zone (AZ) length (μm) and PSD area (nm^2) and PSD length (nm). For myelin analyses, we measured the G-ratio, as the diameter of the axon/outer diameter of the myelinated fiber (of at least 300 myelinated axons in 3 mice group) and the myelin periodicity that was measured as the mean distance between two major dense lines, in at least 45 randomly chosen myelin sheaths in 3 mice group.

FIB-SEM imaging and ion cutting

The following procedure was used to mount specimens with the aim to minimize their electrical charging during the FIB-SEM imaging and ion cutting. Resin blocs were mounted on aluminum specimen pins and trimmed with a glass knife using an ultramicrotome, to expose the tissue on all four sides. Silver paint (#16031 Ted Pella, Redding, US) was used to electrically ground the edges of the tissue block to the aluminum pin. The entire specimen was then coated

with a thin layer of gold by means of a Cressington 208-HR sputter coater (Cressington Scientific Instruments, Watford, UK) equipped with a pure gold target (Ted Pella, Redding, US), to finely mount it into the SEM chamber in view of the FIB-SEM imaging. The sample 3D ultrastructural imaging was performed by using a Thermo Scientific Helios G4 Dual Beam (Eindhoven, NL) being this instrument constituted by the combination of a high-resolution SEM equipped with a Schottky field emission gun and a focused gallium ion beam. First, the region of interest was chosen on the surface of the tissue block, and then, a protective layer of platinum was deposited on top of the area to be imaged using a gallium ion beam with 30 kV of acceleration voltage. Initially, a rough cross-section was milled by a 9.1 nA ion beam current, and used as window for SEM imaging. The exposed surface of this cross-section was finely polished by progressively lowering the ion beam current down to 0.44 nA and keeping the acceleration voltage at 30 kV. Afterward, layers from the finely polished cross-section were successively milled by the gallium ion beam, again using a current of 0.44 nA and an acceleration voltage of 30 kV. To remove each layer, the ion beam was continuously moved closer to the surface of the cross-section by increments of 25 nm. After each slice ion cutting, the milling process was automatically paused, and the newly exposed surface was imaged with a 2 kV acceleration voltage and 0.2 nA electron beam current using the through-the-lens backscattered electron detector (TLD-BSE). The slicing and imaging processes were continuously repeated, and a long series of images were acquired in a automated procedure. SEM images of 2048 \times 1768 pixels were acquired with voxel size of (3 \times 3 \times 25) and (4 \times 4 \times 25) nm, depending on the SEM magnification chosen.

3D reconstruction, rendering, and analysis

Serial SEM images were assembled into volume files aligned using the FIJI software (Schindelin *et al*, 2009) plugin called linear stack alignment with SIFT (Lowe, 2004). Following the images acquisition, recording, and alignment, the 3D shape of samples peculiar features (in our case excitatory and inhibitory synapses) was reconstructed layer by layer by careful segmentation. For performing the latter, and the 3D model generation, electron microscopy image stacks were then converted to 8-bit grayscale tiff format images and manually segmented using AMIRA software package (Thermo Scientific, Eindhoven, NL). Three-dimensional structures in image stacks containing hundreds or thousands of 2D orthoslices were traced individually in each plane and automatically surface rendered. The excitatory and inhibitory synapse density (n° of synapse/ μm^3) was finally measured by using Ilastik-0.5.12 software.

Sample preparation for pre-embedding immunogold labeling

Mice were anesthetized by intraperitoneal injection of 10 mg/ml Avertin (Sigma) and transcardially perfused using pH-shift formaldehyde (Berod *et al*, 1981): 4% paraformaldehyde (P16148 EMS) 0.1 M sodium acetate buffer, pH 6.0, followed by the same fixatives in 0.1 M sodium carbonate buffer, pH 10.5. Brains were removed and post-fixed for additional 24 h at 4°C and 100 μm -thick coronal slices were cut by using a Leica VT1000S vibratome. Sections were collected in 0.1 M sodium carbonate buffer, pH 10.5, and striatum was manually dissected. Striatal sections were incubated with mouse monoclonal antibodies (EM48) 1:50 (MAB5374-Millipore) that reacts with human huntingtin protein (both native

and recombinant protein) in PBS containing 1% NGS 48 hours at 4°C. After rinsing in PBS, samples were incubated with goat anti-mouse secondary antibodies (1:50) conjugated to 10 nm gold particles (Jackson ImmunoResearch) in PBS with 2% NGS overnight at 4°C. After rinsing in PBS, sections were osmicated in 1% OsO₄ in ddH₂O and stained overnight in 2% aqueous uranyl acetate. All sections used for electron microscopy (EM) were dehydrated in ascending concentrations of ethanol and acetone/eponate 12 (1:1) and embedded in Eponate 12 (#14120 EMS). Ultrathin sections (70 nm) were cut using an UltraCut E ultramicrotome (Reichert) and placed on TEM copper grids. Thin sections were counterstained with 1% aqueous uranyl acetate for 5 min followed by 1% lead citrate in ddH₂O for 2 min and examined using a LEO 912AB microscope (Carl Zeiss), equipped with a thermionic W electron source and operating at an acceleration voltage of 100 kV. Images were acquired at a resolution of 1,024 × 1,024 pixels using a bottom mount Esivision CCD-BM/1K system (ProScan Camera).

Sample preparation for post-embedding immunogold labeling

Mice were anesthetized by intraperitoneal injection of 10 mg/ml Avertin (Sigma) and transcardially perfused using pH-shift formaldehyde (Berod *et al*, 1981): 4% paraformaldehyde (P16148 EMS) 0.1 M sodium acetate buffer, pH 6.0, followed by the same fixatives in 0.1 M sodium carbonate buffer, pH 10.5. Brains were removed and post-fixed for additional 24 h at 4°C and 100 μm-thick coronal slices were cut by using a Leica VT1000S vibratome. Sections were collected in 0.1 M sodium carbonate buffer, pH 10.5, and striatum was manually dissected and post-fixed with 1% OsO₄ in ddH₂O and stained with 0.5% uranyl acetate. Samples were dehydrated in ascending concentrations of ethanol and acetone/eponate 12 (1:1) and embedded in Eponate 12 (#14120 EMS). Striatal sections were cut in a UltraCut E ultramicrotome (Reichert). Formvar carbon-coated nickel grids with 70 nm ultrathin sections were processed for GABA immunolabeling. After 5 min incubation in TBST pH 7.6, grids were incubated with rabbit antiserum against GABA (Sigma A2052, 1:10,000 in TBST) overnight at RT in a moist chamber. After the incubation, grids were washed 3 × 10 min TBST pH 7.6, followed by TBST pH 8.2 for 5 min. Grids were incubated for 2 h in goat anti-rabbit IgG conjugated to 12 nm colloidal gold (Jackson ImmunoResearch) diluted 1:20 in TBST pH 8.2. They were then washed twice in TBST pH 7.6 and rinsed in deionized water. After that, the grids were contrast-stained with 1% aqueous uranyl acetate for 5 min followed by 1% lead citrate in ddH₂O for 2 min. Sections were examined using a LEO 912AB microscope (Carl Zeiss), equipped with a thermionic W electron source and operating at an acceleration voltage of 100 kV. Images were acquired at a resolution of 1,024 × 1,024 pixels using a bottom mount Esivision CCD-BM/1K system (ProScan Camera).

FRET analysis

TR-FRET assays were performed as described previously (Weiss *et al*, 2009). Briefly, 15 μl of each homogenate was transferred to a low volume 384-well plate (Greiner) in serial dilutions starting from a defined concentration (4 μg/μl), 3 μl of antibody cocktail was then added. MuHTT aggregates were measured with 4C9-Tb/4C9-Alexa 647, using 1.93 ng/μl of 4C9-Tb and 2 ng/μl of 4C9-Alexa 647-labeled antibodies. Soluble muHTT and other muHTT

The paper explained

Problem

Cholesterol is fundamental for several activities of the brain. Peripheral cholesterol is not able to reach this organ due to the presence of the blood–brain barrier; thus, the majority of cholesterol found in the brain is synthesized locally. *De novo* synthesis of cholesterol is reduced in the Huntington's disease (HD) brain before the clinical disease onset and strategies aimed at providing cholesterol to the HD brain may be beneficial. However, the identification of the therapeutic dose of cholesterol that must reach the brain to have a maximum benefit on the multiple disease-related phenotypes is still unknown and needs to be qualified for a translational perspective.

Results

Here we infused three escalating doses of cholesterol in the brain of HD mice by the use of osmotic mini-pumps, and we identified the dose that is able to reverse both cognitive and motor abnormalities. We found that cognitive decline was prevented by all the three tested doses, while motor dysfunction was reversed only with the highest dose. Moreover, exogenous cholesterol acted at multiple levels by normalizing a plethora of disease-related dysfunctions including those linked to synapse function and morphology and aggregation of mutated Huntingtin.

Impact

Our work highlights the therapeutic dose of exogenous cholesterol capable of improving behavioral, synaptic, and neuropathological abnormalities in HD. This knowledge creates a solid foundation for developing new therapeutic strategies based on cholesterol to fight this disease.

species level was measured with 2B7-Tb/MW1-D2, using 1 ng/μl of 2B7-Tb and 10 ng/μl of MW1-D2-labeled antibody. TR-FRET measurements were routinely performed following overnight incubation at 4°C using an EnVision Reader (Perkin Elmer). Values were collected as the background subtracted ratio between fluorescence emission at 665 nm and 615 nm where the background signal corresponds to the ratio (665/615) measured for the antibodies in lysis buffer. The points in the graphs correspond to the averages of the background subtracted fluorescence ratio relative to the sample. The dilution points of each sample were fitted in a 4 parameters function that describes the curves. The obtained values were also expressed as (1/IC50) per μg of total protein for both assays.

Statistics

Prism 6 (GraphPad software) was used to perform all statistical analyses. Data are presented as means ± standard error of the mean (s.e.m.). Grubbs' test was applied to identify outliers. For each set of data to be compared, we determined whether data were normally distributed or not to select parametric or not parametric statistical tests. The specific statistical test used is indicated in the legend of all results figures. Differences were considered statistically if the *P*-value was < 0.05. G-power software was used to pre-determine group allocation, data collection, and all related analyses. For animal studies, mice were assigned randomly, and sex was balanced in the various experimental groups; animals from the same litter were divided in different experimental groups; blinding of the investigator was applied to *in vivo* procedures and

all data collection. Table EV3 summarizes all the trials and read-outs performed.

Data and software availability

This study does not include data deposited in public repositories.

Expanded View for this article is available online.

Acknowledgments

The authors acknowledge the scientific and technical assistance of Dr. Chiara Cordiglieri, responsible of the INGM Imaging Facility (Istituto Nazionale Genetica Molecolare—INGM, Milan, Italy); Dr. Alex Costa, Dr. Nadia Santo and the NOLIMITS advanced imaging facility established by the University of Milan. The authors also acknowledge Prof. Timothy F. Osborne (Department of Medicine, Johns Hopkins University, Baltimore, Maryland, USA), who supplied the antibody anti-SREBP2. This work was supported by Telethon Foundation, Italy (#GGP17102), the EU projects Neuromics (FP7 #305121), and JPND Research CircProt (643417) to E.C.; by KAUST Baseline funding to A.F.; by the Italian Ministry of Education, University and Research (MIUR) Dipartimenti di Eccellenza Program (2018–2022)—Dept of Biology and Biotechnology “L. Spallanzani”, University of Pavia to G. Biella, F. Talpo and C.M. F. Talpo was supported by Fondazione Umberto Veronesi. The visual abstract was created with BioRender.com.

Author contributions

EDP, MVal, and EC conceived the study; EDP and GBir performed *in vivo* experiments, including surgical implantation of osmotic mini-pumps and behavioral analysis; GBir and MVal performed immunostaining experiments and provided confocal images and quantification; EV prepared samples for the TEM and FIB-SEM imaging and performed the TEM imaging; AF and ES performed the FIB-SEM imaging; EV and AF analyzed the TEM and FIB-SEM data; CM, FTal, and GBie performed and analyzed the electrophysiological recordings; CCac, FTar, and VL performed and analyzed mass spectrometry experiments; LP, CCar, MVVer, and AC performed and analyzed TR-FRET experiments; VDB performed the PCA analysis; PC provided reagents/tools and suggestions for experiments regarding muHTT clearance and autophagy; MVal and GBir collected study data and performed statistical analyses; MVal and EC oversaw and coordinated responsibility for all research activities and their performance and provided experimental advice throughout the work. EC secured the funding, the collaborations, and the execution of the entire project. MVal, GBir, and EC wrote the paper that has been edited and reviewed by all authors.

Conflict of interest

The authors declare that they have no conflict of interest.

For more information

- (i) Website of the laboratory: <http://www.cattaneolab.it/?lang=en>
- (ii) Website of the European Huntington Disease Network, a nonprofit research network committed to advancing research, facilitating the conduct of clinical trials, and improving clinical care in Huntington's disease: <http://www.ehdn.org/>

References

Abildayeva K, Jansen PJ, Hirsch-Reinshagen V, Bloks VW, Bakker AHF, Ramaekers FCS, De Vente J, Groen AK, Wellington CL, Kuipers F *et al*

(2006) 24(S)-hydroxycholesterol participates in a liver X receptor-controlled pathway in astrocytes that regulates apolipoprotein E-mediated cholesterol efflux. *J Biol Chem* 281: 12799–12808

Baldo B, Paganetti P, Grueninger S, Marcellin D, Kaltenbach LS, Lo DC, Semmelroth M, Zivanovic A, Abramowski D, Smith D *et al* (2012) TR-FRET-based duplex immunoassay reveals an inverse correlation of soluble and aggregated mutant huntingtin in Huntington's disease. *Chem Biol* 19: 264–275

Belletti D, Grabrucker AM, Pederzoli F, Menerath I, Vandelli MA, Tosi G, Duskey TJ, Forni F, Ruozi B (2018) Hybrid nanoparticles as a new technological approach to enhance the delivery of cholesterol into the brain. *Int J Pharm* 543: 300–310

Berghoff SA, Gerndt N, Winchenbach J, Stumpf SK, Hosang L, Odoardi F, Ruhwedel T, Böhler C, Barrette B, Stassart R *et al* (2017) Dietary cholesterol promotes repair of demyelinated lesions in the adult brain. *Nat Commun* 8: 14241

Berod A, Hartman BK, Pujol F (1981) Importance of Fixation in Immunohistochemistry. *J Histochem Cytochem* 29: 844–850

Björkhem I, Lütjohann D, Breuer O, Sakinis A, Wennmalm Å (1997) Importance of a Novel Oxidative Mechanism for Elimination of Brain Cholesterol. *J Biol Chem* 272: 30178–30184

Bobrowska A, Donmez G, Weiss A, Guarente L, Bates G (2012) SIRT2 ablation has no effect on tubulin acetylation in brain, cholesterol biosynthesis or the progression of Huntington's disease phenotypes *in vivo*. *PLoS ONE* 7: e34805

Boussicault L, Alves S, Lamazière A, Planques A, Heck N, Mounmé L, Despres G, Bolte S, Hu A, Pagès C *et al* (2016) CYP46A1, the rate-limiting enzyme for cholesterol degradation, is neuroprotective in Huntington's disease. *Brain* 139: 953–970

Brown MS, Goldstein JL (1997) The SREBP pathway: regulation of cholesterol metabolism by proteolysis of a membrane-bound transcription factor. *Cell* 89: 331–340

Camargo N, Brouwers JF, Loos M, Gutmann DH, Smit AB, Verheijen MHG (2012) High-fat diet ameliorates neurological deficits caused by defective astrocyte lipid metabolism. *FASEB J* 26: 4302–4315

Casarotto PC, Giryck M, Fred SM, Moliner R, Enkavi G, Biojone C, Cannarozzo C, Brunello CA, Steinzeig A, Winkel F *et al* (2020) Antidepressants act by binding to the cholesterol-interaction site at TRKB neurotrophin receptor. *bioRxiv* <https://doi.org/10.1101/757989> [PREPRINT]

Castellano BM, Thelen AM, Moldavski O, Feltes M, Van der Welle REN, Mydock-McGrane L, Jiang X, van Eijkeren RJ, Davis OB, Louie SM *et al* (2017) Lysosomal cholesterol activates mTORC1 via an SLC38A9–Niemann Pick C1 signaling complex. *Science* 355: 1306–1311

Cepeda C, Hurst RS, Calvert CR, Hernández-Echeagaray E, Nguyen OK, Jocoy E, Christian LJ, Ariano MA, Levine MS (2003) Transient and progressive electrophysiological alterations in the corticostriatal pathway in a mouse model of Huntington's disease. *J Neurosci* 23: 961–969

Cepeda C, Starling AJ, Wu N, Nguyen OK, Uzgil B, Soda T, André VM, Ariano MA, Levine MS (2004) Increased GABAergic function in mouse models of Huntington's disease: reversal by BDNF. *J Neurosci Res* 78: 855–867

Di Pardo A, Monyror J, Morales LC, Kadam V, Lingrell S, Maglione V, Wozniak RW, Sipione S (2020) Mutant huntingtin interacts with the sterol regulatory element-binding proteins and impairs their nuclear import. *Hum Mol Genet* 29: 418–431.

Dietschy JM, Turley SD (2004) Cholesterol metabolism in the central nervous system during early development and in the mature animal. *J Lipid Res* 45: 1375–1397

- Dietschy JM (2009) Central nervous system: cholesterol turnover, brain development and neurodegeneration. *Biol Chem* 390: 287–293
- DiFiglia M, Sapp E, Chase KO, Davies SW, Bates GP, Vonsattel JP, Aronin N (1997) Aggregation of huntingtin in neuronal intranuclear inclusions and dystrophic neurites in brain. *Science* 277: 1990–1993
- Ferguson SM (2018) Axonal transport and maturation of lysosomes. *Curr Opin Neurobiol* 51: 45–51
- Ferris HA, Perry RJ, Moreira GV, Shulman GI, Horton JD, Kahn CR (2017) Loss of astrocyte cholesterol synthesis disrupts neuronal function and alters whole-body metabolism. *Proc Natl Acad Sci USA* 114: 1189–1194
- Fukui K, Ferris HA, Kahn CR (2015) Effect of cholesterol reduction on receptor signaling in neurons. *J Biol Chem* 290: 26383–26392
- Gauthier LR, Charrin BC, Borrell-Pagès M, Dompierre JP, Rangone H, Cordelières FP, De Mey J, MacDonald ME, Lessmann V, Humbert S et al (2004) Huntingtin controls neurotrophic support and survival of neurons by enhancing BDNF vesicular transport along microtubules. *Cell* 118: 127–138
- Guixà-González R, Albasanz JL, Rodríguez-Espigares I, Pastor M, Sanz F, Martí-Solano M, Manna M, Martínez-Seara H, Hildebrand PW, Martín M et al (2017) Membrane cholesterol access into a G-protein-coupled receptor. *Nat Commun* 8: 14505
- Gunawardena S, Her LS, Bruschi RG, Laymon RA, Niesman IR, Gordesky-Gold B, Sintasath L, Bonini NM, Goldstein LSB (2003) Disruption of axonal transport by loss of huntingtin or expression of pathogenic polyQ proteins in *Drosophila*. *Neuron* 40: 25–40
- Gutekunst CA, Li SH, Yi H, Mulroy JS, Kuemmerle S, Jones R, Rye D, Ferrante RJ, Hersch SM, Li XJ (1999) Nuclear and neuropil aggregates in Huntington's disease: relationship to neuropathology. *J Neurosci* 19: 2522–2534
- Herndon ES, Hladik CL, Shang P, Burns DK, Raisanen J, White CL (2009) Neuroanatomical profile of polyglutamine immunoreactivity in huntington disease brains. *J Neuropathol Exp Neurol* 68: 250–261
- Huang B, Wei W, Wang G, Gaertig MA, Feng Y, Wang W, Li XJ, Li S (2015) Mutant huntingtin downregulates myelin regulatory factor-mediated myelin gene expression and affects mature oligodendrocytes. *Neuron* 85: 1212–1226
- Hulce JJ, Cognetta AB, Niphakis MJ, Tully SE, Cravatt BF (2013) Proteome-wide mapping of cholesterol-interacting proteins in mammalian cells. *Nat Methods* 10: 259–264
- Janowski BA, Grogan MJ, Jones SA, Wisely GB, Kliewer SA, Corey EJ, Mangelsdorf DJ (1999) Structural requirements of ligands for the oxysterol liver X receptors LXR α and LXR β . *Proc Natl Acad Sci USA* 96: 266–271
- Kacher R, Lamazière A, Heck N, Kappes V, Mounier C, Despres G, Dembitskaya Y, Perrin E, Christaller W, Sasidharan Nair S et al (2019) CYP46A1 gene therapy deciphers the role of brain cholesterol metabolism in Huntington's disease. *Brain* 142: 2432–2450
- Koga H, Martínez-Vicente M, Arias E, Kaushik S, Sulzer D, Cuervo AM (2011) Constitutive upregulation of chaperone-mediated autophagy in Huntington's disease. *J Neurosci* 31: 18492–18505
- Lee JH, Tecedor L, Chen YH, Monteys AM, Sowada MJ, Thompson LM, Davidson BL (2015) Reinstating aberrant mTORC1 activity in Huntington's disease mice improves disease phenotypes. *Neuron* 85: 303–315
- Leoni V, Mariotti C, Tabrizi SJ, Valenza M, Wild EJ, Henley SMD, Hobbs NZ, Mandelli ML, Grisoli M, Björkhem I et al (2008) Plasma 24S-hydroxycholesterol and caudate MRI in pre-manifest and early Huntington's disease. *Brain* 131: 2851–2859
- Leoni V, Mariotti C, Nanetti L, Salvatore E, Squitieri F, Bentivoglio AR, Bandettini del Poggio M, Piacentini S, Monza D, Valenza M et al (2011) Whole body cholesterol metabolism is impaired in Huntington's disease. *Neurosci Lett* 494: 245–249
- Leoni V, Long JD, Mills JA, Di Donato S, Paulsen JS (2013) Plasma 24S-hydroxycholesterol correlation with markers of Huntington disease progression. *Neurobiol Dis* 55: 37–43
- Leoni V, Nury T, Vejux A, Zarrouk A, Caccia C, Debbabi M, Fromont A, Sghaier R, Moreau T, Lizard G (2017) Mitochondrial dysfunctions in 7-ketocholesterol-treated 158N oligodendrocytes without or with α -tocopherol: impacts on the cellular profile of tricarboxylic cycle-associated organic acids, long chain saturated and unsaturated fatty acids, oxysterols, chole. *J Steroid Biochem Mol Biol* 169: 96–110
- Lim KL, Ng XH, Grace LGY, Yao TP (2012) Mitochondrial dynamics and Parkinson's disease: focus on parkin. *Antioxid Redox Signal* 16: 935–949
- Lloyd MH, Wolfensohn SE (1998) Practical use of distress scoring systems in the application of humane endpoints. *Int. Conf. Hum endpoints Anim. Exp. Biomed. Res.* 22–25
- Lofthsson T, Jarho P, Másson M, Järvinen T (2005) Cyclodextrins in drug delivery. *Expert Opin Drug Deliv* 2: 335–351
- Lowe DG (2004) Distinctive image features from scale-invariant keypoints. *Int J Comput Vis* 60: 91–110
- Lund EG, Xie C, Kotti T, Turley SD, Dietschy JM, Russell DW (2003) Knockout of the cholesterol 24-hydroxylase gene in mice reveals a brain-specific mechanism of cholesterol turnover. *J Biol Chem* 278: 22980–22988
- Maat-Schieman ML, Dorsman JC, Smoor MA, Siesling S, Van Duinen SG, Verschuuren JJ, den Dunnen JT, Van Ommen GJ, Roos RA (1999) Distribution of inclusions in neuronal nuclei and dystrophic neurites in Huntington Disease brain. *J Neuropathol Exp Neurol* 58: 129–137
- Mangiarini L, Sathasivam K, Seller M, Cozens B, Harper A, Hetherington C, Lawton M, Trotter Y, Leach H, Davies SW et al (1996) Exon 1 of the HD gene with an expanded CAG repeat is sufficient to cause a progressive neurological phenotype in transgenic mice. *Cell* 87: 493–506
- Martin MG, Ahmed T, Korovaichuk A, Venero C, Menchón SA, Salas I, Munck S, Herreras O, Balschun D, Dotti CG (2014) Constitutive hippocampal cholesterol loss underlies poor cognition in old rodents. *EMBO Mol Med* 6: 902–917
- Mauch DH, Nägler K, Schumacher S, Göritz C, Müller EC, Otto A, Pflieger FW (2001) CNS synaptogenesis promoted by glia-derived cholesterol. *Science* 294: 1354–1357
- Merchán-Pérez A, Rodríguez JR, Alonso-Nanclares L, Schertel A, DeFelipe J (2009) Counting synapses using FIB/SEM microscopy: a true revolution for ultrastructural volume reconstruction. *Front Neuroanat* 3: 1–14
- Narita M, Young ARJ, Arakawa S, Samarajiwa SA, Nakashima T, Yoshida S, Hong S, Berry LS, Reichelt S, Ferreira M et al (2011) Spatial coupling of mTOR and autophagy augments secretory phenotypes. *Science* 332: 966–970
- Oddi S, Dainese E, Fezza F, Lanuti M, Barcaroli D, De Laurenzi V, Centonze D, MacCarrone M (2011) Functional characterization of putative cholesterol binding sequence (CRAC) in human type-1 cannabinoid receptor. *J Neurochem* 116: 858–865
- Owen JL, Zhang Y, Bae SH, Farooqi MS, Liang G, Hammer RE, Goldstein JL, Brown MS (2012) Insulin stimulation of SREBP-1c processing in transgenic rat hepatocytes requires p70 S6-kinase. *Proc Natl Acad Sci USA* 109: 16184–16189
- Pavoine S, Dufour AB, Chessel D (2004) From dissimilarities among species to dissimilarities among communities: a double principal coordinate analysis. *J Theor Biol* 228: 523–537

- Pfrierger FW (2003) Cholesterol homeostasis and function in neurons of the central nervous system. *Cell Mol Life Sci* 60: 1158–1171
- Postila PA, Róg T (2020) A perspective: active role of lipids in neurotransmitter dynamics. *Mol Neurobiol* 57: 910–925
- Rahbek-Clemmensen T, Lycas MD, Erlendsson S, Eriksen J, Apuschkin M, Vilhardt F, Jørgensen TN, Hansen FH, Gether U (2017) Super-resolution microscopy reveals functional organization of dopamine transporters into cholesterol and neuronal activity-dependent nanodomains. *Nat Commun* 8: 1–14
- Ritch JJ, Valencia A, Alexander J, Sapp E, Gatune L, Sangrey GR, Sinha S, Scherber CM, Zeitlin S, Sadri-Vakili G et al (2012) Multiple phenotypes in huntington disease mouse neural stem cells. *Mol Cell Neurosci* 50: 70–71
- Rohrbough J, Broadie K (2005) Lipid regulation of the synaptic vesicle cycle. *Nat Rev Neurosci* 6: 139–150
- Rosas HD, Wilkens P, Salat DH, Mercaldo ND, Vangel M, Yendiki AY, Hersch SM (2018) Complex spatial and temporally defined myelin and axonal degeneration in Huntington disease. *Neuroimage Clin* 20: 236–242
- Rüb U, Seidel K, Heinsen H, Vonsattel JP, den Dunnen WF, Korf HW (2016) Huntington's disease (HD): the neuropathology of a multisystem neurodegenerative disorder of the human brain. *Brain Pathol* 26: 726–740
- Saher G, Rudolph F, Corthals K, Ruhwedel T, Schmidt KF, Löwel S, Dibaj P, Barrette B, Möbius W, Nave KA (2012) Therapy of Pelizaeus-Merzbacher disease in mice by feeding a cholesterol-enriched diet. *Nat Med* 18: 1130–1135
- Saher G, Stumpf SK (2015) Cholesterol in myelin biogenesis and hypomyelinating disorders. *Biochim Biophys Acta* 1851: 1083–1094
- Samara A, Galbiati M, Luciani P, Deledda C, Messi E, Peri A, Maggi R (2014) Altered expression of 3-beta-hydroxysteroid delta-24-reductase/selective Alzheimer's disease indicator-1 gene in Huntington's disease models. *J Endocrinol Invest* 37: 729–737
- Saudou F, Humbert S (2016) The biology of huntingtin. *Neuron* 89: 910–926
- Schindelin J, Arganda-Carrera I, Frise E, Verena K, Mark L, Tobias P, Stephan P, Curtis R, Stephan S, Schmid B et al (2009) Fiji – an Open platform for biological image analysis. *Nat Methods* 9: 676–682
- Segatto M, Leboffe L, Trapani L, Pallottini V (2014) Cholesterol homeostasis failure in the brain: implications for synaptic dysfunction and cognitive decline. *Curr Med Chem* 21: 2788–2802
- Seo YK, Jeon T, Chong HK, Beisinger J, Osborne TF (2012) Genome-wide localization of SREBP-2 in hepatic chromatin predicts a role in autophagy. *Cell Metab* 13: 367–375
- Shankaran M, Di Paolo E, Leoni V, Caccia C, Ferrari Bardile C, Mohammed H, Di Donato S, Kwak S, Marchionini D, Turner S et al (2017) Early and brain region-specific decrease of *de novo* cholesterol biosynthesis in Huntington's disease: a cross-validation study in Q175 knock-in mice. *Neurobiol Dis* 98: 66–76
- Sipione S, Rigamonti D, Valenza M, Zuccato C, Conti L, Pritchard J, Kooperberg C, Olson JM, Cattaneo E (2002) Early transcriptional profiles in huntingtin-inducible striatal cells by microarray analyses. *Hum Mol Genet* 25: 210
- Teo RTY, Hong X, Yu-Taeger L, Huang Y, Tan LJ, Xie Y, Vinh To X, Guo L, Rajendran R, Novati A et al (2016) Structural and molecular myelination deficits occur prior to neuronal loss in the YAC128 and BACHD models of Huntington disease. *Hum Mol Genet* 25: 2621–2632
- Upadhyay A, Amanullah A, Mishra R, Kumar A, Mishra A (2018) Lanosterol suppresses the aggregation and cytotoxicity of misfolded proteins linked with neurodegenerative diseases. *Mol Neurobiol* 55: 1169–1182
- Valenza M, Leoni V, Tarditi A, Mariotti C, Björkhem I, Di Donato S, Cattaneo E (2007a) Progressive dysfunction of the cholesterol biosynthesis pathway in the R6/2 mouse model of Huntington's disease. *Neurobiol Dis* 28: 133–142
- Valenza M, Carroll JB, Leoni V, Bertram LN, Björkhem I, Singaraja RR, Di Donato S, Lutjohann D, Hayden MR, Cattaneo E (2007b) Cholesterol biosynthesis pathway is disturbed in YAC128 mice and is modulated by huntingtin mutation. *Hum Mol Genet* 16: 2187–2198
- Valenza M, Leoni V, Karasinska JM, Petricca L, Fan J, Carroll J, Pouladi MA, Fossale E, Nguyen HP, Riess O et al (2010) Cholesterol defect is marked across multiple rodent models of Huntington's disease and is manifest in astrocytes. *J Neurosci* 30: 10844–10850
- Valenza M, Cattaneo E (2011) Emerging roles for cholesterol in Huntington's disease. *Trends Neurosci* 34: 474–486
- Valenza M, Marullo M, Di Paolo E, Cesana E, Zuccato C, Biella G, Cattaneo E (2015a) Disruption of astrocyte-neuron cholesterol cross talk affects neuronal function in Huntington's disease. *Cell Death Differ* 22: 690–702
- Valenza M, Chen JY, Di Paolo E, Ruozi B, Belletti D, Ferrari Bardile C, Leoni V, Caccia C, Brilli E, Di Donato S et al (2015b) Cholesterol-loaded nanoparticles ameliorate synaptic and cognitive function in Huntington's disease mice. *EMBO Mol Med* 7: 1547–1564
- Valenza M, Rigamonti D, Goffredo D, Zuccato C, Fenu S, Jamot L, Strand A, Tarditi A, Woodman B, Racchi M et al (2005) Dysfunction of the cholesterol biosynthetic pathway in Huntington's disease. *J Neurosci* 25: 9932–9939
- Weiss A, Abramowski D, Bibel M, Bodner R, Chopra V, DiFiglia M, Fox J, Kegel K, Klein C, Grueninger S et al (2009) Single-step detection of mutant huntingtin in animal and human tissues: a bioassay for Huntington's disease. *Anal Biochem* 395: 8–15
- Weiss A, Andre R, Tabrizi SJ, Weiss A, Träger U, Wild EJ, Grueninger S, Farmer R, Landles C, Scahill RI et al (2012) Mutant huntingtin fragmentation in immune cells tracks Huntington's disease progression. Find the latest version: brief report Mutant huntingtin fragmentation in immune cells tracks Huntington's disease progression. *J Clin Invest* 122: 3731–3736
- White E, Mehnert JM, Chan CS (2015) Autophagy, metabolism, and cancer. *Clin Cancer Res* 21: 5037–5046
- Xiang Z, Valenza M, Cui L, Leoni V, Jeong HK, Brilli E, Zhang J, Peng Q, Duan W, Reeves SA et al (2011) Peroxisome-proliferator-activated receptor gamma coactivator 1 α contributes to dysmyelination in experimental models of Huntington's disease. *J Neurosci* 31: 9544–9553
- Yecies JL, Manning BD (2011) Transcriptional control of cellular metabolism by mTOR signaling. *Cancer Res* 71: 2815–2820
- Zhao L, Chen XJ, Zhu J, Xi YB, Yang X, Hu LD, Ouyang H, Patel SH, Jin X, Lin D et al (2015) Lanosterol reverses protein aggregation in cataracts. *Nature* 523: 607–611
- Zuccato C, Valenza M, Cattaneo E (2010) Molecular mechanisms and potential therapeutical targets in Huntington's disease. *Physiol Rev* 90: 905–981



License: This is an open access article under the terms of the Creative Commons Attribution 4.0 License, which permits use, distribution and reproduction in any medium, provided the original work is properly cited.

Expanded View Figures

Figure EV1. Behavioral characterization of wt mice following striatal infusion of the high dose of cholesterol and *in vivo* exogenous cholesterol localization.

- A Latency to fall (seconds) from an accelerating rotarod at 10 weeks of age (3 weeks after cholesterol infusion) in wt ($N = 11$); wt ACSF ($N = 11$) and wt chol-high ($N = 7$) mice.
- B–E Global motor activity (B), total distance travelled (C), mean velocity (D), and stereotyped movements (E) in an open field at 11 weeks of age (4 weeks after cholesterol infusion) (wt = 11; wt ACSF = 10; wt chol-high = 7).
- F Discrimination index (%) in the novel object recognition test of wt, wt ACSF, and wt chol-high mice at 11 weeks of age (4 weeks after cholesterol infusion) (wt = 11; wt ACSF = 10; wt chol-high = 7). DI above zero indicates a preference for the novel object; DI below zero indicates a preference for the familiar object.
- G, H Cholesterol content in the infused striatum (G) and ipsilateral cortex (H) of wt ACSF ($N = 3$), wt chol-low ($N = 5$), and wt chol-high ($N = 4$) mice at 12 weeks of age after 4-week striatal cholesterol infusion.
- I–M Representative confocal images showing co-localization of BODIPY-chol (green) and TGN46 (I), calnexin (J), Rab9 (K), PMCA-ATPase (L), and LAMP1 (M) (red) in the striatum of R6/2 mice infused with BODIPY-cholesterol. Scale bars: 5 μm .

Data information: The data in (A–H) are shown as scatterplot graphs with means \pm standard error. Each dot corresponds to the value obtained from each animal. Values in (A–D) were normalized as % above the mean of wt ACSF for each independent analysis. Statistics: one-way ANOVA with Newman–Keuls *post hoc* test (*** $P < 0.001$; **** $P < 0.0001$).

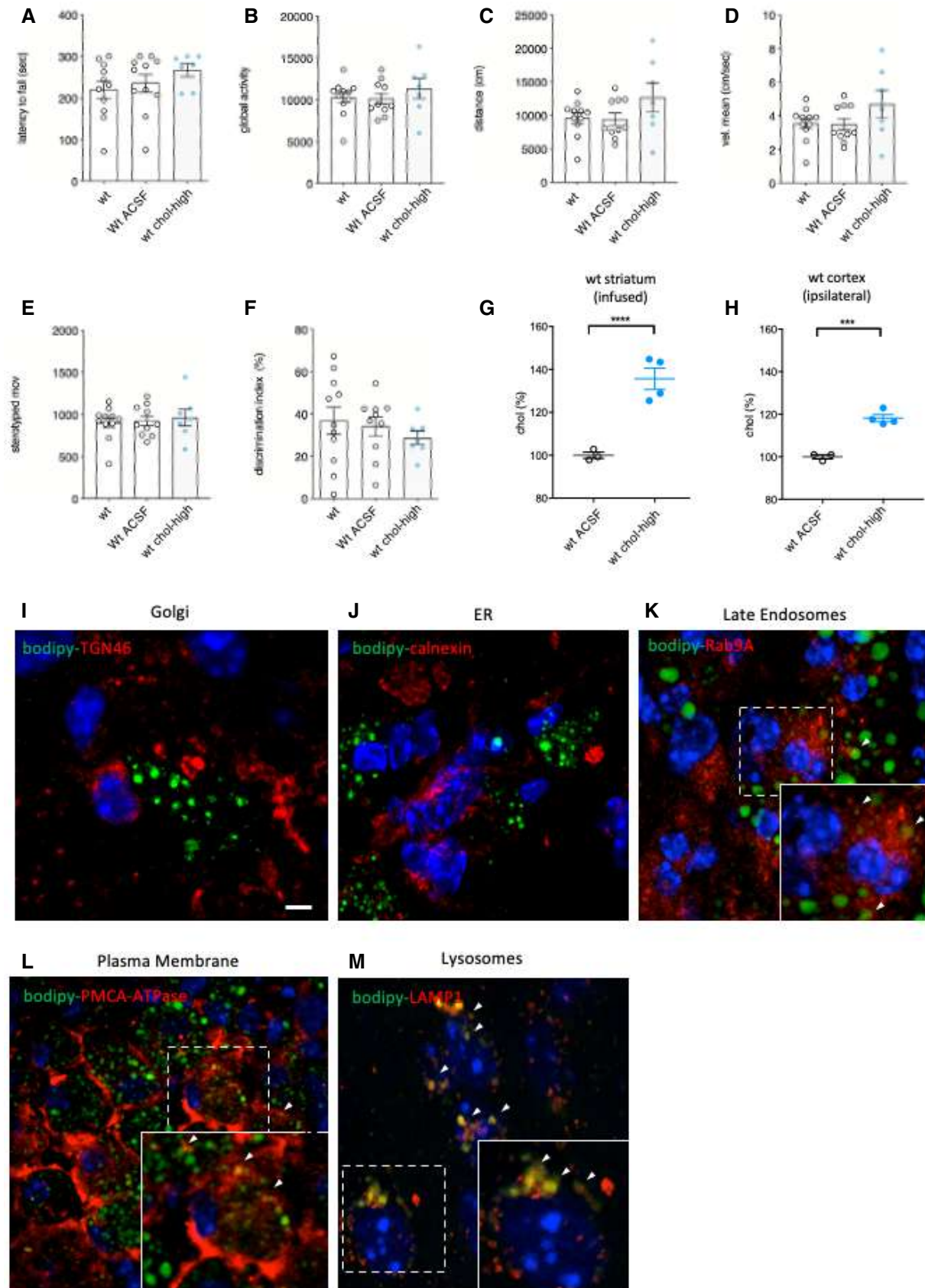


Figure EV1.

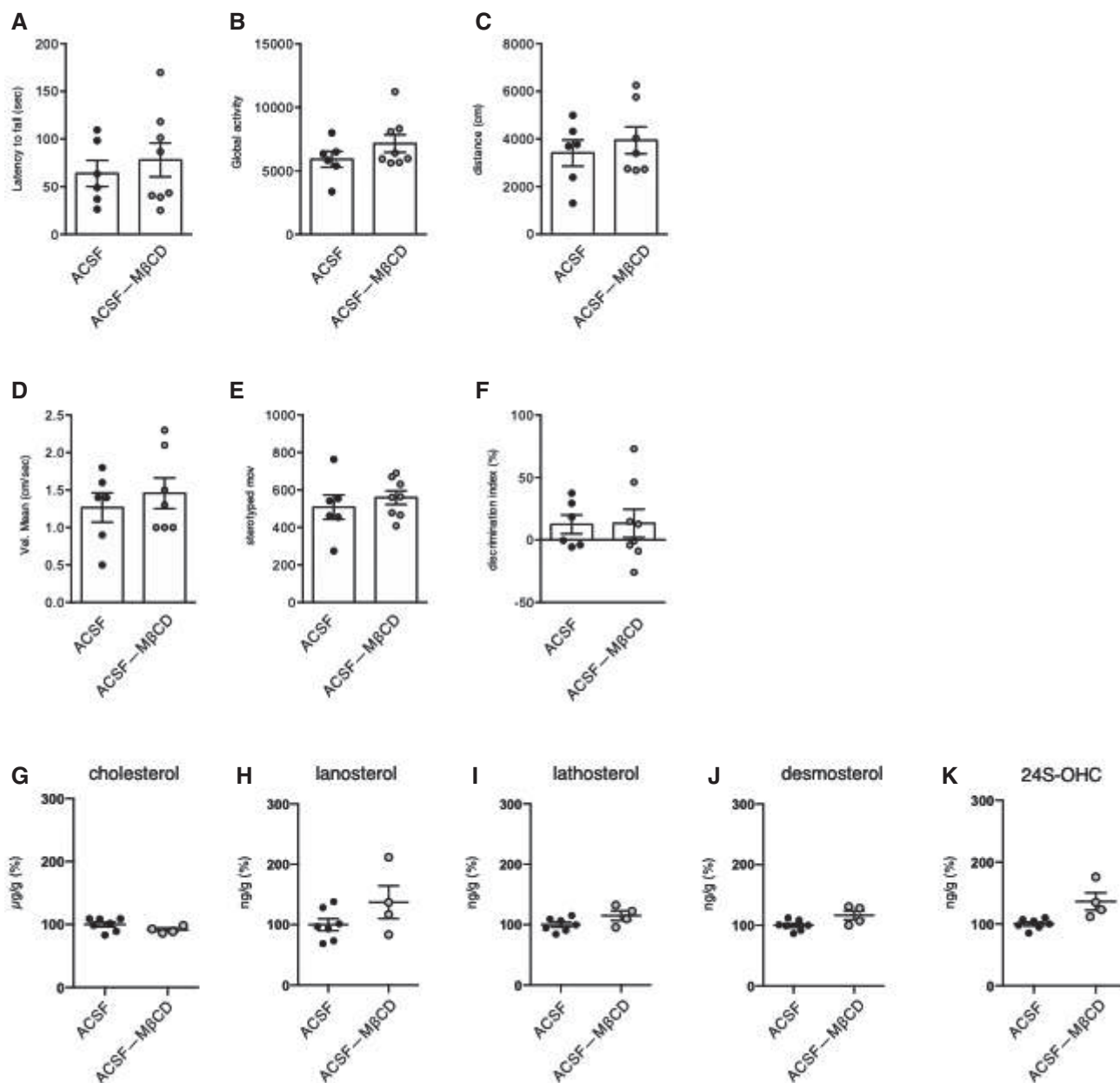


Figure EV2. Behavioral characterization and sterol quantification of R6/2 ACSF and R6/2 ACSF complexed with methyl- β -cyclodextrin.

- A Latency to fall (seconds) from an accelerating rotarod at 10 weeks of age (3 weeks after cholesterol infusion) in R6/2 ACSF ($N = 6$) and R6/2 ACSF-M β CD ($N = 8$) mice.
- B–E Global motor activity (B), total distance travelled (C), mean velocity (D), and stereotyped movements (E) in an open field at 11 weeks of age (4 weeks after cholesterol infusion) (R6/2 ACSF = 6; R6/2 ACSF-M β CD = 6).
- F Discrimination index (%) in the novel object recognition test of R6/2 ACSF and R6/2 ACSF-M β CD mice at 11 weeks of age (4 weeks after cholesterol infusion) (R6/2-ACSF = 6; R6/2 ACSF-M β CD = 8). DI above zero indicates a preference for the novel object; DI below zero indicates a preference for the familiar object.
- G–K Cholesterol (G), lanosterol (H), lathosterol (I), desmosterol (J), and 24S-OHC (K) level measured by mass spectrometry in the infused striatum of R6/2 ACSF ($N = 7$) and R6/2 ACSF-M β CD ($N = 4$) mice at 12 weeks of age after 4-week striatal infusion.

Data information: The data in (A–F) are shown as scatterplot graphs with means \pm standard error. All values in (G–K) are expressed as % above the mean of R6/2 ACSF, and these data are shown as scatterplots with means \pm standard error. Each dot corresponds to the value obtained from each animal.

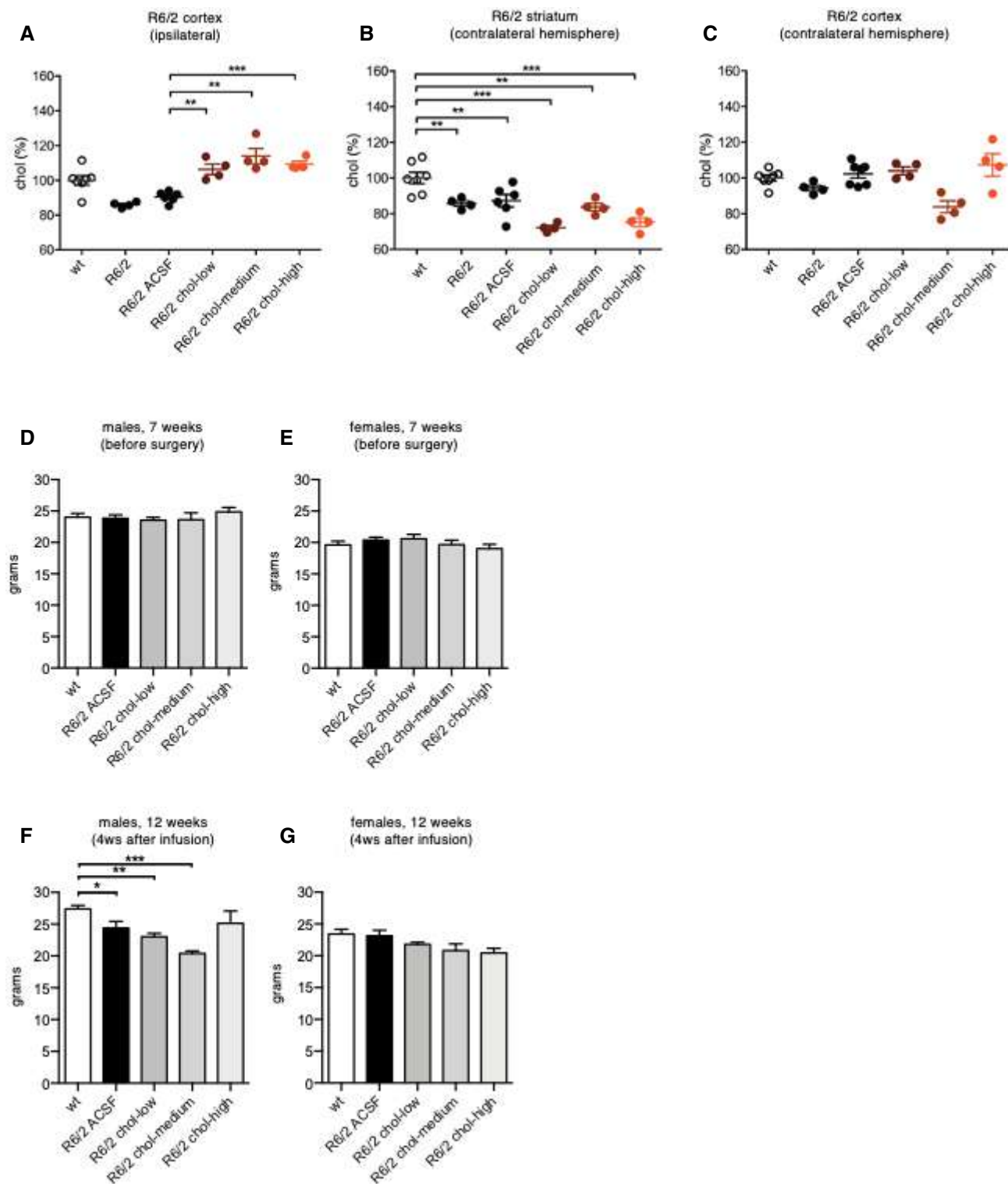


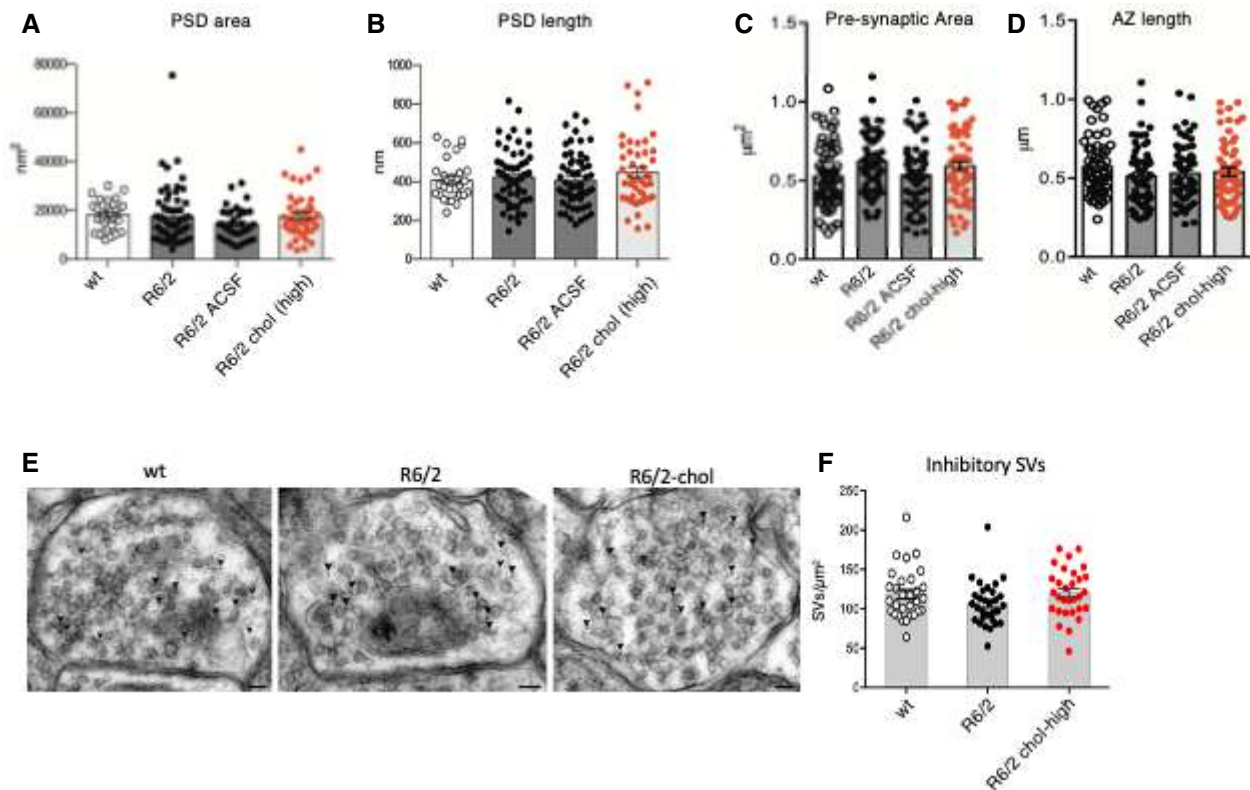
Figure EV3.

Figure EV3. Cholesterol content in the striatum and cortex of R6/2 mice following striatal infusion of cholesterol and mice body weight.

A–C Cholesterol content in the ipsilateral cortex (A), contralateral striatum (B), and contralateral cortex (C) of wt ($N = 7$), R6/2 ($N = 4$), R6/2 ACSF ($N = 6$), R6/2 chol-low ($N = 4$), R6/2 chol-medium ($N = 4$), and R6/2 chol-high ($N = 4$) mice at 12 weeks of age after 4-week striatal cholesterol infusion.

D–G Body weight (expressed in g) of male (D, F) and female (E, G) mice before surgery (7 weeks of age; wt, $N = 19$; R6/2 ACSF, $N = 24$; R6/2 chol-low, $N = 18$; R6/2 chol-medium, $N = 8$; R6/2 chol-high, $N = 12$) and 4 weeks after cholesterol infusion (12 weeks of age; wt, $N = 18$; R6/2 ACSF, $N = 18$; R6/2 chol-low, $N = 13$; R6/2 chol-medium, $N = 8$; R6/2 chol-high, $N = 9$).

Data information: The data (A–C) are shown as scatterplot graphs with means \pm standard error. Each dot corresponds to the value obtained from each animal. The data (D–G) are shown as histograms with means \pm standard error. Statistics: one-way ANOVA with Newman–Keuls *post hoc* test ($*P < 0.05$; $**P < 0.01$; $***P < 0.001$). All values were normalized as % above the mean of wt for each independent analysis.

**Figure EV4. Morphometric analysis of excitatory synapses and of synaptic vesicle (SV) density of inhibitory synapses following striatal infusion of the high dose of cholesterol.**

A–D 60 PSDs (A, B) and 60 pre-synaptic terminals (C, D) were analyzed in 3 mice/group.

E TEM images of inhibitory striatal synapses in wt, R6/2, and R6/2 chol-high mice. GABA-immuno-positive synapses were stained by 12 nm colloidal gold-conjugated secondary antibodies (arrowhead). Scale bar: 50 nm.

F Quantification of SVs density in 30 inhibitory synapses of wt, R6/2 and R6/2 chol-high mice ($N = 3$ mice/group).

Data information: Graphs are means \pm standard error.

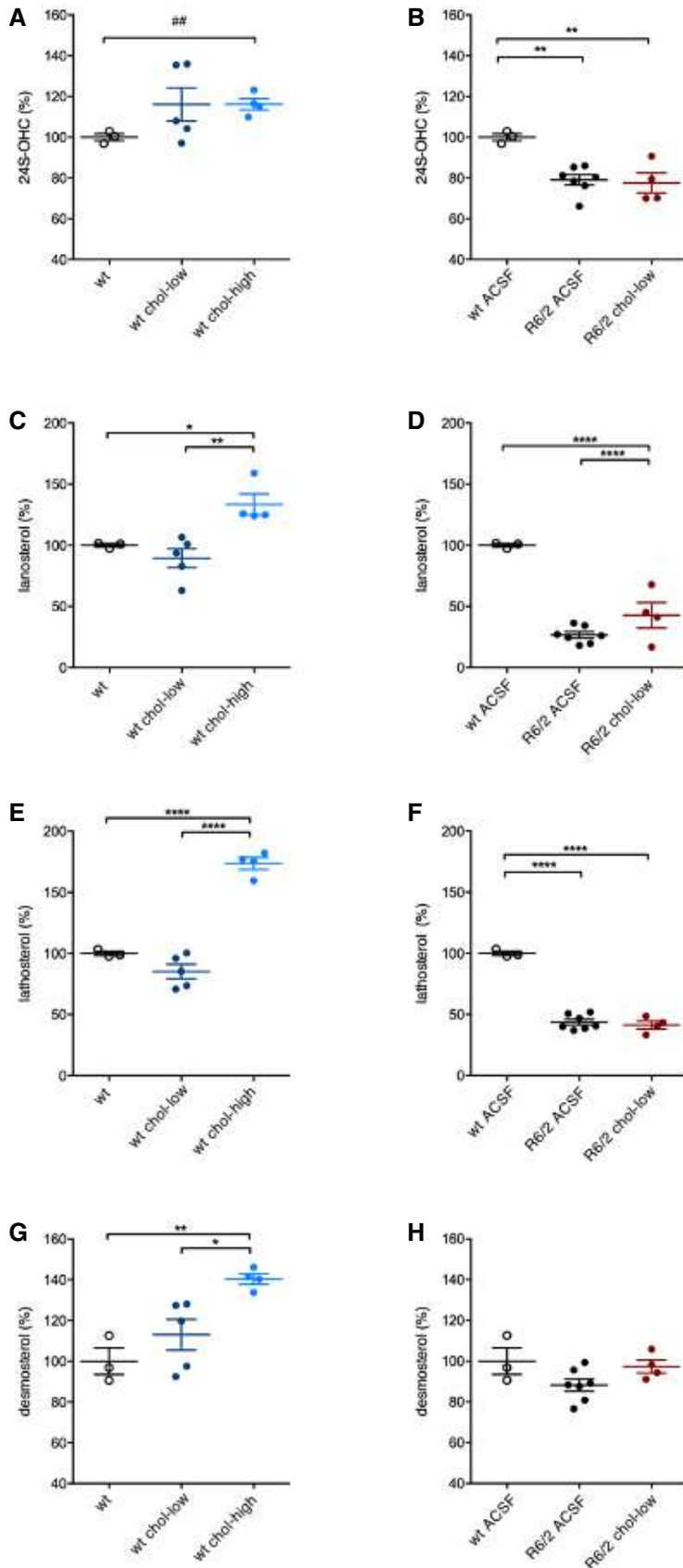


Figure EV5. Levels of cholesterol precursors and 24S-OHC in the striatum of wt and R6/2 groups following striatal infusion of cholesterol.

A, B 24S-OHC level in the infused striatum of wt ACSF ($N = 3$), wt chol-low ($N = 5$), wt chol-high ($N = 4$) (A), and in the infused striatum of wt ACSF ($N = 3$), R6/2 ACSF ($N = 7$), R6/2 chol-low ($N = 4$) (B) at 12 weeks of age after 4-week striatal infusion of cholesterol.

C, D Lanosterol level in the infused striatum of wt ACSF ($N = 3$), wt chol-low ($N = 5$), wt chol-high ($N = 4$) (C), and in the infused striatum of wt ACSF ($N = 3$), R6/2 ACSF ($N = 7$), R6/2 chol-low ($N = 4$) (D) at 12 weeks of age after 4-week striatal infusion of cholesterol.

E, F Lathosterol level in the infused striatum of wt ACSF ($N = 3$), wt chol-low ($N = 5$), wt chol-high ($N = 4$) (E), and in the infused striatum of wt ACSF ($N = 3$), R6/2 ACSF ($N = 7$), R6/2 chol-low ($N = 4$) (F) at 12 weeks of age after 4-week striatal infusion of cholesterol.

G, H Desmosterol level in the infused striatum of wt ACSF ($N = 3$), wt chol-low ($N = 5$), wt chol-high ($N = 4$) (G), and in the infused striatum of wt ACSF ($N = 3$), R6/2 ACSF ($N = 7$), R6/2 chol-low ($N = 4$) (H) at 12 weeks of age after 4-week striatal infusion of cholesterol.

Data information: All values were expressed as % above the mean of wt ACSF. The data of wt ACSF in (A, C, E, G) are the same shown in (B, D, F, H). The data in (A–H) are shown as scatterplot graphs with means \pm standard error with each dot corresponding to the value obtained from each animal. Statistics: one-way ANOVA with Newman–Keuls *post hoc* test (* $P < 0.05$; ** $P < 0.01$; **** $P < 0.001$), and Student's *t*-test (## $P < 0.01$) in (A).

Striatal infusion of cholesterol promotes dose-dependent behavioral benefits and exerts disease-modifying effects in Huntington's disease mice

Giulia Birolini^{1,2‡}, Marta Valenza^{1,2‡*}, Eleonora Di Paolo^{1,2‡}, Elena Vezzoli^{1,2,†}, Francesca Talpo³, Claudia Maniezzi³, Claudio Caccia⁴, Valerio Leoni⁵, Vittoria D. Bocchi^{1,2}, Paola Conforti^{1,2}, Elisa Sogne⁶, Lara Petricca⁷, Cristina Cariulo⁷, Margherita Verani⁷, Andrea Caricasole⁷, Andrea Falqui⁶, Gerardo Biella³, Elena Cattaneo^{1,2*}

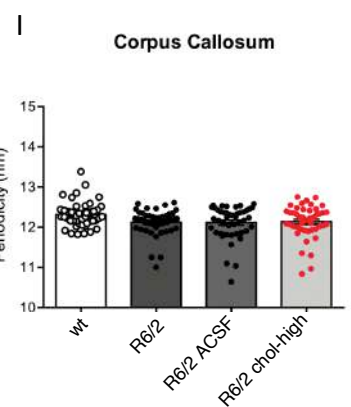
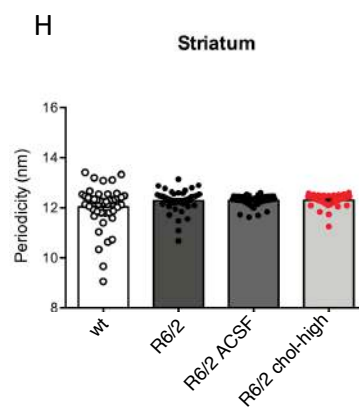
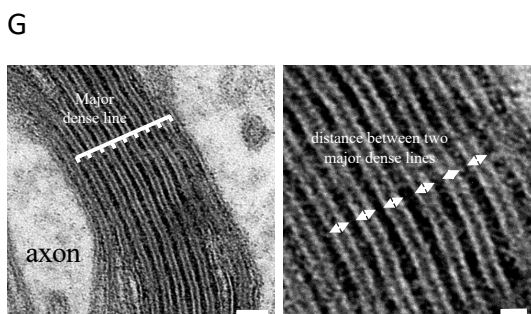
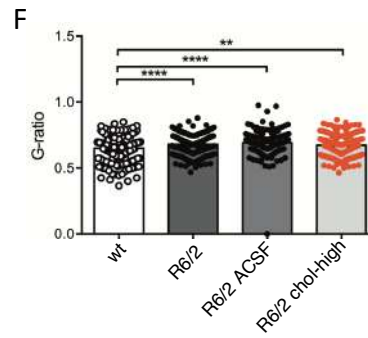
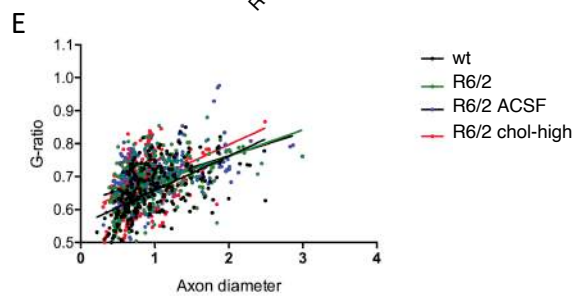
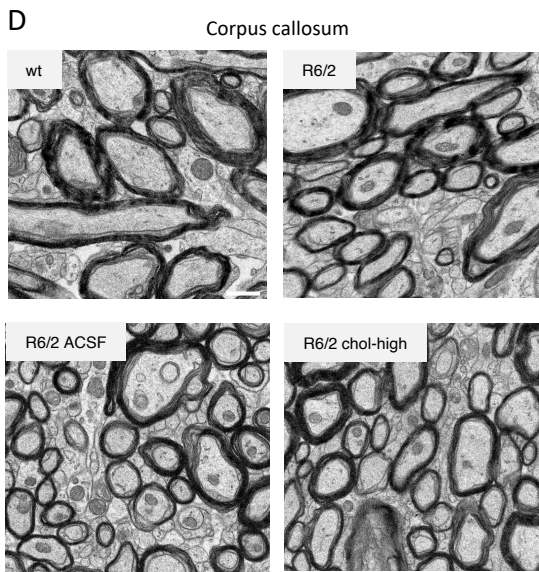
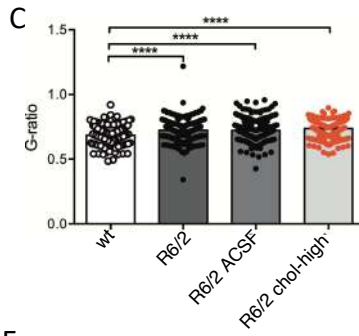
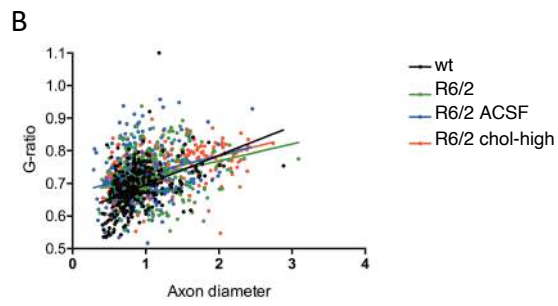
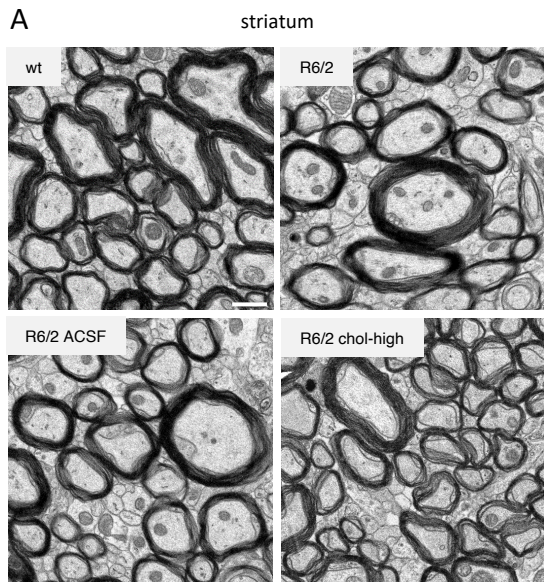
Appendix – table of content:

Appendix Figure S1

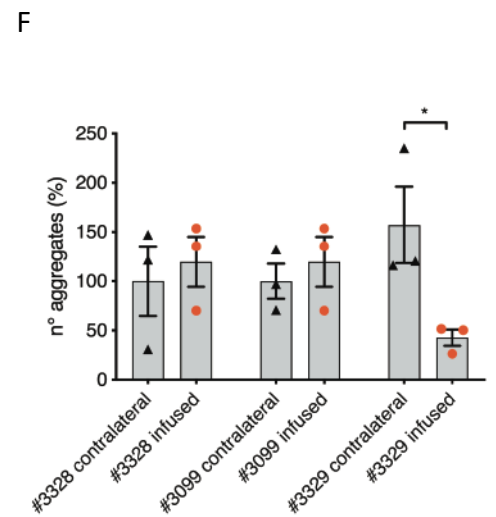
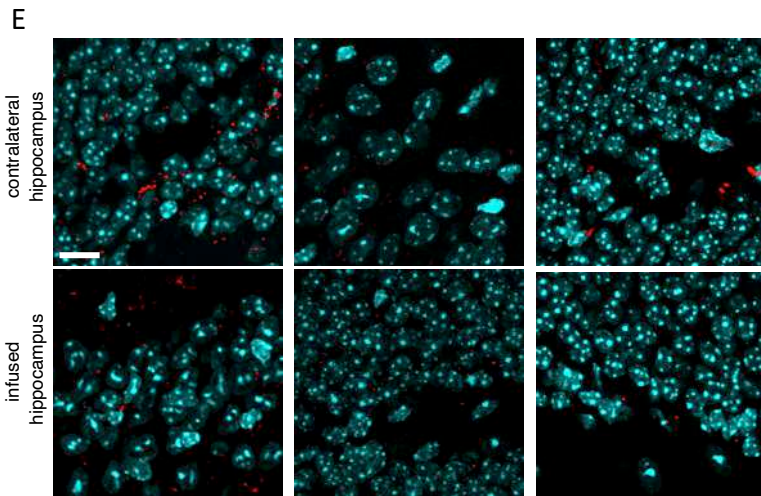
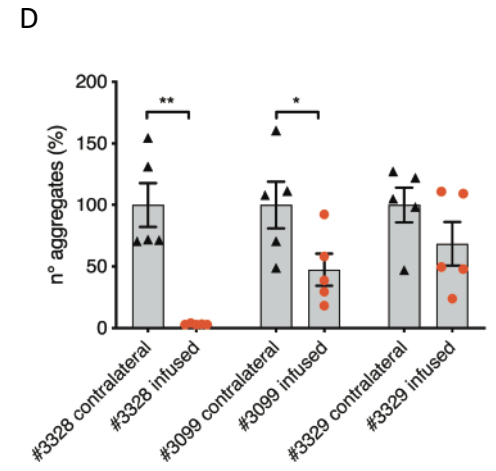
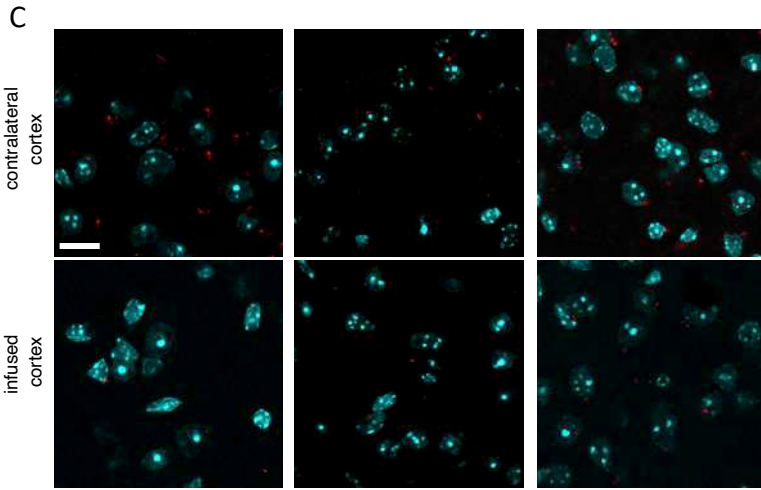
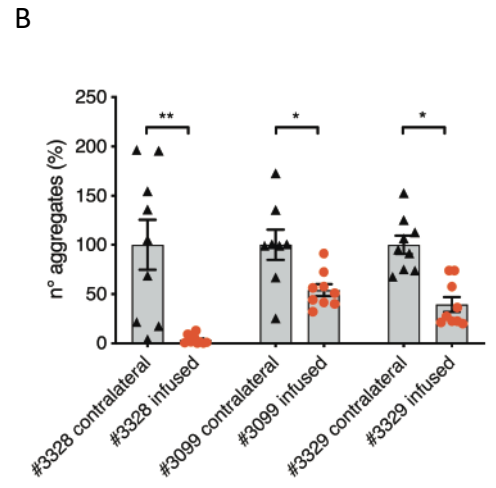
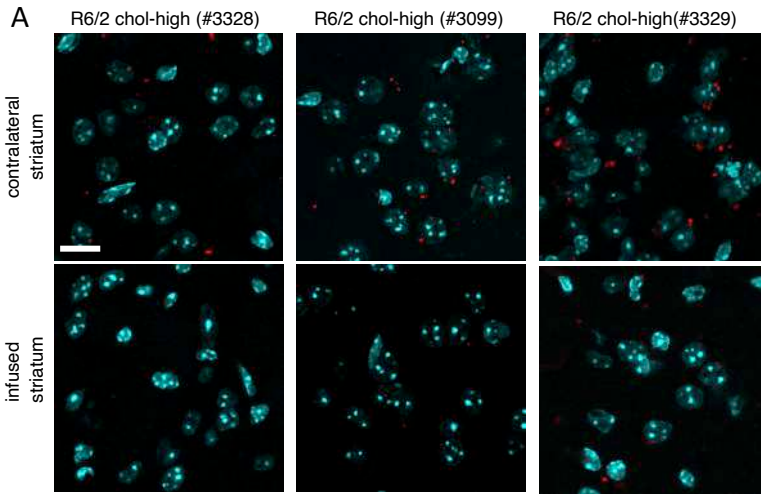
Appendix Figure S2

Appendix Table S3

Appendix Figure S1



Appendix Figure S2



Appendix S3 - Summary of statistics for the main figures

FIGURE 1C			
ANOVA summary			
F	9,635		
P value	< 0,0001		
P value summary	****		
Are differences among means statistically significant? (P < 0.05)	Yes		
R square	0,6769		
Newman-Keuls multiple comparisons test			
	Mean Diff,	Significant?	Summary
wt vs. R6/2-ACSF	15,05	Yes	**
wt vs. R6/2-chol (low)	6,229	No	ns
wt vs. R6/2-chol (medium)	-6,886	No	ns
wt vs. R6/2-chol (high)	-9,614	No	ns
R6/2-ACSF vs. R6/2-chol (low)	-8,819	No	ns
R6/2-ACSF vs. R6/2-chol (medium)	-21,93	Yes	**
R6/2-ACSF vs. R6/2-chol (high)	-24,66	Yes	***
R6/2-chol (low) vs. R6/2-chol (medium)	-13,12	No	ns
R6/2-chol (low) vs. R6/2-chol (high)	-15,84	Yes	*
R6/2-chol (medium) vs. R6/2-chol (high)	-2,727	No	ns

FIGURE 1D			
ANOVA summary - Rotarod 8 weeks			
F	5,132		
P value	0,001		
P value summary	***		
Are differences among means statistically significant? (P < 0.05)	Yes		
R square	0,2002		
Newman-Keuls multiple comparisons test			
	Mean Diff,	Significant?	Summary
wt vs. R6/2-ACSF	87,77	Yes	***
wt vs. R6/2-chol (low)	80,01	Yes	**
wt vs. R6/2-chol (medium)	78,59	Yes	*
wt vs. R6/2-chol (high)	51,56	Yes	*
R6/2-ACSF vs. R6/2-chol (low)	-7,767	No	ns
R6/2-ACSF vs. R6/2-chol (medium)	-9,188	No	ns
R6/2-ACSF vs. R6/2-chol (high)	-36,21	No	ns
R6/2-chol (low) vs. R6/2-chol (medium)	-1,421	No	ns
R6/2-chol (low) vs. R6/2-chol (high)	-28,45	No	ns
R6/2-chol (medium) vs. R6/2-chol (high)	-27,02	No	ns
ANOVA summary - Rotarod 10 weeks			
F	33,78		
P value	< 0,0001		
P value summary	****		
Are differences among means statistically significant? (P < 0.05)	Yes		
R square	0,634		
Newman-Keuls multiple comparisons test			
	Mean Diff,	Significant?	Summary
wt vs. R6/2-ACSF	161,4	Yes	****
wt vs. R6/2-chol (low)	170,6	Yes	****
wt vs. R6/2-chol (medium)	158,1	Yes	****
wt vs. R6/2-chol (high)	116,6	Yes	****
R6/2-ACSF vs. R6/2-chol (low)	9,271	No	ns
R6/2-ACSF vs. R6/2-chol (medium)	-3,283	No	ns
R6/2-ACSF vs. R6/2-chol (high)	-44,72	Yes	*
R6/2-chol (low) vs. R6/2-chol (medium)	-12,55	No	ns
R6/2-chol (low) vs. R6/2-chol (high)	-53,99	Yes	*
R6/2-chol (medium) vs. R6/2-chol (high)	-41,44	No	ns

FIGURE 1E			
ANOVA summary - Global activity 11 weeks			
F	13,45		
P value	<0,0001		
P value summary	****		

Significant diff. among means (P < 0.05)?	Yes		
R squared	0,4476		
Newman-Keuls multiple comparisons test			
	Mean Diff,	Significant?	Summary
wt vs. R6/2-ASCF	5571	Yes	****
wt vs. R6/2-chol (low)	6087	Yes	****
wt vs. R6/2-chol (medium)	4561	Yes	**
wt vs. R6/2-chol (high)	1555	No	ns
R6/2-ASCF vs. R6/2-chol (low)	515,8	No	ns
R6/2-ASCF vs. R6/2-chol (medium)	-1010	No	ns
R6/2-ASCF vs. R6/2-chol (high)	-4016	Yes	***
R6/2-chol (low) vs. R6/2-chol (medium)	-1526	No	ns
R6/2-chol (low) vs. R6/2-chol (high)	-4532	Yes	***
R6/2-chol (medium) vs. R6/2-chol (high)	-3006	Yes	*

FIGURE 1F			
ANOVA summary - Distance 11 weeks			
F	13,17		
P value	<0,0001		
P value summary	****		
Significant diff. among means (P < 0.05)?	Yes		
R squared	0,4126		
Newman-Keuls multiple comparisons test			
	Mean Diff,	Significant?	Summary
wt vs. R6/2-ASCF	7035	Yes	****
wt vs. R6/2-chol (low)	7478	Yes	****
wt vs. R6/2-chol (medium)	6050	Yes	**
wt vs. R6/2-chol (high)	3380	Yes	**
R6/2-ASCF vs. R6/2-chol (low)	442,2	No	ns
R6/2-ASCF vs. R6/2-chol (medium)	-985,1	No	ns
R6/2-ASCF vs. R6/2-chol (high)	-3656	Yes	**
R6/2-chol (low) vs. R6/2-chol (medium)	-1427	No	ns
R6/2-chol (low) vs. R6/2-chol (high)	-4098	Yes	*
R6/2-chol (medium) vs. R6/2-chol (high)	-2671	No	ns

FIGURE 1G			
ANOVA summary - Vel Mean 11 weeks			
F	16,58		
P value	<0,0001		
P value summary	****		
Significant diff. among means (P < 0.05)?	Yes		
R squared	0,4693		
Newman-Keuls multiple comparisons test			
	Mean Diff,	Significant?	Summary
wt vs. R6/2-ASCF	2,042	Yes	****
wt vs. R6/2-chol (low)	2,238	Yes	****
wt vs. R6/2-chol (medium)	1,283	Yes	**
wt vs. R6/2-chol (high)	1,042	Yes	**
R6/2-ASCF vs. R6/2-chol (low)	0,1964	No	ns
R6/2-ASCF vs. R6/2-chol (medium)	-0,7584	No	ns
R6/2-ASCF vs. R6/2-chol (high)	-0,9995	Yes	**
R6/2-chol (low) vs. R6/2-chol (medium)	-0,9548	No	ns
R6/2-chol (low) vs. R6/2-chol (high)	-1,196	Yes	**
R6/2-chol (medium) vs. R6/2-chol (high)	-0,2411	No	ns

FIGURE 1H			
ANOVA summary - Stereotyped Mov 11 weeks			
F	14,63		
P value	<0,0001		
P value summary	****		
Significant diff. among means (P < 0.05)?	Yes		
R squared	0,4383		
Newman-Keuls multiple comparisons test			
	Mean Diff,	Significant?	Summary
wt vs. R6/2-ASCF	442,1	Yes	****
wt vs. R6/2-chol (low)	555,2	Yes	****
wt vs. R6/2-chol (medium)	421	Yes	***
wt vs. R6/2-chol (high)	206,3	Yes	*
R6/2-ASCF vs. R6/2-chol (low)	113,1	No	ns
R6/2-ASCF vs. R6/2-chol (medium)	-21,08	No	ns
R6/2-ASCF vs. R6/2-chol (high)	-235,8	Yes	*

R6/2-choI (low) vs. R6/2-choI (medium)	-134,2	No	ns
R6/2-choI (low) vs. R6/2-choI (high)	-348,9	Yes	**
R6/2-choI (medium) vs. R6/2-choI (high)	-214,8	No	ns

FIGURE 1I

ANOVA summary - Rearings 11 weeks			
F	16,59		
P value	<0,0001		
P value summary	****		
Significant diff. among means (P < 0.05)?	Yes		
R squared	0,4694		
Newman-Keuls multiple comparisons test			
	Mean Diff,	Significant?	Summary
wt vs. R6/2-ACSF	407,7	Yes	****
wt vs. R6/2-choI (low)	378,3	Yes	****
wt vs. R6/2-choI (medium)	350,5	Yes	***
wt vs. R6/2-choI (high)	288,3	Yes	****
R6/2-ACSF vs. R6/2-choI (low)	-29,42	No	ns
R6/2-ACSF vs. R6/2-choI (medium)	-57,23	No	ns
R6/2-ACSF vs. R6/2-choI (high)	-119,5	No	ns
R6/2-choI (low) vs. R6/2-choI (medium)	-27,81	No	ns
R6/2-choI (low) vs. R6/2-choI (high)	-90,04	No	ns
R6/2-choI (medium) vs. R6/2-choI (high)	-62,23	No	ns
R6/2-choI (high) vs R6/2-ACSF			
Unpaired t test			
P value	0,0419		
P value summary	#		
Significantly different (P < 0.05)?	Yes		
One- or two-tailed P value?	Two-tailed		
t, df	t=2,108, df=37		

FIGURE 1K

ANOVA summary - Center vs Periphery 11 weeks			
F	10,06		
P value	<0,0001		
P value summary	****		
Significant diff. among means (P < 0.05)?	Yes		
R squared	0,3651		
Newman-Keuls multiple comparisons test			
	Mean Diff,	Significant?	Summary
wt vs. R6/2-ACSF	12,25	Yes	***
wt vs. R6/2-choI (low)	14,96	Yes	**
wt vs. R6/2-choI (medium)	8,864	No	ns
wt vs. R6/2-choI (high)	-5,886	No	ns
R6/2-ACSF vs. R6/2-choI (low)	2,717	No	ns
R6/2-ACSF vs. R6/2-choI (medium)	-3,383	No	ns
R6/2-ACSF vs. R6/2-choI (high)	-18,13	Yes	****
R6/2-choI (low) vs. R6/2-choI (medium)	-6,1	No	ns
R6/2-choI (low) vs. R6/2-choI (high)	-20,85	Yes	***
R6/2-choI (medium) vs. R6/2-choI (high)	-14,75	Yes	**

FIGURE 1L

ANOVA summary - NORT 11 weeks			
F	6,031		
P value	0,0003		
P value summary	***		
Significant diff. among means (P < 0.05)?	Yes		
R squared	0,2434		
Newman-Keuls multiple comparisons test			
	Mean Diff,	Significant?	Summary
wt vs. R6/2-ACSF	31,91	Yes	***
wt vs. R6/2-choI (low)	3,245	No	ns
wt vs. R6/2-choI (medium)	3,101	No	ns
wt vs. R6/2-choI (high)	2,28	No	ns
R6/2-ACSF vs. R6/2-choI (low)	-28,66	Yes	**
R6/2-ACSF vs. R6/2-choI (medium)	-28,81	Yes	*
R6/2-ACSF vs. R6/2-choI (high)	-29,63	Yes	**
R6/2-choI (low) vs. R6/2-choI (medium)	-0,1444	No	ns
R6/2-choI (low) vs. R6/2-choI (high)	-0,9654	No	ns
R6/2-choI (medium) vs. R6/2-choI (high)	-0,8209	No	ns

FIGURE 2D			
ANOVA summary			
F	37,74		
P value	<0,0001		
P value summary	****		
Significant diff. among means (P < 0.05)?	Yes		
R squared	0,8531		
Newman-Keuls multiple comparisons test	Mean Diff,	Significant?	Summary
wt vs. R6/2-ACSF	1,817	Yes	****
wt vs. R6/2-chol	1,189	Yes	****
R6/2-ACSF vs. R6/2-chol	-0,6276	Yes	*

FIGURE 2G			
ANOVA summary			
F	10,15		
P value	<0,0001		
P value summary	****		
Significant diff. among means (P < 0.05)?	Yes		
R squared	0,14		
Newman-Keuls multiple comparisons test	Mean Diff,	Significant?	Summary
wt vs. R6/2	0,1492	Yes	***
wt vs. R6/2-ACSF	0,1537	Yes	***
wt vs. R6/2-chol	0,2027	Yes	****
R6/2 vs. R6/2-ACSF	0,004505	No	ns
R6/2 vs. R6/2-chol	0,05353	No	ns
R6/2-ACSF vs. R6/2-chol	0,04903	No	ns

FIGURE 2J			
ANOVA summary			
F	20,24		
P value	<0,0001		
P value summary	****		
Significant diff. among means (P < 0.05)?	Yes		
R squared	0,2089		
Newman-Keuls multiple comparisons test	Mean Diff,	Significant?	Summary
wt vs. R6/2	42	Yes	****
wt vs. R6/2 ACSF	33,38	Yes	****
wt vs. R6/2-chol	12,77	Yes	*
R6/2 vs. R6/2 ACSF	-8,618	No	ns
R6/2 vs. R6/2-chol	-29,23	Yes	****
R6/2 ACSF vs. R6/2-chol	-20,61	Yes	***

FIGURE 2K			
ANOVA summary			
F	5,643		
P value	0,0009		
P value summary	***		
Significant diff. among means (P < 0.05)?	Yes		
R squared	0,06693		
Newman-Keuls multiple comparisons test	Mean Diff,	Significant?	Summary
wt vs. R6/2	1,203	Yes	*
wt vs. R6/2-ACSF	1,154	Yes	**
wt vs. R6/2-chol	0,1562	No	ns
R6/2 vs. R6/2-ACSF	-0,04863	No	ns
R6/2 vs. R6/2-chol	-1,046	Yes	*
R6/2-ACSF vs. R6/2-chol	-0,9978	Yes	**

FIGURE 3C			
ANOVA summary			
F	14,85		
P value	0,0003		
P value summary	***		
Significant diff. among means (P < 0.05)?	Yes		
R squared	0,6644		
Newman-Keuls multiple comparisons test	Mean Diff,	Significant?	Summary

wt vs. R6/2-ACSF	-1,212	Yes	***
wt vs. R6/2-chol	0,06288	No	ns
R6/2-ACSF vs. R6/2-chol	1,275	Yes	***

FIGURE 3E			
ANOVA summary			
F	8,363		
P value	0,0001		
P value summary	***		
Significant diff. among means (P < 0.05)?	Yes		
R squared	0,3213		
Newman-Keuls multiple comparisons test			
	Mean Diff,	Significant?	Summary
wt vs. R6/2	-0,01566	Yes	***
wt vs. R6/2-ACSF	-0,013	Yes	**
wt vs. R6/2-chol	-0,002188	No	ns
R6/2 vs. R6/2-ACSF	0,002663	No	ns
R6/2 vs. R6/2-chol	0,01348	Yes	**
R6/2-ACSF vs. R6/2-chol	0,01081	Yes	**

FIGURE 4B			
ANOVA summary - contralateral striatum			
F	67,45		
P value	< 0,0001		
P value summary	****		
Are differences among means statistically significant? (P < 0.05)	Yes		
R square	0,9375		
Newman-Keuls multiple comparisons test			
	Mean Diff,	Significant?	Summary
wt vs. R6/2-ACSF	29,55	Yes	****
wt vs. R6/2-Chol	44,2	Yes	****
R6/2-ACSF vs. R6/2-Chol	14,64	Yes	**
ANOVA summary - infused striatum			
F	23,75		
P value	0,0003		
P value summary	***		
Are differences among means statistically significant? (P < 0.05)	Yes		
R square	0,8407		
Newman-Keuls multiple comparisons test			
	Mean Diff,	Significant?	Summary
wt vs. R6/2-ACSF	19,74	Yes	**
wt vs. R6/2-Chol	-18,3	Yes	**
R6/2-ACSF vs. R6/2-Chol	-38,04	Yes	***

FIGURE 4C			
ANOVA summary - contralateral striatum			
F	89,53		
P value	< 0,0001		
P value summary	****		
Are differences among means statistically significant? (P < 0.05)	Yes		
R square	0,9521		
Newman-Keuls multiple comparisons test			
	Mean Diff,	Significant?	Summary
wt vs. R6/2-ACSF	76,57	Yes	****
wt vs. R6/2-Chol	76,88	Yes	****
R6/2-ACSF vs. R6/2-Chol	0,3097	No	ns
ANOVA summary - infused striatum			
F	52,46		
P value	< 0,0001		
P value summary	****		
Are differences among means statistically significant? (P < 0.05)	Yes		
R square	0,921		
Newman-Keuls multiple comparisons test			
	Mean Diff,	Significant?	Summary
wt vs. R6/2-ACSF	73,2	Yes	****

wt vs. R6/2-Chol	46,2	Yes	***
R6/2-ASCF vs. R6/2-Chol	-27	Yes	**

FIGURE 4D

ANOVA summary - contralateral striatum			
F	212,1		
P value	< 0,0001		
P value summary	****		
Are differences among means statistically significant? (P < 0.05)	Yes		
R square	0,9792		
Newman-Keuls multiple comparisons test			
	Mean Diff,	Significant?	Summary
wt vs. R6/2-ASCF	71,21	Yes	****
wt vs. R6/2-Chol	69,49	Yes	****
R6/2-ASCF vs. R6/2-Chol	-1,711	No	ns
ANOVA summary - infused striatum			
F	23,16		
P value	0,0003		
P value summary	***		
Are differences among means statistically significant? (P < 0.05)	Yes		
R square	0,8373		
Newman-Keuls multiple comparisons test			
	Mean Diff,	Significant?	Summary
wt vs. R6/2-ASCF	59,22	Yes	***
wt vs. R6/2-Chol	8,048	No	ns
R6/2-ASCF vs. R6/2-Chol	-51,17	Yes	***

FIGURE 4E

ANOVA summary - contralateral striatum			
F	8,488		
P value	0,0085		
P value summary	**		
Are differences among means statistically significant? (P < 0.05)	Yes		
R square	0,6535		
Newman-Keuls multiple comparisons test			
	Mean Diff,	Significant?	Summary
wt vs. R6/2-ASCF	26,6	Yes	*
wt vs. R6/2-Chol	32,73	Yes	**
R6/2-ASCF vs. R6/2-Chol	6,137	No	ns
ANOVA summary - infused striatum			
F	9,097		
P value	0,0069		
P value summary	**		
Are differences among means statistically significant? (P < 0.05)	Yes		
R square	0,669		
Newman-Keuls multiple comparisons test			
	Mean Diff,	Significant?	Summary
wt vs. R6/2-ASCF	11,66	No	ns
wt vs. R6/2-Chol	-35,89	Yes	*
R6/2-ASCF vs. R6/2-Chol	-47,55	Yes	**

FIGURE 4G and 4I

R6/2 vs wt			
Unpaired t test			
P value	<0,0001		
P value summary	****		
Significantly different (P < 0.05)?	Yes		
One- or two-tailed P value?	Two-tailed		
t, df	t=8,618, df=8		
R6/2 chol high (infused) vs R6/2 chol high (contralateral)			
Unpaired t test			
P value	0,001		
P value summary	**		
Significantly different (P < 0.05)?	Yes		

One- or two-tailed P value?	Two-tailed		
t, df	t=4,432, df=11		

FIGURE 5B			
ANOVA summary			
F	12,14		
P value	<0,0001		
P value summary	****		
Significant diff. among means (P < 0.05)?	Yes		
R squared	0,2651		
Newman-Keuls multiple comparisons test			
ACSF contralateral vs. ACSF infused	Mean Diff, 14,74	Significant? No	Summary ns
ACSF contralateral vs. Chol contralateral	-4,615E-10	No	ns
ACSF contralateral vs. Chol infused	67,62	Yes	****
ACSF infused vs. Chol contralateral	-14,74	No	ns
ACSF infused vs. Chol infused	52,88	Yes	****
Chol contralateral vs. Chol infused	67,62	Yes	****

FIGURE 5C			
ANOVA summary			
F	4,5		
P value	0,0053		
P value summary	**		
Significant diff. among means (P < 0.05)?	Yes		
R squared	0,1179		
Newman-Keuls multiple comparisons test			
ACSF contralateral vs. ACSF infused	Mean Diff, -0,2515	Significant? No	Summary ns
ACSF contralateral vs. Chol contralateral	-0,27	No	ns
ACSF contralateral vs. Chol infused	0,9782	Yes	*
ACSF infused vs. Chol contralateral	-0,01846	No	ns
ACSF infused vs. Chol infused	1,23	Yes	**
Chol contralateral vs. Chol infused	1,248	Yes	*

FIGURE 5E			
Chol infused vs Chol contralateral			
Unpaired t test			
P value	<0,0001		
P value summary	****		
Significantly different (P < 0.05)?	Yes		
One- or two-tailed P value?	Two-tailed		
t, df	t=5,281, df=28		

FIGURE 5G			
Chol infused vs Chol contralateral			
Unpaired t test			
P value	<0,0001		
P value summary	****		
Significantly different (P < 0.05)?	Yes		
One- or two-tailed P value?	Two-tailed		
t, df	t=4,738, df=28		

FIGURE 5L			
R6/2-Chol vs R6/2-ACSF			
Unpaired t test with Welch's correction			
P value	0,1594		
P value summary	ns		
Significantly different? (P < 0.05)	No		
One- or two-tailed P value?	Two-tailed		
Welch-corrected t, df	t=1,689 df=4,430		
How big is the difference?			
Mean ± SEM of column A	0,01035 ± 0,001016, n=5		
Mean ± SEM of column B	0,00859 ± 0,0002371, n=4		
Difference between means	-0,001762 ± 0,001043		
95% confidence interval	-0,004550 to 0,001026		
R squared	0,3918		
F test to compare variances			
F,DFn, Dfd	22,95, 4, 3		

P value	0,0276		
P value summary	*		
Significantly different? (P < 0.05)	Yes		

FIGURE 5M			
R6/2-Chol vs R6/2-ACSF			
Unpaired t test			
P value	0,0481		
P value summary	*		
Significantly different? (P < 0.05)	Yes		
One- or two-tailed P value?	Two-tailed		
t, df	t=2,390 df=7		
How big is the difference?			
Mean ± SEM of column A	0,01716 ± 0,002016, n=5		
Mean ± SEM of column B	0,01083 ± 0,001526, n=4		
Difference between means	-0,006334 ± 0,002650		
95% confidence interval	-0,01260 to -6,843e-005		
R squared	0,4494		
F test to compare variances			
F,DFn, Dfd	2,183, 4, 3		
P value	0,5473		
P value summary	ns		
Significantly different? (P < 0.05)	No		

FIGURE 6B			
ANOVA summary			
F	22,35		
P value	<0,0001		
P value summary	****		
Significant diff. among means (P < 0.05)?	Yes		
R squared	0,5828		
Newman-Keuls multiple comparisons test			
	Mean Diff,	Significant?	Summary
wt vs. ACSF contralateral	-92,4	Yes	****
wt vs. ACSF infused	-98,63	Yes	****
wt vs. Chol contralateral	-92,4	Yes	****
wt vs. Chol infused	-104,3	Yes	****
ACSF contralateral vs. ACSF infused	-6,231	No	ns
ACSF contralateral vs. Chol contralateral	-0,00001	No	ns
ACSF contralateral vs. Chol infused	-11,86	No	ns
ACSF infused vs. Chol contralateral	6,231	No	ns
ACSF infused vs. Chol infused	-5,625	No	ns
Chol contralateral vs. Chol infused	-11,86	No	ns

FIGURE 6D			
ANOVA summary			
F	16,24		
P value	<0,0001		
P value summary	****		
Significant diff. among means (P < 0.05)?	Yes		
R squared	0,5076		
Newman-Keuls multiple comparisons test			
	Mean Diff,	Significant?	Summary
wt vs. ACSF contralateral	-91,86	Yes	****
wt vs. ACSF infused	-129,2	Yes	****
wt vs. Chol contralateral	-91,86	Yes	****
wt vs. Chol infused	-23,15	No	ns
ACSF contralateral vs. ACSF infused	-37,32	No	ns
ACSF contralateral vs. Chol contralateral	0,000008	No	ns
ACSF contralateral vs. Chol infused	68,72	Yes	***
ACSF infused vs. Chol contralateral	37,32	No	ns
ACSF infused vs. Chol infused	106	Yes	****
Chol contralateral vs. Chol infused	68,72	Yes	***

Appendix Figures Legends

Appendix Figure S1 Electron microscopy analysis of myelin sheaths in wt and R6/2 groups.

(A) Representative EM images of myelinated fibers taken from the striatum of wt, R6/2, R6/2 ACSF and R6/2 chol-high (Scale bar: 500 nm). (B) Scatterplot graph of G-ratios against axonal diameters with linear regression. The slope of the best-fit line was significantly higher for R6/2 compared with wt mice, indicating thinner myelin sheaths in HD mice with and without treatment with cholesterol. (C) Mean G-ratios were higher in R6/2 mice compared with their wt controls, indicating that HD mice had thinner myelin sheaths (*** $p < 0.001$). At least 300 axons in 3 mice group were subjected to G-ratio analysis. Statistics: one-way ANOVA with Newman–Keuls post-hoc test (* $p < 0.05$; ** $p < 0.01$; *** $p < 0.001$). (D) Representative EM images of myelinated fibers taken from the corpus callosum of wt, R6/2, R6/2 ACSF and R6/2 chol-high (Scale bar: 500 nm). (E) Scatterplot graph of G-ratios against axonal diameters with linear regression. The slope of the best-fit line was significantly higher for R6/2 compared with wt mice, indicating thinner myelin sheaths in HD mice with and without treatment with cholesterol. (F) Mean G-ratios were higher in R6/2 mice compared with their wt controls, indicating that HD mice had thinner myelin sheaths (*** $P < 0.001$). At least 300 axons in 3 mice group were subjected to G-ratio analysis. Error bars represent the standard error of the mean. Statistics: one-way ANOVA with Newman–Keuls post-hoc test (* $p < 0.05$; ** $p < 0.01$; *** $p < 0.001$). (G) Representative EM images of myelinated fibers and its magnification taken from the striatum of wt mice in which the major dense lines in the myelin sheath are indicated. Periodicity was measured as the mean distance between two major dense lines from at least 45 randomly chosen myelin sheaths in 3 mice group. (Scale bars: 30 nm and 10 nm). (H-I) Quantification of the mean periodicity in wt, R6/2, R6/2 ACSF and R6/2 chol-high mice. Error bars represent the standard error of the mean. Statistics: one-way ANOVA with Newman–Keuls post-hoc test (* $p < 0.05$; ** $p < 0.01$; *** $p < 0.001$).

Appendix Figure S2 MuHTT aggregates in the striatum, cortex and hippocampus of R6/2 chol-high mice.

(A–F) Zoom of representative confocal images of immunostaining against EM48 antibody, specific for muHTT aggregates, in the infused and the contralateral striatum (A), cortex (C) and hippocampus (E) of R6/2 chol-high mice (N=3) and relative quantification (B, D, F) of number of aggregates. Hoechst (Ho, blue) was used to counterstain nuclei. Scale bars in A, C, E: 10 μ m. 18 images/animal were analyzed from 9 sections throughout the entire striatum; 10 images for each animal were analyzed from 3 sections of the cortex; 6 images for each animal/condition were analyzed from 3 sections of the hippocampus. All values are expressed as % above the mean of aggregates in the contralateral tissue of R6/2 chol-high mice. The data are shown as scatterplot graphs with means \pm standard. Each dot corresponding to number of aggregates counted in all the images. Statistics: one-way ANOVA with Newman–Keuls post- hoc test (*p<0.05; **p<0.01; ***p<0.001).

SREBP2 delivery to striatal astrocytes enhances cholesterol biosynthesis and ameliorates pathological features in Huntington's disease

Giulia Birolini^{1,2}, Gianluca Verlengia³⁻⁴, Francesca Talpo⁵, Claudia Maniezzi⁵, Lorena Zentilin⁶, Mauro Giacca^{6,7}, Paola Conforti^{1,2}, Claudio Caccia⁸, Valerio Leoni⁹, Franco Taroni⁸, Gerardo Biella⁵, Michele Simonato³⁻⁴, Elena Cattaneo^{1,2} and Marta Valenza^{1,2}

Manuscript ready to be submitted

¹Department of Biosciences, University of Milan, via G. Celoria 26, 20133, Milan, Italy.

²Istituto Nazionale di Genetica Molecolare "Romeo ed Enrica Invernizzi" via F. Sforza 35, 20122, Milan, Italy.

³School of Medicine, University Vita-Salute San Raffaele, via Olgettina 58, 20132, Milan, Italy.

⁴Department of Medical Sciences, University of Ferrara, via Savonarola 9, 44121, Ferrara, Italy.

⁵Department of Biology and Biotechnologies, University of Pavia, Via Adolfo Ferrata, 9, 27100, Pavia, Italy.

⁶International Centre for Genetic Engineering and Biotechnology, ICGEB, Padriciano 99, 34149 Trieste, Italy.

⁷School of Cardiovascular Medicine & Sciences, King's College London (UK).

⁸Unit of Medical Genetics and Neurogenetics. Fondazione I.R.C.C.S. Istituto Neurologico Carlo Besta, Via Celoria 11, 20131 Milan, Italy

⁹School of Medicine and Surgery, University of Milano-Bicocca, Via Cadore 48, 20900, Monza and Laboratory of Clinical Pathology, Hospital of Desio, ASST-Monza

Abstract

Brain cholesterol is produced mainly by astrocytes and is important for neuronal function. Its biosynthesis is severely reduced in mouse models of Huntington's Disease (HD). One mechanism implicates diminished nuclear translocation of the transcription factor sterol regulatory element binding protein 2 (SREBP2) and consequently reduced activation of SREBP-controlled genes in the cholesterol biosynthesis pathway.

Here we evaluated the efficacy of gene therapy by the unilateral intra-striatal injection of a recombinant adeno-associated virus 2/5 (AAV2/5) targeting astrocytes specifically and carrying the N-terminal fragment of human SREBP2 (hSREBP2).

Robust hSREBP2 expression in striatal glial cells in HD mice activated the transcription of cholesterol biosynthesis pathway genes, restored synaptic transmission, reversed both *Drd2* transcript levels in an *in vivo* reporter assay and behavioral decline, and cleared muHTT aggregates. We conclude that glial SREBP2 participates in HD brain pathogenesis *in vivo* and that AAV-based delivery of SREBP2 to astrocytes counteracts key features of HD.

Keywords: cholesterol, astrocytes, Huntington's disease, SREBP2

Introduction

Cholesterol is a multifaceted molecule that plays key roles in the brain during development and in adulthood. Its concentration in the brain is higher than in any other tissue (15–20 mg/g tissue). Up to 70–80% of cholesterol in the adult brain is of developmental origin and localized in myelin sheaths, while the rest is located in the plasma membranes of astrocytes and neurons (Bjorkhem *et al.* 2004). In neurons cholesterol plays important roles in synaptic transmission, as it is required for synaptic vesicle formation and function (Mauch *et al.* 2001; Göritz *et al.* 2002; Göritz *et al.* 2005) and for optimal neurotransmitter release (Pfrieger 2003a; Pfrieger 2003b; Pfrieger 2003c). As the blood-brain barrier (BBB) efficiently prevents the passage of peripheral cholesterol, brain cholesterol is synthesized locally (Jurevics & Morell, 1995). Of note, in adulthood astrocytes are believed to synthesize most cholesterol, which is transferred to the neurons via ApoE-containing lipoproteins (Mauch *et al.* 2001; Nunes *et al.* 2018).

Cholesterol biosynthesis is regulated by sterol regulatory element binding protein 2 (SREBP2), the master transcription factor that activates the transcription of most cholesterol biosynthesis genes. When the cholesterol level is low, SREBP2 is cleaved by SREBP cleavage activation protein (SCAP), leading to SREBP2 activation and translocation from the endoplasmic reticulum (ER) to the Golgi apparatus. Within the Golgi apparatus, SREBP2 is cleaved by two proteases called the site 1 (S1P) and site 2 (S2P) proteases, resulting in an active 68-kDa N-terminal fragment that moves to the nucleus, binds the sterol response element (SRE) in the promoters of target genes, and activates their transcription (Jeon & Osborne 2013). When cells do not need to produce cholesterol, SREBP2 is retained in the ER by the insulin-induced gene 1 (INSIG1) and insulin-induced gene 2 (INSIG2) proteins (Yang *et al.* 2002).

Dysregulation of brain cholesterol homeostasis has been linked to several neurodegenerative diseases (Valenza & Cattaneo 2011, Martin *et al.* 2014). Among these conditions is Huntington's disease (HD), an adult-onset disorder characterized by motor, cognitive, and psychiatric features. HD is caused by a CAG expansion in the HTT(IT15) gene encoding the huntingtin (HTT) protein and it is characterized by progressive loss of striatal medium-sized spiny neurons (MSNs) and cortical pyramidal neurons (Vonsattel & DiFiglia 1998; Rub *et al.* 2016).

A large number of studies conducted in different HD rodent models have demonstrated significantly reduced biosynthesis of cholesterol in the brain, with the striatum being affected first (Valenza *et al.* 2005; Valenza *et al.* 2007a; Valenza *et al.* 2007b; Valenza *et al.* 2010; Shankaran *et al.* 2017). In the adult HD mouse brain, this dysfunction is evidenced by a reduced rate of de novo cholesterol biosynthesis, precedes the onset of motor symptoms, and is CAG-dependent, as confirmed by studies in an allelic series of HD mice, and leads to a reduced content of total cholesterol (and of some of its

metabolites and catabolites) at late symptomatic stages (Shankaran *et al.* 2017). The underlying molecular mechanism implicates reduced activity of SREBP2 in the presence of mutant HTT (Valenza *et al.* 2005; Valenza *et al.* 2015a), likely through sequestration in the cytoplasm of the SREBP2/importin β complex required for nuclear import (Di Pardo *et al.* 2020).

Astrocytes are central in this dysfunction, as highlighted by *in vitro* studies. In fact, SREBP2 gene silencing in wild-type (wt) astrocytes has detrimental effects on HD neurons (Valenza *et al.* 2015a), while the forced expression of the N-terminal active fragment of SREBP2 in HD astrocytes reverses neurite outgrowth and synaptic defects in HD neurons (Valenza *et al.* 2015a). Despite these findings, the impacts of reduced astrocyte-mediated cholesterol synthesis *in vivo* in the HD brain and its reversal are not yet documented.

To gain mechanistic insights and confidence in the therapeutic potential of targeting this pathway *in vivo*, we forced the expression of the N-terminal active fragment of human SREBP2 (hSREBP2) in striatal astrocytes of a transgenic HD mouse model by using a recombinant adeno-associated virus 2/5 (AAV2/5). We demonstrated that increasing the level of hSREBP2 specifically in the nucleus of astrocytes stimulated cholesterol biosynthesis in the striatum of HD mice. As a consequence, synaptic transmission of both inhibitory and excitatory synapses was restored, the number of striatal MSNs expressing *Drd2* receptors was normalized, mutant HTT (muHTT) aggregation was reduced, motor defects were ameliorated, and cognitive decline was completely rescued in HD mice.

Results

Setting up an in vivo method for SREBP2 delivery to striatal astrocytes

To over-express hSREBP2 in astrocytes *in vivo* in HD mice, we employed a recombinant serotype of an adeno-associated virus (AAV2/5) that is known to be highly specific for glial cells (Tong *et al.* 2014). We modified it to express the reporter gene *tdTomato* under the control of a glial promoter (AAV2/5-gfaABC1D-tdTomato), and together with the active N-terminal fragment of human SREBP2 (AAV2/5-gfaABC1D-hSREBP2-tdTomato). We first verified the spread and tropism over time of the AAV2/5-gfaABC1D-tdTomato backbone using an *in vivo* method compatible with its application to R6/2 HD mice (Fig. 1A; Fig. S1A). Seven-week-old wild-type (wt) mice were given a single unilateral intracranial injection of virus directly into the striatum, and 4 weeks later animals were sacrificed and subjected to different analyses as summarized in Fig. 1B. Analysis of coronal sections of the brain by confocal microscopy demonstrated significant distribution of the AAV2/5-gfaABC1D-tdTomato in the infused striatum and in some parts of the cortex in several subsequent slices, indicating good spread from the injection site. In particular, tdTomato fluorescence was

detectable over a span of 2.5 mm and it covered $61.51\% \pm 4.85$ of the infused hemi-brain (Fig. 1C; Fig. S1B). AAV2/5-gfaABC1D-tdTomato tropism was analyzed by studying the co-localization of the tdTomato signal with the signals of neuronal (DARPP32, NeuN) and glial (GFAP, S100B, IBA1) markers. Figure 1D shows that AAV2/5 had a specific tropism for glial cells. In particular, the count of cells positive for tdTomato and for glial markers revealed that almost 80–90% of GFAP- or S100B-positive cells and 40% of IBA1-positive cells also expressed tdTomato. In contrast, when counting cells positive for tdTomato and neuronal markers, no double-positive cells were found. A parallel study conducted by employing herpes simplex virus (HSV) as a backbone to deliver the same gfaABC1D-tdTomato construct resulted in expression of the transgene only in neurons (Fig. S1C). We therefore proceeded with AAV2/5 to express hSREBP2 in astrocytes in HD mice.

Delivery of AAV2/5-gfaABC1D-hSREBP2-tdTomato to the HD striatum

To establish the efficiency of the *hSrebp2* transgene expression in vivo, AAV2/5-gfaABC1D-tdTomato or AAV2/5-gfaABC1D-hSREBP2-tdTomato were injected into the right striatum of R6/2 mice (herein R6/2-Tom or R6/2-hBP2 respectively), a well-known HD animal model characterized by rapidly developing symptoms, when the mice were 7 weeks old. Four weeks later, when mice were at the end of the symptomatic stage, cortical and striatal tissues were collected and RNA transcripts and relative amounts of hSREBP2 protein were measured. For this experiment we decided to pool the cortex and striatum because in our preliminary analyses (Fig. 1C) some viral spread was also observed in the cortex.

As shown in Fig. 1E, RNA transcripts of *tdTomato* were not detected in the cortico-striatal samples of uninfected wt and R6/2 mice, while they were detected and quantified in R6/2-Tom and R6/2-hBP2 samples. As expected, RNA transcripts of *hSrebp2* were detected only in R6/2-hBP2 mice (Fig. 1F).

Western blotting revealed a tdTomato immunoreactive band in the lysates from all R6/2-Tom injected mice but not from the R6/2-hBP2 mice, indicating that *tdTomato* fused downstream to *hSrebp2* was not efficiently translated in AAV2/5-gfaABC1D-hSREBP2-tdTomato (Fig. 1G and H). Importantly, western blot analysis with an antibody that recognizes both the endogenous (mouse) and exogenous (human) SREBP2 revealed an increase in total SREBP2 protein level in three out of four R6/2-hBP2 mice (Fig. 1I). The over-expression of hSREBP2 and its co-localization with astrocytes in the infused striatum was confirmed further in additional R6/2-hBP2 mice by immunofluorescent staining for GFAP and SREBP2 (Fig. 1J) and by performing stitching of multiple images following immunofluorescent staining that allowed a global view of hSREBP2 spread in the entire brain section (Fig. 1J).

Because there are no antibodies available that reliably distinguish human from mouse SREBP2, we were not able to calculate the amount of protein generated by the AAV2/5-gfaABC1D-hSREBP2-tdTomato vector in the infected R6/2-hBP2 mice compared with the endogenous mouse SREBP2 (mSREBP2). To overcome this problem, we designed sets of primers that specifically recognize the mRNA of *mSrebp2* or *hSrebp2* for quantitation. Notably, we measured a significant reduction of the endogenous *mSREBP2* transcripts in R6/2, R6/2-Tom and R6/2-hBP2 mice compared with wt mice (Fig. 1K). Importantly, Fig. 1L shows that *hSrebp2* mRNA was between 1.7-fold and 2.1-fold more abundant than the endogenous transcript in R6/2-hBP2 mice.

Glial hSREBP2 over-expression enhances cholesterol biosynthesis in HD mice

We next sought to test whether the AAV2/5-gfaABC1D-hSREBP2-tdTomato construct would express a functional SREBP2 protein capable of increasing transcription of SREBP-controlled genes of the cholesterol biosynthesis pathway.

Gene expression analysis was performed on the pooled striatum and cortex from the injected hemisphere by measuring transcript levels of cholesterol biosynthesis genes (*Hmgcr*, *Mvk*, *Sqs/Fdft1*, *Cyp51*, *Dhcr7*; Fig. 2A) using qRT-PCR. The mRNA levels from all these genes were significantly reduced in R6/2 and R6/2-Tom mice compared with controls (Fig. 2B–F). Importantly, hSREBP2 over-expression in R6/2 mice rescued the transcript levels of *Hmgcr*, *Mvk*, *Fdft1*, and *Cyp51* (Fig. 2B–E) but not of *Dhcr7* (Fig. 2F). The transcript level of *Cyp46a1*, which encodes the enzyme that catalyzes the conversion of cholesterol to 24S-hydroxycholesterol (24S-OHC), was reduced in all R6/2 groups compared with controls but was not affected by exogenous hSREBP2 (Fig. 2G).

To explore whether the increased transcription of SREBP2-controlled genes corresponded to an increased activity of the pathway, we measured cholesterol precursors (lanosterol, lathosterol, and desmosterol) as surrogate markers of cholesterol biosynthesis. As expected, the steady-state levels of all cholesterol precursors were reduced in the striata of R6/2-Tom mice compared with wt-Tom mice (Fig. 2H–J) (Valenza et al. 2007b; Valenza et al. 2010; Valenza et al. 2015; Birolini et al. 2020). hSREBP2 delivery in glial cells, although unable to affect lanosterol and lathosterol levels (Fig. 2H–I), led to a significant increase in desmosterol in the striata of R6/2-hBP2 mice compared with R6/2-Tom mice (Fig. 2J), suggesting a preferential stimulation of the Bloch pathway of cholesterol biosynthesis (Fig. 2A). This was accompanied by an increase in 24S-OHC (Fig. 2K), consistent with the notion that cholesterol synthesis and catabolism are also in balance in the HD brain (Shankaran et al. 2017).

To assess whether the enhancement of cholesterol biosynthesis genes following striatal injection of AAV2/5-gfaABC1D-hSREBP2-tdTomato was accompanied by changes in the expression levels of

genes involved in cholesterol efflux (*Abca1*), transport (*ApoE*), and uptake (*Lrp1*), we measured their mRNA levels in cortico-striatal tissues. *Abca1* mRNA levels were increased in R6/2, R6/2-Tom, and R6/2-hBP2 mice with respect to wt mice (Fig. S2A), while *ApoE* and *Lrp1* mRNA levels were similar in all conditions (Fig. S2B and C), indicating that hSREBP2 delivery in glial cells did not affect transcript levels of these genes. Similarly, AAV2/5-gfaABC1D-hSREBP2-tdTomato did not influence transcript levels of genes involved in astrocytic homeostasis. The *Glt1* mRNA level was similarly reduced in R6/2, R6/2-Tom, and R6/2-hBP2 mice compared with controls (Fig. S2D), while levels of *S100B* and *Kir4.1* were similar in all groups (Fig. S2E and F). The mRNA levels of synapse-related genes such as *Bdnf*, *Cplx2*, *Shank3*, *Homer*, and *Gap43*, which were altered in R6/2 and R6/2-Tom mice, were not influenced by the forced expression of hSREBP2 in glial cells (Fig. S2G and H). Transcript levels of genes related to pathways such as energy and mitochondrial metabolism and autophagy were also not affected by the over-expression of hSREBP2 (Fig. S3A–I).

Glial hSREBP2 over-expression influences the levels of synaptic proteins in HD mice

Since cholesterol secreted from glial cells participates in synapse formation and maintenance and influences the intracellular distribution of proteins involved in the synaptic machinery (Pfrieger 2003), we decided to purify synaptosomes from the infused hemibrains of wt-Tom, R6/2-Tom, and R6/2-hBP2 mice and perform semi-quantitative western blot analysis for pre- and post-synaptic proteins.

We found that R6/2-Tom mice exhibited higher expression levels of the pre-synaptic protein SYP than wt-Tom mice and that glial hSREBP2 over-expression completely reversed this parameter (Fig. 2L and M). SNAP25 levels were similar in wt-Tom and R6/2-Tom, while a 38% increase was found in R6/2-hBP2 tissues (Fig. 2L and M). VAMP1 levels were similar in all conditions (Fig. 2L and M). Regarding the post-synaptic site, our densitometric analyses of the immunoreactive bands indicated a weak but significant increase ($p = 0.0138$) in PSD95 level in R6/2-hBP2 mice compared with wt-Tom and R6/2-Tom animals (Fig. 2N and O), even though differences between wt-Tom and R6/2-Tom mice were not observed (Fig. 2I and K). Conversely, SHANK3 levels were similar in all the tested mice, including R6/2-hBP2 mice (Fig. 2N and O). Finally, R6/2-Tom mice exhibited reduced NMDAR1 protein levels compared with wt-Tom mice, and forced expression of hSREBP2 normalized its levels to that of wt-Tom mice (Fig. 2N and O).

We conclude that glial hSREBP2 over-expression influences and partially reverses altered levels of synaptic proteins in synaptosomes of HD mice.

Glial hSREBP2 over-expression restores synaptic communication in HD mice

As R6/2 striatal MSNs exhibit altered synaptic transmission (Cepeda *et al.* 2003; Cepeda *et al.* 2004), we performed electrophysiological studies to evaluate whether synaptic dysfunction was reversed in R6/2-hBP2 mice.

In these studies, biocytin was included in the patch pipette to post hoc recover the morphological details of the recorded neurons (Fig. 3A). We first analyzed the passive membrane properties of striatal MSNs from brain slices of wt-Tom and R6/2-hBP2 mice. For R6/2-hBP2 mice, we compared data obtained from MSNs of the contralateral and the infused hemispheres. The comparison between R6/2-hBP2 and wt-Tom mice highlighted the fact that the membrane capacitance (C_m), which is proportional to cell size, was significantly lower in R6/2-hBP2 compared with wt-Tom MSNs, while it was similar between the contralateral and the infused hemispheres of R6/2-hBP2 mice (Fig. 3B). On the other hand, input resistance (R_{in}), reflecting the number of ion channels expressed by the cell, was significantly higher in both the infused and the contralateral hemispheres of R6/2-hBP2 compared with wt-Tom mice, and unchanged in the infused striata of R6/2-hBP2 mice compared with the contralateral ones (Fig. 3C).

No significant differences in the average amplitude of spontaneous excitatory postsynaptic currents (sEPSC) from MSNs were found between groups (Fig. 3D, E; the recorded events were AMPA-mediated since they were completely abolished by administration of 10 μ M NBQX). In contrast, the average frequency of sEPSCs in MSNs from the contralateral hemisphere of R6/2-hBP2 mice was significantly lower compared with wt-Tom mice, and glial over-expression of hSREBP2 led to a partial rescue of this defect (Fig. 3F).

To test if the inhibitory synapses were also influenced by hSREBP2 treatment, we recorded spontaneous inhibitory synaptic currents (sIPSCs) at a holding potential of 0 mV (Fig. 3G). The recorded events were GABA-mediated since they were completely abolished by administration of 10 μ M bicuculline (Fig. 3G). The average amplitude of sIPSCs was not affected (Fig. 3H). In contrast, the average frequency of sIPSCs in MSNs in the R6/2-hBP2-contralateral hemisphere was significantly higher compared with wt-Tom mice, and glial over-expression of hSREBP2 led to a significant reduction in the average frequency of sIPSCs in the infused hemisphere (Fig. 3I), bringing it closer to that in the wt-Tom mice.

Glial hSREBP2 over-expression reduces muHTT aggregates in HD mice

A hallmark of HD is the presence of intracellular aggregates of muHTT (DiFiglia *et al.* 1997). To test whether glial over-expression of hSREBP2 in the HD striatum influenced muHTT aggregation, we performed immunofluorescence staining on coronal sections of brains from R6/2-Tom and R6/2-hBP2 mice by using the EM48 antibody, which is specific for the expanded polyQ tract prone to

aggregate (Fig. 4A). As expected, tdTomato did not influence the number and the size of muHTT aggregates. Of note, the number and the size of EM48-positive aggregates were reduced in the infused striata of R6/2-hBP2 mice compared with the contralateral ones (Fig. 4B and C).

Glial hSREBP2 over-expression increases the number of Drd2-expressing MSNs in HD mice as detected by X-Clarity technology

Neuronal dysfunction of striatal neurons precedes their degeneration, and the dopamine receptor D2 (DRD2) MSNs of the indirect pathway are the first affected in HD models and patients (Reiner *et al.* 1988; Albin *et al.* 1989; Galvan *et al.* 2012; Sebastianutto *et al.* 2017). Although R6/2 mice (similar to other HD mouse models) do not show overt signs of neuronal loss (Mangiarini *et al.* 1996), the downregulation of *Drd2* transcript in striatal MSNs is an established early mark of disease progression that has been proposed as a sensitive measure of the effects of therapeutics (Crook *et al.* 2012). In particular, Crook and Housman developed a *Drd2* dysregulation assay by crossing *Drd2*-eGFP mice with different HD mice to obtain animals with DRD2-MSNs labeled with eGFP, and then used FACS sorting as a quantitative and reproducible readout of the efficacy of their therapeutics (Crook *et al.* 2012).

Here we adopted the same strategy to obtain animals with DRD2-MSNs labeled with eGFP (herein *Drd2*-wt and *Drd2*-R6/2 mice) but used the X-Clarity technology to obtain a measurement of the number of MSNs expressing DRD2 in situ, without dissociation, and in a large volume of striatum (approx. 0.108 ± 0.005 mm³) following forced expression of hSREBP in astrocytes.

To accomplish this goal, we injected AAV2/5-gfaABC1D-tdTomato or AAV2/5-gfaABC1D-hSREBP2-tdTomato into the right striata of 7-week-old *Drd2*-wt and *Drd2*-R6/2 mice (herein *Drd2*-wt-Tom, *Drd2*-R6/2-Tom, and *Drd2*-R6/2-hBP2). Animals were sacrificed 4 weeks later. From each animal, two brain coronal slices which were 1 mm thick (including the striatum) were prepared from the infused and contralateral hemispheres and the area corresponding to the striatum was isolated and clarified using the X-Clarity technology (Fig. 4D). The images acquired with two-photon microscopy in the clarified striata of *Drd2*-wt-Tom mice confirmed distinct signals of tdTomato and eGFP, which labeled infected astrocytes and DRD2-MSNs, respectively (Fig. 4E). The subsequent quantification of the eGFP signal in the different experimental groups revealed a reduced number of DRD2-MSNs in the infused striata of *Drd2*-R6/2-Tom mice and in the contralateral striata of *Drd2*-R6/2-hBP2 compared with *Drd2*-wt-Tom mice (Fig. 4F and G). Of note, the number of DRD2-MSNs measured in the infused striata of *Drd2*-R6/2-hBP2 was similar to that quantified in *Drd2*-wt-Tom mice (Fig. 4F and G), indicating that over-expression of hSREBP2 in astrocytes allows these neurons to regain DRD2 expression and, supposedly, functionality.

Glial hSREBP2 over-expression ameliorates motor defects and completely restores cognitive decline in HD mice

To assess whether the described amelioration of synaptic activity and disease phenotypes following over-expression of hSREBP2 in astrocytes was correlated with a beneficial effect on behavioral abnormalities, we subjected wt-Tom, R6/2-Tom, and R6/2-hBP2 mice to motor and cognitive tasks. As expected, 11-week-old R6/2-Tom mice exhibited a severe hypokinetic phenotype as demonstrated by reduced global activity, total distance traveled, and number of rearings in the activity cage test (Fig. 5A–C). Glial over-expression of hSREBP2 led to a slight but significant rescue of these parameters (Fig. 5A–C). We also evaluated the time that mice spent exploring the peripheral or central area of the arena during the activity cage test as a measure of anxiety-like behavior (Fig. 5D). R6/2-Tom mice showed anxiety-related behavior as they spent more time in the periphery compared with wt-Tom mice. Of note, R6/2-hBP2 mice behaved similarly to wt-Tom mice (Fig. 5E). When we measured the neuromuscular function of mice with the grip-strength test, we observed reduced muscle strength in R6/2-Tom mice compared with wt-Tom mice and, again, glial over-expression of hSREBP2 had a beneficial effect on this feature (Fig. 5F). Furthermore, we performed the paw-clasping test to study the clasping behavior of mice as an index of neuronal dysfunction. As expected, R6/2-Tom mice had a worse performance compared with wt-Tom, but in this case the treatment was not able to significantly rescue this behavior (Fig. 5G). Finally, to analyze the effect of treatment on cognitive decline, we performed the novel-object recognition (NOR) test: at 11 weeks of age, R6/2-Tom mice were not able to discriminate between the novel object and the familiar one, in contrast to the wt-Tom mice. Of note, glial over-expression of hSREBP2 completely prevented cognitive decline and R6/2-hBP2 mice behaved as the wt-Tom (Fig. 5H).

Discussion

In this work, we highlight the therapeutic value of forcing cholesterol biosynthesis *in vivo* in an HD mouse model via a gene therapy approach that delivers the active form of the master transcription factor SREBP2 specifically to astrocytes. In the brain, the physiological cross-talk between astrocytes and neurons provides the latter with the cholesterol produced by the former, which is then utilized by neurons to support their function. This cross-talk is severely damaged *in vitro* in the presence of the mutation, due to reduced activity of SREBP2, but it can be rescued when HD astrocytes over-expressing SREBP2 are co-cultured with HD neurons. In these conditions, we showed that neuronal function and morphology are fully reestablished (Valenza *et al.* 2015a). Here, we now provide *in vivo* evidence that this altered communication between astrocytes and neurons is a key pathological feature

of HD astrocytes, which can be targeted at a cellular level and their pathology reversed, leading to substantial amelioration of HD phenotypes in the living animals. Accordingly, we show that hSREBP2 delivery to astrocytes *in vivo*, by enhancing the cholesterol biosynthesis pathway, can revert molecular, biochemical, electrophysiological, and behavioral abnormalities associated with neuronal dysfunction typically observed in the R6/2 mouse model.

We show that unilateral AAV-delivery of SREBP2 in glial cells is sufficient to completely rescue cognitive decline in R6/2 mice. Similar data were obtained upon cholesterol delivery to the brain of this mouse model via brain-permeable polymeric nanoparticles or mini-pumps (Valenza *et al.* 2015; Birolini *et al.* 2020). The fact that genetic deletion of SCAP or SREBP2 in astrocytes of adult mice results in cognitive defects (Van Deijk *et al.* 2017; Ferris *et al.* 2017) confirms the role of astrocytes in memory and cognition *in vivo*, and that altered cross-talk between astrocytes and neurons at synaptic contacts may contribute to cognitive disturbances (Santello *et al.* 2019). Moreover, cholesterol synthesis is downregulated in aging astrocytes (Boisvert *et al.* 2018; Allen & Lyons 2018), suggesting that lack of cholesterol production in these cells may contribute to the synaptic and cognitive defects observed in aging. Here, we provide further evidence that cholesterol produced from astrocytes *in vivo* is also a critical player in memory recognition in the HD context.

Unilateral AAV-delivery of SREBP2 also ameliorated motor defects in R6/2 mice, suggesting that this approach is able to produce the optimal content of newly synthesized cholesterol needed to partially restore motor-dependent circuits. These results are in agreement with our recent work that evaluated the effect of three escalating doses of cholesterol infused directly into the striata of R6/2 mice through osmotic mini-pumps. Indeed, we demonstrated that all three doses prevented cognitive defects, while only the highest dose attenuated motor phenotypes (Birolini *et al.* 2020).

Mechanistically, our findings indicate that hSREBP2 over-expression in glial cells carries out its beneficial effect by acting on different aspects of the disease. The synaptic effect of AAV delivery of hSREBP2 is certainly the relevant one, and it is supported by the evidence of normalization in the level of synaptic proteins and of both inhibitory and excitatory synaptic communication of MSNs.

Newly synthesized cholesterol from astrocytes may facilitate synaptic vesicle fusion and exocytosis (Linetti *et al.* 2010) or bind to proteins involved in synaptic transmission (Thiele *et al.* 2000; Pfrieder 2003c; Allen *et al.* 2007).

Our current data also suggest that the mechanisms by which stimulation of cholesterol biosynthesis counteracts synaptic dysfunction in HD mice do not involve major transcriptional changes. Nor are the mRNA levels of a subset of genes involved in glial or energy metabolism influenced by exogenous hSREBP.

At the neuropathological level, increased hSREBP2 in the striatum of R6/2 mice reduced the number and size of muHTT aggregates, supporting the notion that enhanced cholesterol biosynthesis may participate in inducing clearance pathways, as we recently showed in the striata of HD mice following striatal infusion of cholesterol through osmotic mini-pumps (Biolini *et al.* 2020). The fact that in the current study the transgene was delivered to astrocytes suggests that clearance may also occur by a non-cell autonomous mechanism.

Importantly, hSREBP2 over-expression in glial cells rescues specific neurochemical features in MSNs. In fact, reduced striatal DRD2 was consistently demonstrated in patients (Andrews *et al.* 1999; Weeks *et al.* 1996; Glass *et al.* 2000; Feigin *et al.* 2007; Van Oostrom *et al.* 2009) and murine models (Cha *et al.* 1998; Ariano *et al.* 2002; Pouladi *et al.* 2012; Crook & Housman 2012; Valenza *et al.* 2015b) and its dysregulation is a sensitive measure of HD pathology (Crook & Housman 2012). Of note, a loss of dopamine receptors has also been correlated with early cognitive decline (Backman and Farde, 2001). Our X-Clarity approach applied to the striatum allowed for the first time an accurate measurement and quantification of striatal MSNs in situ and confirmed the decrease in the level of DRD2 in MSNs (Crook & Housman 2012). Importantly, we show that HD neurons, which receive more cholesterol from hSREBP2 over-expressing astrocytes, increase DRD2 expression and are quantifiable through two-photon imaging. These findings also suggest that within the striatum, the astrocyte-neuron signaling may be synapse- and cell-specific by acting at least on the DRD2-MSNs, as recently proposed (Martin *et al.* 2015). The observed rescue in DRD2-MSNs, and in other synaptic features, may be favored by a closer contact between neurons and astrocytes, which is reduced in R6/2 astrocytes (Octeau *et al.* 2018).

In a similar gene therapy approach, the gene encoding for CYP46A1, the enzyme that converts cholesterol into the neuronal cholesterol catabolite 24S-OHC, was delivered into striatal neurons of HD mice by use of an AAVrh10 vector (Boussicault *et al.* 2016; Kacher *et al.* 2019). The treatment decreased the number and size of muHTT aggregates and improved motor deficits in R6/2 mice (Boussicault *et al.* 2016) and provided long-lasting improvement in zQ175 HD mice (Kacher *et al.* 2019). In both studies, levels of cholesterol precursors were restored or increased in the HD striatum following AAV-delivery of CYP46A1. In our study, we show increased levels of 24S-OHC following AAV-delivery of hSREBP2 in glial cells, although *Cyp46A1* mRNA remained unchanged, supporting the close balance between cholesterol synthesis and catabolism in the diseased brain.

In conclusion, our findings confirm the role of astrocytes as important regulatory cell types in brain function and behavior (Araque *et al.* 2014; Santello *et al.* 2019) and in neurodegenerative disorders, including HD (Khakh *et al.* 2017; Covelo & Araque 2018). By targeting astrocytic cholesterol signaling in the striatum we were able to rescue biochemical, neuropathological, functional, and

behavioral features in HD mice. Thus, SREBP2 gene transfer to astrocytes may be a therapeutic option to fight core features of this disease.

Materials and Methods

Colony management

Our R6/2 colony lifespan was approximately of 13 weeks and it was maintained through the male line exclusively (Mangiarini *et al.* 1996). Transgenic R6/2 males were paired with non-carrier females (B6CBAF1/J, purchased from Charles River). The CAG repeat length of the animals used in this study is 130-170 CAGs (Laragen). Changes that could affect strain productivity, general behavior, litter size, pup survival, genotype frequency, and phenotype were constantly monitored.

The Drd2-eGFP colony is a transgenic mouse line generated in 2003 by the GENSAT (Gene Expression Nervous System Atlas) project at Rockefeller University in New York (Gong *et al.* 2003). Primary labelling was found to occur in Drd2 positive medium spiny neurons from the indirect basal ganglia pathway. In this work, this model was crossed with R6/2 mice in order to label *in vivo* Drd2-expressing medium spiny neurons.

All mice were weaned at 21 day (+/- 3 days). Mice were housed under standard conditions (22 ± 1°C, 60% relative humidity, 12 hours light/dark cycle, 3–4 mice/cage, with food and water provided ad libitum). After PCR genotyping (Mangiarini *et al.* 1996; Gong *et al.* 2003), male and female mice were included and randomly divided into experimental groups. Littermates were included as controls. Animal care was conducted in accordance with standard ethical guidelines approved by the Italian Governing Law (D.lgs 26/2014; Authorization n.324/2015-PR issued May 6, 2015 by Ministry of Health); the NIH Guide for the Care and Use of Laboratory Animals (2011 edition) and the EU directives and guidelines (EEC Council Directive 2010/63/UE) and the local ethics committee approved the experiments.

Viral production

Starting from pZac2.1 gfaABC1D-tdTomato (from Addgene) and pcDNA3.1 hSREBP2(402)-eGFP (from T. Osborne; Zoumi *et al.* 2005) we produced a pZac vector expressing hSREBP2 fused with tdTomato. These vectors were used to produce the viral constructs AAV2/5-gfaABC1D-tdTomato (1,7 x 10¹⁴ U/mL) and AAV2/5-gfaABC1D-hSREBP2-tdTomato (1,7 x 10¹³ U/mL) contained the expression cassette consisting of either tdTomato or the active N-terminal fragment of hSREBP2 (1-482 aa), driven by the minimal GFAP promoter (gfaABC1D) surrounded by inverted terminal repeats of AAV2/5.

HSV1-JDNI8/gfaABC1D-tdTomato (5×10^9 pfu/mL) was produced and purified as previously described (Verlengia *et al.* 2017). Briefly, ICP4/ICP27-complementing U2OS cells were transfected with purified BAC-DNA engineered to contain the HSV1-JDNI8/gfaABC1D-tdTomato vector genome. Depending upon kinetics of cytopathic effects, 7-10 days from transfection supernatant was collected and reused for virus amplification in the same cell line, in order to obtain a highly concentrated vector stock. Estimation of vector titer was carried out by qPCR for quantitatively detecting the glycoprotein D gene (Miyagawa *et al.* 2015).

Stereotaxic injection of JDNI8-gfaABC1D-tdTomato, AAV2/5-gfaABC1D-tdTomato and AAV2/5-gfaABC1D-hSREBP2-tdTomato

7-weeks-old mice were deeply anesthetized with Avertin 2.5% (15 μ L/gr body weight). The virus was injected by implantation of a borosilicate glass needle into the right striatum of mice via stereotaxic surgery using an automated infusion syringe pump (KD Scientific, KDS100), on which a 50 μ L Gastight Syringe Model 1705 TLL with PTFE Luer Lock (Hamilton, 80920) could be mounted. In order to favor needle entry and vector spread in the injected striata, we used borosilicate needles customized by laser shaping with the Leica Laser Microdissector CTR6000 (Leica Microsystems), that allowed a 45 degrees edge chamfering of tip (inner diameter at tip = 60 μ m) and, moreover, to open an additional circular hole (\varnothing 20 μ m) about 100 μ m from the beveled edge (Paolone *et al.* 2018). The following stereotaxic coordinates were used: 2 mm lateral to midline, 0.74 mm rostral to the bregma, 3.5 mm ventral to the skull surface; from Paxinos G and Watson C. The Rat Brain in Stereotaxic Coordinates. Academic Press, San Diego. The rate of injection was 12 μ l/min with a total volume of 2 μ L.

Assessment of post-operative pain and distress was performed using a specific table for pain scoring based on behavioral indicators of well-being and monitoring mice body weight (Lloyd & Wolfensohn 1998).

Immunohistochemistry analysis

4 weeks after the infection anesthetized mice were transcardially perfused with PFA 4%. Brains were post-fixed overnight in PFA 4% at 4°C and then in 30% sucrose to prevent ice crystal damage during freezing in OCT.

15 μ m coronal sections or 30 μ m coronal sections were prepared for immunohistochemical analysis. Epitopes were demasked at 98°C with NaCitrate 10 mM and then slices were incubated with the following primary antibodies for 3h at RT: rabbit anti-SREBP2 (1:100; Ls-Bio, LS-C179708), rabbit anti-RFP (1:100, MBL, PM005), mouse anti-RFP (1:100, Thermo Fisher, MA5-15257), anti-

DARPP32 (1:100; Cell Signalling, 2306), mouse anti-NeuN (1:100; Millipore, MAB377); rabbit anti-GFAP (1:250; Dako, Z0334), rabbit anti-IBA1 (1:100, Wako, 019-19741), rabbit anti-Huntingtin clone EM48 (1:100; Millipore, MAB5374). Anti-rabbit Alexa Fluor 568-conjugated goat secondary antibodies (1:500; Invitrogen), anti-rabbit Alexa Fluor 633-conjugated goat secondary antibodies (1:500; Invitrogen) or anti-mouse Alexa Fluor 488-conjugated goat secondary antibodies (1:500; Invitrogen) were used for detection (1h at RT). Sections were counterstained with the nuclear dye Hoechst 33258 (1:10.000, Invitrogen) and then mounted under cover slips using Vectashield (Vector Laboratories).

Image acquisition and quantification

To study the spread of the viruses, large images were acquired with a Nikon Crest X-Light V2 microscope at 4×.

To study the tropism of the viruses and to count muHTT aggregates, confocal images (5 to 10-z steps) were acquired with a LEICA SP5 laser scanning confocal microscope. Laser intensity and detector gain were maintained constant for all images. To count aggregates in the striatum 18 images/mice from 9 sections throughout the entire striatum were taken from three R6/2-hBP2 mice at 40×. To quantify the number and the size of aggregates, ImageJ software was used to measure the fluorescence. Images were divided into three-color channels and the same global threshold was set.

RNA extraction and qRT-PCR

4 weeks after the infection, mice were sacrificed by cervical dislocation and tissues were isolated and frozen. Total RNA from the infused striatum and the ipsi-lateral cortex of treated mice was extracted with TRIzol reagent (Life Technologies, 15596026). RNA quality check was carried out on 1% agarose gel. Potential contamination of DNA was removed using the Ambion® DNA-free™ Kit (Invitrogen, AM1906). 500 ng of RNA was retrotranscribed to single-stranded cDNA using the iScript cDNA synthesis kit (Bio-Rad, 1708891). The analyses were performed in 3 animals/group. For each sample, two different reverse transcription were performed. For each cDNA reaction, one or two conventional qPCR were performed in a CFX96 Real-Time System (Bio-Rad) in a 15 μ l volume containing diluted cDNA and 7.5 μ L iQ EVA Green Supermix (Bio-Rad, 172-5204), 7.5 μ L nuclease-free water and 0.33 μ M forward and reverse primers. The amounts of target transcript were normalized to β -actin as reference gene. Table S1 summarizes the primer sequences and melting temperature used in this work.

Synaptosomes preparation and WB analysis

Mice were sacrificed by cervical dislocation and the tissues were isolated and frozen. Syn-PER Synaptic Protein Extraction Reagent (Thermo Fisher Scientific, 87793) was used for synaptosome purification from the striatum and the ipsi-lateral cortex accordingly to the manufacturer instruction. Briefly, a volume of 10 mL of Syn-PER Reagent per gram of tissue was added and tissues were homogenized on ice. The homogenate was centrifuged at 1,200 x g for 10 min at 4°C. The supernatant was centrifuged at 15,000 x g for 20 min at 4°C to pellet synaptosomes. The pellet was resuspended in Syn-PER Reagent. Proteins were quantified with Pierce™ BCA Protein Assay Kit (Thermo Fisher Scientific, 23225).

Criterion TGX Stain Free Precast Gels 7.5% (Bio-Rad, 5678023) or Any kD (Bio-Rad, 5678123) were used for Western Blot analysis. Membranes were incubated with the following primary antibodies over night at 4°C: rabbit anti-RFP (1:1000; MBL, PM005), rabbit anti-SREBP2 (1:1000; LS-Bio, LS-B4695), mouse anti-SYP (1:500; Abcam, ab8049), mouse anti-SNAP25 (1:1000; Abcam, ab66066), rabbit anti-VAMP1 (1:1000; Abcam, ab151712), mouse anti-PSD95 (1:1000; SySy, 124011), rabbit anti-SHANK3 (1:1000; SySy, 162302), rabbit anti-NMDAR1 (1:500; MerckMillipore, Ab9864), rabbit anti-GAPDH (1:5000; Abcam, ab37168). Goat anti-mouse IgG-HRP (1:3000; Bio-Rad, 1706516) or Goat anti-rabbit IgG-HRP (1:3000; Bio-Rad, 1706515) were used for detection (1h at RT). Proteins were detected using Clarity Western ECL Substrate (Bio-Rad, 1705061) or SuperSignal West Femto Maximum Sensitivity Substrate (Thermo Fisher Scientific, 34096) using ChemiDoc MP System (Bio-Rad). Protein levels were normalized using GAPDH (for the cytosolic fraction) or using 6 different protein bands of the stain-free technology (for synaptosomes). 4 animals/group were analyzed by western blotting and for each protein, two or three technical replicates were performed.

X-clarity and 2-photon imaging

4 weeks after the infection anesthetized mice were transcardially perfused with PFA 4%. Brains were post-fixed overnight and sliced with a Leica VT1000S Vibrating blade microtome (Leica Biosystems). From each mouse, two 1-mm thick coronal brain slices were prepared, from which the infused and the contra-lateral striatum were isolated. Tissues were clarified using the X-Clarity system (Logos Biosystem) according to manufacturer instructions. Briefly, tissues were incubated in embedding solution (Logos Biosystems, C13104) at 4°C for 24h at most, allowing hydrogel monomers to diffuse uniformly throughout the samples and to covalently link biomolecules including proteins, nucleic acids and small molecules. Polymerization was performed by placing the samples within the X-CLARITY™ Polymerization at 37°C for 3 hours under vacuum condition (-90kPa). Following washing steps, the hydrogel-embedded tissues were rinsed with Electrophoretic Tissue

Clearing (ETC) Solution (Logos Biosystems, C13001) and moved into the X-CLARITY™ Tissue Clearing System II (Logos Biosystems, C30001) chamber, filled with the ETC solution in which the application of a uniform electric current (1.5 A) at a controlled temperature of 37°C enabled the active extraction of lipids from tissues in about 2-3 hours.

After clearing, samples were washed with PBS 1X overnight at RT to remove residual SDS. The endogenous signal (eGFP) was acquired by using a A1 MP+ microscope (Nikon) equipped with Ti:Sapphire MP tunable laser (680 - 1080 nm) using the water plan-Apo LWD 25 X objective (NA 1.1). Images were acquired with the following settings: 16 bit, Z-stack of approximately 400 μm with a Z step size of 5 μm . The endogenous fluorescent protein eGFP was excited at a wavelength of 900 nm. For each striatum, 2-3 images were acquired. Images were processed using the software NIS-Elements (Nikon). First, a 3D deconvolution algorithm was applied to improve image quality. Afterwards, background was removed using the rolling ball correction. To quantify the number of cells expressing eGFP, a mask was applied using a plugin for 3D reconstruction. For each image, the number of cells expressing eGFP was normalized on the Z volume acquired.

Electrophysiological analysis

Experiments were performed on submerged brain slices obtained from 12 week old mice. Animals were anesthetized by inhalation of isoflurane and decapitated. The head was rapidly submerged in ice-cold ($\sim 4^\circ\text{C}$) and oxygenated (95% O_2 - 5% CO_2) cutting solution containing: Sucrose 70 mM, NaCl 80 mM, KCl 2.5 mM, NaHCO_3 26 mM, Glucose 15 mM, MgCl_2 7 mM, CaCl_2 1 mM and NaH_2PO_4 1.25 mM. Striatal coronal slices (300- μm -thick) were cut using a vibratome (DTK-1000, Dosaka EM, Kyoto, Japan) and allowed to equilibrate for at least 1 hour in a chamber filled with oxygenated ACSF containing: NaCl 125 mM, KCl 2.5 mM, NaHCO_3 26 mM, Glucose 15 mM, MgCl_2 1.3 mM, CaCl_2 2.3 mM and NaH_2PO_4 1.25 mM. The slices collected from the hemisphere ipsilateral to the infusion site were transferred to a submerged-style recording chamber at room temperature (~ 23 - 25°C) and were continuously perfused at 1.4 ml/min with ACSF. The chamber was mounted on an E600FN microscope (Nikon) equipped with 4X and 40X water-immersion objectives (Nikon) and connected to a near-infrared CCD camera for cells visualization.

Data were obtained from MSNs using the whole-cell patch-clamp technique in both voltage- and current-clamp mode. The patch pipette was produced from borosilicate glass capillary tubes (Hilgenberg GmbH) using a horizontal puller (P-97, Sutter instruments) and filled with an intracellular solution containing: Cs-methanesulphonate 120 mM, KCl 5 mM, CaCl_2 1 mM, MgCl_2 2 mM, EGTA 10 mM, Na_2ATP 4 mM, Na_2GTP 0.3 mM, Hepes 8 mM and lidocaine N-ethylbromide 5 mM (added to inhibit firing by blocking intracellularly the voltage-sensitive Na^+ channels) (pH

adjusted to 7.3 with KOH). Spontaneous excitatory postsynaptic currents (sEPSCs), mediated by the activation of ionotropic glutamate receptors, were recorded from MSNs at a holding potential of -70 mV, whereas spontaneous inhibitory postsynaptic currents (sIPSCs), elicited by the activation of GABA_A receptors, were assessed at a holding potential of 0 mV. The signals were amplified with a MultiClamp 700B amplifier (Molecular Devices) and digitized with a Digidata 1322 computer interface (Digitata, Axon Instruments Molecular Devices, Sunnyvale, CA). Data were acquired using the software Clampex 9.2 (Molecular Devices, Palo Alto, CA, U.S.A.), sampled at 20 kHz and filtered at 2 kHz.

The off-line detection of spontaneous postsynaptic currents (sPSCs) were performed manually using a custom-made software in Labview (National Instruments, Austin, TX, U.S.A.). The amplitudes of sPSCs obeyed a lognormal distribution. Accordingly, the mean amplitude was computed as the peak of the lognormal function used to fit the distribution. Intervals (measured as time between two consecutive sPSCs) for spontaneous events were distributed exponentially and the mean interval was computed as the tau (τ_{interval}) value of the mono-exponential function that best fitted this distribution. The reciprocal of τ ($1/\tau$) is the mean of the instantaneous frequencies of sPSCs. Furthermore, the analysis of the membrane capacitance (C_m) and the input resistance (R_m) was performed using Clampfit 10.2 (Molecular Devices, Palo Alto, CA, U.S.A.). C_m was estimated from the capacitive current evoked by a -10 mV pulse, whereas R_m was calculated from the linear portion of the I-V relationship obtained by measuring steady-state voltage responses to hyperpolarizing and depolarizing current steps.

Behavioral tests

Mice behavior was evaluated at 11 weeks of age. Animals were assigned randomly and sex was balanced in the various experimental groups. All the behavioral analyses were performed in blind.

Activity Cage: spontaneous locomotor activity was evaluated by the activity cage test, in presence of a low-intensity white light source. The animal was placed in the center of the testing, transparent, arena (25 cm × 25 cm) (2Biological Instrument) and allowed to freely move for an hour. Following 15 minutes of habituation, both horizontal and vertical motor activities were assessed by an automated tracking system (Actitrack software, 2Biological Instrument) connected to infrared sensors surrounding the arena. Total distance travelled, mean velocity speed, stereotyped movements and numbers of rearings were evaluated. The % of time that mice explored the periphery or the center area of the was evaluated as a measure of anxiety-like behavior.

Novel Object Recognition (NOR) test: long-term memory was evaluated by the NOR test, using a grey-colored, non-reflective arena (44 × 44 × 44 cm). All phases of the test were conducted with a

low-intensity white light source. In a first habituation phase, mice were placed into the empty arena for 10 min. The habituation phase was followed by the familiarization one, in which two identical objects (A' and A'') were presented to each animal for 10 min. Twenty-four hours later, during the testing phase, the same animals were exposed to one familiar object (A'') and a new object (B) for 10 min. A measure of the spontaneous recognition memory was represented by the index of discrimination, calculated as (time exploring the novel object – time exploring the familiar object) / (time exploring both objects) × 100. Mice exploring less than 7 sec. were excluded from the analysis due to their inability to perform the task.

Grip strength test: mice were lifted by the lower back and tail and lowered towards the grip (Ugo Basile) until the animal grabbed it with both front paws. The animal was then lowered toward the platform and gently pulled straight back with consistent force until it released its grip. The forelimb grip force, measured in grams, was recorded. The test was repeated for 5 times, and measures were averaged. After testing, animals were placed back into their home cage.

Paw clasping test: mice were suspended by the tail for 30 s and the clasping phenotype was graded according to the following scale: level 0, no clasping; level 1, one hindlimb retracted toward the abdomen; level 2, both hindlimbs retracted toward the abdomen; level 3, both hindlimbs entirely retracted and touching the abdomen. After testing, animals were placed back into their home cage.

Statistics

Prism 8 (GraphPad software) was used to perform all statistical analyses. Data are presented as means ± standard error of the mean (SEM). Grubbs' test was applied to identify outliers. For each set of data to be compared, we determined whether data were normally distributed or not to select parametric or not parametric statistical tests. The specific statistical test used is indicated in the legend of all results figures. Differences were considered statistically if the p-value was less than 0.05. To pre-determine sample sizes, we used G-power analysis based on pilot or previous studies. For animal studies, mice were assigned randomly, and sex was balanced in the various experimental groups; animals from the same litter were divided in different experimental groups; blinding of the investigator was applied to *in vivo* procedures and all data collection. Table S2 summarizes all the trials and read-outs performed.

Acknowledgments

The authors acknowledge the scientific and technical assistance of Dr. Chiara Cordiglieri, responsible of the INGM Imaging Facility (Istituto Nazionale Genetica Molecolare – INGM, Milan, Italy); Dr. Cesare Covino and Advanced Light and Electron Microscopy BioImaging Center (ALEMBIC) at San Raffaele Institute, Milan (EuBI_PIRI081); Dr. Laura Madaschi and NOLIMITS, an advanced imaging facility established by the University of Milan; Monica Favagrossa and Marta Vittani for technical contribution on this study during the preparation of their experimental thesis.

This research was partially supported by Telethon Foundation (GGP17102), NeurostemcellRepair (FP7, GA no. 602278, 2013-17), NSC-Reconstruct (H2020, GA no 874758, 2020-23) (to E.C.); by Linea 2-2017, Department of Biosciences, University of Milan (to M.V.); by the Italian Ministry of Education, University and Research (MIUR): Dipartimenti di Eccellenza Program (2018–2022) - Dept. of Biology and Biotechnology "L. Spallanzani", University of Pavia (to G. Biella, F.T., M.C.). F.T. was supported by Fondazione Umberto Veronesi.

Author contributions

M.V., M.S. and E.C. conceived the study; G.V. and M.S. provided HSV vectors; L.Z. and M.G. provided AAV vectors; G. Birolini and M.V. performed *in vivo* experiments, including mice infection with viral vectors and behavioral analysis; G. Birolini performed immunostaining experiments and provided confocal images and quantification; G. Birolini, M.V. and G.V. performed Clarity experiments; G. Birolini performed western blot analysis; P.C. provided advices for qRT-PCR experiments; M.V. produced the plasmids and contributed to perform qRT-PCR experiments; C.M., F.T., and G. Biella performed and analyzed the electrophysiological recordings; C.C., V.L. and F.T. performed and analysed mass spectrometry data; M.V. and G. Birolini collected study data and performed statistical analyses; M.V. and E.C. oversaw and coordinated responsibility for all research activities and their performance and provided experimental advice throughout the work; E.C. and M.V. secured the funding, the collaborations and the execution of the entire project. M.V., G. Birolini, and E.C. wrote the paper that has been edited and reviewed by all authors.

Competing interests

All authors declare no competing interests.

Figure 1. In vivo characterization of AAV2/5-gfaABC1D-tdTomato and AAV2/5-gfaABC1D-hSREBP2-tdTomato

A–B. Scheme of the viruses and experimental paradigm used in the study, and readouts performed. Mice at 7 weeks of age were unilaterally infected in the right striatum with HSV or AAV expressing tdTomato under the control of the gfaABC1D promoter (A). Mice were sacrificed 4 weeks later and brains were collected to study viral spread and tropism (B).

C. Representative large images of coronal brain slices of wt mice infected with AAV2/5-gfaABC1D-tdTomato with immunostaining against tdTomato (red) to visualize AAV spread. Scale bar is 1000 μm .

D. Representative confocal images of coronal brain slices of wt mice infected with AAV2/5-gfaABC1D-TdTomato with immunostaining against tdTomato (red) and GFAP, IBA1, S100B, NeuN, and DARPP32 (green) to visualize viral tropism with relative signal quantification. Scale bar is 5 μm .

E–F. mRNA levels of *tdTomato* (E) and *hSrebp2* (F) in the striatum and cortex from wt, R6/2, R6/2-Tom, and R6/2-hBP2 mice ($n = 3$ mice/group).

G–I. Protein levels (G) and relative densitometry quantification of tdTomato (H) and hSREBP2 (I) in cytosolic fractions from the infused hemibrains from R6/2-Tom or R6/2-hBP2 ($n = 4$ mice/group). Stain-free imaging and GAPDH were used for normalization.

J. Representative large image and high-magnification confocal image (crop) of coronal brain slices of R6/2-hBP2 mice with immunostaining against GFAP (green) and SREBP2 (red).

K. mRNA levels of *mSrebp2* in the hemi-brains of wt and R6/2 mice, and in the infused hemi-brains of R6/2-Tom and R6/2-hBP2 mice ($n = 3$ mice/group).

L. mRNA levels of *mSrebp2* and *hSrebp2* in the infused hemi-brains from R6/2-hBP2 mice ($n = 3$).

Hoechst was used to counterstain nuclei (blue) in C, D, J. Scale bar is 1000 μm (C), 5 μm (D), 2000 μm (J, up), and 10 μm (J, down). Data (E, F, H, I, K, and L) are shown as scatterplot graphs with means \pm SEM. Each dot corresponds to the value obtained from each animal. Statistics: one-way ANOVA with Newman–Keuls post-hoc test (** $p < 0.01$).

Figure 2. mRNA transcript levels of cholesterol biosynthesis genes and levels of synaptic proteins following glial hSREBP2 over-expression

A. Genes encoding enzymes of cholesterol biosynthesis whose expression was analyzed by qPCR (red). Products of the Bloch and Kandutsch-Russell pathways are in blue and pink, respectively.

B–G. mRNA levels of hydroxymethylglutaryl-coenzyme A reductase (*Hmgcr*) (B), mevalonate kinase (*Mvk*) (C), squalene synthase/farnesyl-diphosphate farnesyl transferase 1 (*Sqs/Fdft1*) (D), cytochrome p450 lanosterol 14-alpha-demethylase (*Cyp51*) (E), 7-dehydroxycholesterol reductase (*Dhcr7*) (F), and cholesterol 24-hydroxylase (*Cyp46a1*) in the hemibrain from wt, R6/2, R6/2-Tom mice, and R6/2-hBP2 mice ($n = 3$ mice/group).

H–K. Lanosterol (H), Lathosterol (I), desmosterol (J), and 24-OHC (K) levels measured by GC-MS in the infused striata of wt-Tom, R6/2-Tom, and R6/2-hBP2 mice ($n = 4–6$ mice/group).

L–M. Protein levels (L) and relative densitometry quantification (M) of synaptophysin (SYP), synaptosome-associated protein 25 (SNAP25), and vesicle-associated membrane protein 1 (VAMP1) in synaptosomes purified from the infused hemi-brains from wt-Tom mice, R6/2-Tom mice, and R6/2-hBP2 mice ($n = 4$ mice/group).

N–O. Protein levels (N) and relative densitometry quantification (O) of postsynaptic density protein 95 (PSD95), SH3 and multiple ankyrin repeat domains 3 (SHANK3), and N-methyl-D-aspartate receptor (NMDAR1) in synaptosomes purified from the infused hemi-brains from wt-Tom mice, R6/2-Tom mice, and R6/2-hBP2 mice ($n = 4$ mice/group). Stain-free imaging was used as a loading control and for normalization. Data (B–K, M, and O) are shown as scatterplot graphs with means \pm SEM. Each dot corresponds to the value obtained from each animal. See Supplementary Figures S4 and S5 for full-length pictures of the blots shown in L and N. Statistics: one-way ANOVA with Newman–Keuls post-hoc test ($*p < 0.05$; $**p < 0.01$; $***p < 0.001$) or unpaired Student's t-test ($\#p < 0.05$).

Figure 3. Electrophysiological analysis in MSNs of R6/2 mice following glial hSREBP2 over-expression

A. Schematic representation of the electrophysiological parameters analyzed in striatal MSNs of mice (stained with biocytin) following 4 weeks of AAV infusion. Scale bar is $5 \mu\text{m}$.

B–C. Membrane capacitance (Cm, B) and input resistance (Rin, C) recorded from wt-Tom MSNs ($n=8$) and from the contralateral ($n = 5$) and infused ($n = 8$) MSNs of R6/2-hBP2 mice.

D–F. Spontaneous EPSCs recorded from MSNs at a holding potential of -70 mV (D). Average amplitude (E) and average frequency (F) of EPSCs from wt and R6/2-hBP2 mice MSNs.

G–I. Spontaneous IPSCs recorded from MSNs at a holding potential of 0 mV (G). Average amplitude (H) and average frequency (I) of IPSCs from wt and R6/2-hBP2 mice MSNs.

Data (B, C, E, F, H, and I) are shown as scatterplot graphs with means \pm SEM. Each dot corresponds to the value obtained from each animal. Statistics: one-way ANOVA with Newman–Keuls post-hoc test ($*p < 0.05$; $**p < 0.01$; $****p < 0.0001$; $***p < 0.001$).

Figure 4. muHTT aggregation and number of Drd2 neurons in R6/2 mice following glial hSREBP2 over-expression

A–C. Immunolabeling of muHTT aggregates (green) (A) and relative quantification of number (B) and size (C) in infused and contralateral striata of R6/2-Tom mice or R6/2-hBP2 mice ($n = 3–5$ /group). Hoechst (blue) was used to counterstain nuclei. Scale bar is $10 \mu\text{m}$.

D. Experimental paradigm used in the X-Clarity experiment. R6/2 mice were crossed with mice having Drd2-expressing MSNs tagged with GFP to obtain an HD line with neurons from the indirect pathway expressing GFP. Drd2 mice at 7 weeks of age were infected with AAV2/5-gfaABC1D-tdTomato (Drd2-wt-Tom) while Drd2-R6/2 mice were infected with AAV2/5-gfaABC1D-tdTomato (Drd2-R6/2-Tom) or with AAV2/5-gfaABC1D-hSREBP2-tdTomato (Drd2-R6/2-hBP2). Mice were sacrificed 4 weeks later and two 1 mm -thick brain coronal slices (comprehending the striatum) were prepared from each animal. From each slice, the

portion including the infused and the contralateral striatum was isolated and clarified using the X-clarity technology ($n = 5$ mice/group).

E. Representative two-photon imaging of the endogenous signals of GFP (green) and TdTomato (red) of 1-mm thick brain coronal slices from Drd2-wt-Tom (infused hemisphere).

F–G. Representative two-photon imaging (F) of the endogenous signal of GFP (green) of 1-mm thick brain coronal slices from Drd2-wt-Tom (infused hemisphere), Drd2-R6/2-Tom (infused hemisphere), and Drd2-R6/2-hBP2 (contralateral and infused hemisphere) with relative 3D reconstruction and quantification (G).

Data (B, C and G) are shown as scatterplot graphs with means \pm SEM. Each dot corresponds to an image. The number of neurons was normalized on the z-stack acquired. Statistics: one-way ANOVA with Newman–Keuls post-hoc test (* $p < 0.05$; ** $p < 0.01$; **** $p < 0.0001$).

Figure 5. Cognitive and motor abilities of R6/2 mice following glial hSREBP2 over-expression

A–E. Global activity (A), distance traveled (B), and number of rearings (C) in an open-field test in wt-Tom ($n = 13$), R6/2-Tom ($n = 14$), and R6/2-hBP2 ($n = 13$). Representative track plots (D) from the open-field test from wt-Tom ($n = 13$), R6/2-Tom ($n = 14$), and R6/2-hBP2 ($n = 13$) and relative quantification (E) of the time spent (%) in the center and in the periphery of the arena.

F. Grip strength (grams) in wt-Tom ($n = 13$), R6/2-Tom ($n = 15$), and R6/2-hBP2 ($n = 13$).

G. Paw clasping in wt-Tom ($n = 13$), R6/2-Tom ($n = 15$), and R6/2-hBP2 ($n = 13$).

H. Discrimination index (DI %) in the novel object recognition test of wt-Tom ($n = 12$), R6/2-Tom ($n = 15$), and R6/2-hBP2 ($n = 13$). DI above zero indicates a preference for the novel object; DI below zero indicates a preference for the familiar object.

Data (A–C and F–H) are shown as scatterplot graphs with means \pm SEM. Each dot corresponds to the value obtained from each animal. Statistics: one-way ANOVA with Newman–Keuls post-hoc test (* $p < 0.05$; ** $p < 0.01$; *** $p < 0.001$; **** $p < 0.0001$) or unpaired Student's t-test (# $p < 0.05$; ## $p < 0.01$).

Supplementary Figures Legend

Figure S1. Spread and tropism of HSV-gfaABC1D-TdTomato

A. Representative large images of coronal brain slices of wt mice infected with HSV-gfaABC1D-TdTomato with immunostaining against TdTomato (red) to visualize viral spread. Hoechst were used to counterstain nuclei (blue). Scale bar is 1000 μ m.

B. Representative confocal images of coronal brain slices of wt-HSV-gfaABC1D-TdTomato mice with immunostaining against TdTomato (red) and DARPP32, NeuN, and GFAP (green) to visualize viral tropism. Hoechst were used to counterstain nuclei (blue). Scale bar is 10 μ m.

Figure S2. Gene expression analysis of genes involved in cholesterol metabolism, glial metabolism and synaptic activity

A-D. mRNA level of ATP-binding cassette transporter (*Abca1*) (A), Apolipoprotein E (*ApoE*) (B), Low density lipoprotein receptor-related protein 1 (*Lrp1*) (C), and Cholesterol 24-hydroxylase (*Cyp46a1*) (D). in the hemi-brain of wt and R6/2 mice and in the infused hemibrain from R6/2-Tom, and R6/2-hBP2 mice ($n = 3$ mice/group).

E-G. mRNA level of Glutamate transporter 1 (*Glt1*) (E), S100 calcium binding protein B (*S100b*) (F), and potassium inwardly-rectifying channel, subfamily J, member 10 (*Kir4.1*) (G) in the hemi-brain of wt and R6/2 mice and in the infused hemibrain from R6/2-Tom, and R6/2-hBP2 mice ($n = 3$ mice/group).

H-L. mRNA levels of Brain derived neurotrophic factor (*Bdnf*) (H), Complexin-2 (*Cplx2*) (I), SH3 and multiple ankyrin repeat domains 3 (*Shank3*) (J), Homer scaffolding protein (*Homer*) (K), and Growth-associated protein 43 (*Gap43*) (L) in the hemi-brain of wt and R6/2 mice and in the infused hemibrain from R6/2-Tom, and R6/2-hBP2 mice ($n = 3$ mice/group).

Data (A-L) are shown as scatterplot graphs with means \pm SEM. Each dot corresponds to the value obtained from each animal. Statistics: one-way ANOVA with Newman–Keuls post-hoc test (* $p < 0.05$; ** $p < 0.01$; *** $p < 0.001$; **** $p < 0.0001$).

Figure S3. Gene expression analysis of genes involved in energy metabolism and autophagy

A-I. mRNA levels of GTP-binding protein Rhes (*Rhes*) (A), Peroxisome proliferator-activated receptor gamma coactivator 1-alpha (*Pgc1a*) (B), Superoxide dismutase 2 (*Sod2*) (C), Peroxisomal adenine nucleotide transporter 1 (*Ant1*) (D), cytochrome complex (*Cyt-c*) (E), Inhibitor Of Nuclear Factor Kappa B Kinase Subunit Beta (*Ikkbb*) (F), Histone deacetylase 4 (*Hdac4*) (G), Microtubule-associated proteins 1A/1B light chain 3B (*Lc3b*) (H), and Autophagy Related 4D Cysteine Peptidase (*Atg4d*) (I) in the hemi-brain of wt and R6/2 mice and in the infused hemibrain from R6/2-Tom, and R6/2-hBP2 mice ($n = 3$ mice/group).

Data (A-I) are shown as scatterplot graphs with means \pm SEM. Each dot corresponds to the value obtained from each animal. Statistics: one-way ANOVA with Newman–Keuls post-hoc test (*** $p < 0.001$; **** $p < 0.001$).

Figure 1

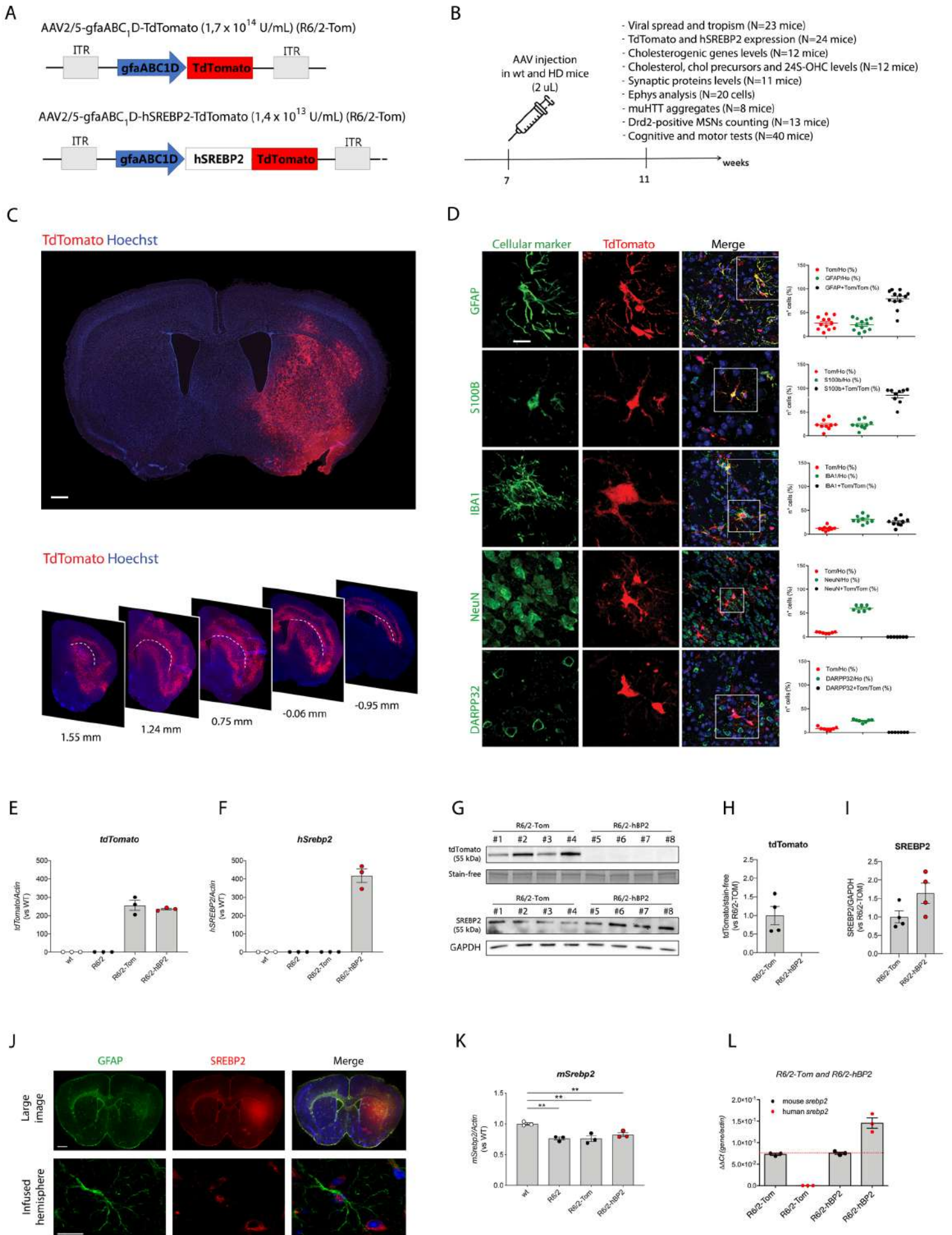


Figure 2

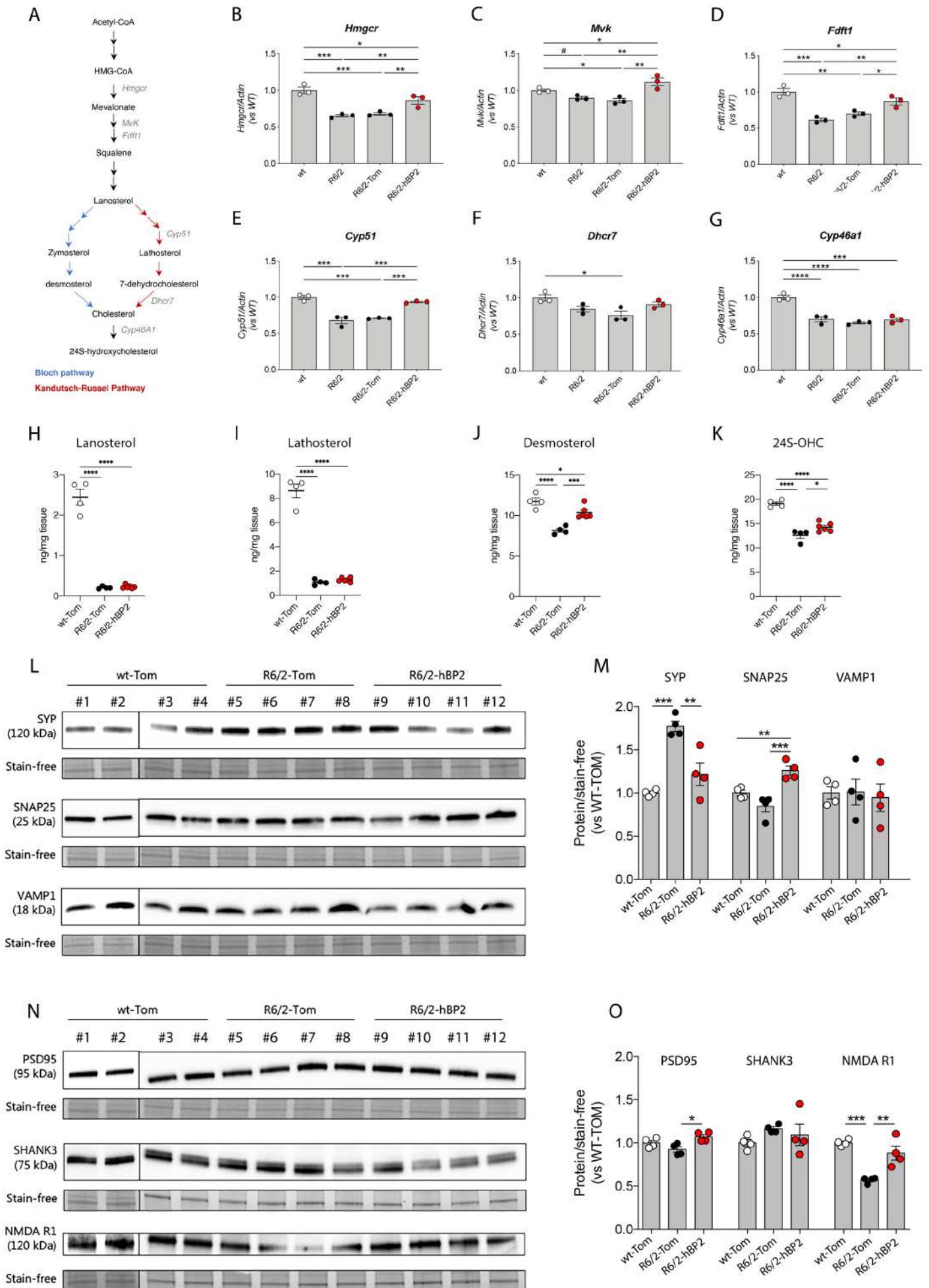


Figure 3

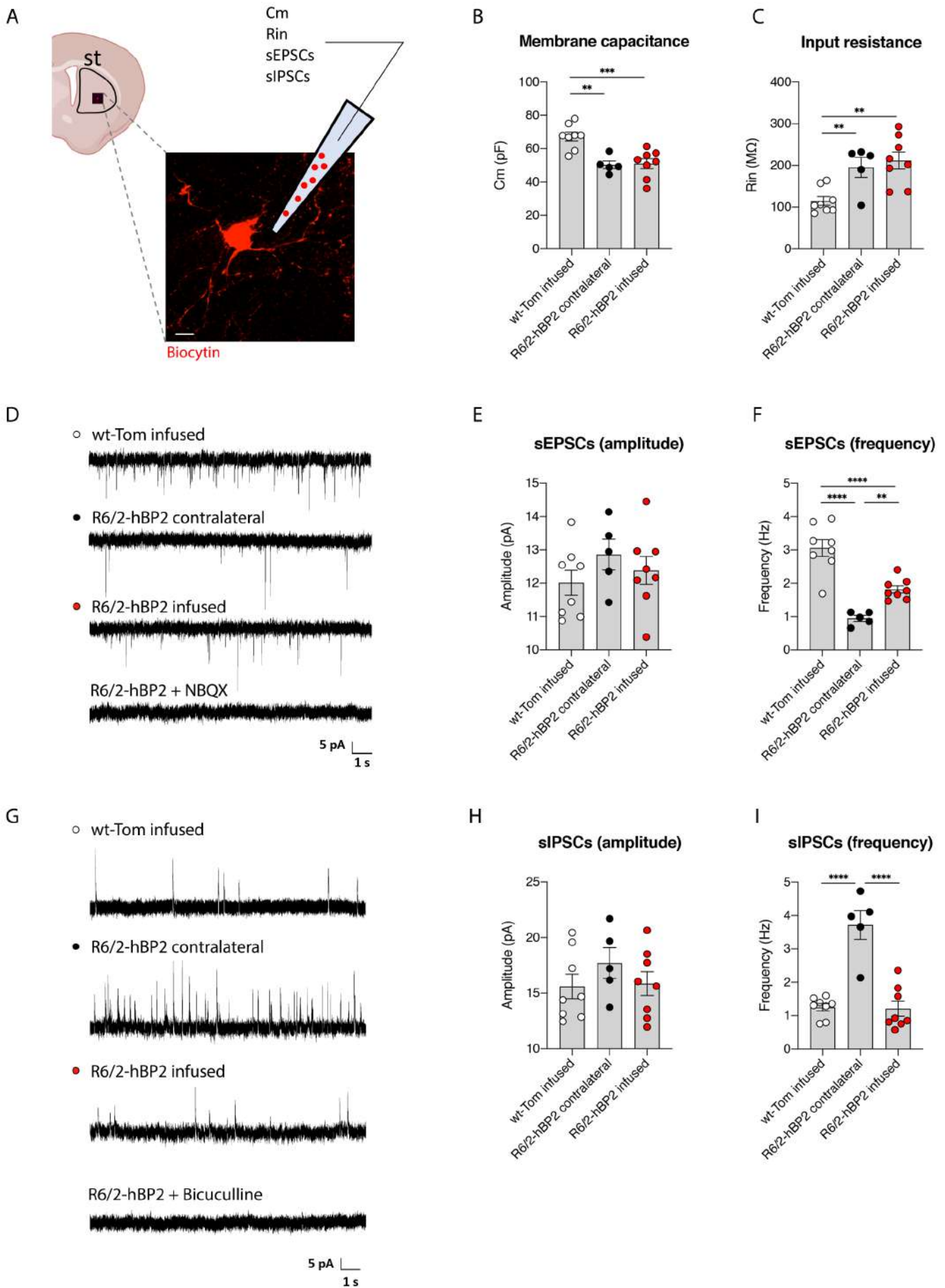
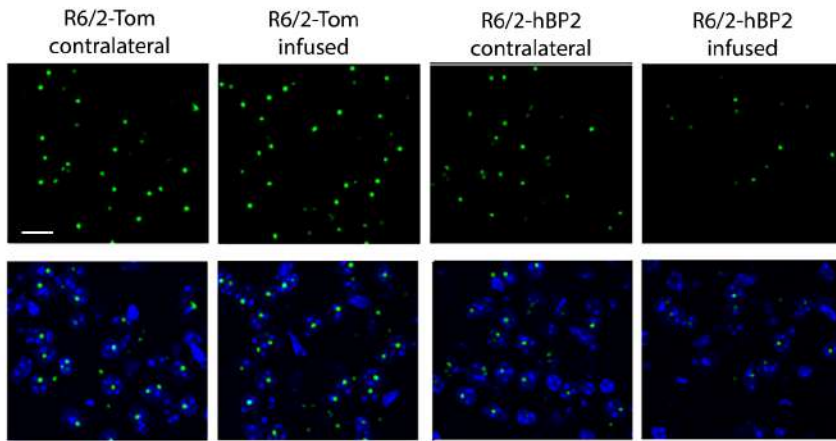


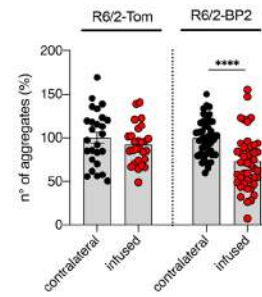
Figure 4

A

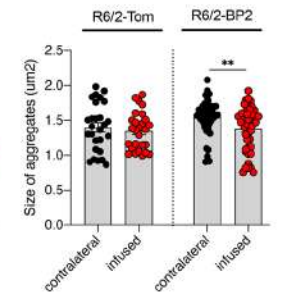


Hoechst EM48

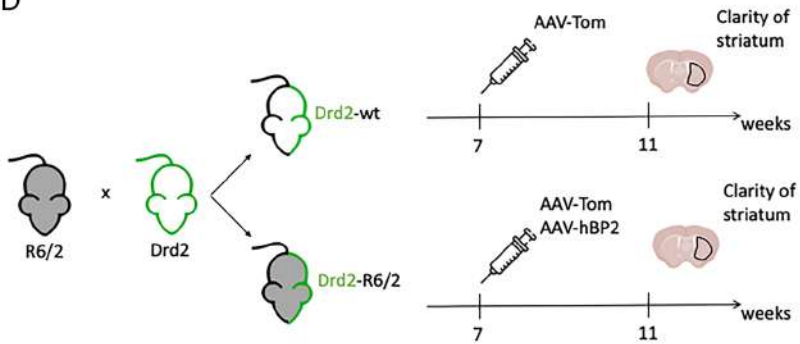
B



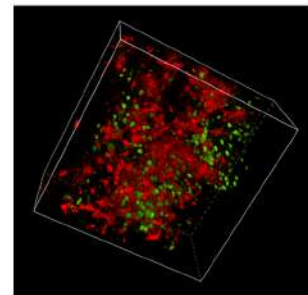
C



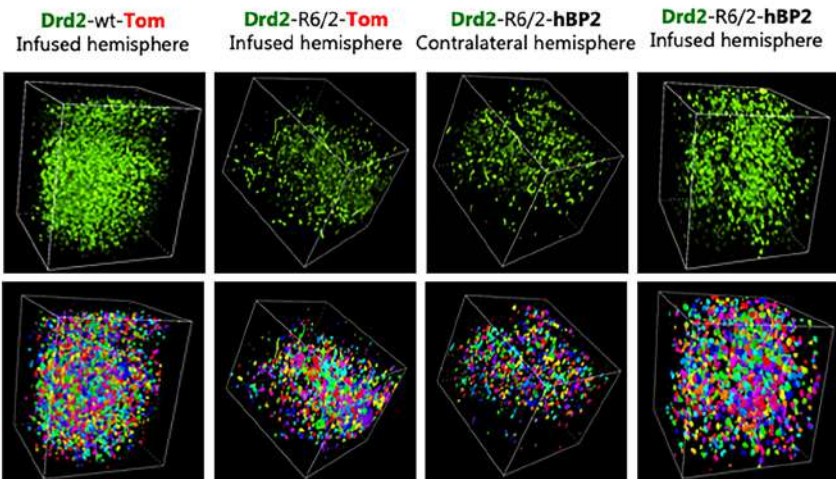
D



E



F



G

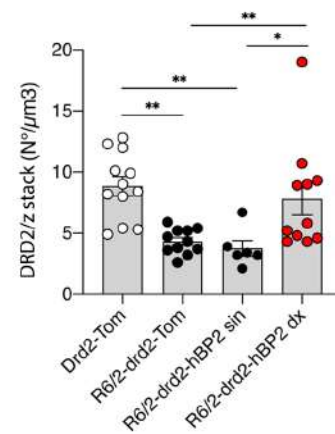
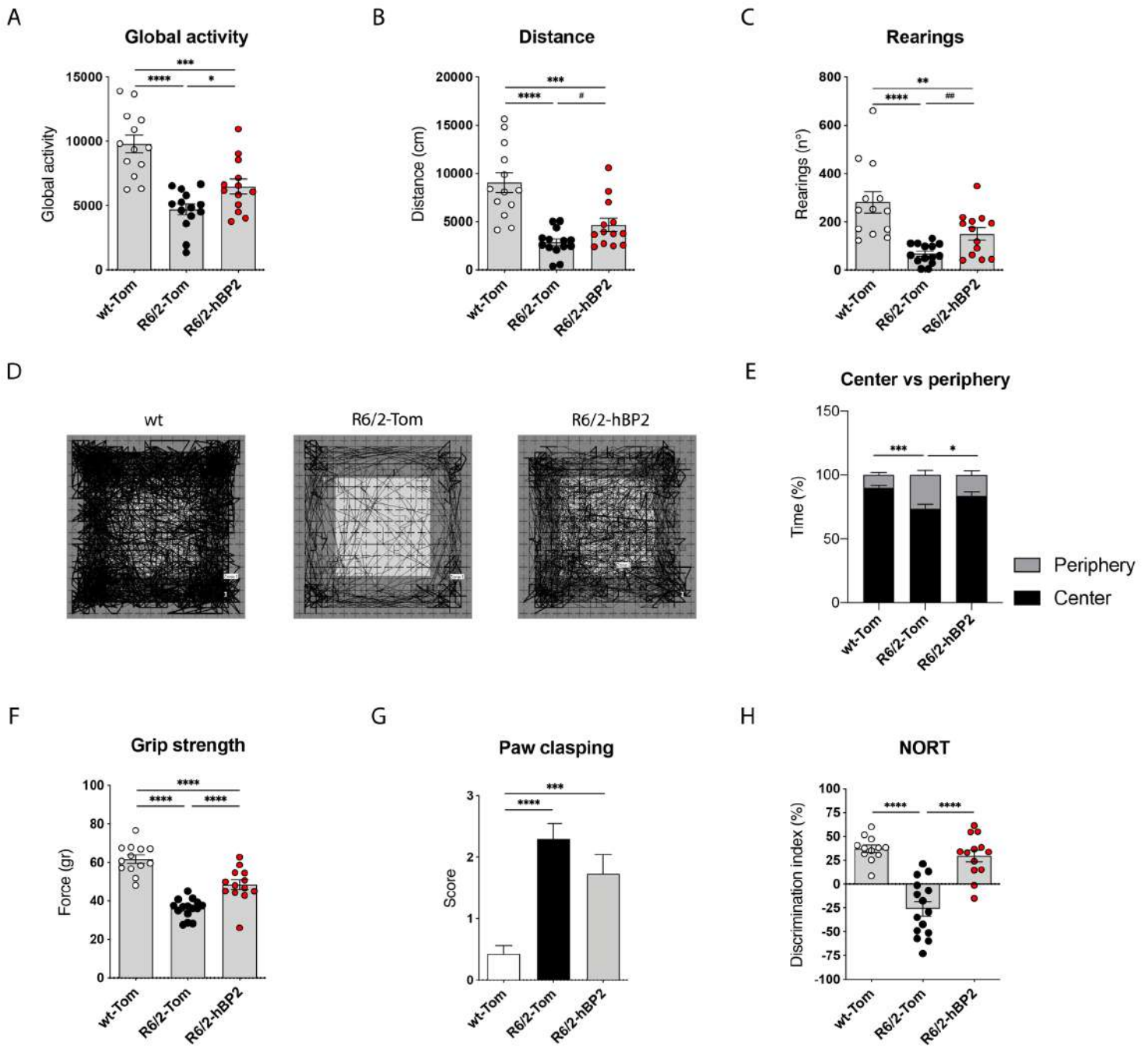
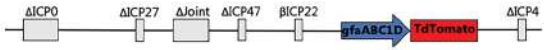


Figure 5



Supplementary Figure S1

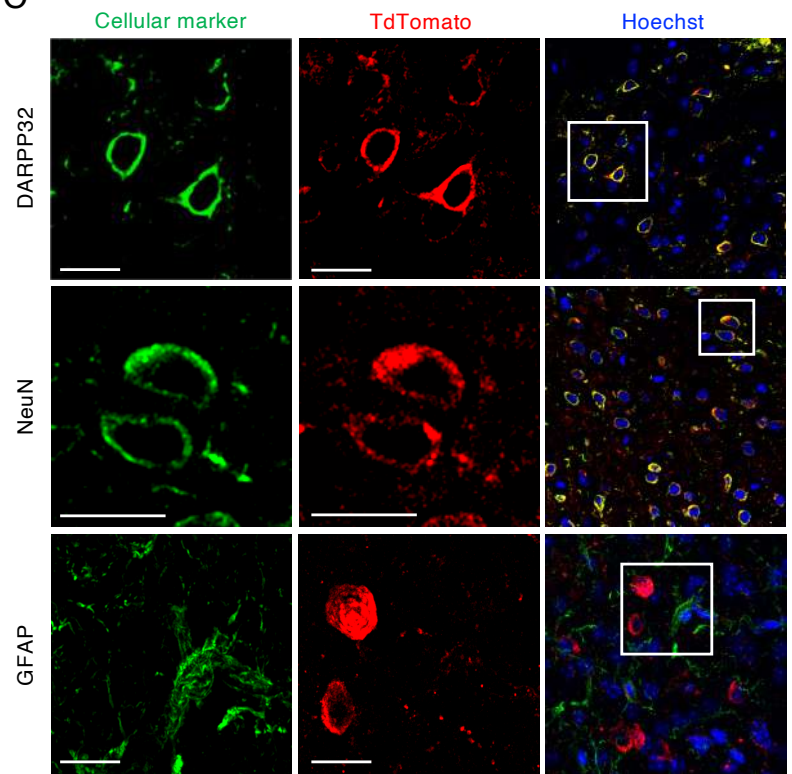
A



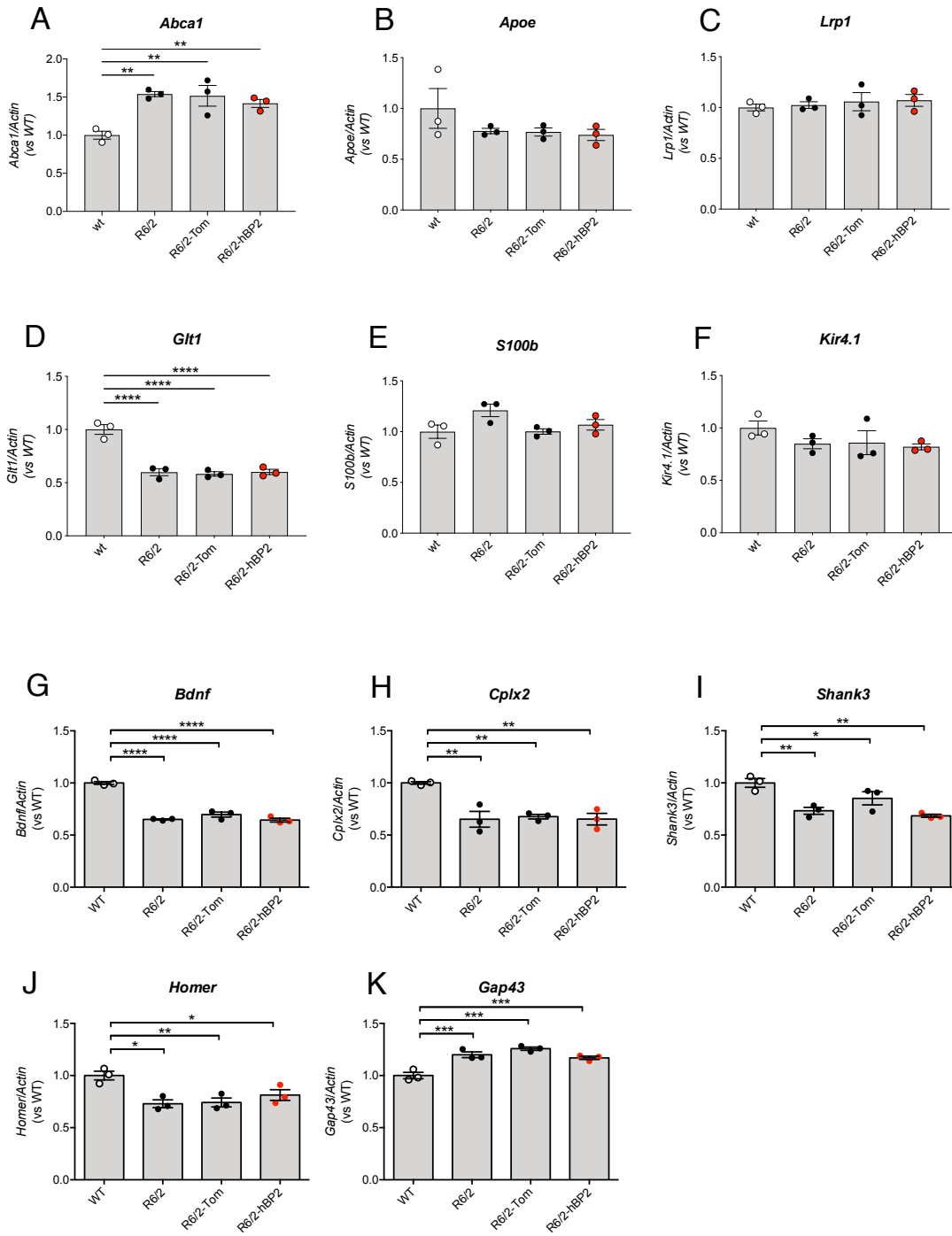
B



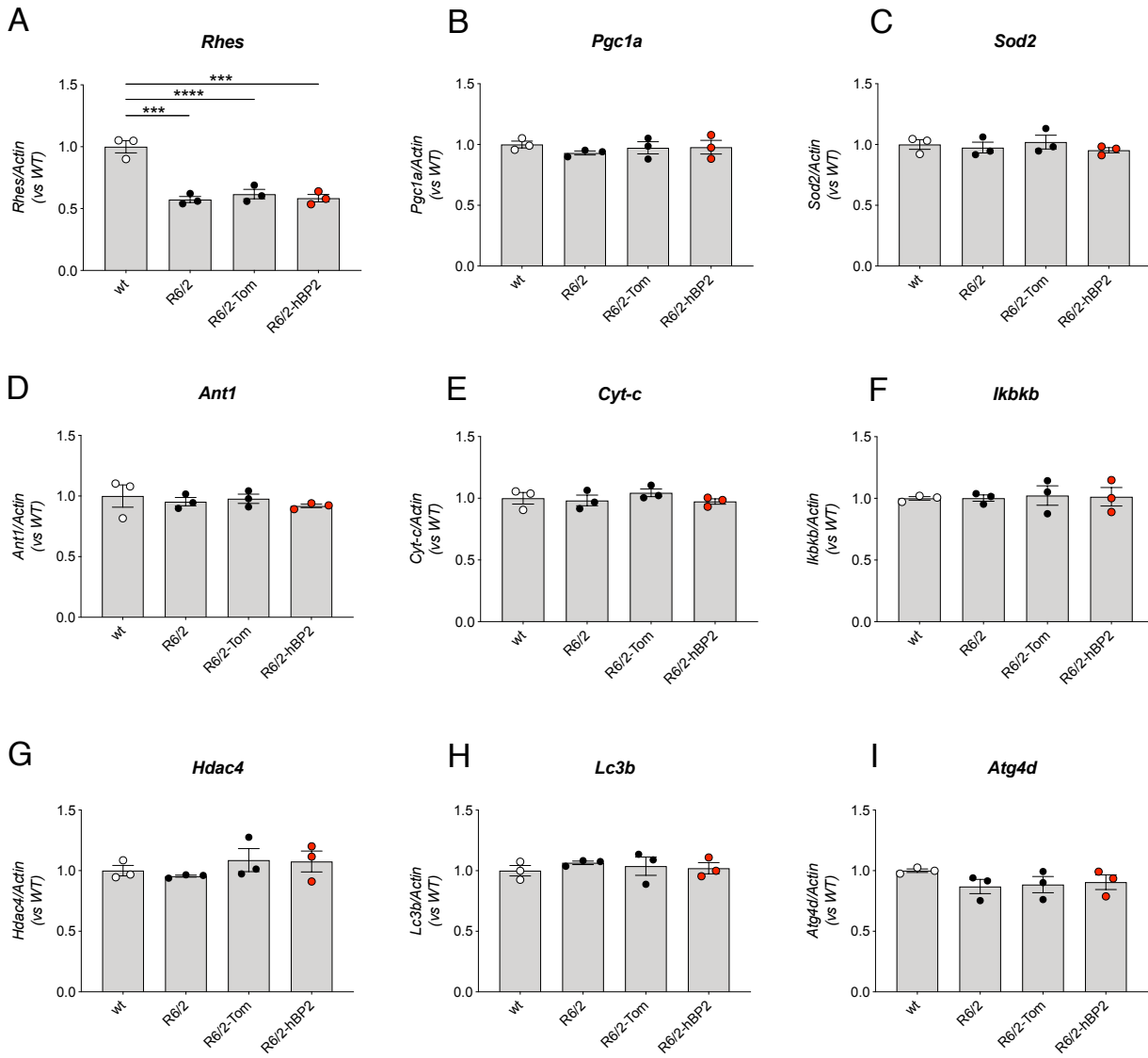
C



Supplementary Figure S2

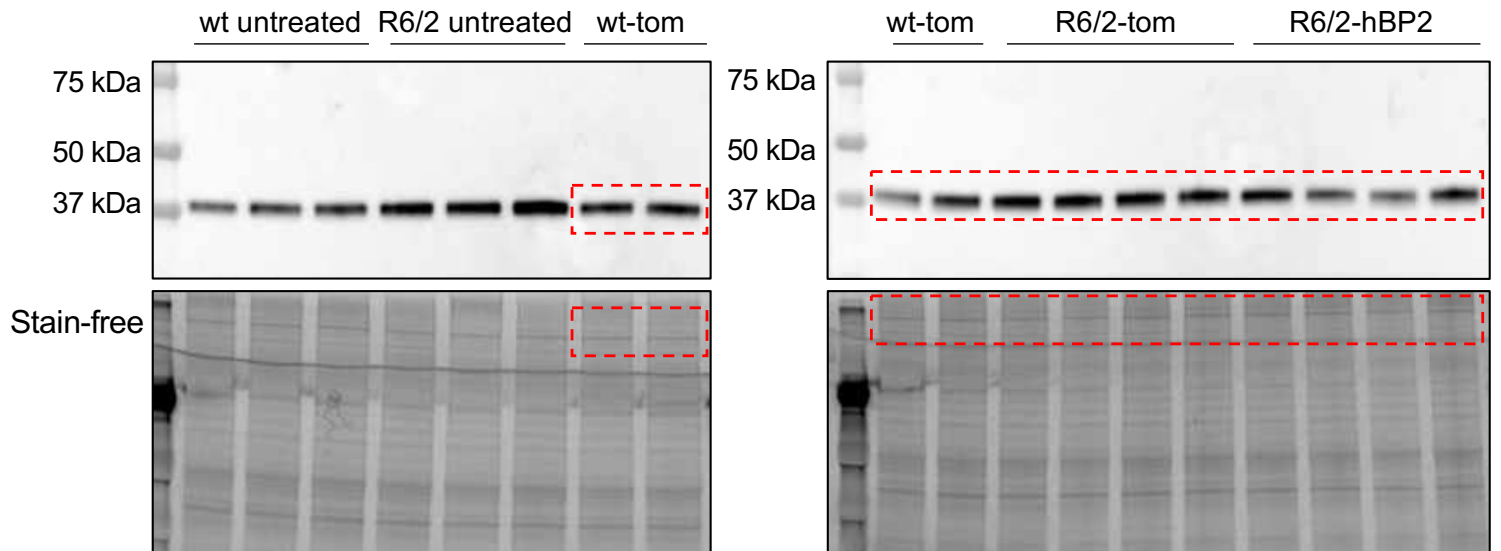


Supplementary Figure S3

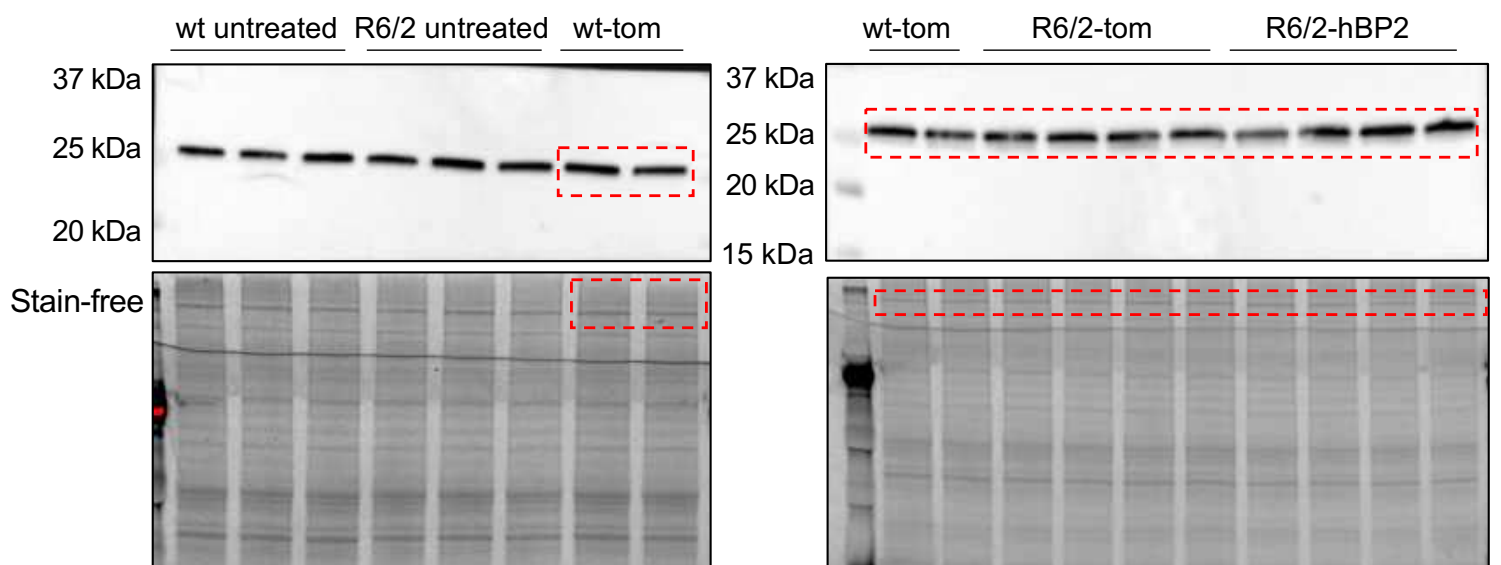


Supplementary Figure S4

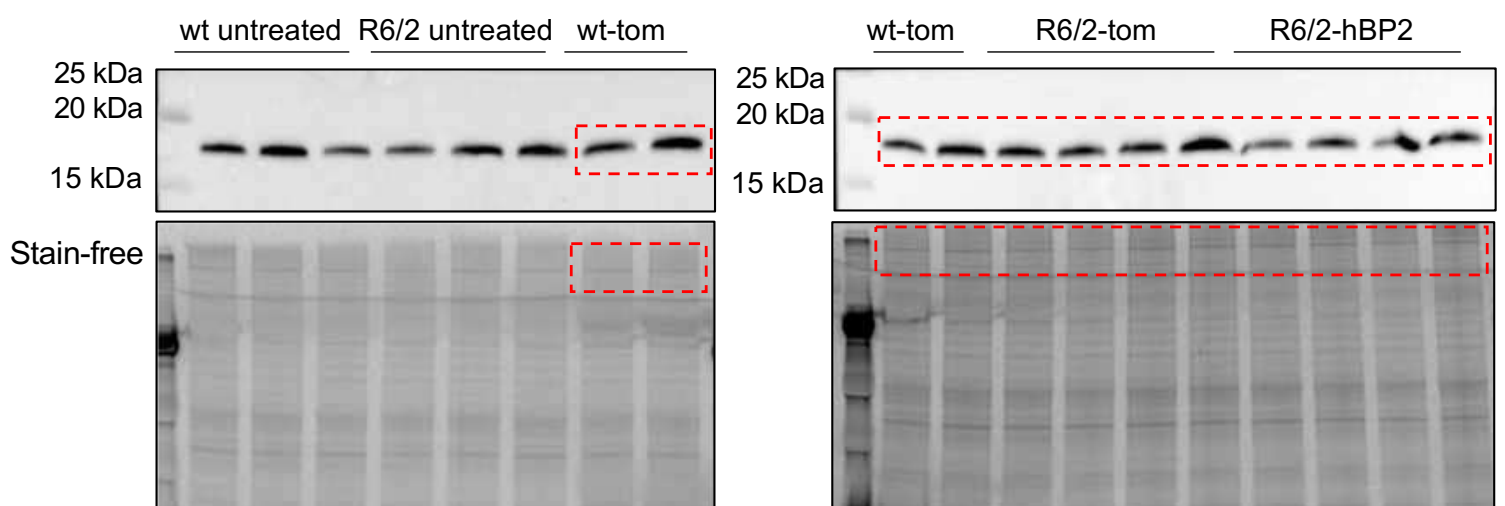
SYP (40kDa)



SNAP25 (25kDa)

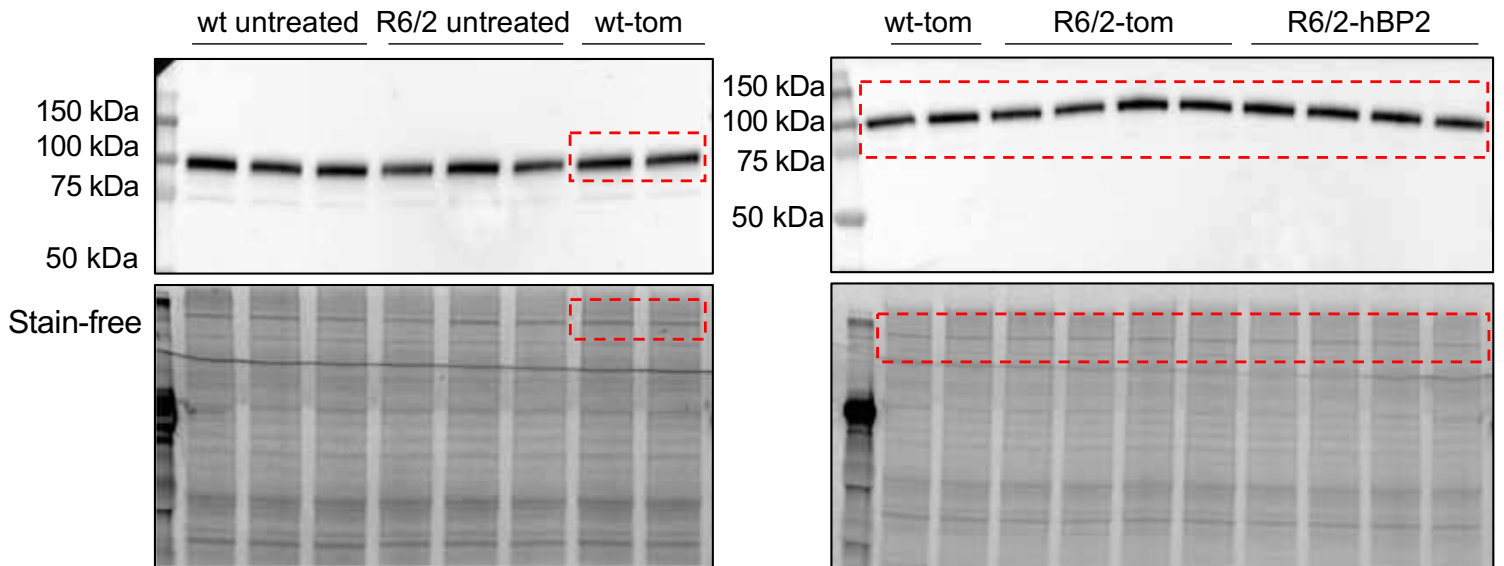


VAMP1 (18kDa)

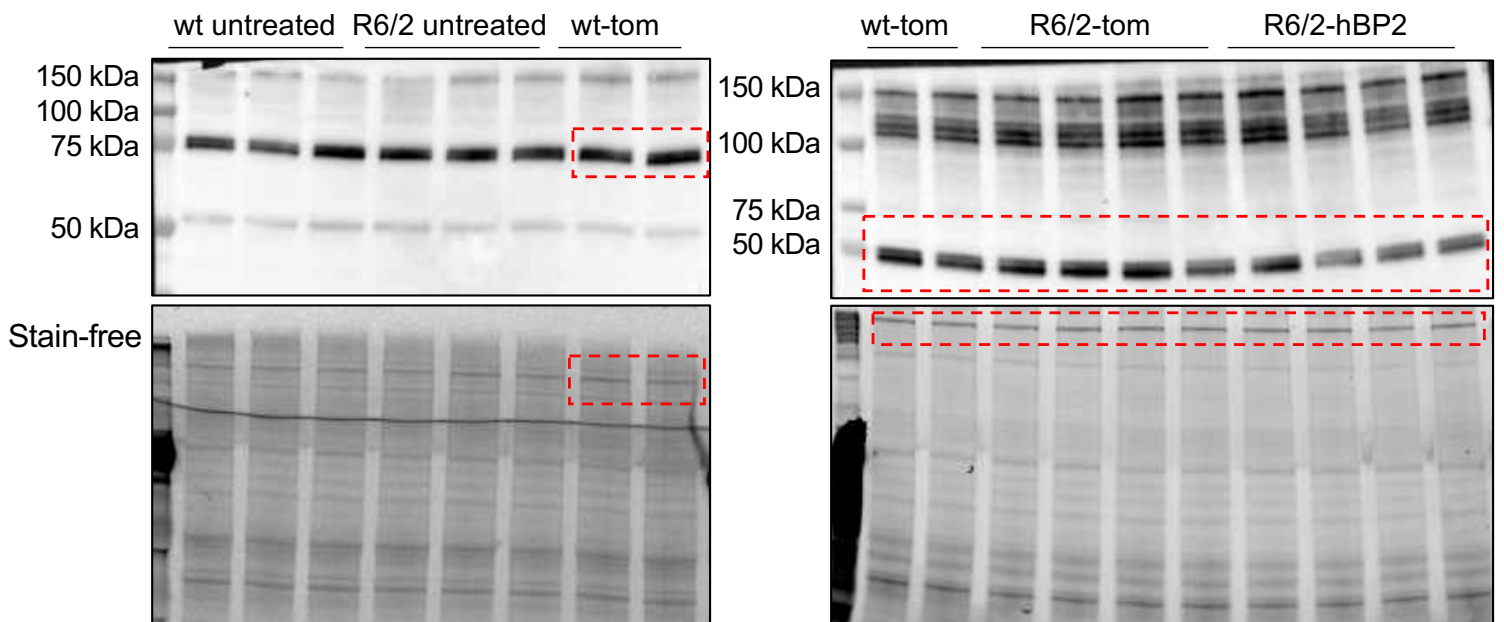


Supplementary Figure S5

PSD95 (95kDa)



Shank3 (75kDa)



NMDA R1 (120kDa)

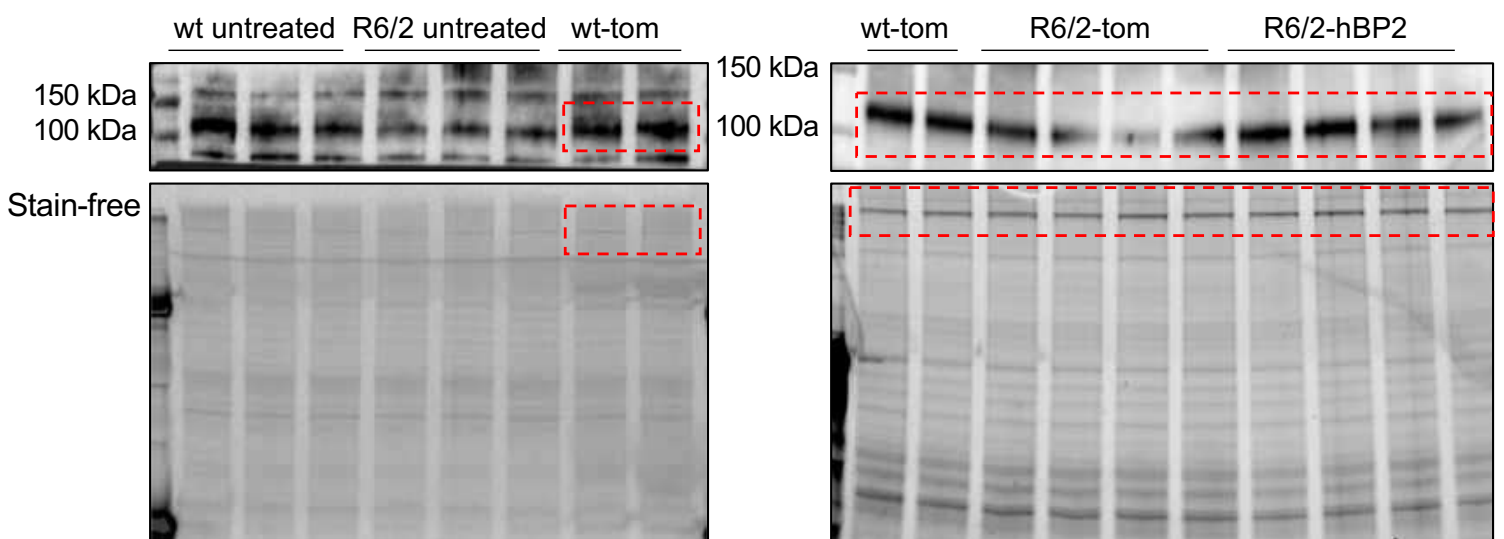


Table S1

Table S1. Primers List									
Target	Pathway	Oligo Name	Sequence	Tm [°C]	GC %	Length [mer]	Protocol	Ta [°C]	PCR product (bp)
mActin	Reference	mActin-FW	AGTGTGACGTTGACATCCGTA	57,9	47,6	21	EvaGreen	60	112
		mActin-RV	GCCAGAGCAGTAATCTCCTCT	60,3	50	22			
hSREBP2	Transgene	hSREBP2-FW	GTACAGCCGGTCAACATTCA	59,4	55	20	EvaGreen	60	74
		hSREBP2-RV	CCATTGGCCGTTTGTGTGAG	59,4	55	20			
mSREBP2	Cholesterol Synthesis	mSREBP2-FW	GCCTCTCTTAAACCCCTTG	59,4	55	20	EvaGreen	60	131
		mSREBP2-RV	CCAGTCAAACCCAGCCCCAG	63,5	65	20			
mHMGCR	Cholesterol Synthesis	mHMGCR-FW	GGAGCATAGGCGGTACATA	58,2	61	18	EvaGreen	60	191
		mHMGCR-RV	ACCACCCAGGTTCTTACTCT	59,4	55	20			
Mevalonate Kinase	Cholesterol Synthesis	MVK-FW	CCCTCTGAAGCCAGGTCTA	61,4	60	20	EvaGreen	60	87
		MVK-RV	TGGTCTCCAGCAGTCAAAC	59,4	55	20			
mFDF1	Cholesterol Synthesis	mFDF1-FW	ACTCAGCAGCAGTTGAAGACC	62,1	55	22	EvaGreen	60	152
		mFDF1-RV	TGTCATCTCCACTGTATCCAG	60,3	50	22			
Lanosterol 14-alpha demethylase	Cholesterol Synthesis	CYP51-FW	GGCAGAGCGCTGGACTTTA	59,4	55	20	EvaGreen	60	97
		CYP51-RV	ATGACGCCAGCTCAAATG	59,4	55	20			
7-dehydrocholesterol reductase	Cholesterol Synthesis	DHCR7-FW	GCTCTGACTTCTGCCACA	59,4	55	20	EvaGreen	57	86
		DHCR7-RV	TGTTTACAACCCCTGCTGGA	57,3	50	20			
mCYP46A1	Cholesterol Catabolism	mCYP46A1-FW	AGGACGATGAGGTTCTGCTGGA	62,1	54,5	22	EvaGreen	60	175
		mCYP46A1-RV	TCGTAGTCCAGGTGCTCTCT	59,4	55	20			
mAPOE	Cholesterol Efflux	mAPOE-FW	GACAGATCAGCTGAGTGGC	61,4	60	20	EvaGreen	60	170
		mAPOE-RV	CTTCGTCATAGTCTCCTCAT	60,3	50	22			
mABCA1	Cholesterol Efflux	mABCA1-FW	GTCAGCTGTACTGGAAGTGG	59,8	52	21	EvaGreen	60	198
		mABCA1-RV	CGCCGGAGTTGGATAACGG	63,5	65	20			
LRP1	Neuronal Cholesterol Uptake	LRP1-FW	AGGCCACTCTGCAAGTGT	61	63,2	19	EvaGreen	60	112
		LRP1-RV	GCTCGGATCTGTTGTCTC	61,8	57,1	21			
mBDNF	Synaptic Gene	mBDNF-FW	TCGTTCTTTCGAGTTAGCC	57,3	50	20	EvaGreen	60	97
		mBDNF-RV	TTGGTAAACGGCACAAAAC	52,4	42,11	19			
mCPLX1	Synaptic Gene	mCPLX1-FW	AGTGGCTTAGAGGTTGCTG	59,4	55	20	EvaGreen	60	78
		mCPLX1-RV	TTCCGATTCAGCACTCCTGG	59,4	55	20			
mShank3	Synaptic Gene	mShank3-FW	AGGAACTTGCTTCATCGGA	57,9	48	21	EvaGreen	57	160
		mShank3-RV	ATCTCAGCAGGGGTATCTCT	59,4	55	20			
mHomer	Synaptic Gene	mHomer-FW	TGGACTGGGATTCCTCTG	59,4	55	20	EvaGreen	57	216
		mHomer-RV	TGTGTACATCGGGTGTCT	57,3	50	20			
mGAP43	Synaptic Gene	mGAP43-FW	GGAGAAAGACGCTGAGACGAA	60,3	50	22	EvaGreen	60	72
		mGAP43-RV	TCGGGGTCTCTTACCCTCA	59,8	52	21			
mGLT1	Channels & Transporters	mGLT1-FW	TTGGTGCAAGCAGTATCCC	59,4	55	20	EvaGreen	60	119
		mGLT1-RV	TCTATCCAGCAGCCAGTCCA	59,4	55	20			
mS100β	Marker for Glia	mS100β-FW	CGAGCTCTCACTCTCTG	58,8	58	19	EvaGreen	60	72
		mS100β-RV	TCGTCAGCGTCTCCACTCACT	61,8	57	21			
mKIR4.1	Channels & Transporters	mKIR4.1-FW	TCTGTTTCATCTGCCCCCTGC	61,8	57,14	21	EvaGreen	60	70
		mKIR4.1-RV	GACGTCATCTGGCTCGAAGG	61,8	57,14	21			
mRHE5	mTOR & Its Regulators	mRHE5-FW	AGGTGTACACATCCACGGG	59,4	55	20	EvaGreen	60	107
		mRHE5-RV	GACATCTCTGTGAGGATGGAG	62,1	55	22			
mPGC1α	Mitochondrial Activity	mPGC1α-FW	AGTCCCATACACAACCCGAG	59,4	55	20	EvaGreen	60	94
		mPGC1α-RV	CCCTGGGGTCAATTTGGTGA	59,4	55	20			
mSOD2	Mitochondrial Activity	mSOD2-FW	AGGAGCAAGGTCGCTACAG	59,4	55	20	EvaGreen	57	75
		mSOD2-RV	GCGGAATAAGGCTGTTGTT	57,3	50	20			
mANT1	Mitochondrial Activity	mANT1-FW	GGCTGTGCTTCATCCGTTT	59,35	55	20	EvaGreen	60	76
		mANT1-RV	ATAATATCAGCCCTTCCGGC	60,3	50	22			
mCYTC	Mitochondrial Activity	mCYTC-FW	ACCAGCCCGAAGCAATTAATA	58,4	45	22	EvaGreen	60	114
		mCYTC-RV	GGTCCAGTCTTATGCTGCCT	59,8	52	21			
mIKK	mHTT Clearance	mIKK-FW	ATGAACGAGGACGAGAGGAC	59,4	55	20	EvaGreen	60	96
		mIKK-RV	ACCTCGGACTTGTCTACAGG	59,4	55	20			
mHDAC4	mHTT Clearance	mHDAC4-FW	CAGACGCAAGCCCTCTAC	61,4	60	20	EvaGreen	60	161
		mHDAC4-RV	GGACTGACATGGGGAAGGTG	61,4	60	20			
mLC3B	Autophagy	mLC3B-FW	CCGTCGAGAAGACCTCAA	59,4	55	20	EvaGreen	60	108
		mLC3B-RV	TCGCTCTATAATCACTGGGATCT	58,9	43,48	23			
mLC3B	Autophagy	mLC3B-FW	CCGTCGAGAAGACCTCAA	59,4	55	20	EvaGreen	60	108
		mLC3B-RV	TCGCTCTATAATCACTGGGATCT	58,9	43,48	23			
mATG4D	Autophagy	mATG4D-FW	ACGTCAAGTATGGTTGGCA	57,3	50	20	EvaGreen	57	103
		mATG4D-RV	ATGTCACCTCTCCCTCGAA	59,4	55	20			

Table S2

Table S2. Animals used in all the experiments										
N° Trial	Date	Experimental Groups	Spread and tropism	qRT-PCR	Synaptosomes	Ephys analysis	Drd2 quantification	muHTT analysis	Mass spect analysis	Behavioral analysis
			N mice	N mice	N mice	N mice	N mice	N mice		N mice
1	Aug-Sept 2017	wt-HSV	4							
		wt-Tom	3							
		R6/2-Tom	3							
		R6/2-hBP2	5							
2	Nov 2017	wt		3						
		R6/2		3						
		R6/2-Tom	3	3						
		R6/2-hBP2	2	3						
3	Ott 2018	wt-Tom			4					
		R6/2-Tom			4					
		R6/2-hBP2	3		4					
4	Dic 2019	wt				5				
		R6/2-hBP2				5				
5	Gen 2020	wt-Tom								8
		R6/2-Tom						3		8
		R6/2-hBP2						5		7
6	Feb 2020	Drd2-wt-Tom					5			
		Drd2-R6/2-Tom					4			
		Drd2-R6/2-hBP2					4			
7	Giu 2020	wt-Tom				5			4	4
		R6/2-Tom				5			4	7
		R6/2-hBP2				3			4	6

Brain-targeted hybrid nanoparticles boost cholesterol delivery to the central nervous system and rescues behavioral phenotypes in Huntington's disease

Giulia Birolini^{1,2}, Ilaria Ottonelli^{3,7}, Jason T. Duskey³, Alice Passoni⁴, Monica Favagrossa⁴, Claudio Caccia⁵, Valerio Leoni⁶, Laura Colombo⁴, Mauro Bombaci², Renzo Bagnati⁴, Franco Taroni⁵, Maria Angela Vandelli³, Flavio Forni³, Barbara Ruozi³, Mario Salmona⁴, Giovanni Tosi³, Marta Valenza^{1,2}, Elena Cattaneo^{1,2}

Paper ready to be submitted

¹Department of Biosciences, University of Milan, via G. Celoria 26, 20133, Milan, Italy.

²Istituto Nazionale di Genetica Molecolare "Romeo ed Enrica Invernizzi" via F. Sforza 35, 20122, Milan, Italy.

³Nanotech Lab, Department of Life Sciences, University of Modena and Reggio Emilia, Modena, Italy

⁴Istituto di Ricerche Farmacologiche Mario Negri IRCCS, via Mario Negri 2 , 20156 Milan , Italy.

⁵Unit of Medical Genetics and Neurogenetics. Fondazione I.R.C.C.S. Istituto Neurologico Carlo Besta, Via Celoria 11, 20131 Milan, Italy

⁶School of Medicine and Surgery, University of Milano-Bicocca, Via Cadore 48, 20900, Monza and Laboratory of Clinical Pathology, Hospital of Desio, ASST-Monza, Italy

⁷ Clinical and Experimental Medicine PhD Program, University of Modena and Reggio Emilia, via G. Campi 289, 411214, Modena, Italy

Abstract

Cholesterol delivery to the brain is emerging as a potential treatment for Huntington's disease (HD), a genetic neurodegenerative disorder characterized by decreased brain cholesterol biosynthesis. However, this approach is challenging due to the blood-brain barrier (BBB) that hinders reaching especially the striatum with the therapeutically relevant dose.

Here we show that hybrid polymeric nanoparticles (hybrid-g7-NPs-chol), made of PLGA and cholesterol, modified with g7-peptide for BBB crossing, let cholesterol access to different brain regions and cells *in vivo*. Kinetic studies demonstrated that the release of cholesterol from hybrid-g7-NPs-chol occurs in a slow and controlled manner in the brain allowing its accumulation over-time, while it is rapidly released and removed from peripheral tissues and plasma.

Moreover, systemic and multiple injections of hybrid-g7-NPs-chol enhanced endogenous cholesterol biosynthesis, prevented cognitive decline, and ameliorated motor defects in HD animals without induction of inflammation.

In summary, this study provides insights about kinetics, release, safety, and benefits of cholesterol delivery through advanced brain-permeable nanoparticles for HD treatment.

Targeting the brain with therapeutic agents has always been critical due to the presence of the blood-brain barrier (BBB). During the years, several strategies have been developed to overcome this problem and to enhance drug delivery to the central nervous system (CNS), including momentary disruption of BBB, conjugation of ligands to drug of interest to improve BBB permeability, intranasal delivery, or direct delivery of molecules into the brain using invasive strategies (Gao *et al.* 2016). Recently, several efforts were made to develop non-invasive methods based on the use of nanocarriers loaded with the drug of interest and decorated on their surface with antibodies or ligands to reach the brain (Hersh *et al.* 2016; Saraiva *et al.* 2016). Accordingly, it has been demonstrated that polymeric nanoparticles (NPs) made of the FDA-approved polymer poly(D,L-lactide-co-glycolide) (PLGA) and surface-engineered with the peptide Gly-L-Phe-D-Thr-Gly-L-Phe-L-Leu-L-Ser(O-beta-D-glucose)-CONH₂ (g7) are able to transport, after systemic administration, molecules into the CNS (Vergoni *et al.* 2009). In fact, g7-glycopeptide stimulates membrane curvatures and, following endocytosis process of the whole carrier at BBB level, it promotes BBB crossing by multiple pathways (Tosi *et al.* 2011). This system was exploited to deliver drugs to cope with Huntington's disease (HD), a neurodegenerative genetic disorder caused by a CAG repeat expansion in the gene encoding for the Huntingtin protein (HTT) and characterized by motor, cognitive and psychiatric disturbances (Zuccato *et al.* 2010).

One pathway affected in HD regards the reduced synthesis of brain cholesterol since pre-symptomatic stages (Valenza *et al.* 2005; Valenza *et al.* 2007; Valenza *et al.* 2010; Shankaran *et al.* 2017) and indirect measures indicate that this occurs also in HD patients before symptoms manifestation (Leoni *et al.* 2008; 2013). Brain cholesterol derives from local synthesis by astrocytes and it is fundamental for synaptic functions (Pfrieger 2003; Björkhem *et al.* 2004), thus, delivering cholesterol to the HD brain may be therapeutically significant. The therapeutic potential of such strategies has been recently demonstrated by using different delivery systems (Valenza *et al.* 2015; Birolini *et al.* 2020). In the first study, systemic injections of PLGA-g7-NPs loaded with cholesterol prevented synaptic and cognitive defects in a transgenic mouse model of HD (Valenza *et al.* 2015). In the second study, cholesterol was infused for 4 weeks in the striatum of HD mice through osmotic minipumps, a well-characterized system for controlled drug delivery widely used in preclinical research. Although this system is not yet transferable to the clinic, it allowed to identify the optimal dose of cholesterol to reach the striatum for restoring synaptic and neuropathological features and motor and cognitive abnormalities in HD mice more broadly than PLGA-g7-NPs-chol (Birolini *et al.* 2020). Moreover, a recent study also supports the effectiveness of nose-to-brain delivery of cholesterol in the HD brain (Passoni *et al.* 2020) opening new future investigations in HD mice. With a view to develop a cholesterol-based therapy for HD patients in the future, new generations of NPs were produced with

improved pharmacological properties. These NPs, herein named as **hybrid-g7-NPs-cho**, were prepared using a new formulation based on a specific combination of polymers (g7-PLGA, PLGA, and cholesterol as starting materials for formulation; Belletti *et al.* 2018). In particular, hybrid-g7-NPs-cho were formulated using nanoprecipitation (MIX-N) and single emulsion (MIX-SE). Pluronic was used as a surfactant in MIX-N while PVA was used in MIX-SE. The maximal percentage of cholesterol present in hybrid-g7-NPs-cho MIX-N and MIX-SE with respect to PLGA content was $32,7 \pm 2\%$ and $41,5 \pm 1,5\%$ respectively. Thus, cholesterol content is around 40 times higher than the amount estimated in PLGA-g7-NPs-cho (Valenza *et al.* 2015). This upgrade should allow to deliver to the HD brain a therapeutic dose of cholesterol similar to that previously identified with the osmotic minipumps (Birolini *et al.* 2020), but with a low-invasive and more-translatable strategy. This study aims to describe the distribution and the kinetic of hybrid-g7-NPs-cho in different brain regions, in peripheral tissues, and in circulation, their benefits on the behavior, and eventually side effects following chronic treatment in HD mice.

Previous studies indicated that about 10% of the injected g7-NPs are estimated to penetrate the brain (Costantino *et al.* 2005; Tosi *et al.* 2007; Tosi *et al.* 2011a; Tosi *et al.* 2011b; Tosi *et al.* 2014a; Tosi *et al.* 2014b). Both hybrid-g7-NPs-cho MIX-N and MIX-SE produced demonstrated to be in line with previous studies in terms of size, homogeneity, surface charge, cholesterol content and morphology (Table S1 and Figure S1) and were tested in 7-weeks old wild-type (wt) mice to verify their uptake and distribution *in vivo*. Mice were treated with a single or multiple (3) intraperitoneal (I.P.) injection of hybrid-g7-NPs-cho MIX-N or MIX-SE labelled with cyanine 5 (cy5). Animals were sacrificed at different time points (4h, 24h, 1week, 2 weeks) following the last I.P. injection (Fig. 1A) and fluorescence analysis were performed on brain and peripheral slices to analyze the localization of the red signals (cy5) of both MIXs (Fig. 1B and 1C; Fig. S2). 4h after a single I.P. injection, cy5 was detected in the striatum, cortex (Fig. 1B and 1C) and hippocampus, as well as in lung and liver (Fig. 1B and 1C and Fig. S2A and B), indicating that BBB crossing is a fast process. Quantification of cy5 dots revealed that the kinetic of both MIXs in peripheral tissues was quite fast, since cy5 signal strongly decreased 24h after the I.P. injection (Fig. 1B and 1C; Fig. S2). Importantly, NPs were accumulating in the brain over time since the cy5 signal was still present 24h, 1 weeks and 2 weeks after the I.P. injection (Fig. 1B and 1C; Fig. S2) and more nanoparticles were detected following multiple injections (Fig. 1B and 1C; Fig. S2). Although the biodistribution was similar between MIX-N and MIX-SE, the latter showed higher aggregation in peripheral tissues, and this was more evident after multiple I.P. injections (Fig. S2). High-magnification confocal images indicated the presence of hybrid-g7-NPs-cho in different neuronal and glial cell types as demonstrated by the

co-localization between cy5 (NPs) and GFAP (marker of astrocytes), IBA1 (marker of microglia), and DARPP32 (marker of striatal medium spiny neurons) (Fig. 1D).

Overall, these results demonstrate that hybrid-g7-NPs-chol rapidly reach the brain and accumulate over time, while in peripheral tissues they do not accumulate and disappeared within 24 h – 1 week.

To track cholesterol delivery and intracellular release from hybrid-g7-NPs-chol, we performed specific experiments using g7-NPs-chol labelled with cy5 and loaded with the fluorescent analogue bodipy cholesterol (hybrid-cy5-g7-NPs-bodipy-chol). 7 weeks-old wt and HD (R6/2 model; Mangiarini *et al.* 1996) mice were treated with a single I.P. injection of hybrid-cy5-g7-NPs-bodipy-chol MIX-N or MIX-SE and sacrificed at different time points (24h and 2 weeks after the I.P. injection) (Fig. 2A). Following confocal analysis in brain slices, we monitored and quantified the co-localization of red spots (cy5, NPs) and the green signal (bodipy cholesterol) to evaluate NPs degradation and bodipy cholesterol release. With both MIXs, 24h after a single I.P. injection of hybrid-cy5-g7-NPs-bodipy-chol, cy5 and bodipy-chol signals nicely co-localized in striatum and cortex, as indicated by the scatterplot of red and green pixel intensities (Fig. 2B and 2C). However, analysis performed 2 weeks after the I.P. injection revealed a partial separation between cy5 and bodipy-chol signals (Fig. 2B, C), indicating a slow and controlled release of cholesterol over time. The kinetic of cholesterol release in the liver of mice treated with MIX-N was faster compared to the brain. In fact, a complete overlap of red and green signal was found 24h after the I.P. injection while 1 week after the I.P. injection all the cholesterol was released from the nanoparticles (Fig. S3).

These findings indicate that around 10% of bodipy-chol is released from hybrid-g7-NPs-chol in the brain starting from 2 weeks after I.P. injection, in parallel with a reduction in cy5 signal. No differences in cholesterol release kinetic were found between wt and HD mice, indicating that cholesterol release does not depend on mice genotype.

Moreover, we did not find substantial differences between MIX-N and MIX-SE as they showed similar bio-distribution profile and kinetic of cholesterol release. However, as MIX-N showed lower NPs aggregation in liver and was produced using Pluronic as a surfactant, that is approved by FDA (Pitto-Barry & Barry 2014), aiming to a faster translatability of preclinical results in clinical practice, we decided to test only this formulation for the subsequent studies.

To study the kinetic of exogenous cholesterol and to quantify the total amount of cholesterol delivered *in vivo*, we performed two experiments using hybrid-g7-NPs-chol loaded with cholesterol labelled with six deuterium (d6-chol) (hybrid-g7-NPs-d6-chol).

First, 7 weeks-old HD mice were treated with a single I.P. injection of hybrid-g7-NPs-d6-chol and sacrificed at different time points (30', 6h, 24h, 1 week and 2 weeks after the I.P. injection) (Fig. 3A). Blood, kidney, lung, liver, cortex, striatum, and cerebellum were collected to measure the amount of d6-chol in different tissues using liquid chromatography mass spectrometry (LC-MS). Quantification of d6-chol was performed in striatum, cortex, and cerebellum starting from 6h after the I.P. injection (Fig 3B). Starting from 24h after the treatment, the content of d6-chol increased in the same tissues over 2-week as indicative of its slow and controlled release from the NPs (Fig 3B). In the liver, d6-chol was rapidly released 30' after the I.P. injection and it was degraded over the time. In lung and kidney, NPs were detected around 6h after the I.P. injection, the peak of cholesterol release occurred 1 week after the I.P. injection and then it was rapidly eliminated (Fig. 3B). When analyzing the plasma, the maximum amount of cholesterol was detected 24h after the I.P. injection (Fig. 3B). Importantly, this concentration is not significant compared to the physiological amount of cholesterol that is present in the mouse blood (128 mg/100 mL). Secondly, to quantify cholesterol delivered with the therapeutic regimen of interest, HD mice were treated from 5 to 9 weeks of age with 2 I.P. injections/week and sacrificed 2 weeks after the last I.P. injection (Fig. 3D). MS analysis revealed that the concentration of d6-chol measured in each tissue following 10 I.P. injections was around 10 times the concentration of d6-chol measured 2 weeks after a single I.P. injection (Fig. 3D and E) meaning that exogenous cholesterol accumulates in all tissues, although with different kinetics. These results demonstrated that the kinetic of cholesterol release is different between brain, plasma and peripheral tissues and that this delivery system allows a slow release and accumulation of cholesterol in different brain regions that can be used by the cells over time. Moreover, the fast elimination of cholesterol in blood and in peripheral tissues potentially avoids systemic side effects after a chronic treatment. Finally, these data, combined with the data obtained with bodipy-chol (Fig 2B and C), support further the hypothesis that the release of cholesterol from NPs is quite slow.

We have recently demonstrated that a therapeutically relevant dose of cholesterol delivered to the striatum through osmotic minipumps indirectly induced endogenous cholesterol synthesis and fully recovered both motor and cognitive abnormalities in HD mice (Biolini *et al.* 2020). On the contrary, lower doses delivered to the striatum through osmotic minipumps (Biolini *et al.* 2020), or to the brain using PLGA-g7-NPs-chol (Valenza *et al.* 2015) led to a complete rescue of cognitive decline without significant change in the endogenous brain cholesterol biosynthesis or in motor performance.

Since hybrid-g7-NPs-chol (Belletti *et al.* 2018), with their hybrid structure, have more cholesterol than the amount found in PLGA-g7-NPs-chol previously used (Valenza *et al.* 2015), we sought to test whether the increased amount of cholesterol in hybrid-g7-NPs-chol was sufficient to indirectly

stimulate endogenous cholesterol synthesis in the diseased brain. Cholesterol precursors (lanosterol, lathosterol, desmosterol) were quantified by isotopic dilution mass spectrometry (ID-MS) in the striatum of HD mice after a chronic treatment. Accordingly, HD mice were treated with PLGA-g7-NPs-chol or with hybrid-g7-NPs-chol from 5 to 9 weeks of age with 2 I.P. injections/week and sacrificed 2 weeks after the last I.P. injection (Fig. 4A). As expected, a robust deficit in levels of lanosterol, lathosterol and desmosterol was found in the striatum of HD mice treated with saline compared to wt littermates (Fig. 4B-D), confirming previous results (Valenza *et al.* 2007b; Valenza *et al.* 2010; Birolini *et al.* 2020). Of note, a significant increase of lanosterol and desmosterol levels was found in striatal tissues of HD mice treated with hybrid-g7-NPs-chol compared to those treated with PLGA-g7-NPs-chol (Fig. 4B-D).

Taken together, these results suggest that the hybrid-g7-NPs-chol transport and release in the brain more cholesterol compared to PLGA-g7-NPs and such dose, conversely to that released by PLGA-g7-NPs, is able to indirectly enhance endogenous cholesterol biosynthesis in HD mice.

To assess the power of hybrid-g7-NPs-chol to counteract motor and cognitive defects in HD mice, hybrid-g7-NPs-chol were I.P. injected in R62 mice with the same experimental paradigm described in Fig. 4A and their motor and cognitive performance was compared to R6/2 and wt mice treated with saline solution.

First, we analyzed motor coordination by evaluating the latency of mice to fall when tested on a rotating bar with accelerating speed in the rotarod test. Starting from 8 weeks of age, HD mice exhibited a progressive deterioration in motor coordination, as shown by the shorter latency to fall compared to wt controls. Systemic and chronic administration of hybrid-g7-NPs-chol did not rescue this defect in HD mice (Fig. 5A).

To test further motor abilities, we analyzed spontaneous locomotion activity in the activity cage test. During disease progression, HD mice showed a severe hypokinetic phenotype as demonstrated by reduced global activity, total distance travelled, and number of rearings compared to wt mice both at 9 and 11 weeks of age. At 9 weeks, HD mice treated with hybrid-g7-NPs-chol had a better performance for global activity and total distance travelled compared to HD mice treated with saline, even if they did not reach the same performance observed in wt mice. Moreover, these differences were lost at 11 weeks of age, suggesting that the amount of cholesterol delivered in the brain is not sufficient to counteract motor deficits at a late symptomatic time point, when the HD phenotype worsen (Fig. 5B and C). When we looked at the number of rearings, no rescue was measured in HD mice treated with hybrid-g7-NPs-chol (Fig. 5D). As a measure of anxiety-like behavior, the time that mice spent exploring the periphery or center area of the arena during the activity cage test was also

evaluated (Fig. 5E). HD animals spent more time in the periphery compared to wt mice, indicating anxiety related behavior. Cholesterol delivery did not rescue this parameter (Fig. 5F).

To study neuromuscular functions and strength we determined the force developed by the mice with grip strength test. Muscular strength was reduced in HD mice from 9 weeks of age and it was completely rescued by hybrid-g7-NPs-chol at both 9 and 11 weeks of age (Fig. 5G).

As marker of disease progression, we measured hindlimb clasping with the paw clasping test, a test widely used to measure neurological features in several mouse models of neurodegeneration. HD mice treated with hybrid-g7-NPs-chol ameliorated this phenotype (Fig. 5H).

Furthermore, we found that 44% of the analyzed R6/2 animals treated with saline suffered from epileptic seizures, while only 18% of R6/2 mice injected with hybrid-g7-NPs-chol were affected.

Finally, to evaluate cognitive function we performed the novel object recognition (NOR) test. As expected, long-term memory declined during disease progression in HD mice, with a marked impairment in the ability to discriminate novel and familiar objects at 11 weeks of age. HD mice treated with hybrid-g7-NPs-chol performed similarly to wt mice, indicating that this treatment completely prevents cognitive decline in these animals (Fig. 5I). Weight loss was observed in R6/2 mice starting from late time point (10 weeks of age). Remarkably, this parameter was rescued in male R6/2 mice treated with hybrid-g7-NPs-chol (Fig. 5L and M).

Collectively, these results indicate that the dose of cholesterol delivered and released in the brain with chronic treatment is sufficient to prevent cognitive decline over time and ameliorate some motor defects at 9 weeks of age. However, the fast and aggressive phenotype of this HD mouse model does not allow to evaluate the long-term effect of this treatment when all cholesterol is released from the NPs, which may require several weeks.

To explore eventual side effects of chronic administration of hybrid-g7-NPs-chol, we then sought to analyze the inflammation status of treated mice. Cytokines, chemokines, and growth factors are cell signaling proteins, mediating a wide range of physiological responses, including immunity and inflammation and are also associated with a spectrum of neurodegenerative diseases (Rocha *et al.* 2016; Nagatsu *et al.* 2000). Through the simultaneous detection of 23 analytes in a single well of a 96-well microplate, we analyzed the inflammation status in striatum, cortex, liver, and plasma from HD mice treated with saline or with hybrid-g7-NPs-chol. In general, we did not observe gross changes in the level of the analytes analyzed, except increased level of IL-2 in the striatum, decreased level of Eotaxin in cortex and of IL-1a and IL2 in plasma of R6/2 mice treated with hybrid-g7-NPs-chol compared to R6/2 mice treated with saline (Table 1). These findings suggest that the chronic treatment with hybrid-g7-NPs-chol is safe in R6/2 mice. Moreover, clinical observation of the mice during

chronic administration regimens did not reveal any cases of mortality in the treated and control groups. As well, there were no signs of abnormal behavioral reactions and general clinical symptoms. Overall, these results suggest that chronic administration of hybrid-g7-NPs-chol does not lead to side effects in HD mice.

Conclusion Remarks

Previous studies pointed out the benefits of strategies aimed at delivering cholesterol to the HD brain (Valenza *et al.* 2015, Birolini *et al.* 2020) but the dose of cholesterol that reaches the brain is critical to have a complete rescue of both motor and cognitive defects. With the aim of develop a new and non-invasive strategy that is testable in patients, hybrid-g7-NPs-chol were produced with improved chemical-physical properties and increased cholesterol loading due to their hybrid structure (Belletti *et al.* 2018). Here, we characterized hybrid-g7-NPs-chol *in vivo* in a transgenic mouse model of HD. We demonstrated that hybrid-g7-NPs-chol are up-taken and reach different cell types in the brain, where they accumulate over the time and release cholesterol that becomes available for neuronal functions. Importantly, NPs are rapidly degraded in the plasma and in peripheral tissues without a detectable inflammation response. Once released, cholesterol exerts its functions in the brain, by inducing endogenous cholesterol synthesis and rescuing behavioral deficits in R6/2 mice. These systems can be optimized further in order to transport not only cholesterol but also other molecules that can be useful for HD and other brain pathologies. Importantly, intranasal administration (Passoni *et al.* 2020) of these systems can be also exploited to increase the efficacy of drug delivery to the brain. Finally, we highlighted the utility of cholesterol as drug model to define delivery systems based on nanoparticles.

Materials and methods (in Supplementary Material)

1. Production and characterization of hybrid-g7-NPs-chol

Starting from published results (Belletti et al, 2018; Valenza et al, 2015), we produced hybrid-g7-NPs-chol using a nanoprecipitation method. In details, hybrid-g7-NPs-chol (MIX-N and MIX-SE) were formulated starting from 50 mg of a mixture of cholesterol (Sigma-Aldrich, Milan, Italy), PLGA (PLGA R503H Evonik, Essen, Germany) and PLGA-g7 in a weight ratio of 1:0.8:0.2 (25mg chol, 20mg PLGA, 5mg PLGA-g7).

PLGA-g7 was synthesized via amide formation in the Laboratory of Nanomedicine of the University of Modena and Reggio Emilia, following a previously described protocol (Rigon et al., 2019; Tosi et al., 2007). Pure g7 was purchased from Mimotopes (Clayton, Victoria, Australia).

To obtain MIX-N, cholesterol and PLGA mixture was dissolved in acetone (4 mL). The organic phase was added dropwise into 50 mL of a 0.5% (w/v) Pluronic-F68 aqueous solution at 45 °C under magnetic stirring (1300 rpm). After 20 minutes, the organic solvent was removed at 30 °C under reduced pressure (10 mm Hg). Hybrid-g7-NPs-chol were recovered and purified three times by an ultracentrifugation process carried out at 14,500 rpm for 10 min (4 °C; Sorvall RC28S, Dupont, Brussels, Belgium) to remove the unformed material and the free surfactant fraction in the solution. NPs were re-suspended in 3 mL of a 0.2% (w/v) Pluronic-F68 aqueous solution at room temperature and gently sonicated until completely resuspended.

As cryoprotectant, 150 mg of threalose (Sigma-Aldrich, Milan, Italy) dissolved in 0,5mL of 0.2% Pluronic-F68 solution were added to the NPs suspension before flash freezing with dry ice and methanol bath. NPs were stored at -20°C until use.

Hybrid-g7-NPs-d6-chol were obtained using the same protocol described above. For the formulation, 50 mg of a mixture of D6 Chol:PLGA:PLGA-g7 in weight ratio of 1:0.8:0.2 (25mg D6 Chol, 20mg PLGA, 5mg PLGA-g7) were used.

Hybrid-cy5-g7-NPs-bodipy-chol were produced with the same protocol described above, adding 2% in weight of cy5 derived PLGA and 2% in weight of bodipy cholesterol (Avanti, Alabama, USA). Cy5-PLGA was synthesized in the Laboratory of Nanomedicine of the University of Modena and Reggio Emilia using a protocol published in Duskey *et al.* 2020. The total composition was a mixture of Chol:Chol-Bodipy:PLGA:PLGA-Cy5:PLGA-g7 in weight ratio of 0.96:0.04:0.76:0.04:0.2 (24 mg Chol, 1 mg Chol-Bodipy, 19 mg PLGA, 1 mg PLGA-Cy5, 5 mg PLGA-g7). After centrifugation, NPs were resuspended in an aqueous solution of Pluronic-F68 2% and added of trehalose as previously reported before flash freezing.

Chemico-physical and morphological characterization

100ul of each type of NPs suspension was freeze-dried (-60 °C, 1 · 10⁻³ mm/Hg for 48 h; LyoLab 3000, Heto-Holten, Allerod, Denmark) and the yield (Yield%) was calculate as follows:

$$\text{Yield (\%)} = \frac{(\text{mg of freeze dried MIX-N or MIX-SE})}{(\text{mgPLGA} + \text{mg Chol})} \times 100$$

Mean particle size (Z-Average) and polydispersity index (PDI) of the samples were determined using a Zetasizer Nano ZS (Malvern, UK; Laser 4 mW He-Ne, 633 nm, Laser attenuator Automatic, transmission 100–0.0003%, Detector Avalanche photodiode, Q.E.>50% at 633 nm). Samples were diluted in MilliQ water

at about 0.1 mg/mL. The results were also expressed as intensity distribution, i.e. the size 10% [D (10)], 50% [D(50)] and 90% [D(90)], below which all the MIX NPs are placed. The zeta potential (ζ -pot l) was measured using the same equipment with a combination of laser Doppler velocimetry and phase analysis light scattering (PALS). All data are expressed as means of at least three determinations carried out for each prepared lot (three lots for each sample).

The morphology of the samples was evaluated by atomic force microscopy (AFM) (Park Instruments, Sunnyvale, CA, USA) and scanning transmission electron microscopy (STEM) as reported in Belletti et al 2018, confirming the same results as reported in supplementary figure S1.

AFM analysis were conducted at about 20 °C operating in air and in non-contact mode using a commercial silicon tip-cantilever (high resolution noncontact “GOLDEN” Silicon Cantilevers NSG-11, NT-MDT, tip radius 10 nm; Zelenograd, Moscow, Russia) with stiffness of about 40 Nm⁻¹ and a resonance frequency around 160 kHz. A drop of each MIX-NPs suspension was diluted with distilled water (about 1:5 v/v) before application on a small mica disk (1 cm×1 cm).

After 2 minutes, the excess of distilled water was removed using a paper filter and the sample analyzed. Two kinds of images were obtained: the first is a topographical image and the second is indicated as “error signal”. This error signal is obtained by comparing two signals: the first one representing the amplitude of the vibrations of the cantilever, and the second the amplitude of a reference point. The images obtained by this method show small superficial variations of the samples. Images were processed and analyzed using software from Gwyddion (Department of Nanometrology, Czech Metrology Institute, Brno, Czech Republic).

The internal structure/architecture of the samples was analyzed by scanning transmission electron microscopy (STEM). Briefly, a drop of a water-diluted suspension of the samples (about 0.03 mg/mL) was placed on a 200-mesh copper grid (TABB Laboratories Equipment, Berks, UK), allowed to adsorb, and the suspension surplus was removed by filter paper. All grids were analyzed using a Nova NanoSEM 450 (FEI, Oregon, USA) transmission electron microscope operating at 30 kV using a STEM II detector in Field free mode.

Quantification of cholesterol content

To quantify the amount of cholesterol hybrid-g7-NPs-chol, NPs previously lyophilized to calculate the yield (~1 mg) were dissolved in 0.3 mL of chloroform, followed by addition of 0.6 mL of isopropyl alcohol to precipitate the polymer. The mixture was vortexed (15 Hz for 1 min; ZX3, VelpScientifica, Usmate, Italy) and then filtered (polytetrafluoroethylene filter, porosity 0.20 μ m, Sartorius). The amount of Chol in the sample was quantified by RP-HPLC using an HPLC apparatus comprised a Model PU980 pump provided with an injection valve with a 50 μ L sample loop (Model 7725i Jasco) and an UV detector at 210 nm (UV975, Jasco). Chromatography separation was carried out on a Synchronics C18 (250×4.6 mm; porosity 5 μ m; Thermo Fisher Scientific, Waltham, MA, USA) at r.t. and with a flow rate of 1.2 mL/min, operating in an isocratic mode using 50:50 v/v acetonitrile:ethanol as mobile phase. The solvents of the mobile phase were filtered through 0.45 μ m hydrophilic polypropylene membrane filters (Sartorius) before their use. Chromatographic peak areas of

the standard solutions were collected and used for the generation of calibration curves. Linearity was assumed in the range of 50-500 $\mu\text{g}/\text{mL}$ ($r^2=0.99$). All data are expressed as the mean of at least three determinations. The chemico-physical properties, concentration and cholesterol amount in g7-NPs used in this work are described in Table S1 along with morphological analysis with AFM and STEM (Figure S1).

2. Colony management

All animal experiments were approved and carried out in accordance with Italian Governing Law (D.lgs 26/2014; Authorization n.581/2019-PR issued July 29, 2019 by Ministry of Health); the NIH Guide for the Care and Use of Laboratory Animals (2011 edition) and EU directives and guidelines (EEC Council Directive 2010/63/UE).

Our R6/2 colony lifespan was approximately of 12-13 weeks and only males were used to maintain it (Mangiarini *et al.* 1996). Transgenic 6-weeks old R6/2 males were mated with wild type females (B6CBAF1/J, purchased from Charles River). CAG repeat length that could affect strain productivity, general behavior, litter size, pup survival, genotype frequency, phenotype was monitored every 6 months with a range between 150-180 CAGs.

Mice were weaned and then genotyped at 3 weeks of age (\pm 3 days) and they were housed under standard conditions in enriched cage ($22 \pm 1^\circ\text{C}$, 60% relative humidity, 12 hours light/dark schedule, 3–4 mice/cage, with food and water ad libitum).

3. Mice treatments

For biodistribution studies, cholesterol release study and quantitative analysis, 7-weeks-old wt or R6/2 mice were treated with 1, 2 or 3 I.P. injections. For chronic experiments, R6/2 mice were treated with 2 I.P. injections at week, from 5 to 9 weeks of age. Wt and R6/2 littermates treated with saline solution was used as controls. In all the experiments, mice received 660 μg of cholesterol in each injection.

4. Immunohistochemistry and image acquisition

Animals were deeply anesthetized with Avertin 2.5% and transcardially perfused with PFA 4%. Brains, lungs and liver were collected in PFA 4% for 2h and then in 30% sucrose to prevent ice crystal damage during freezing in OCT. 15 μm -thick brain coronal sections or lung and liver sections were counterstained with the nuclear dye Hoechst 33258 (1:10.000, Invitrogen) and then mounted under cover slips using Vectashield (Vector Laboratories). To study the co-localization of g7-NPs-*chol*_2.0 with neuronal and glial markers, 15 μm -thick brain coronal sections were incubated with the following primary antibodies for 3h at RT: rabbit anti-DARPP32 (1:100, Cell Signalling, 2306); mouse anti-NeuN (1:100, Millipore, MAB377); rabbit anti-GFAP (1:250, Dako, Z0334); rabbit anti-IBA1 (1:100, Wako, 019-1971). Anti-rabbit Alexa Fluor 488-conjugated goat secondary antibodies (1:500; Invitrogen) or anti-mouse Alexa Fluor 488-conjugated goat secondary antibodies (1:500; Invitrogen) were used for detection (1h at RT). Sections were counterstained

with the nuclear dye Hoechst 33258 (1:10.000, Invitrogen) and then mounted under cover slips using Vectashield (Vector Laboratories).

Images were acquired the following day with a confocal microscope (Leica SP5). Laser intensity and detector gain were maintained constant for all images and 3-z steps images were acquired at 40x. To quantify hybrid g7-NPs-chol in different tissues, ImageJ software was used to measure the fluorescence of cy5 (n=4 images/mouse/tissue).

To quantify the released bodipy cholesterol from g7-NPs-chol_2.0, Volocity software was used using the plug-in “find objects” and “calculate object correlation” (n=6 images/mouse/tissue).

5. liquid chromatography-mass spectrometry (LC-MS) analysis for d6-chol

A recently validated method was used (Passoni et al., 2020). Briefly, 50 µL of plasma was diluted with 200 µL of ethanol containing 200 ng of beta-sitosterol, used as internal standard. Samples were vortexed and centrifuged at 13 200 rpm for 15 min and aliquots of the supernatants were injected directly into the LC-MS system. Forty milligrams of each brain area and peripheral tissue were homogenized in 1 mL of ethanol/water 4:1 (v/v), containing 500 ng of internal standard. Homogenates were centrifuged for 15 min at 13 200 rpm at 4 °C, and aliquots of the supernatants were injected into the LC-MS system. D6-chol levels were determined using a 1200 Series HPLC system (Agilent Technologies, Santa Clara, CA, U.S.A.) interfaced to an API 5500 triple quadrupole mass spectrometer (Sciex, Thornhill, Ontario, Canada). The mass spectrometer was equipped with an atmospheric pressure chemical ionization (APCI) source operating in positive ion and multiple reaction monitoring (MRM) mode to measure the product ions obtained in a collision cell from the protonated [M – H₂O]⁺ ions of the analytes. The transitions identified during the optimization of the method were m/z 375.3–152.1 (quantification transition) and m/z 375.3–167.1 (qualification transition) for D6-chol; m/z 397.3–147.1 (quantification transition) and m/z 397.3–161.1 (qualification transition) for β-sitosterol (IS). D6-chol and beta-sitosterol were separated on a Gemini C18 column (50 × 2 mm; 5 µm particle size), using an isocratic gradient in 100 % methanol at 35 °C.

6. Gas chromatography-mass spectrometry (GC-MS) analysis for neutral sterols and 24S-OHC

Experiments were performed as described in Birolini *et al.* 2020.

7. Behavioral tests

Mice behavior was evaluated at 9 and 11 weeks of age.

Rotarod test: mice were tested over three consecutive days. Firstly, animals were trained on a rotating bar at 4 rpm for 5 minutes (apparatus model 47600, Ugo Basile). One hour later, mice were tested for three consecutive accelerating trials of 5 minutes with the rotarod speed linearly increasing from 4 to 40 rpm. The latency to fall from the rod was recorded for each trial and averaged.

Activity Cage test: animals were placed in an arena (25 cm × 25 cm) (2Biological Instrument) and allowed to freely move for an hour in presence of a low-intensity white light source. Movements were assessed by an

automated tracking system (Actitrack software, 2Biological Instrument) connected to infrared sensors surrounding the arena. Total distance travelled, mean velocity speed, and numbers of rearings were analyzed. The % of time that mice explored the periphery or the center area of the was evaluated as a measure of anxiety-like behavior.

Novel Object Recognition (NOR) test: in the habituation stage, mice were placed into an empty non-reflective arena (44 × 44 × 44 cm) for 10 minutes. In the familiarization stage, two identical objects (A' and A'') were presented to each animal for 10 minutes. The day after, during the test stage, animals were exposed to one familiar object (A'') and a new object (B) for 10 minutes. All phases of the test were conducted with a low-intensity white light source. The index of discrimination was calculated as (time exploring the novel object–time exploring the familiar object)/(time exploring both objects) × 100. Mice exploring less than 7 sec. were excluded from the analysis due to their inability to perform the task.

Paw clasping test: animals were suspended by the tail for 30 seconds and the clasping phenotype was graded according to the following scale: level 0, no clasping; level 1, clasping of the forelimbs only or both fore- and hindlimbs once or twice; and level 2, clasping of both fore- and hindlimbs more than three times or more than 5 s.

Grip strength test: animals were lifted by the tail, lowered towards the grip (Ugo Basile) and gently pulled straight back with consistent force until they released its grip. The forelimb grip force, measured in grams, was recorded. The test was repeated for 5 times, and measures were averaged.

8. Bio-Plex

Animals were deeply anesthetized with Avertin 2.5% to collect blood which was centrifuged at 13.000 rpm at 4°C for 15 minutes to obtain the plasma. Striatum, cortex, and liver were isolated and frozen. 10 mg of striatum, cortex and liver were homogenize using a tissue grinder in 1 mL of lysing solution according to manufacturer instructions (Bio-Plex® Cell Lysis Kit, Biorad, #171304011). The lysate was frozen at -80°C, sonicated at 40% for 20 seconds and centrifuged at 4.500 rcf at 4°C for 4 minutes to collect the supernatant. The supernatant was quantified using DC™ Protein Assay Kit I (Biorad, #5000111) and samples were diluted to a final concentration of 500 ug/mL. To perform the Bio-Plex assay, 150 uL of assay buffer were added to 150 uL of samples.

Concerning the plasma, samples were centrifuged at 1.500 rcf at 4°C for 5 minutes. 60 uL of assay buffer and 120 uL of sample diluent were added to 60 uL of plasma.

Cytokine levels were measured by using a Bio-Plex murine cytokine 23-Plex assay kit (Biorad, #M60009RDPD) according to manufacturer instructions using the Luminex 200 System, Multiplex Bio-Assay Analyzer.

9. Statistics

Prism 8 (GraphPad software) was used to perform statistical analyses. G-power software was used to pre-determine group allocation, data collection and all related analyses. For animal studies, mice were assigned

randomly, and sex was balanced in the various experimental groups; animals from the same litter were divided in different experimental groups; blinding of the investigator was applied to *in vivo* procedures and all data collection. Grubbs' test was applied to identify outliers. For each set of data to be compared, we determined whether data were normally distributed or not to select parametric or not parametric statistical tests. The specific statistical test used is indicated in the legend of all results figures. **Table S2** summarizes all the trials and read-outs performed.

Acknowledgments

The authors acknowledge the scientific and technical assistance of Dr. Chiara Cordiglieri, responsible of the INGM Imaging Facility (Istituto Nazionale Genetica Molecolare – INGM, Milan, Italy). This research was supported by Telethon Foundation (GGP17102) to E.C. and by Italian Ministry of Health (RF-2016- 02361928) to M.S. and E.C.

Author contributions

M.V., G.T., B.R. and E.C. conceived the study; G.B. performed *in vivo* experiments, performed immunostaining experiments and provided confocal images and quantification; G.T., B.R. and M.A.V. conceptualized and developed NPs; J.T.D., I.O., F.DR., produced and characterized chemico-physical features of NPs. C.C., V.L. and F.T. performed GC-MS analysis and analyzed the data; A.P., M.F., L.C., R.B. and M.S. performed LC-MS analysis for d6-chol and analyzed the data; G.B., M.V. and M.B. performed bioplex analysis; M.V. and G.B. collected study data and performed statistical analyses; M.V. and E.C. oversaw and coordinated responsibility for all research activities and their performance and provided experimental advice throughout the work; E.C. secured the funding, the collaborations and the execution of the entire project. M.V., G.B., and E.C. wrote the paper that has been edited and reviewed by all authors.

Figure Legends

Figure 1. *In vivo* distribution of hybrid-cy5-g7-NPs-chol

A. Experimental paradigm used in the study. Wild type mice (n=2 mice/MIX/time point) were treated with a single or multiple I.P. injection of hybrid-cy5-g7-NPs-chol (MIX-N or MIX-SE) and sacrificed at different time point. Brain, liver and lung were collected for distribution analysis.

B-C. Representative confocal images of cortex and striatum slices from wt mice that received 1 or 3 I.P. injection hybrid-cy5-g7-NPs-chol (MIX-N in B or MIX-SE in C) and sacrificed after 4h, 24h, 1w, and 2w with relative quantification.

D. Representative confocal images of immunostaining against DARPP32, GFAP, and IBA1 (green) on coronal sections of brains isolated from wt mice I.P. injected with hybrid-cy5-g7-NPs-chol labelled with cy5 (red) and sacrificed 2 weeks after the injection. White arrowheads indicate intracellular g7-NPs. Hoechst were used to counterstain nuclei (Ho, blue).

Data are expressed as the number of g7-NPs for 1 field of view \pm standard error of the mean.

Figure 2. Cholesterol release from hybrid-cy5-g7-NPs-bodipy-chol: qualitative analysis

A. Experimental paradigm used in the study. Wild type and R6/2 mice (n=3 mice/genotype/MIX/time point) were treated with a single I.P. injection of hybrid-cy5-g7-NPs-bodipy-chol (MIX-N or MIX-SE) and sacrificed at different time point. Brain and liver were collected for the analysis.

B-C. Representative confocal image of brain slices from R6/2 mice I.P. injected with hybrid-cy5-g7-NPs-bodipy-chol (MIX-N in B or MIX-SE in C) and sacrificed after 24 h or 2 weeks and relative co-localization of bodipy-chol and g7-NPs.

Figure 3. Cholesterol release from hybrid-g7-NPs-d6-chol: quantitative analysis

A. Experimental paradigm used in the study. R6/2 mice were treated with a single I.P. injection of hybrid-g7-NPs-d6-chol (MIX-N) and sacrificed at different time point. Striatum, cortex, cerebellum, liver, lung, kidney, and plasma and liver were collected for mass spectrometry analysis (n=3 mice/time point).

B-C. Levels of d6-chol in striatum, cortex, cerebellum (B), liver, lung, kidney, and plasma (C) measured by LC-MS.

D. Experimental paradigm used in the study. R6/2 mice were treated with hybrid-g7-NPs-d6-chol (MIX-N) from 5 weeks of age to 9 weeks of age with 2 I.P. injection/week and sacrificed 2 weeks after the last I.P. injection. Striatum, cortex, cerebellum, liver, lung, kidney, and plasma and liver were collected for mass spectrometry analysis (n=3 mice).

E-F. Levels of d6-chol in striatum, cortex, cerebellum (E), liver, lung, kidney, and plasma (F) measured by LC-MS (red dots). Black dots refer to the measurement represented in figure 3B-C.

Data are expressed as means \pm standard error of the mean.

Figure 4. Endogenous cholesterol synthesis and catabolism in the striatum of HD mice following systemic and chronic administration of hybrid-g7-NPs-d6-chol

A. Experimental paradigm used in the study. R6/2 mice were treated with PLGA-g7-NPs-chol and hybrid-g7-NPs-chol from 5 weeks of age to 9 weeks of age with 2 I.P. injection/week. Wt and R6/2 littermates were treated with saline solution as controls. Striatum and cortex were collected at 11 weeks of age for mass spectrometry analysis (n=3-4 mice/group).

B-D. Lanosterol (B), lathosterol (C), and desmosterol (D) level measured by GC-MS in the striatum of wt saline, R6/2 saline, R6/2 + PLGA-g7-NPs-chol, and R6/2 + hybrid-g7-NPs-chol mice at 11 weeks of age (n=3-4 mice/group).

Data are expressed as means \pm standard error of the mean. Each dot corresponds to the value obtained from each animal.

Statistics: one-way ANOVA with Newman-Keuls post-hoc test (*p<0.05; **p<0.01; ***p<0.001).

Figure 5. Cognitive and motor abilities of R6/2 mice following systemic and chronic administration of hybrid-g7-NPs-d6-chol

A. Latency to fall (seconds) from an accelerating rotarod at 8 and 10 weeks of age in wt saline (n=24-25), R6/2 saline (n=15-17), and R6/2 + hybrid-g7-NPs-chol (n=17).

B-F. Global motor activity (B), total distance traveled (C), and number of rearings (D) in an open-field test at 9 and 11 weeks of age in wt saline (n=24-25), R6/2 saline (n=15-17), and R6/2 + hybrid-g7-NPs-chol (n=17). Representative track plots (E) generated from the open-field test from wt saline (n=24-25), R6/2 saline (n=15-17), and R6/2 + hybrid-g7-NPs-chol (n=17) and relative quantification (F) of the time spent in the center and in the periphery (%) of the arena at 11 weeks of age.

G. Grip strength (grams) at 9 and 11 weeks of age in wt saline (n=16-24), R6/2 saline (n=11-22), and R6/2 + hybrid-g7-NPs-chol (n=17).

H. Paw clasping at 9 and 11 weeks of age in wt saline (n=25), R6/2 saline (n=22), and R6/2 + hybrid-g7-NPs-chol (n=17).

I. Discrimination index (DI %) in the novel object recognition test of wt saline (n=22-23), R6/2 saline (n=13-19), and R6/2 + hybrid-g7-NPs-chol (n=10-13) at 9 and 11 weeks of age. DI above zero indicates a preference for the novel object; DI below zero indicates a preference for the familiar object.

L-I. Body weight (grams) of male (L) and female (M) mice at different time point.

Data are from three independent trials and shown as scatterplot graphs with means \pm standard error. Each dot corresponds to the value obtained from each animal.

Statistics: one-way ANOVA with Newman-Keuls post-hoc test (*p<0.05; **p<0.01; ****p<0.0001; ***p<0.001) or unpaired Student t-test (#p<0.05; ##p<0.01).

Table 1. Inflammatory response of R6/2 mice following systemic and chronic administration of hybrid-g7-NPs-d6-chol

Analysis of cytokines and chemokines by Bio-Plex array on the striatum, cortex, liver, and plasma of R6/2 saline vs R6/2 + hybrid-g7-NPs-chol mice (n=4-5 mice/group).

Data are normalized on R6/2 saline mice and are expressed as means \pm standard error of the mean.

Statistics: unpaired Student t-test (*p<0.05).

Figure S1. Morphological characterization of hybrid-cy5-g7-NPs-chol

Morphological analysis with AFM and STEM.

Figure S2. *In vivo* distribution of hybrid-cy5-g7-NPs-chol in other brain and peripheral tissues

A-B. Representative confocal images of hippocampus, lung, and liver slices from wt mice that received 1 or 3 I.P. injection hybrid-cy5-g7-NPs-chol (MIX-N in A or MIX-SE in B) and sacrificed after 4h, 24h, 1w, and 2w with relative quantification. Hoechst were used to counterstain nuclei (Ho, blue).

Data are expressed as the number of g7-NPs for 1 field of view \pm standard error of the mean.

Figure S3. Cholesterol release from hybrid-cy5-g7-NPs-bodipy-chol: qualitative analysis

Representative confocal image of liver brain slices from R6/2 mice I.P. injected with hybrid-cy5-g7-NPs-bodipy-chol (MIX-N) and sacrificed after 24 h, 1 week or 2 weeks and relative co-localization of bodipy-chol and g7-NPs.

Table S1. Chemico-physical properties of NPs involved in the study

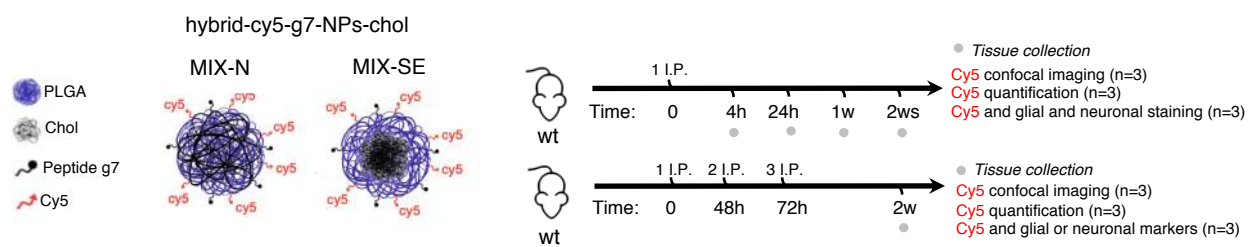
Amount of nanoparticles in each lot is expressed as concentration (mg/mL); dimensions of samples is expressed with Z-Average values (nm); homogeneity of the samples is expressed as Polydispersity Index (PDI); surface charge is expressed as ζ potential (mV); amount of cholesterol is expressed in mg.

Table S2. Summary of all the trial performed

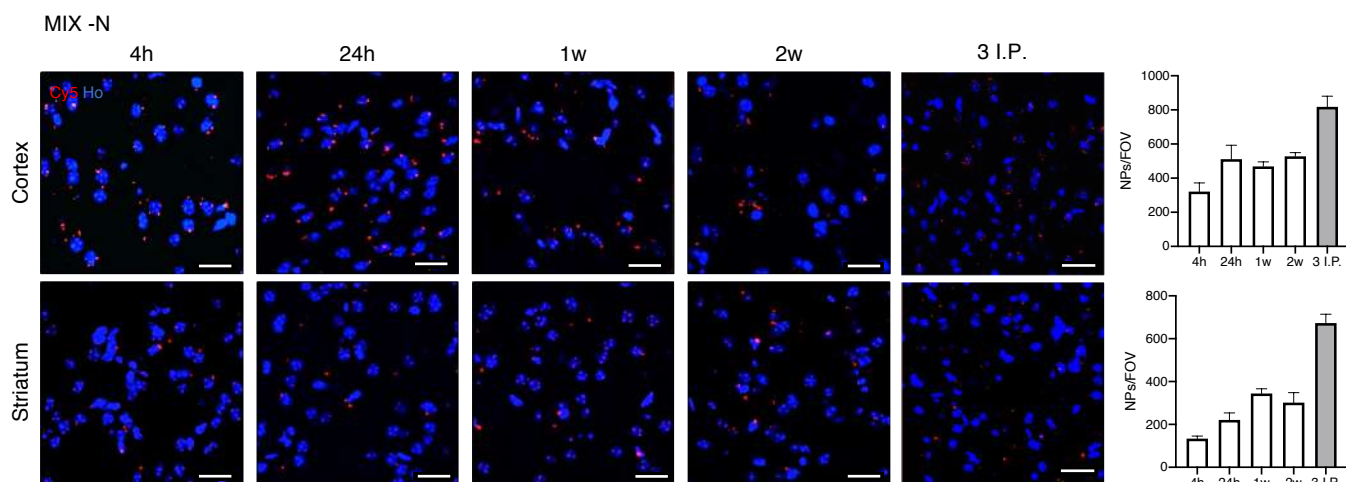
Summary of all the trial performed and the animals used for this study.

FIGURE 1: In vivo distribution of hybrid-cy5-g7-NPs-cholesterol

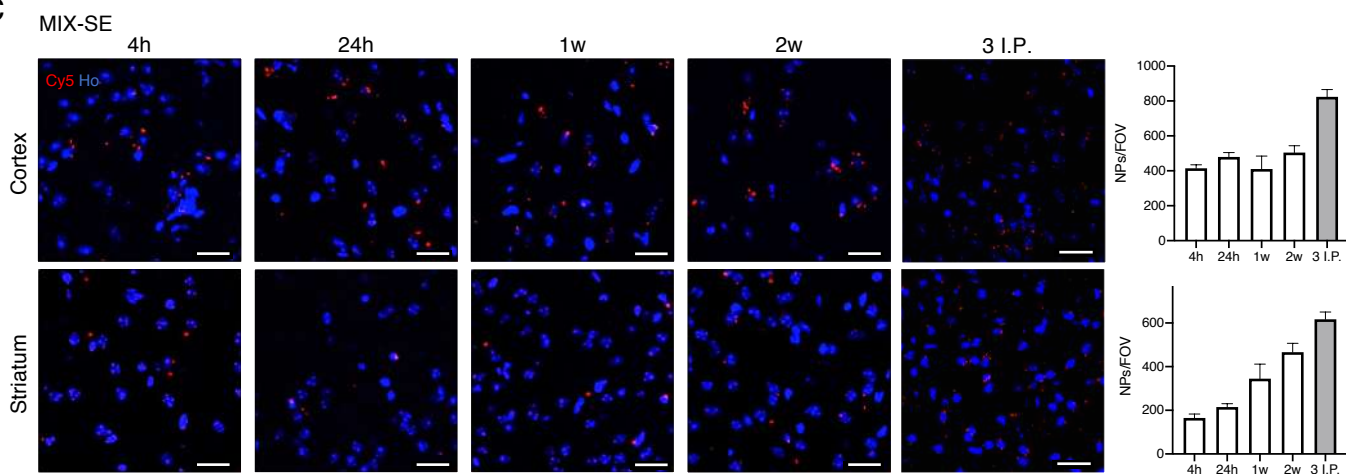
A



B



C



D

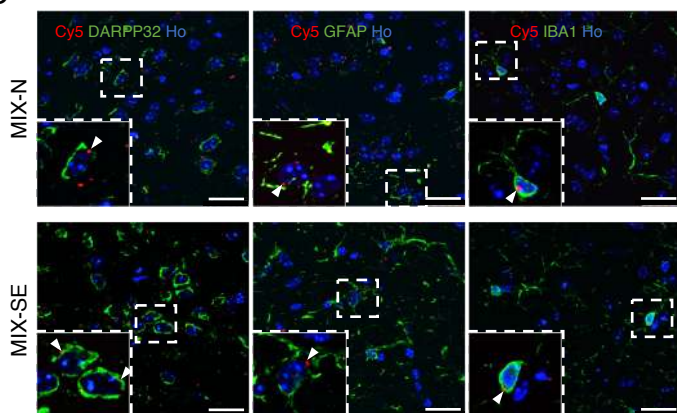
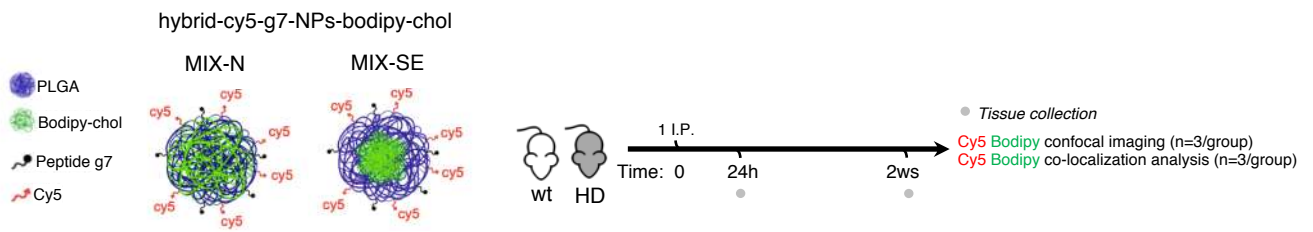
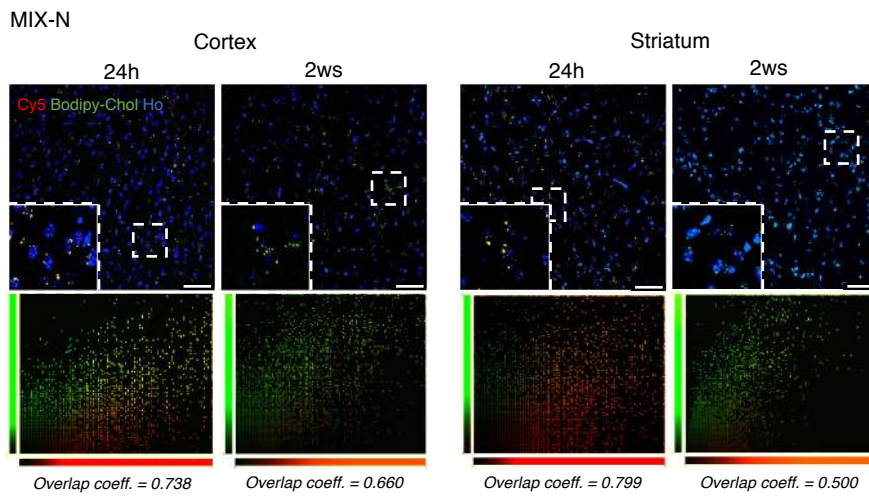


FIGURE 2: Cholesterol release from hybrid-cy5-g7-NPs-bodipy-cholesterol: qualitative analysis

A



B



C

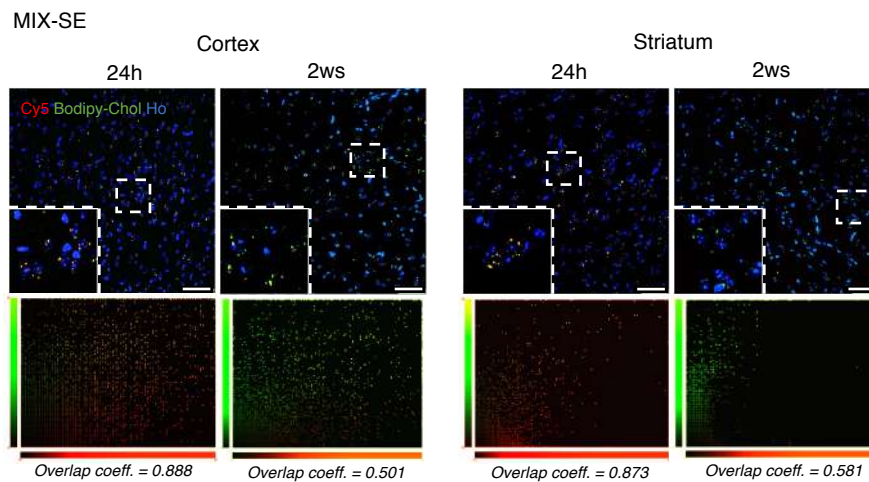
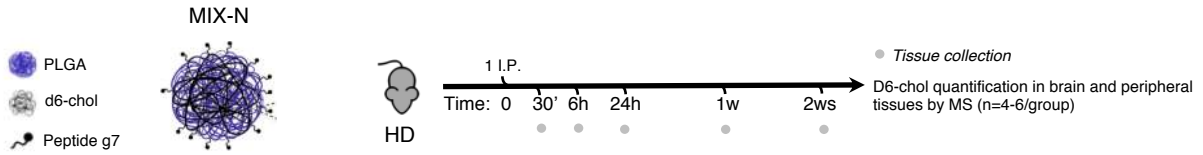


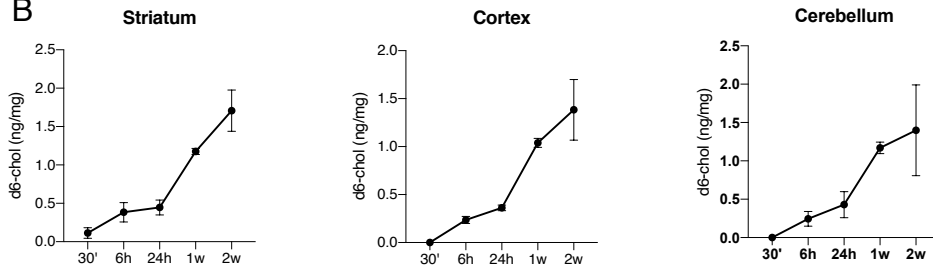
FIGURE 3: Cholesterol release from hybrid-cy5-g7-NPs-d6-chol: quantitative analysis

A

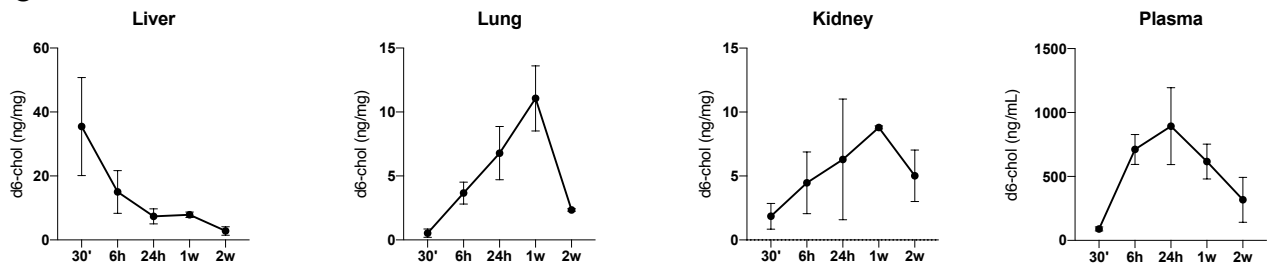
hybrid-cy5-g7-NPs-d6-chol



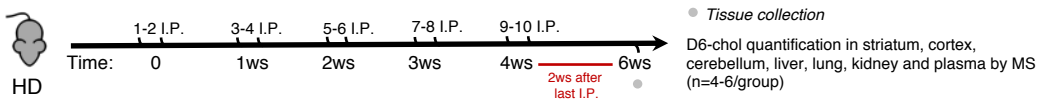
B



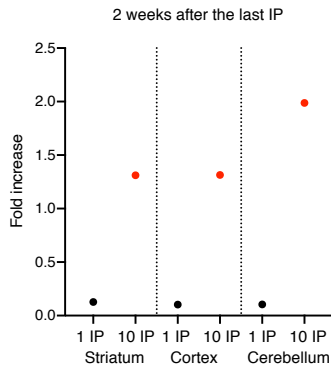
C



D



E



F

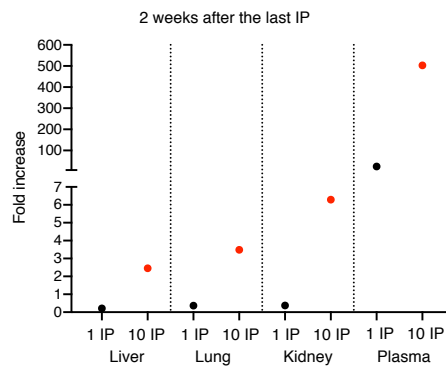
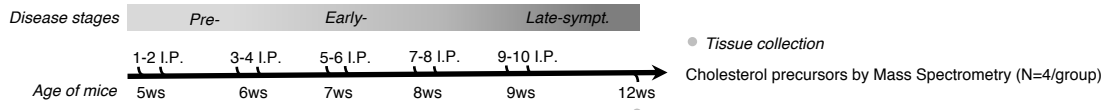
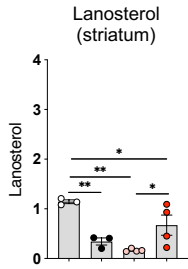


FIGURE 4: endogenous cholesterol catabolism and synthesis following cholesterol supplementation

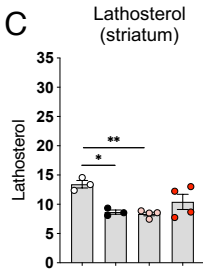
A



B



C



D

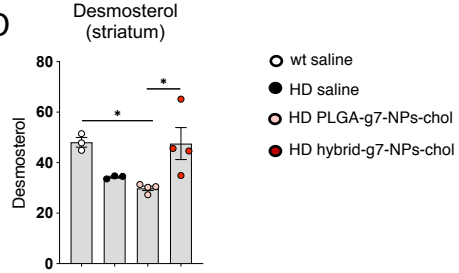


FIGURE 5: Cognitive and motor abilities of R6/2 mice following cholesterol supplementation

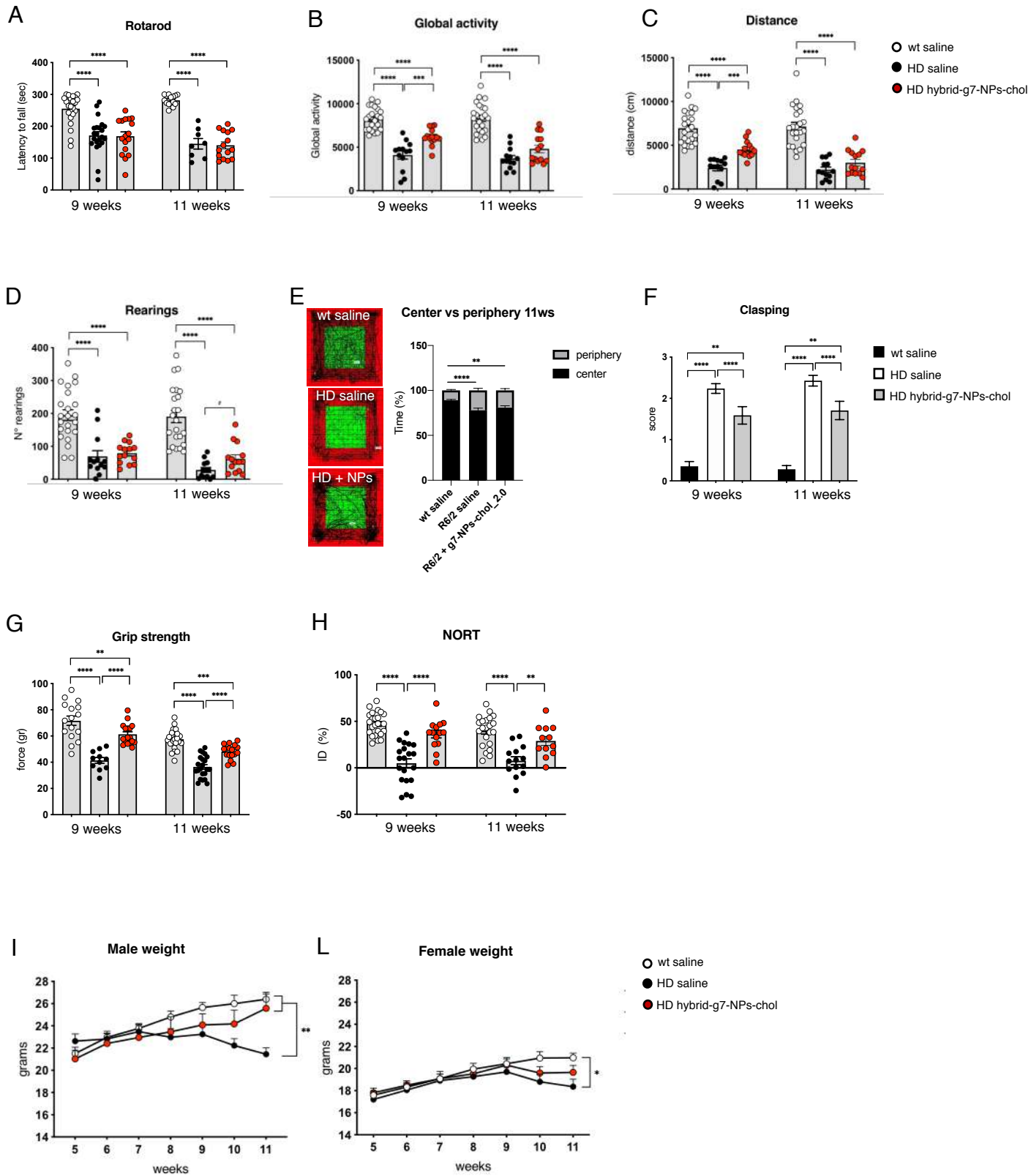


Table 1: Inflammatory response of R6/2 mice following cholesterol supplementation

Analyte	Striatum		Cortex		Liver		Plasma	
	R6/2 + hybrid-g7-NPs-choI (vs R6/2 saline)		R6/2 + hybrid-g7-NPs-choI (vs R6/2 saline)		R6/2 + hybrid-g7-NPs-choI (vs R6/2 saline)		R6/2 + hybrid-g7-NPs-choI (vs R6/2 saline)	
	Mean \pm SEM	p-value	Mean \pm SEM	p-value	Mean \pm SEM	p-value	Mean \pm SEM	p-value
IL-1a	1,010 \pm 0,025	0,9348	0,927 \pm 0,033	0,3884	0,976 \pm 0,111	0,8622	0,212 \pm 0,032	0,0078 **
IL-1b	1,055 \pm 0,200	0,8435	0,747 \pm 0,134	0,3254	1,088 \pm 0,184	0,7466	0,920 \pm 0,381	0,8608
IL-2	1,415 \pm 0,076	0,0081 **	0,708 \pm 0,013	0,1058	1,159 \pm 0,179	0,4831	0,398 \pm 0,081	0,0467 *
IL-3	1,012 \pm 0,298	0,9739	0,771 \pm 0,097	0,2840	1,031 \pm 0,038	0,7151	N/D	
IL-4	0,632 \pm 0,110	0,5871	1,472 \pm 0,499	0,4103	0,744 \pm 0,182	0,4333	0,429 \pm 0,184	0,3575
IL-5	1,264 \pm 0,165	0,5834	1,276 \pm 0,561	0,6831	0,924 \pm 0,158	0,7211	0,330 \pm 0,085	0,1610
IL-6	1,061 \pm 0,132	0,7723	1,019 \pm 0,102	0,9132	0,889 \pm 0,133	0,5446	N/D	
IL-9	0,789 \pm 0,143	0,4046	0,836 \pm 0,145	0,5136	0,900 \pm 0,112	0,6095	N/D	
IL-10	1,020 \pm 0,291	0,9593	0,677 \pm 0,123	0,1301	1,109 \pm 0,354	0,8100	1,175 \pm 0,002	0,1610
IL-12 (p40)	1,666 \pm 0,435	0,2450	0,667 \pm 0,176	0,3861	1,843 \pm 0,113	0,1025	0,921 \pm 0,236	0,8124
IL-12 (p70)	0,944 \pm 0,242	0,8601	0,798 \pm 0,138	0,3859	0,803 \pm 0,116	0,4620	N/D	
IL-13	0,950 \pm 0,072	0,5667	0,835 \pm 0,069	0,2902	0,977 \pm 0,097	0,8460	1,099 \pm 0,152	0,5886
IL-17	1,345 \pm 0,414	0,5198	0,892 \pm 0,125	0,2902	1,194 \pm 0,104	0,3108	1,345 \pm 0,414	0,5198
Eotaxin	1,695 \pm 0,359	0,1447	0,447 \pm 0,078	0,0228 *	0,958 \pm 0,215	0,8927	0,809 \pm 0,195	0,5637
G-CSF	0,943 \pm 0,203	0,8490	0,914 \pm 0,153	0,6571	1,001 \pm 0,120	0,9970	0,987 \pm 0,148	0,9529
GM-CSF	1,025 \pm 0,222	0,9314	1,060 \pm 0,220	0,8302	1,090 \pm 0,080	0,4218	0,724 \pm 0,188	0,2956
ING-gamma	1,413 \pm 0,272	0,2607	0,899 \pm 0,102	0,5404	1,155 \pm 0,184	0,4968	0,749 \pm 0,322	0,7225
KC	1,337 \pm 0,302	0,3446	1,340 \pm 0,169	0,1438	0,988 \pm 0,313	0,9742	0,489 \pm 0,086	0,1494
MCP-1	0,947 \pm 0,375	0,9216	0,907 \pm 0,196	0,8058	1,657 \pm 0,414	0,2082	1,365 \pm 0,689	0,7636
MIP-1a	1,133 \pm 0,326	0,7593	0,816 \pm 0,138	0,4708	1,065 \pm 0,126	0,6874	0,525 \pm 0,222	0,5987
MIP-1b	1,511 \pm 0,186	0,1488	0,731 \pm 0,137	0,3533	0,920 \pm 0,192	0,7806	0,614 \pm 0,452	0,4762
Ranteg	1,010 \pm 0,075	0,9520	1,020 \pm 0,134	0,9271	0,882 \pm 0,087	0,5915	0,998 \pm 0,231	0,9954
TNF-a	1,173 \pm 0,276	0,6227	0,854 \pm 0,249	0,6447	1,100 \pm 0,352	0,8135	0,851 \pm 0,371	0,8106

data expressed as fold-change (HD + hybrid-g7-NPs-choI vs HD saline)

FIGURE S1: size, homogeneity, surface charge, cholesterol content and morphology of the hybrid-g7-NPs-cho

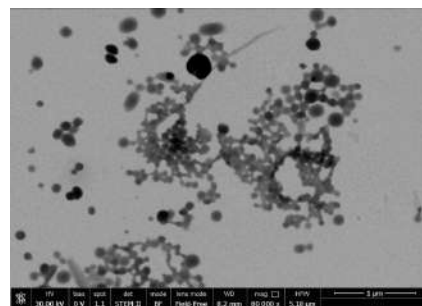
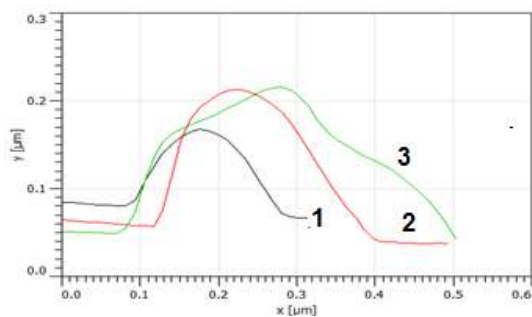
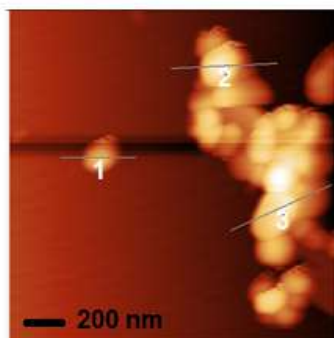
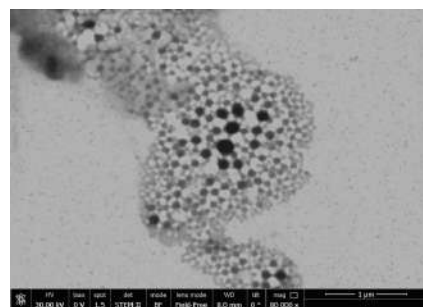
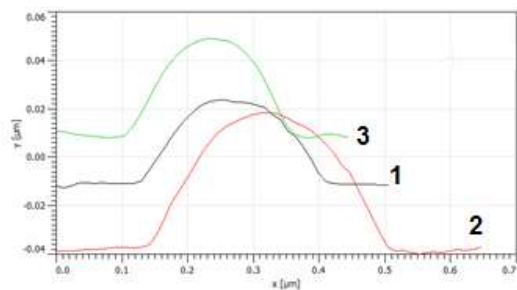
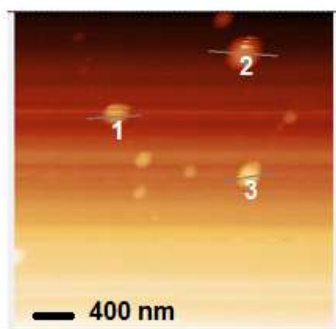


FIGURE S2: *In vivo* distribution of hybrid-cy5-g7-NPs-chol

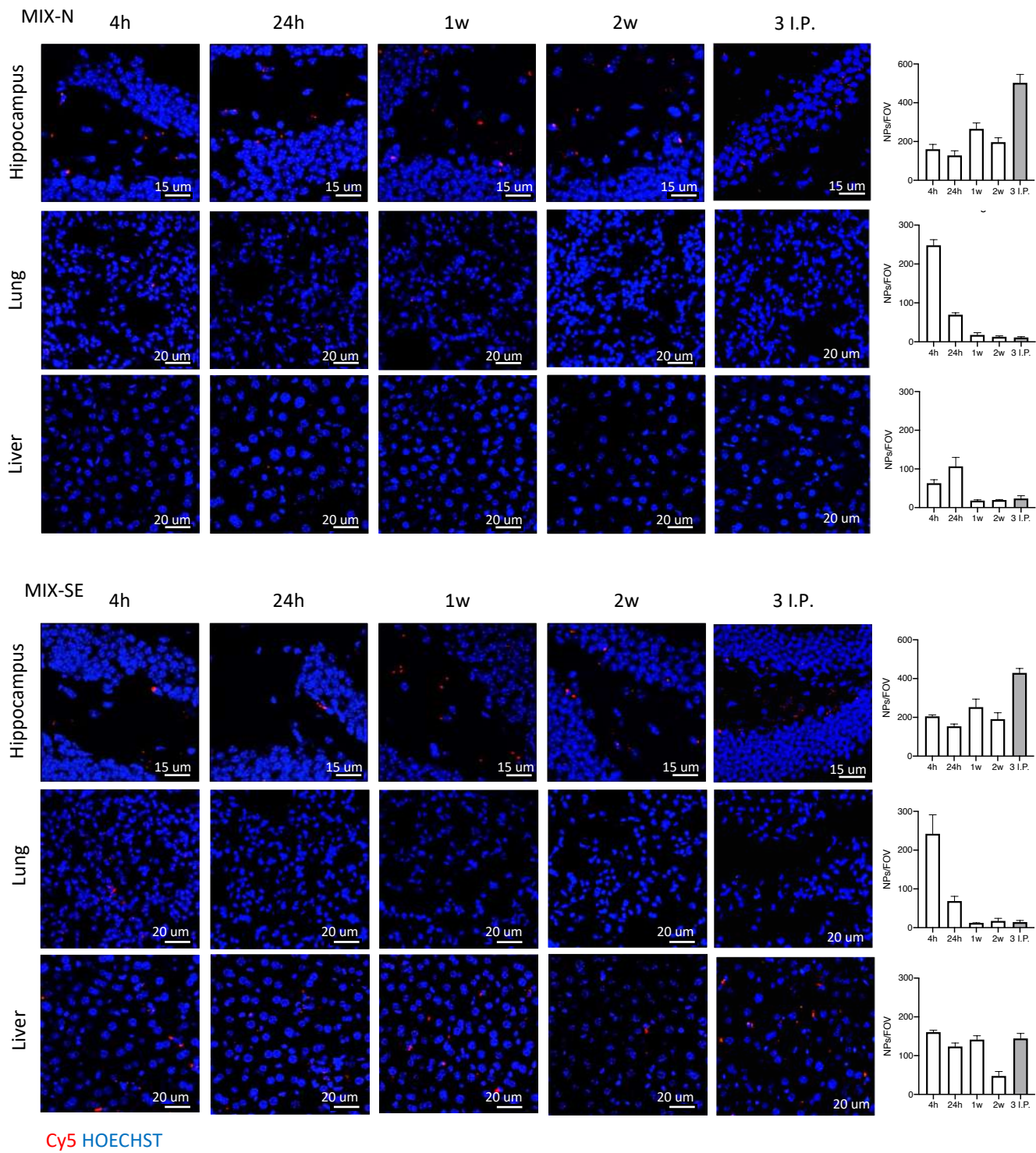


FIGURE S3: Cholesterol release from hybrid-cy5-g7-NPs-bodipy-cho: qualitative analysis

A

MIX-N

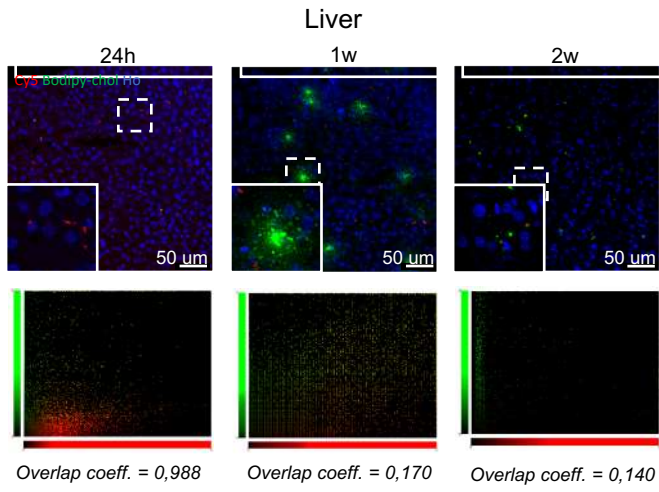


Table S1

Experiment	NPs	Concentration (mg/mL)	Z-av (nm)	PDI	Z-pot (mV)	Amount of chol (mg)
Bio-distribution	hybrid-cy5-g7-NPs-chol MIX-N	5,9	287	0,23	-22	N/D
	hybrid-cy5-g7-NPs-chol MIX-N	7,5	240	0,18	-20	N/D
	hybrid-cy5-g7-NPs-chol MIX-SE	7,8	234	0,18	-21	N/D
	hybrid-cy5-g7-NPs-chol MIX-SE	7	250	0,13	-21	N/D
Chol release: qualitative analysis	hybrid-cy5-g7-NPs-bodipy-chol MIX-N	8,5	246	0,21	-18	N/D
	hybrid-cy5-g7-NPs-bodipy-chol MIX-SE	8,8	270	0,16	-19	N/D
Chol release: quantitative analysis	hybrid-g7-NPs-d6-chol	8,9	230	0,21	-14	33
	hybrid-g7-NPs-d6-chol	8,5	225	0,195	-22	29
	hybrid-g7-NPs-d6-chol	7,3	203	0,253	-21	22
	hybrid-g7-NPs-d6-chol	9	225	0,234	-22	22
Behavioral analysis	PLGA-g7-NPs-chol	9	180	0,05	-22	0,9
	hybrid-g7-NPs-chol	8,5	255	0,28	-23	35
	hybrid-g7-NPs-chol	8,5	244	0,26	-24	36
	hybrid-g7-NPs-chol	9,4	240	0,27	-24	35
	hybrid-g7-NPs-chol	9,8	256	0,28	-24	42
	hybrid-g7-NPs-chol	7,7	243	0,26	-29	38
	hybrid-g7-NPs-chol	8	255	0,31	-19	34,9

Table S2

Trial number and date	Experimental groups	Bio-distribution	Chol release: quantitative analysis	Chol release: quantitative analysis	Mass spectrometry analysis	Behavioral analysis	Bioplex analysis
		N mice	N mice	N mice	N mice	N mice	N mice
1 - September 2017	wt + hybrid-cy5-g7-NPs-chol MIX-N	10					
	wt + hybrid-cy5-g7-NPs-chol MIX-SE	10					
2 - November 2017	wt + hybrid-cy5-g7-NPs-chol MIX-N	10					
	wt + hybrid-cy5-g7-NPs-chol MIX-SE	10					
3 - February 2018	wt + hybrid-cy5-g7-NPs-bodipy-chol MIX-N		9				
	wt + hybrid-cy5-g7-NPs-bodipy-chol MIX-SE		9				
	R6/2 + hybrid-cy5-g7-NPs-bodipy-chol MIX-N		9				
	R6/2 + hybrid-cy5-g7-NPs-bodipy-chol MIX-SE		9				
4 - May 2018	R6/2 + hybrid-g7-NPs-d6-chol MIX-N			21			
5 - January 2019	wt saline				3	10	
	R6/2 saline				3	8	
	R6/2 + hybrid-g7-NPs-chol				3	10	
6 - November 2019	wt saline					5	
	R6/2 saline					4	4
	R6/2 + PLGA-g7-NPs-chol					10	
	R6/2 + hybrid-g7-NPs-chol					7	5